Departamento de Física de la Materia Condensada

Instituto de Nanociencia de Aragón (INA)

Instituto de Ciencias de Materiales de Aragón (ICMA)

Universidad de Zaragoza-CSIC

TESIS DOCTORAL

Electrical conduction and magnetic properties of nanoconstrictions and nanowires created by focused electron/ion beam and of Fe_3O_4 thin films

Memoria presentada por D. Amalio Fernández-Pacheco Chicón a la Facultad de Ciencias de la Universidad de Zaragoza, para optar al grado de Doctor en Ciencias Físicas

Zaragoza, mayo de 2009

Resumen de la tesis doctoral

La tecnología existente en los discos duros de los ordenadores actuales, de usotan generalizado en la sociedad actual, representa uno de los primeros ejemplos de aplicación directa de la nanotecnología en el campo de la electrónica, donde coexisten la producción en masa del producto con los límites existentes del nanomagnetismo, es decir, con los procesos magnéticos fundamentales en la escala nanométrica. El extremo control de los granos constituyentes de la información, respecto a su estabilidad térmica y sus campos de inversión de la imanación, han permitido un grado de almacenamiento 10^7 veces mayor desde la salida al mercado, en 1957 por IBM, del primer disco duro.

Este aumento exponencial en el rendimiento de almacenaje ha sido llevado a cabo gracias a avances tecnológicos de gran impacto. Un ejemplo paradigmático es el descubrimiento de la magnetorresistencia gigante (GMR) por Albert Fert [1] y Peter Grunberg [2], por lo que recibieron el premio Nobel en 2007. Este fenómeno relaciona la configuración magnética de ciertas estructuras y su resistencia eléctrica con una sensibilidad inusitada hasta la fecha, lo que abrió la puerta a la miniaturización de ciertos dispositivos. Este descubrimiento es también el *alma mater* de otros tipos de estructuras basados en un gran control del crecimiento de láminas delgadas, con espesores de nanómetros.

Además, a lo largo de los últimos años se han desarrollado técnicas de nanofabricación que permiten tallar materiales y fabricar dispositivos en los que las dimensiones laterales de los mismos alcanzan tallas nanométricas. Este enorme desarrollo en técnicas litográficas ha sido básicamente consecuencia de la necesidad de una mayor miniaturización de los transistores en circuitos integrados [3]. Así pues, otro tipo de dispositivos electrónicos se están ahora

postulando como candidatos a sustituir a los actuales, donde el magnetismo da un paso más en su interacción con la electrónica, lo que se conoce como el área de *espintrónica*.

En esta tesis se han estudiado las propiedades de transporte eléctrico, tanto de láminas delgadas magnéticas, donde las anchuras al paso de corriente fueron litografiadas a tamaño de micras, como otras estructuras de talla lateral nanométrica, tanto magnéticas como no magnéticas, de gran interés tanto para la comprensión de ciertos fenómenos físicos que se producen en estos materiales como para su potencial aplicación en espintrónica, y en otros campos de la nanotecnología.

Uno de las aproximaciones propuestas para el almacenamiento de la información en el futuro son las denominadas MRAM ("Magnetic Random Acces Memory"), memorias no volátiles magnéticas, donde la información queda almacenada en una unión túnel magnética (MTJ), de rápido acceso y escritura. Una MTJ consiste es un "emparedado" formado por dos electrodos magnéticos separados por una barrera aislante (Al_2O_3, MgO,...). Al aplicar una tensión eléctrica aparece una corriente constituida por electrones que realizan el efecto túnel entre los electrodos a través de la barrera. Si al aplicar un campo magnético permutamos entre las configuraciones magnéticas de los electrodos paralela y antiparalela, obtenemos un efecto magnetorresistivo (magnetorresistencia túnel: TMR) [4]. A partir de 1995 se ha desarrollado extraordinariamente la tecnología necesaria para la realización de las uniones túnel. Gracias a su minúsculo tamaño pueden integrarse como sensores magnetorresistivos en cabezas lectoras así como realizar memorias no volátiles de alta densidad de información y bajo consumo [5]. El valor de la magnetorresistencia túnel depende de forma fundamental de una magnitud

clave: la polarización de espín, que es la diferencia normalizada de espines "up" menos el "down" existentes en el nivel de Fermi, es decir, los responsables de la conducción eléctrica. En la tesis doctoral hemos estudiado el óxido de hierro Fe_3O_4, denominado magnetita, donde se ha predicho teóricamente que existe un 100% de polarización de espín (a estos materiales se les denomina "half metals"), lo cual daría en principio valores de TMR muy altos. Previo a su implementación en dispositivos, es necesario un conocimiento fundamental de sus propiedades de magnetotransporte en el material en forma de lámina delgada. Resultados previos en la literatura se han centrado en el estudio de la MR derivada de defectos estructurales, denomiandos anti-phase boundaries, que cambian sustancialmente las propiedades de transporte de la magnetita [6-8]. En nuestro caso, hemos estudiado otros efectos como son el Efecto Hall Planar o el efecto Hall, de vital importancia desde un punto de vista fundamental en la física del estado sólido [9, 10].

Otros tipos de estructuras muy interesantes de los que se han reportado en la literatura efectos de MR superiores al 100% son los presentes en constricciones magnéticas de tamaño atómico, donde el hecho de que la conducción de electrones sea de tipo balístico, y no difusivo, da lugar a una fenomenología radicalmente diferente a la del mundo macroscópico. Experimentos iniciales en contactos de Ni, realizados por electrodeposición y mecánicamente, mostraron efectos acuñados como magnetorresistencia balística (BMR) superiores a los existentes por magnetorresistencia gigante [11, 12]. Valores también enormes se encontraron para la MR anisótropa (BAMR) [13, 14], debidos a un aumento sustancial del acoplamiento espín-órbita, junto con modificaciones sustanciales en la estructura electrónica [15, 16]. Sin embargo, una gran cantidad de voces en la comunidad científica se han

opuesto a estos resultados, asociándolos a efectos espurios, relacionados con la magnetoestrición o reconfiguraciones atómicas dentro del contacto [17, 18]. Experimentos limpios, donde se minimicen posibles artefactos, parecen de esta manera, cruciales para determinar si estos efectos son intrínsecos, o no.

Recientemente, otro tipo de memorias sugeridas por Stuart Parkin en IBM son las denominadas "racetrack memories" [19], donde la información viene dada por las diferentes paredes de dominio existentes en nanohilos planares (normalmente de permaloy: Ni_xFe_{1-x}). La enorme reducción de las dimensiones, junto con la posibilidad de construir las memorias en una configuración tridimensional, permitiría alcanzar límites insospechados hasta la fecha. Este campo está de gran actualidad, con avances significativos como la creación de una lógica aritmética análoga a la existente en la actualidad, basada en el movimiento de estas paredes [20], o el cambio de la imanación del material sin necesidad de aplicar campos magnéticos externos, sino mediante el momento de espín ("spin torque") que produce una densidad de corriente apreciable [21].

La tesis doctoral realizada podría dividirse en dos objetivos fundamentales. El primero se centra en la fabricación de materiales de tamaño micro- o nanométrico, mediante el uso de técnicas de litografía (óptica, y de haces focalizados de electrones/iones). El segundo, el estudio de las propiedades de transporte eléctrico, así como el magnetismo, de las estructuras fabricadas. De forma fundamental, se han estudiado las propiedades magnéticas y de transporte eléctrico en estructuras con alto interés en aplicaciones en espintrónica y nanomagnetismo. A continuación, y de una

forma cronológica, se esbozan los objetivos concretos, las tareas realizadas, así como la metodología llevada a cabo durante la tesis en los temas desarrollados. Por completitud, las publicaciones derivadas de la investigación son también incluidas.

A) LÁMINAS EPITAXIALESDE MAGNETITA

En primer lugar, con la llegada de los equipos de litografía óptica al Instituto de Nanociencia de Aragón (INA), se desarrollaron y optimizaron, junto con el equipo técnico del INA, los procesos necesarios para dicha litografía, en láminas de magnetita (Fe_3O_4) crecidas epitaxialmente en la dirección (001) sobre sustratos de óxido de magnesio (MgO). Como resultado de dichos procesos, se fabricaron estructuras micrométricas de Fe_3O_4, con materiales metálicos como oro o aluminio en los pads,derivados de una segunda etapa de litografía, para minimizar la alta resistencia de contacto existente en dicho óxido, de manera que el estudio se llevara a cabo en el mayor rango de espesores y temperaturas posibles. En paralelo a dicho trabajo, se instaló un equipo de medidas de magnetotransporte en el Instituto de Ciencias de Materiales de Aragón (ICMA), constituido por un criostato de ciclo cerrado y un electroimán, junto con una fuente de corriente y un nanovoltímetro. Dicha instalación consistió, entre otras tareas, en el desarrollo de todos los programas de control de los dispositivos vía PC.

Las propiedades de magnetotransporte de los electrodos de Fe_3O_4 fueron ampliamente estudiados. En concreto, láminas de varios espesores (2 nm – 350 nm) mediante el método de Van der Paw, a temperatura ambiente; además electrodos de espesores: 40, 20 y 10 nm en función de la temperatura, por encima y por debajo de la transición de Verwey (transición metal-aislante), típica de este material medio-metálico. El estudio sistemático fue hecho en

medidas de magnetorresistencia (MR) en diferentes configuraciones, y de voltajes transversales al paso de la corriente, como son el efecto Hall anómalo y el efecto Hall Planar, de alto interés fundamental y tecnológico. Al efecto Hall ordinario no se pudo acceder con los campos utilizados en un laboratorio convencional, con lo que el estudio se completó realizando experimentos en una gran infraestructura europea en Nijmegen (Holanda), el laboratorio de altos campos magnéticos (HFML) perteneciente a la Universidad de Radboud-Nijmegen. Como consecuencia de todo este trabajo se han realizado 4 publicaciones científicas [I-IV].

B) NANOCONSTRICCIONES DE METALES MAGNÉTICOS

El siguiente paso de la tesis fue la creación de estructuras de variado carácter, con la llegada al INA de un equipo "Dual Beam". Dicho instrumento consta de una columna de haces focalizados de electrones (FEB) y de iones de Galio (FIB), con energía de aceleración máxima de 30 kV. Dichas columnas permiten visualizar y fabricar estructuras con tamaños mínimos del orden de 10 nm. Este magnífico equipo de nanolitografía fue complementado con una plataforma para la medida de transporte eléctrico, de manera simultánea a la toma de imágenes o procesado de la muestra.

Así pues, en primer lugar comentaremos el trabajo realizado en la fabricación de nanoconstricciones de tamaño atómico en materiales metálicos magnéticos, con importantes aplicaciones en dispositivos para espintrónica. En la tesis, se llevó a cabo el desarrollo de un proceso para la fabricación de estos nanocontactos atómicos, con control simultáneo de la resistencia, lo que permite tallar dichos materiales a tamaños muy por debajo de la resolución del

equipo de litografía. La estabilización de los contactos en contacto con la atmósfera, así como el estudio de magnetorresistencia balística (BMR) y magnetorresistencia anisótropa balística (BAMR) ha sido estudiada en una cantidad sustancial de muestras. Como resultado, 3 publicaciones científicas se han llevado a cabo [V-VII].

C) NANOHILOS FABRICADOS MEDIANTE HACES FOCALIZADOS DE ELECTRONES E IONES

Una gran cantidad de la tesis ha estado relacionada con la creación de nanoestructuras mediante el depósito de materiales con el FEB o FIB (focused-electron/ion-beam- induced-deposition: FEBID/FIBID). Esta técnica de nanolitografía consiste en el depósito mediante fase vapor (CVD) de metales inducido por el haz de electrones o iones, una vez que un gas precursor ha sido introducido en la cámara. Los haces focalizados disocian las moléculas del gas, que ha quedado adsorbido en la superficie, creando un depósito localizado donde el haz ha sido escaneado. La resolución nanométrica del haz se traduce en depósitos también nanométricos. Esta técnica no está muy extendida entre la comunidad científica, si es comparada por ejemplo con la litografía electrónica (EBL). Sin embargo, tiene una ventaja evidente respecto a ésta, y es que se consigue una resolución espacial similar, usando una técnica de un solo paso, evitando el depósito intermedio de resinas poliméricas, lo que permite una flexibilidad mucho mayor en la creación de nanoestructuras. Durante mi tesis, he estudiado nanohilos fabricados con esta técnica usando los gases precursores: $(CH_3)_3Pt(CpCH_3)$, $W(CO)_6$ y $Co_2(CO)_8$. La gran riqueza de procesos que acaecen en este tipo de técnica da lugar a una riquísima fenomenología que he estudiado en gran profundidad, especialmente en el caso del primer y tercer precursor.

En concreto, para los depósitos de Pt-C con el primer gas [$(CH_3)_3Pt(CpCH_3)$], hemos observado diferencias sustanciales en la composición de los depósitos, dependiendo de si el proceso se llevaba a cabo con FEB o FIB [VIII], habiendo detectado una transición metal-aislante en función de la cantidad de Pt existente en los nanohilos [IX]. Esto puede entenderse en el marco de la teoría de sólidos desordenados establecida por Mott [22], donde la matriz carbonosa que acoge las inclusiones metálicas de Pt es un semiconductor amorfo, que es dopado con dichas impurezas, y que a consecuencia del desorden existente tiene niveles localizados dentro del gap del semiconductor, así como un alargamiento de las bandas.

En el caso de depósitos usando el segundo precursor [$W(CO)_6$] crecidos por FIBID, el importante grado de desorden, así como la naturaleza amorfa del material, da lugar a un superconductor con una temperatura crítica de unos 5 K, temperatura sustancialmente mayor que el W metálico puro [23]. Mediante una colaboración con el grupo del profesor Vieira en la Universidad Autónoma de Madrid, se ha podido observar mediante espectroscopia túnel (STS) que depósitos de dicho material es un paradigma de superconductor de tipo II que sigue la teoría BCS [X]. Además, se ha podido estudiar la dependencia de la red de Abrikosov de los vórtices en dicho material en función de la temperatura y campo magnético con gran detalle mediante STS [XI], observando que la fusión de dicha red 2D se produce a través de una fase hexática intermedia [XII]. Mi aportación fundamental a este estudio ha sido el análisis composicional y químico de los depósitos de W-C mediante espectroscopía fotoelectrónica de rayos X (XPS). Posteriormente, se ha hecho un estudio comparativo de las propiedades de transporte superconductoras de micro- y nanohilos mediante esta técnica, llegando a la conclusión que las propiedades superconductoras son similares para tallas laterales del orden de 100 nm, lo que

da cuenta de una buena funcionalidad superconductora de dicho material a escala nanométrica [XIII].

Por último, con el último precursor se han crecido nanohilos de cobalto. La alta eficacia de disociación de este precursor permite crear nanoilos tremendamente puros (del orden del 90% atómico). Este hecho, determinado por análisis de dispersión de electrones (EDX), ha sido corroborado mediante medidas de magnetotransporte [XIV] y de magnetometría óptica de efecto Kerr logitudinal (MOKE) con alta resolución espacial [XV]. Esta última técnica se usó en el transcurso de una estancia de dos meses en el Blackett laboratory en el Imperial College (Londres), en el grupo del profesor Russel Cowburn. Durante esta estancia se realizó un estudio de los campos de propagación y nucleación de paredes de dominio de estos nanohilos (XVI], para determinar si dichas estructuras son interesantes en aplicaciones de lógica aritmética basada en el movimiento de paredes de dominio [20], así como en memorias magnéticas no volátiles ("racetrack memories") [19]. Además, se estudió el acoplamiento magnético de electrodos de diferentes formas unidos mediante una constricción de unos 400 nm de anchura, estudio complementado con el trabajo con otro grupo localizado en Berkeley (California), que estudió esos mismos dispositivos mediante microscopía de transmisión de rayos X (STXM), lo que permite resolver zonas magnéticas de la muestra (mediante dicroísmo magnético) con una resolución espacial de unos 40 nm). Estas configuraciones han sido estudiadas mediante simulaciones micromagnéticas, usando el código de acceso libre OOMMF [24].

Publicaciones de la tesis doctoral

[I] J. M. De Teresa, A. Fernández-Pacheco, L. Morellón, J. Orna, J. A. Pardo, D. Serrate, P.A. Algarabel, M.R. Ibarra, *Magnetotransport properties of Fe_3O_4 thin films for applications in Spin Electronics*, Micr. Eng. **84** 1660 (2007)

[II] A. Fernández-Pacheco, J. M. De Teresa, J. Orna, L. Morellón, P.A. Algarabel, J. A. Pardo, M.R. Ibarra*, Universal Scaling of the Anomalous Hall Effect in Fe_3O_4 thin films, Phys. Rev. B (Rapid com.)* **77,** 100403(R) (2008)

[III] A. Fernández-Pacheco, J. M. De Teresa, J. Orna, L. Morellon, P. A. Algarabel, J. A. Pardo, M. R. Ibarra, C. Magen, E. Snoeck, *Giant planar Hall effect in epitaxial Fe_3O_4 thin films and its temperature dependence*, Phys. Rev. B **78**, 212402 (2008)

[IV] A. Fernández-Pacheco, J. M. De Teresa, P.A. Algarabel, J. Orna, L. Morellón, J. A. Pardo, M.R. Ibarra*, Hall Effect and magnetoresistance measurements in Fe_3O_4 thin films up to 30 Tesla, manuscript in preparation.*

[V] A. Fernández-Pacheco, J. M. De Teresa, R. Córdoba, and M. R. Ibarra, *Exploring the conduction in atomic-sized metallic constrictions created by controlled ion etching* Nanotechnology **19**, 415302 (2008)

[VI] J. V. Oboňa, J. M. De Teresa, R. Córdoba, A. Fernández-Pacheco, and M. R. Ibarra, *Creation of stable nanoconstrictions in metallic thin films via progressive narrowing by focused-ion-beam technique and in-situ control of resistance,* Microel. Eng. (2009) in press

[VII] A. Fernández-Pacheco, J. M. De Teresa, R. Córdoba, and M. R. Ibarra, *Tunneling and anisotropic-tunneling magnetoresistance in iron nanoconstrictions fabricated by focused-ion-beam*, submitted to MRS proceedings (2009)

[VIII] J. M. De Teresa, R.Córdoba, A. Fernández-Pacheco, O. Montero, P. Strichovanec, and M.R. Ibarra, *Origin of the Difference in the Resistivity of As-Grown Focused-Ion and Focused-Electron-Beam-Induced Pt Nanodeposits*, *J. Nanomat.* **2009**, 936863 (2009)

[IX] A. Fernández-Pacheco, J. M. De Teresa, R. Córdoba, M. R. Ibarra, *Conduction regimes of Pt-C nanowires grown by Focused-Ion–Beam induced deposition: Metal-insulator transition,* Phys. Rev. B, **79**, 174204 (2009)

[X] I. Guillamón, H. Suderow, S. Vieira, A. Fernández-Pacheco, J. Sesé, R. Córdoba, J. M. De Teresa, M. R. Ibarra, *Nanoscale superconducting properties of amorphous W-based deposits grown with a focused-ion-beam* , New Journal of Physics **10**, 093005 (2008)

[XI] I. Guillamón, H. Suderow, S. Vieira, A. Fernández-Pacheco, J. Sesé, R. Córdoba, J. M. De Teresa, M. R. Ibarra, *Direct observation of melting in a 2-D superconducting vortex lattice*, manuscript in preparation

[XII] I. Guillamón, H. Suderow, S. Vieira, A. Fernández-Pacheco, J. Sesé, R. Córdoba, J. M. De Teresa, M. R. Ibarra, *Superconducting density of states at the border of an amorphous thin film grown by focused-ion-beam*, Journal of Physics: Conference Series (2009), in press

[XIII] J. M. De Teresa, A. Fernández-Pacheco, R. Córdoba, J. Sesé, M. R. Ibarra, I. Guillamón, H. Suderow, S. Vieira***,*** *Transport properties of superconducting amorphous W-based nanowires fabricated by focused-ion-beam-induced-deposition for applications in Nanotechnology*, submitted to MRS proceedings (2009)

[XIV] A. Fernández-Pacheco, J. M. De Teresa, R. Córdoba, M. R. Ibarra, *Magnetotransport properties of high-quality cobalt nanowires grown by focused-electron-beam-induced deposition*, J. Phys. D: Appl. Phys. **42** 055005 (2009)

[XV] A. Fernández-Pacheco, J. M. De Teresa, R. Córdoba, M. R. Ibarra D. Petit , D. E. Read, L. O'Brien, E. R. Lewis, H. T. Zeng, R. P. Cowburn, *Systematic study of the magnetization reversal in Co wires grown by focused-electron-beam-induced deposition,* manuscript in preparation

[XVI] A. Fernández-Pacheco, J. M. De Teresa, R. Córdoba, M. R. Ibarra D. Petit , D. E. Read, L. O'Brien, E. R. Lewis, H. T. Zeng, R. P. Cowburn, *Domain wall conduit behaviour in cobalt nanowires grown by Focused-Electron-Beam Induced Deposition,* Appl. Phys. Lett. **94**, 192509 (2009)

REFERENCIAS

[1] M. N. Baibich et al., Phys. Rev. Lett. **61** 2472 (1988)

[2] G. Binasch, et al., Phys. Rev. B **39**, 4828 (1989)

[3] G. E. Moore, *Int. Electronic Devices Meeting (IEDM)* **75**, 11(1975)

[4] M. Julliere, Phys. Lett. A **54**, 225(1975)

[5] S. S. S. Parkin et al., J. Appl. Phys. **85**, 5828 (1999)

[6] W. Eerenstein et al., Phys. Rev. Lett. **88**, 247204 (2002)

[7] W. Eerestein et al, Phys. Rev. B **66**, 201101(R) (2002)

[8] D. T. Margulies et al., Phys. Rev. Lett. **79**, 5162 (1997)

[9] H. X. Tang et al, Phys. Rev. Lett **90**, 107201 (2003)

[10] S. Onoda et al, Phys. Rev. Lett. **97**, 126602 (2006)

[11] N. García et al, *Phys. Rev. Lett.* **82**, 2923 (1999)

[12] J. J. Verlslujis et al, Phys. Rev. Lett. **87**, 026601 (2001)

[13] A. Sokolov et al, *Nat. Nanotechnology* **2**, 171 (2007)

[14] M. Viret et al, *Eur. Phys. J. B* **1**, 1 (2006)

[15] W. F. Egelhoff et al, J. Appl. Phys **95**, 7554 (2004)

[16] S. –F. Shi et al, Nat. Nanotech. **2**, 522 (2007)

[17] J. Velev et all, Phys. Rev. Lett. **94**,127203 (2005)

[18] D. Jacob et al, Phys. Rev. B **77**, 165412 (2008)

[19] S. S. P. Parkin et al, *Science* **320** 190 (2008)

[20] D. A. Alwood et al, Science **309** 1688 (2005)

[21] D. C. Ralph et al, J. Magn. Magn. Mat. **320**, 1190 (2008)

[22] N. F. Mott, and E. A. Davis, *Electronic Processes in Non-Crystalline Materials,* Oxford University Press (1971)

[23] E. S. Sadki, et al, Appl. Phys. Lett. **85** 6206 (2004)

[24] El código OOMMF está disponible en la dirección web

http://math.nist.gov/oommf/

Conclusiones y perspectivas

Esta tesis doctoral se ha basado en el estudio de las propiedades de magnéticas y de transporte eléctrico en materiales nanométricos, en un amplio rango de escalas: láminas delgadas de Fe_3O_4, nanoconstricciones de tamaño atómico, y nanohilos. En este capítulo se resumen las principales conclusiones de dicho trabajo, así como perspectivas de futuro resultantes de éste. Primero se expondrán conclusiones generales, relacionadas con las técnicas experimentales usadas, así como los métodos de nueva creación desarrollados. En segundo lugar, se expondrán conclusiones específicas de la tesis, en los temas en los que se ha trabajado: láminas delgadas de Fe_3O_4, nanoconstricciones creadas por haces focalizados de iones, y nanohilos creados mediante el depósito local de materiales, usando haces focalizados de electrones e iones.

Conclusiones generales

Esta tesis doctoral ha sido posible gracias a la sinergia de dos institutos de investigación de Zaragoza: el Instituto (mixto, CSIC-Universidad de Zaragoza) de Ciencias de Materiales de Aragón (ICMA), con una larga y reputada experiencia en la investigación de ciencias de materiales, y el Instituto (Universidad de Zaragoza) de Nanociencia de Aragón (INA), de reciente creación. Ésta es la primera tesis defendida en esta región donde se han usado equipos de micro y nanolitografía "top-down" pertenecientes a instituciones de Zaragoza. Durante ésta, nuevos métodos y procedimientos se han desarrollado, que serán usados en el futuro por integrantes de ambos institutos. De especial relevancia son el desarrollo y optimización de algunos de los procesos de litografía óptica y nanolitografía, la puesta en marcha de un equipo para medidas de magnetotransporte, así como protocolos para el control eléctrico de dispositivos, durante el proceso de nanolitografía en un equipo "Dual Beam", pioneros en el ámbito internacional.

Láminas epitaxiales de Fe_3O_4

Debido a su alta polarización de espín, Fe_3O_4 es de alto interés en aplicaciones de espintrónica. Por ello, las propiedades de magnetotransporte en láminas de Fe_3O_4 crecidas de forma epitaxial en MgO (001) han sido estudiadas exhaustivamente. Los procesos de fotolitografía llevados a cabo, han permitido el estudio de las componentes longitudinal y transversal del tensor resistividad, así como su dependencia con la imanación del material, por encima y debajo de la transición de Verwey.

Medidas de resistividad y magnetorresistencia reproducen resultados previos en la literatura, evidenciando el carácter epitaxial de las láminas. Las propiedades de transporte de las láminas ultra-finas están sustancialmente dominadas por la presencia

de “antiphase-boundaries”. Este hecho es también evidente en el estudio sistemático del Efecto Hall Planar, que tiene como consecuencia un valor récord para dicho voltaje transversal a temperatura ambiente. Por debajo de la transición de Verwey, hemos medido valores colosales, hasta la fecha nunca conseguidos en ningún otro material, en el rango de los mΩcm. Los cambios observados en la magnetorresistencia anisótropa, tanto en lo concerniente a su signo como valor absoluto, en función de a temperatura, no están todavía bien entendidos, y deberían ser estudiados en profundidad en ele futuro.

El estudio del efecto Hall Anómalo a lo largo de cuatro órdenes de magnitud de la conductividad longitudinal, ha dado como consecuencia un resultado experimental relevante. La dependencia $\sigma_H \propto \sigma_{xx}^{1.6}$ se cumple en todos los casos, sin importar qué mecanismo de conducción sea responsable del transporte, el mayor o menor grado de importancia en la dispersión de las “anti-phase boundaries”, etc. Esta dependencia es universal para toda clase (material masivo, policristalino, láminas finas epitaxiales…) de magnetita donde se ha medio el efecto Hall anómalo, así como para todos los compuestos cuya conducción es bastante baja (en el régimen “sucio” de conductividades). En nuestra opinión, se deberían desarrollar teorías que clarifiquen cómo el modelo que explica este comportamiento, se adecua a un transporte no metálico, como son la mayoría de materiales en este régimen.

Las primeras uniones-túnel magnéticas, basadas en electrodos de Fe_3O_4 con barrera túnel de MgO están en este momento (2009) siendo crecidas en nuestro laboratorio por J. Orna. Esperamos que la importante experiencia adquirida en esta tesis en lo referente a las propiedades de magnetotransporte y procesos de fotolitografía contribuya a un exitoso desarrollo de estos complejos dispositivos.

Creación de constricciones de tamaño atómico usando un haz focalizado de iones

Se ha desarrollado un nuevo método para la creación controlada de constricciones de tamaño atómico en metales, mediante la medida simultánea de la conducción eléctrica al mismo tiempo que se realiza un ataque usando un haz focalizado de iones. Se ha demostrado que la técnica funciona para los materiales metálicos cromo y hierro, fabricando constricciones atómicas estables dentro de la cámara de preparación, en alto vacío. Este método tiene dos ventajas esenciales respecto a otras técnicas bien establecidas en la literatura, como pueden ser el uso de microscopios túnel, o la fractura mecánica controlada. Primero, es posible la implantación de procesos usando un haz focalizado de iones dentro de los protocolos estándar para la fabricación de circuitos integrados, con lo que posibles aplicaciones basadas en nanocontactos serían incorporadas fácilmente a la industria actual. Segundo, y concerniente a la creación de contactos atómicos en materiales magnéticos, en los que efectos magnetorresistivos de gran cuantía se han descrito previamente, y que han dado pie a una gran polémica debido a que no está claro si son debidos a fenómenos intrínsecos, la adhesión de los átomos formando la constricción a un sustrato, deberían minimizar efectos espurios, haciendo esta técnica más conveniente que otras para este tipo de estudios.

La fragilidad de los contactos al exponerlos a condiciones ambientales ha sido evidente en nanocontactos de hierro. Los resultados obtenidos no son sistemáticos, aunque es claro que en algunos de los dispositivos, el carácter magnético del material se mantiene, a pesar del ataque con iones. Los prometedores resultados de muestras en el régimen túnel de conductividades nos hacen pensar que un estudio sistemático de la magnetorresistencia balística y la magnetorresistencia anisótropa balística se podrá hacer en el futuro. El desarrollo de nuevas estrategias para proteger las constricciones, así como la posibilidad de implementar un equipo de medidas magnéticas adosado a la cámara de fabricación, para evitar la exposición a condiciones ambientales, supondría enormes avances para esta investigación

Nanohilos creados mediante el depósito local inducido mediante haces de electrones e iones focalizados

Una parte importante de la tesis está dedicada al estudio de nanohilos creados mediante estas prometedoras técnicas. El trabajo se ha realizado con tres tipos de gases precursores: $(CH_3)_3Pt(CpCH_3)$, $W(CO)_6$ and $Co_2(CO)_8$, usando, en el primera caso, tanto haces focalizados de electrones como de iones para disociar las moléculas del precursor, mientras que en el segundo y en el tercero se usaron iones o electrones, respectivamente. En este tipo de depósitos locales, de forma general, el material está compuesto de una mezcla de carbono y metal. El profundo trabajo realizado ha permitido tener una visión general de los complejos fenómenos físicos que acaecen en estos procesos, que producen microestructuras completamente diferentes en los materiales depositados. En el caso del primer precursor, dicha microestructura está compuesta de "clusters" de platino dentro de una matriz carbonosa amorfa. Con el segundo gas, se forman depósitos con una estructura completamente amorfa de carbono-wolframio, mientras que en tercero, es posible, mediante el uso de altas corrientes focalizadas, el crecimiento de cobalto policristalino prácticamente puro. Una gran cantidad de fenómenos físicos se han estudiado en cada caso, todos ellos consecuencia de la microestructura particular del material.

En el caso de nanohilos de Pt-C, hemos observado una transición metal-aislante en función de la concentración carbono/metal. Esto parece explicar los resultados contradictorios que existían hasta la fecha con este material, en relación a sus propiedades de transporte. Este trabajo pone de relevancia la importancia de los parámetros elegidos, ya que en este caso particular, nanohilos metálicos o aislantes pueden ser fabricados "a la carta". El descubrimiento de que la conductancia diferencial decrece en un rango de voltajes, en el caso de las muestras más resistivas, demuestra la validez de las teorías desarrolladas para el transporte vía "hopping" bajo altos campos eléctricos, en estructuras nanométricas. El método usado para controlar

la resistencia mientras el depósito se lleva a cabo, análogo al usado para la creación de constricciones, ha demostrado ser de gran utilidad, siendo ahora usado de forma general en nuestro laboratorio.

Mediante el estudio a baja temperatura de las propiedades eléctricas de micro y nanohilos de wolframio depositados mediante haces focalizados de iones, se ha demostrado que estructuras con talla lateral ligeramente menor que 100 nm mantienen sus propiedades superconductoras. Esto, junto con el hecho de que este material posee unas propiedades sin igual, como demuestran las medidas realizadas mediante espectroscopía túnel, en el grupo del profesor Vieira, hacen que este material sea un superconductor nanométrico con enorme potencialidad. Dispositivos como "Nano-SQUIDS" o nanocontactos para medir reflexión Andreev son ejemplos de aplicaciones muy prometedoras, que en este momento se están llevando a cabo en nuestro grupo.

El trabajo llevado a cabo con cobalto depositado mediante haces focalizados de electrones, demuestra que es posible crecer este material con hasta un 90% de pureza, mediante el uso de corrientes moderadamente altas. Como resultado, las propiedades de magnetotransporte de nanohilos de cobalto depositados en esas condiciones son similares a las de hilos del mismo material, fabricados mediante técnicas de nanolitografía más convencionales. El efecto de usar corrientes menores ha sido evidenciado, mediante la degradación de dichas propiedades. Mediante el uso del efecto magneto-óptico Kerr, resuelto en espacio, hemos estudiado ciclos de histéresis en hilos individuales, en un amplio rango de relaciones de aspecto. Los campos coercitivos de estas estructuras presentan una relación lineal con el cociente espesor/anchura, lo cual es una evidencia de que la energía magnetoestática es la que domina las posibles configuraciones de la imanación en los hilos. En el caso de relaciones de aspecto altas, la imanación, en remanencia, queda alineada en la dirección longitudinal del nanohilo. Mediante la creación de nanohilos con forma de L, y utilizando rutinas de campo magnéticas en dos direcciones, hemos demostrado que este material presenta un buen comportamiento en conducción de paredes de

domino, fenómeno denominado en la comunidad científica como “domain wall conduit”. Las ventajas únicas que esta técnica presenta para la fabricación de estructuras tridimensionales, hace este resultado especialmente interesante. Pasos en esta dirección están ahora empezándose a dar. Además, la realización de experimentos en los que la imanación de estos nanohilos sea revertida mediante una alta densidad de corriente, el denominado efecto de momento de espín (“spin-torque”), en vez de mediante la aplicación de un campo magnético externo, son objetivos futuros de esta línea de investigación.

Estudios posteriores, desde un punto de vista general, deberían ser dedicados al estudio de los límites en resolución de estas técnicas de nanolitografía, así como a la determinación de cuán afectadas son sus propiedades funcionales cuando alguna de sus dimensiones se reduce sustancialmente. Otro punto importante es el de obtener materiales metálicos completamente puros, con interés en el campo de la nanoelectrónica, ya que una mayor funcionalidad es altamente deseada en una amplia variedad de aplicaciones. Finalmente, la combinación de varios de estos materiales para crear estructuras híbridas, tales como dispositivos magnéticos/superconductores, en combinación con el buen control de la resistencia de éstos durante su crecimiento, pueden implicar la posibilidad de estudiar nuevos y apasionantes fenómenos.

Acronyms

AF	Antiferromagnetic
AFM	Atomic Force Microscope
AHE	Anomalous Hall effect
AMR	Anisotropic Magnetoresistance
APB	Antiphase Boundary
APD	Antiphase Domain
BAMR	Ballistic Anisotropic Magnetoresistance
BMR	Ballistic Magnetoresistance
BSE	Backscattered electrons
CCR	Closed Cycle Refrigerator
CIP	Current In-plane configuration
CPP	Current Perpendicular-to-plane configuration
CPU	Microprocessor
CVD	Chemical Vapor Deposition
DW	Domain Wall
EBJ	Electrical Break Junction
EBL	Electron Beam Lithography
EDX	Energy Dispersive X-Ray spectroscopy
ES-VRH	Efros-Shklovskii Variable Range Hopping
FCC	Face centered cubic structure
FEB	Focused Electron Beam
FEBID	Focused Electron Beam Induced Deposition
FEG	Field Emission Gun
FIB	Focused Ion Beam
FIBID	Focused Ion Beam Induced Deposition
FM	Ferromagnetic
GIS	Gas Injection System
GMR	Giant Magnetoresistance
GPHE	Giant Planar Hall effect
HDD	Hard Disk
HR-	High Resolution
IT	Information Technology
LG	Longitudinal geometry
LMIS	Liquid Metal Ion Source
MBE	Molecular Beam Epitaxy
MBJ	Mechanical Break Junctions
MOKE	Magneto Optical Kerr Effect
MR	Magnetoresistance
MTJ	Magnetic Tunnel Junction
NW	Nanowire
OHE	Ordinary Hall effect
PE	Primary electrons
PG	Perpendicular Geometry
PECVD	Plasma Enhanced Chemical Vapor Deposition
PHE	Planar Hall effect
PLD	Pulsed Laser Deposition
PPMS	Physical Properties Measurement System
RAM	Random Access Memory
SCs	Superconductor Materials
SE	Secondary Electrons

SEM	Scanning Electron Microscope
SP	Superparamagnetism
SQUID	Superconducting Quantum Interference Device
SRIM	Stopping & Range of Ions in Matter
STEM	Scanning Transmission Electron Microscopy
STM	Scanning Tunneling Microscopy
STS	Scanning Tunneling Spectroscopy
TEM	Transmission Electron Microscopy
TG	Transversal Geometry
TMR	Tunneling Magnetoresistance
TAMR	Tunneling Anisotropic Magnetoresistance
VRH	Variable Range Hoping
XPS	X-Ray Photoelectron Spectroscopy
XRD	X-Ray Diffraction

Index

Acronyms

Chapter 1

Introduction

This chapter intends to serve as a general introduction to nanoelectronics. The existing limits in the current information, silicon-based, technology are exposed. The breakthrough that the discovery of Giant-Magnetoresistance supposed for the information storage in hard-disk-drives is explained, as an example of how nanoelectronics can overcome these limits. Some of the most promising materials and effects for the future of nanoelectronics are briefly summarized, paying special attention to the spintronics field. Finally, the types of nanostructures studied in this thesis, from a geometrical point of view, are compared.

1.1. Introduction to nanotechnology

Richard Feynman, Nobel Prize in Physics in 1965, is considered to be the father of Nanotechnology. On December, 29th 1959, he gave a talk at the annual meeting of the American Physical Society, at the California Institute of Technology (Caltech), called "There's Plenty of Room at the Bottom" [1]. On this famous lecture, he predicted a vast number of applications would result from manipulating matter at the atomic and molecular scale.

"I would like to describe a field, in which little has been done, but in which an enormous amount can be done in principle.[…] it would have an enormous number of technical applications. […] What I want to talk about is the problem of manipulating and controlling things on a small scale. […] Why cannot we write the entire 24 volumes of the Encyclopedia Britannica on the head of a pin?..."

Nanotechnology and Nanoscience could be defined as the study and control of matter in structures between 1 and 100 nm (1 nm=10^{-9} m, about ten times the size of an atom). It is a multidisciplinary field, involving areas such as physics, chemistry, materials science, engineering or medicine. It is expected that Nanotechnology will have an enormous impact on our economy and society during the following decades; some perspectives even assure that the ramifications of this emerging technology portend an entirely new industrial revolution [2]. Science and technology research in nanotechnology promises breakthroughs in such areas as materials and manufacturing, nanoelectronics, medicine and healthcare, energy, biotechnology, information technology, and national security.

The reduction in size of materials supposes that any of their dimensions becomes comparable to fundamental lengths governing the physics of the system. Therefore, classical laws are not suitable anymore to explain many phenomena, being necessary the use of quantum physics.

Nanomaterials can be classified as a function of the number of dimensions which are nanometric, with the rest being macroscopic: three (nanoparticles or nanospheres), two (nanowires or nanotubes), or one (thin films).The fabrication and characterization

of nanometric structures requires the use of specific sophisticated instruments, with two main strategies for its fabrication. The top-down approximation is based on the use of micro and nanolithography techniques to define nano-objects, starting from bigger structures. This approach is currently used to fabricate integrated circuits. Bottom-up, however, consists on the fabrication of complex structures by assembling single atoms and molecules into supramolecular entities (see figure 0.1.). Applications of this second strategy in the market are expected to arrive in two or three decades [3].

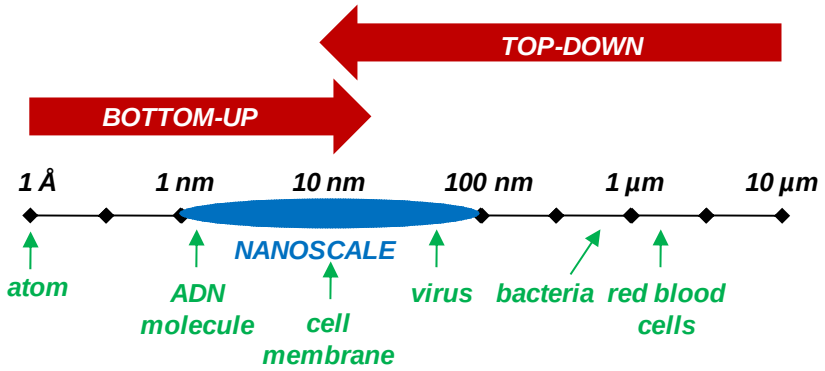

Fig. 0.1. Scheme illustrating the scale-range where the Nanoscience acts, including the two types of philosophies for fabrication. Some nature entities are included, for didactic comparison.

This thesis is devoted, in a general form, to the creation of micro and nanostructures using top-down methods, for possible applications in nanoelectronics and information storage, with special emphasis in magnetic nanostructures for applications in Spintronics. In the following sections of this introductory chapter a general overview of these areas will be given. However, the reader is encouraged to consult the references provided for a deeper knowledge of this so extensive field.

In chapter 1 we will give a general overview of nanoelectronics. The existing limits in current technology, evidenced by the archetypical example of Moore's law, will be introduced. The first example of a nanotechnology-based device integrated in industry, as it is the Giant-Magnetoresistance read heads, will be explained. We will also summarize some of the main routes in future nanoelectronic research, to finish with a geometrical comparison of the different nanostructures studied in the thesis: thin films, nanowires and atomic-sized nanoconstrictions.

In chapter 2, the main experimental techniques used during the thesis will be summarized. For fabrication: micro- (photolithography processes) and nanolithography (Dual Beam system). And for characterization: magneto-electrical (during and after fabrication of the structures) spectroscopic (XPS and EDX), microscopy (SEM and AFM) and magnetometry (spatially-resolved MOKE) techniques.

Chapter 3 is devoted to the wide study performed of the magnetotransport properties of Fe_3O_4 epitaxial thin films, grown on MgO (001), which is ferrimagnetic material with possible applications in Spintronics. The study comprises a systematic study, as a function of temperature and film thickness, of resistivity, MR in several geometries, AMR, PHE and AHE.

The method developed for the fabrication of atomic-sized constrictions, by the control of the resistance of the device while a FIB etching process is done, is shown in chapter 4. The study is centered in two metals: chromium and iron. The success in the method in both cases, the promising MR results in the magnetic material, as well as the problems associated with the fragility of the constrictions, are presented.

Pt-C nanowires grown by both FEBID and FIBID are studied in chapter 5. By the in-situ and ex-situ measurement of the electrical properties of the wires, together with a spectroscopic and microstructural characterization, a full picture for this material is obtained, where the metal-carbon composition ratio can be used to tune their electrical conduction properties.

In chapter 6, we present the results for W-based deposits grown by FIBID. The electrical superconductor properties of this outstanding material are studied systematically for micro and nanowires. The study is completed with spectroscopy and high resolution microscopy measurements.

The compositional, magnetotransport, and magnetic measurements done in cobalt nanowires grown by FEBID is shown in chapter 7. The influence of the beam current in the purity of the structures, the dependence in the reversal of the magnetization with shape, as well as the possibility to control domain walls in wires will be presented.

Finally, chapter 8 shows the main conclusions and perspectives of this thesis.

Last pages are dedicated to the bibliography of the different chapters, as well as to the articles published as a consequence of this work. A list of acronyms can be found at the beginning of the book.

1.2. Introduction to nanoelectronics

1.2.1. The information technology. Current limits.

The tremendous impact of information technology (IT) has become possible because of the progressive downscaling of integrated circuits and storage devices. IT is a key driver of today's information society which is rapidly penetrating into all corners of our daily life. The IT revolution is based on an "exponential" rate of technological progress. The paradigmatic example is computer's integration, where famous Moore's (empirical) law [4], predicts that the number of silicon transistors in an integrated circuit will double roughly every 18 months (see figure 1.1.).

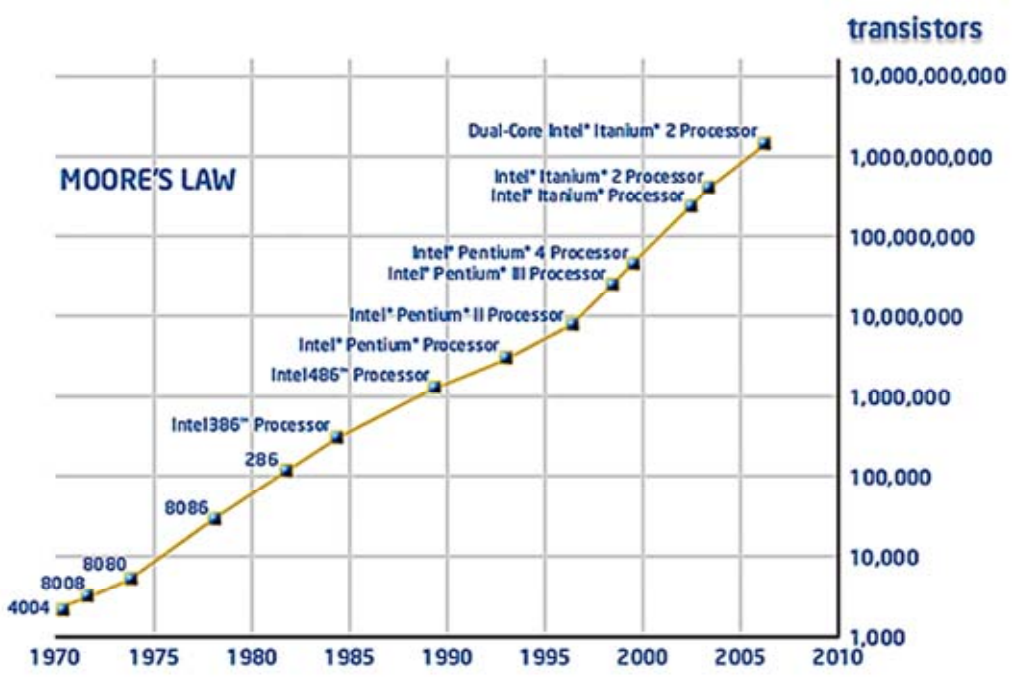

Fig. 1.1. Moore's law. Image taken from reference 5.

In a computer, the two key aspects to take into account are its ability to process information (logics), and to store/read such information (memory). The transistor is the basic component of the microprocessor (CPU), in charge of performing the logical operations, as well as of the Random-Access-Memories (RAM), the fast and volatile

(information is lost when power is off) type of memory in a computer. A CPU chip is an extremely complex integrated circuit made of silicon which includes a huge number of transistors and connecting circuitry. Nowadays, a CPU chip with an area of 1 cm^2 encloses about 109 transistors [6]. This high density is obtained by the use of projection optical lithography processes, which are able to overcome the diffraction limit of light far away [7, 8]. In fact, the transistors are currently fabricated using the so called 45 nm-technology [9]. This spectacular downscaling is however, reaching its technological limits, and even before these physical limits are reached, there are strong indications that severe engineering problems, as well as the need for huge investment, may slow down the growth in integrated circuit performance [10]. As the limits for the current technology are approaching, the continuation of the IT revolution must be supported by new ideas for information storage or processing, leading to future applications. New technologies should result in a higher integration, together with an operation speed of hundreds of GHz, or THz. Three different routes or strategies are today established to improve current electronics:

i. The *More Moore* approach: The same electronic components than currently used are decreased in size. It is also based in designing more efficient electronic components and better system architectures

ii. The *More than Moore* approach: It uses of the new functionalities appearing, as a consequence of the gradual integration of CMOS technology.

iii. The *Beyond Moore* approach: It is based on the design of new system architectures, whose building blocks may be atomic and molecular devices. Besides, the boolean logic is substituted by more efficient algorithms, possibly based on quantum computation.

Moore's law is an example of a general trend for IT areas. Thus, internet traffic doubles every 6 months, wireless capacity doubles every 9, optical capacity doubles every 12, magnetic information storage doubles every 15, etc [11].

1.2.2. GMR Heads. Impact in the information storage.

To illustrate how nanoelectronics can overcome the limits of current technology, we will show in this introduction one of the first examples where fundamental physics concepts in the nanoscale has been a technological breakthrough, incorporated in the mass production market, with applications widespread: the discovery of the Giant Magnetoresistance (GMR) effect, implying the implementation of new read heads for magnetic hard-disk drives (HDDs).

Just as a first brief introduction, HDDs are non-volatile storage devices, storing binary information using magnetic materials. They consist on three components (see figure 1.2.). The *storage medium*, which is the disk in which the data is actually stores in the form of small magnetic areas. The *write heads*, consisting of a wire coil wound around a magnetic material, which generates a magnetic field (by electromagnetic induction), when current flows through the coil. The magnetic field writes the data by magnetizing the small data bits in the medium. Finally, the *read heads* sense the recorded magnetized areas. We will only go into detail for the impact of nanotechnology on this third component (for further information of the two others, see, for instance, references 12 and 13).

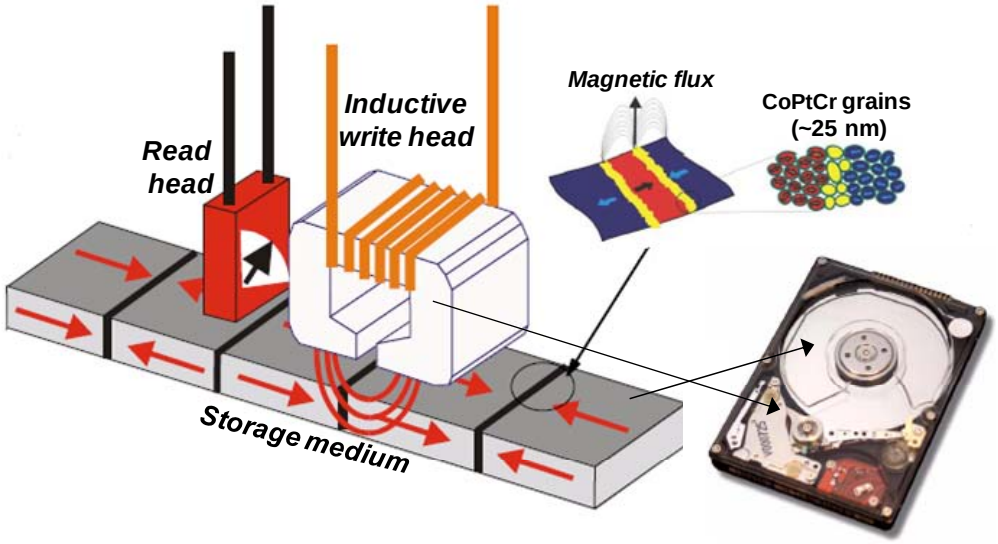

Fig. 1.2. Magnetic hard disk drive for information storage. Bits are stored in nanometric CoPtCr grains, where "1" and "0" are defined by the direction of the magnetization in grains. The information is written by inductive heads, which create a magnetic field. Read heads were initially inductive, and currently based on magnetoresistance effects. The bottom-right image shows a real HDD. Images adapted from reference 14.

In figure 1.3., the evolution of areal density of magnetic HDDs is shown during the last decades. The introduction in 1997 by IBM of the Giant Magnetoresistance (GMR) sensor to replace the previously used Anisotropic-Magnetoresistance (AMR) sensor supposed that the growth rate for storage immediately increased up to 100% per year. By providing a sensitive and scalable read technique, the HDD areal recording density increased by three orders of magnitude (from ~0.1 to ~100 Gbit/inch^2) between 1991 and 2003.

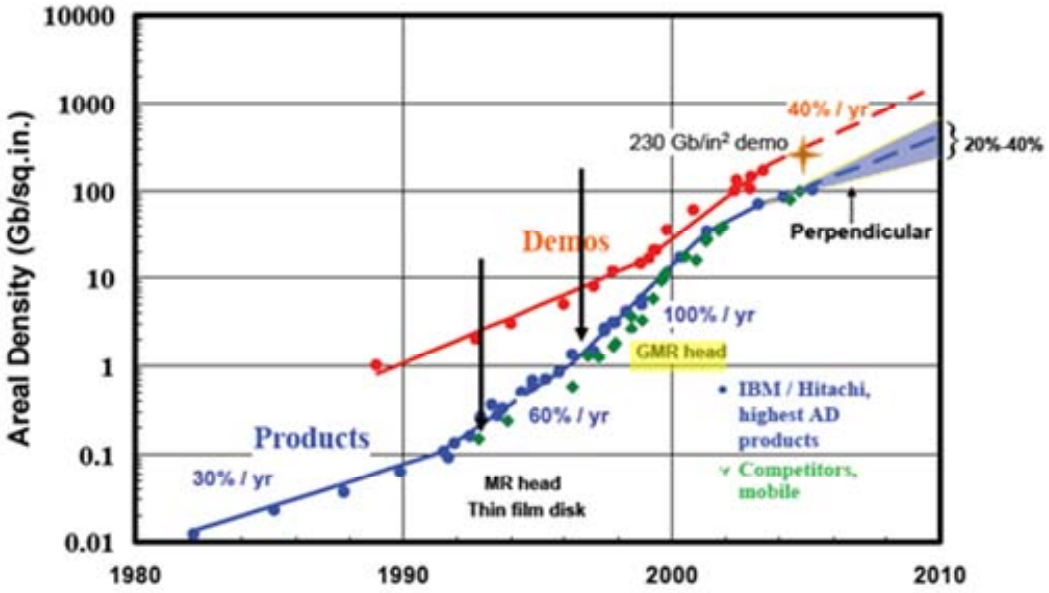

Fig. 1.3. Evolution of the HDD areal density in the last decades. In 1991, the introduction of AMR-based reads supposed a growth in the areal density up to 60% per year. In 1997, the substitution of AMR-based read heads by GMR heads supposed an immediate growth rate increase, from 60% up to 100% per year. Future next strategies are perpendicular storage and Tunneling magnetoresistance read heads. Image taken from reference 14.

We will briefly discuss the physical origin of GMR. Its discovery should be contextualized in a time (end of 1980s) where most of the research of magnetic nanostructures was dedicated to studies in which only one dimension of the material was reduced to the nanoscale via thin-film deposition. The excellent control of these processes gave rise to extensive research in the field of metallic superlattices and heterostructures. A fascinating outcome of this research was the observation of interlayer coupling between ferromagnetic (FM) layers separated by a non-magnetic metallic (M) spacer [15]. This coupling oscillates from FM to antiferromagnetic (AF) with increasing the spacer layer thickness, as RKKY interaction [16] describes. When the FM layers thickness become comparable to the mean free path of electrons, spin-dependent transport effects appear. In figure 1.4(a), the simplest model of the GMR effect is schematically shown, where electrons are conducted through alternating FM and M materials.

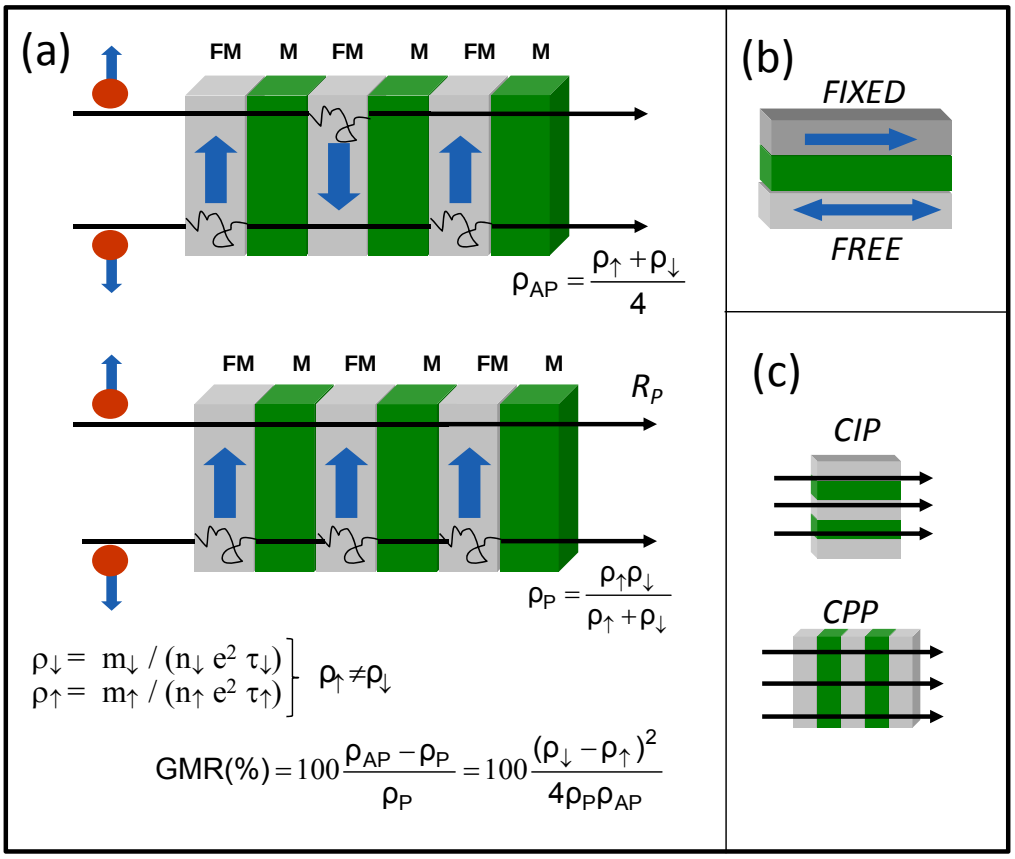

Fig. 1.4. (a) Scheme of the GMR effect. Spin-up and down electrons are conducted in two separated channels. As a consequence, the parallel configuration is less resistive than the antiparallel one (see text for details). **(b)** Scheme of the simplest spin-valve device, formed by a fixed-FM((top), a M, and a free-FM (bottom). **(c)** Two geometries for the GMR. The CPP gives higher MR effects than CIP.

The two-current model proposed by Mott [17] and applied in ferromagnetic metals by Fert and Campbell [18] establishes that spin-up and spin-down electrons are conducted in two separated channels, as a consequence of the different spin-dependent scattering probabilities. Electrons passing though the first FM get spin polarized. If the next M layer is thin enough, this polarization is maintained, and interacts with the second FM. This interaction results in a different resistance, depending on the relative orientation of the FM layers (see figure 1.4(a)). For applications, devices called spin-valves are constructed (see figure 1.4(b)), where these effects are up to 20 % at 10-20 Oe [19]. The simple concept behind spin valves consist on fixing one FM layer along

one orientation (normally by the AF interaction with adjacent layers), and leaving the other free. This free layer "opens" or closes" the flow of electrons. Two types of geometries are possible, the current-in-plane geometry (CIP), used today in sensors, and the current-out-of-plane (CPP) (see figure 1.4(c)). The underlying GMR physical effects are more complex than this simple explanation, being necessary the introduction of intrinsic potentials, models in the ballistic regime of conduction, spin-accumulation concept, etc. For details see, for instance, references 19-24.

The GMR was discovered almost simultaneously by Albert Fert's [25] and Peter Grünberg's [26] groups, and, due to the huge influence in the IT, with applications in magnetic storage, sensors and electronics [22], supposed the 2007 Nobel Prize in Physics for both scientists. GMR is the founding effect for Spintronics. In conventional electronic devices, the charge is the property of the electron which is exploited. In magnetic recording, the spin (through its macroscopic manifestation, the magnetization) is used. In Spintronics, effects where both charge and spin, and its interplay, are studied, which are manifested in nanoscale magnetic materials. Spintronics effects is one of the main research lines nowadays in nanoelectronics.

1.3. Promising future routes in nanoelectronics

We will now show some effects and devices that recently have, and will have in the future, importance in nanoelectronics. For it, five main areas will be cited [27]: semiconductor nanostructures, Spintronics, molecular and carbon electronics, interconnectors, and quantum computation. The aim of this section is to show some typical quantum effects appearing in nanomaterials (discretization of energy levels, conduction by tunneling, resonance effects, change of the energy dominating magnetic configurations, interplay between current and spin, quantum logic…), as well as try to give a wide idea of the most important routes that research in electronics is devoted nowadays. The nanostructures studied during the thesis are inside one of the points of this classification, but the physics behind them are explained in detail not here, but in the introductory part of the corresponding chapter. The section for Spintronics is significantly more extensive than the others, since most of the nanostructures studied in this thesis are classified within this field.

1.3.1. Semiconductor nanostructures

As explained previously, the silicon transistors are smaller and faster every time. One of the main problems with the miniaturization in silicon CMOS devices is the increasing leakage currents, between transistor source and drain, or gate-oxide leakage (see figure 1.5(a)), which could eventually suppose a 50% of power consumption in future [28]. Strained silicon in source and drain (instead of silicon), which increases carrier mobility, or high-K/metal gate dielectrics (instead of traditional SiO_2 dielectric), have been demonstrated to be excellent solutions to this problem, and will continue playing a significant role over next years [10]. A transition from the currently established planar structure to a non-planar structure [10] (the so-called tri-gate transistor, see figure 1.5(b)) seems to be a good solution to improve performance. This three-dimensional approach is also followed for those who use Si or other semiconductor nanowires for the fabrication of transistors [9].

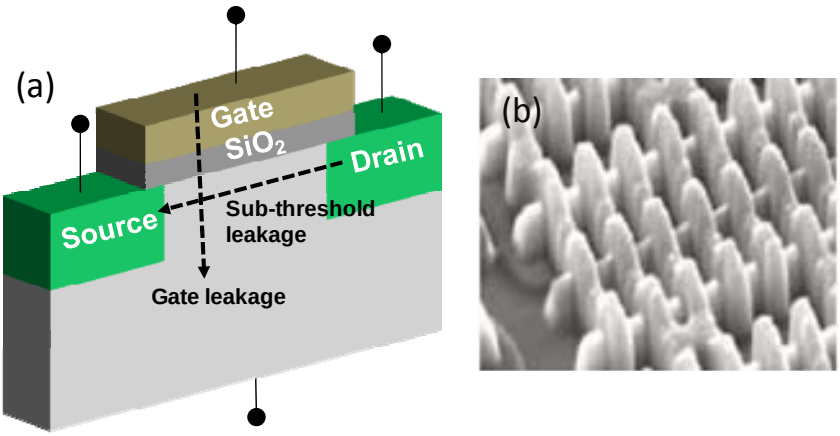

Fig. 1.5. (a) Two of the main leakage currents in transistors, of great importance as dimensions are reduced. **(b)** Tri-gate SRAM transistors. Image taken from reference 10.

We will cite other two main devices:

(i) Single-electron-tunneling (SET) devices. These are three terminal devices based on the Coulomb blockade, where the number of electrons on an island (or dot) is controlled by a gate. The island (or dot) may have up to thousands of electrons depending on the size and material. The most common islands are either metallic or semiconducting quantum dots. The basic operation (figure 1.6.) requires an island of electrons with a capacitance C which is small enough that a charging energy for the island, (e^2/C) is much larger than the thermal fluctuations in the system, (k_BT). Electrons may only flow through the circuit by tunneling onto the first unoccupied energy level, μ_{N+1}. Therefore, electrons will only flow one by one if the bias voltage V is increased, such that $\mu_L > \mu_{N+1} > \mu_R$, or a gate is used to change the electrostatics of the island to produce the same tunneling conditions. SET devices have been recently demonstrated to work at

room temperature [30].

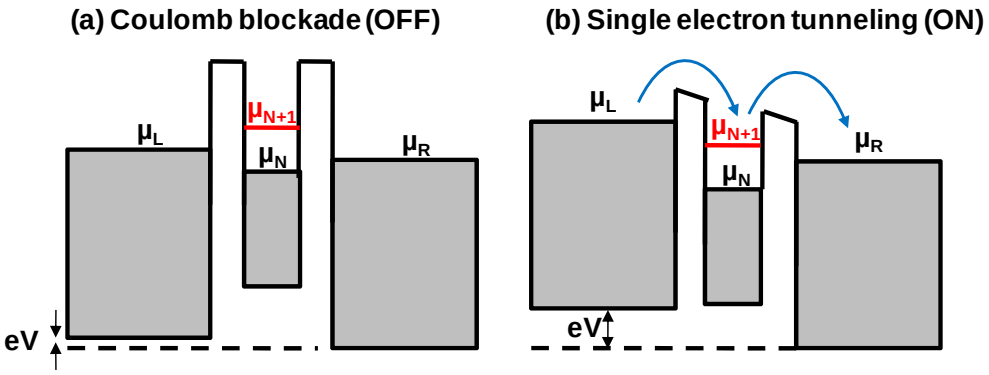

Fig. 1.7. Principle of a Single Electron Transistor. For an island with N electrons and a total capacitance C, the chemical potential of the highest filled and first empty levels are μ_N and μ_{N+1}, respectively. μ_L and μ_R are the potential of the left and right electrodes. The energy to add an additional electron to the island is $\mu_{N+1} - \mu_N = e^2/C$ (>> k_BT) **(a)** No electrons flow from left to right electrode, since V is such that $\mu_{N+1} > \mu_L$. This state is known as Coulomb blockade **(b)** V is increased, such that $\mu_L > \mu_{N+1} > \mu_R$. Empty states in the island are populated and single electrons can tunnel through it. The Fermi level of the island can be changed by a gate voltage, switching the single electron current on or off.

(ii) Resonant tunneling diodes (RTD). The basic RTD is formed by AlAs/InGaAs heterostructures [31], incorporating a double barrier quantum well, where electrons can tunnel resonantly. As a consequence, negative differential resistance (NDR) is produced (see figure 1.8.), with a resonance peak at voltage V corresponding to resonant tunnelling of electrons through a sub-band energy, in the quantum well between the barriers. NDR characteristics are very interesting for oscillators in the Terahertz range, and ultrafast digital electronic circuits. Based on the RTD, a wide variety of resonant tunneling transistors have been constructed [32].

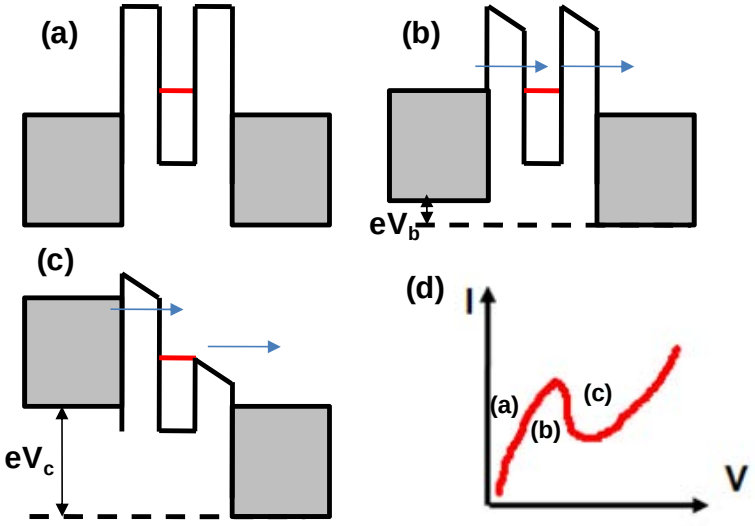

Fig. 1.8. Principle of the resonant tunneling diode. The peak in the I-V curve occurs when the incident electrons match the energy of the sub-band and the electrons resonantly tunnel from the source to the drain.

Finally in this part, we should cite other type of nano-devices, based on semiconductor technologies, called MEMS and NEMS (Micro and Nano-Electro-Mechanical-System). They consist on semiconductor chips, in which, together with the conventional electronic functions (microprocessors), new functional elements are included: sensors, actuators, microfluidics, nanomotors, optical components...[33] An especially relevant multidisciplinary application of these devices is the so called biochips [34], where thousands of selected biomolecules are immobilized on a surface, for instance, for an effective sequencing and analyzing of DNA genes.

1.3.2. Spintronics and magnetic nanostructures

A commented previously, Spintronics devices use the interplay between charge and spin in electrons. We briefly summarize some interesting effects in nanometric magnetic materials, different from GMR.

1.3.2.1. Magnetic tunnel junctions

These devices (MTJ) are similar to those exhibiting GMR (CPP configuration), but instead of metallic barriers separating FM layers, a very thin non-magnetic insulator, I (typically 1-3 nm) is used as barrier (see figure 1.8(a)). Electrons pass from one FM to the other by tunnel effect, which conserves the spin. A high or low resistance state defines a magnetoresistance (tunneling magnetoresistance, TMR) as we previously explained in the case of GMR. More details of TMR are given in section 3.1.2. Since the observation of a very high tunnel magnetoresistance at room temperature by Moodera *et al* [35] in 1995, a great deal of research has been devoted to this new form of spin-dependent transport. TMR values much higher than GMR can obtained, with record values at low temperature of hundreds per cent, using MgO barriers and half-metal electrodes [36]. From the point of view of applications, MTJs with TMR~ 50% are used. The higher sensitivity of TMR versus GMR makes it, in principle, more suitable for nanoelectronics. TMR read heads are, indeed, commercial since 2005 [37], substituting the spin valve heads in HDDs. These high values have resulted in a use for MTJs, not only for sensing, but also as another type of non-volatile memory, to substitute HDDs: The Magnetic-Random-Access-Memory (MRAM), see figure 1.8(c). However, the future of MTJs-based technology is now uncertain, since MTJs have intrinsic high resistances, making impossible to maintain current high signal-to-noise ratios with further downscaling. CPP spin valves-memories are nowadays proposed as an alternative [19].

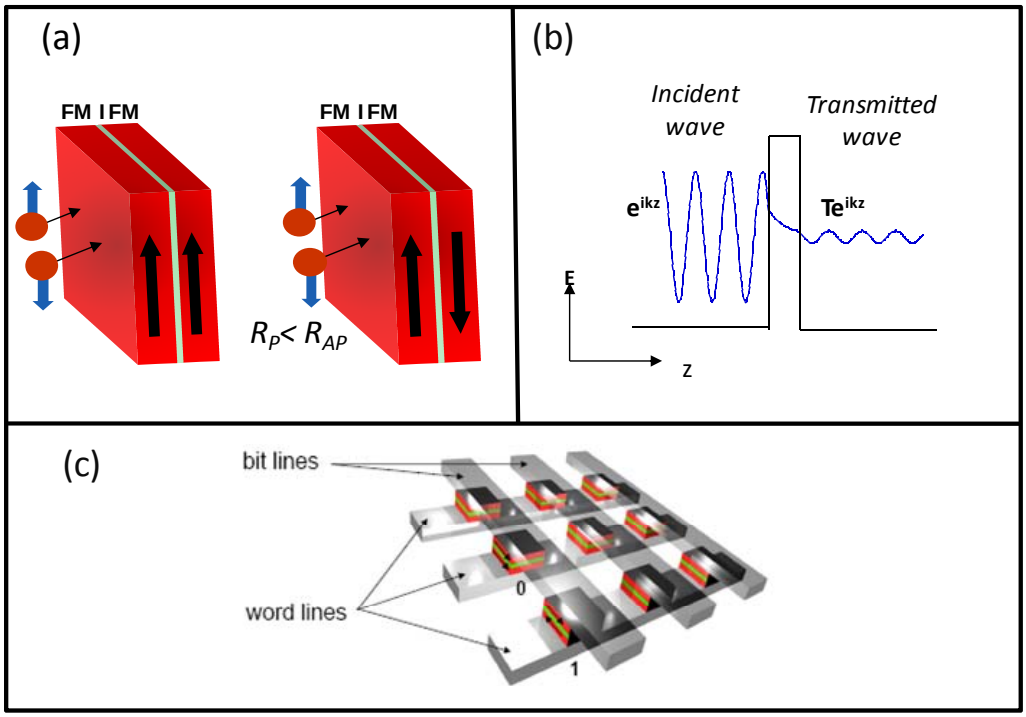

Fig. 1.8. Magnetic tunnel junction. **(a)** Scheme for the low (parallel electrodes) and high (antiparallel electrodes) states **(b)** Tunnel effect representation, where the evanescent wave of an electron tunnel trough a squared barrier. **(c)** MRAM architecture. Bits are stored in the MTJs (0: P; 1:AP). Information is read by measuring the TMR value, whereas it is written, either by the magnetic field generated by the flow of current though the two read lines, or by a spin-transfer effect (see section 3.1.1.6.).

1.3.2.2. Magnetic semiconductors

Spintronics based on semiconductors is a really attractive field, since could provide storage, detection, and logic elements in a single material system. Besides, such combination would facilitate the integration of magnetic components into existing semiconducting processing methods. The longer spin lifetime of semiconductor with respect to the conducting materials [38], novel effects based on the quantization levels existing in quantum wells, or the possibility of transforming magnetic data into an optical signal, are examples of attractive applications of this

type of materials. The main concern in this area is the difficulty of injecting a spin into a metal/semiconductor interface [39, 40]. The spin injection in diluted magnetic semiconductors, such as (Ga_xMn_{1-x}) has shown promising results [41], and this line of research could be exploited in the future. The spin-FET (spin field effect transistor) by Datta and Das [42], is one of maybe the most famous device proposed, where a semiconductor channel between spin-polarized source and drain would transform the spin information in large and tunable (by gate voltage) electrical signal.

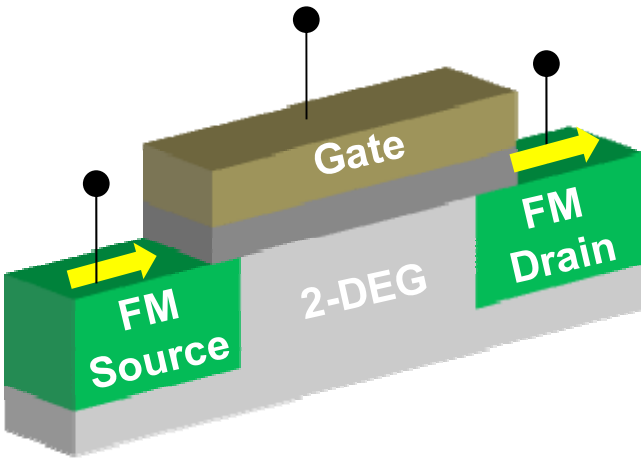

Fig. 1.9. Spin-effect transistor. The source and drain are ferromagnetic materials, with parallel magnetizations. The injected spin polarized electrons move ballistically along a quasi-one dimensional channel. The gate voltage controls the spin direction of electrons that arrive at the drain, modulating the effective resistance of the device.

1.3.2.3. Spintronics in single electron devices

The paradigmatic example is the spin-SET [43, 44], analogous to the SET explained in section 1.3.1., but now all electrodes are magnetic, including the central one (typically a particle). The interplay between the Coulomb effect and the magnetism produces a coherent co-tunneling between electrodes, resulting in an important enhancement of the TMR values.

1.3.2.4. Spintronics with organic materials: molecules, carbon nanotubes and graphene

The use of organic molecules for Spintronics is really attractive. These materials have a weak spin–orbit and hyperfine interactions, which leads to the possibility of preserving spin-coherence over times and distances much longer than in conventional metals or semiconductors [45]. Spectacular MR results have been obtained using the organic molecule Alq_3 in structures type FM/Alq_3/FM [46] or FM/ Alq_3/I/FM [47, 48], although more systematic studies are necessary to clear out some aspects of these devices.

MR effects of ~60% at low temperature have also been reported for carbon nanotubes (CNTs) connecting highly spin-polarized LSCMO electrodes [49], implying a high efficiency in spin injection in CNTs. As in the case of molecules, the small spin-orbit coupling of carbon, together with the high Fermi velocity that limits the carrier dwell time, are the differential aspects for a so long spin lifetime (preserved along ~1-2 μm). Similar results are expected in spintronic devices based on graphene (the nanometric version of graphite, formed of a few monolayers of sp^2 carbon), where spin polarization has also been demonstrated to survive over submicron distances [50].

1.3.2.5. Domain walls in nanostructures

Domain walls in nanostructures exhibit complex spin arrangements that strongly deviate from the wall types commonly encountered in magnetic thin-film systems, and they can be modified by changing the geometry of the element [51]. Lateral confinement leads to pronounced geometrical effects. Various types of domain walls arise in micro- and nanostructures because of the demagnetizing energy at the edges [52]. This in turn offers the possibility to finely tune the wall properties, such as the wall width. This is an important aspect, because it enables the use of domain walls as individual tailored objects [53], and determines, for instance, the resistance or the dynamic properties of the domain wall. Aspects such as the velocity of displacement of domain walls, or the movement of these domains by applying external spin-polarized currents (see next section) are now attracting much attention. The control of

domain walls in nanowires, for memory [54] and logic devices [55] is especially attractive, being treated in more detail in section 7.6.1. Vortex domains in circular and squared nanostructures are also attracting much interest [56, 57], by their possible application in information storage. The advance in a number of methods for direct, real-space imaging in magnetic microscopy is remarkable [58], and techniques such as the magnetic microscopy using X-ray dichroism in synchrotron sources permits, not only sub-100nm spatial resolution, but also sub-ns time resolution observing the magnetism dynamics in nanostructures [56, 57].

1.3.2.6. Spin-transfer effects

The normal way to change the magnetization of a ferromagnet is to apply an external magnetic field. However, in the 1970s, theoretical [59] and experimental [60] results indicated that a new way was possible, by the direct transfer of spin angular momentum from a spin polarized current. Much effort has been done in the last years regarding this effect, since the possibility to manipulate magnetization with current would suppose a breakthrough in spin storage. The physical effect underneath is called spin-transfer-torque, which consists on an effective torque on the magnetization of a material, by the absorption and transfer of the transverse component of the spin current. Spin-torque effect can be modeled by the modification of the Landau-Lifshitz-Gilbert equation, describing the damped precession of the magnetization, in the presence of a spin-torque effect, which compensates the damping [59, 61]:

$$\frac{d\mathbf{m}}{dt} = -\gamma_0 \mathbf{m} \times \mathbf{H}_{\mathbf{eff}} + \alpha \mathbf{m} \times \frac{d\mathbf{m}}{dt} + \gamma_0 J \mathbf{m} \times (\mathbf{m} \times \mathbf{H}) \qquad (1.1.)$$

where γ_0 is the gyromagnetic ratio, and α the damping coefficient. In figure 1.10. the three terms are represented.

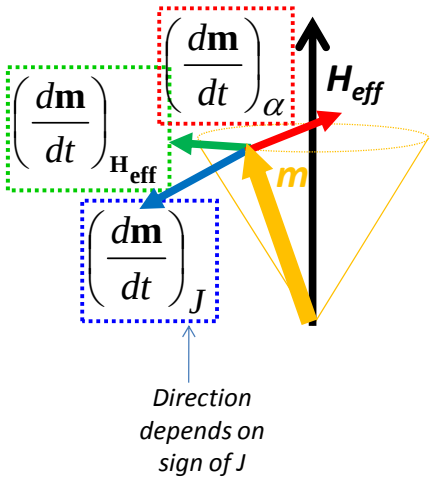

Fig. 1.10. Diagram of the components included in the Landau-Lifschitz-Gilbert equation, in the presence of spin-torque effect.

The spin-torque amplitude is proportional to the injected current density, with critical currents around 10^7A/cm^2. Nanometric structures are suitable for this effect to occur, using moderated currents if the section is reduced below ~100 nm. A recent review can be found in reference 61. The effect has mainly demonstrated basically in two types of structures:

(i) Multilayer geometries [62-64], where two magnetic layers are separated by a thin non-magnetic spacer layer. The electrical contact, in this case, is done in two different ways. The first one is the fabrication of a ‘‘point-contact’’ which is connected to an extended multilayer. The other approach is to make ‘‘nanopillar’’ devices in which at least the free magnetic layer and sometimes both the free and the fixed magnetic layers are patterned to a desired cross section. The spin-torque effect is measured as a GMR or TMR. Besides, the high density currents produce important effects on the magnetic dynamics, with the generation of microwaves as an interesting application [65, 66].

(ii) Nanowires, where the movement of domains by spin polarized

currents has been demonstrated [54, 67]. This possibility is really attractive, combined with applications cited in section 1.3.2.5.

1.3.3. Molecular and carbon electronics

The field of molecular electronics has had intense activity since the beginning of 1990s. Molecules have a series of advantages with respect to inorganic silicon [6]:

- Their synthesis is easily, and with low cost in many cases
- They can be grown in three dimensions as opposed to the typical 2D semiconductor lithographic layout
- They can self-assemble
- Heat and noise production are expected to be reduced
- They can display a whole new world of properties and functionalities
- Very promising in Spintronic devices (see previous section)

Important developments have been done during the last years in molecular electronics. We will cite [6] signal rectification, current-light converters, switches and logic gates, realization of transistors based on molecules, heat transport and themopower, or the study of transport in single molecules by insertion in nanogaps.

Special attention requires carbon nanotubes (CNTs) [68], perhaps the most famous of all the nanostructures. CNT are formed by sp^2 layers rolled to form a tube. They possess unique mechanical and thermal properties. But furthermore, their electrical properties are amazing. Electrical transport is ballistic, enabling them to carry high currents with essentially no heating, they can exhibit metallic or semiconducting behavior depending on their structure and dimensions… [69]. CNTs are one of the most promising materials for the future in nanoelectronics. Devices such

as rectifiers or transistors have been already developed.

1.3.4. Interconnectors

Between the main challenges in the fabrication of nanoelectronic devices, one finds the connection between the different components. One of the main problems when miniaturization is the increase of resistance in components, implying higher power dissipation. This effect is more important the faster the velocity of the devices is. The use of metallic connections with dimensions smaller than the mean free path of electrons (a few Å), would imply a ballistic transport [70] (without scattering), minimizing energy losses. The use of superconducting connections [71] is also an attractive route to solve this problem. The breakdown of metallic connections at high current densities, and fields by electromigration [69], is also an emerging problem. CNTs combine good conduction properties with extremely mechanical robustness, making them suitable candidates in the future [69, 72]. Alternatively, molecular nanoelectronics could interconnect systems optically [6].

Today, the progressive miniaturization is carried out maintaining planar architectures. New 3-dimensional architectures, based on nanowires or nanotubes connections, would avoid fatal interconnection bottlenecks [28, 54, 69, 72, 73].

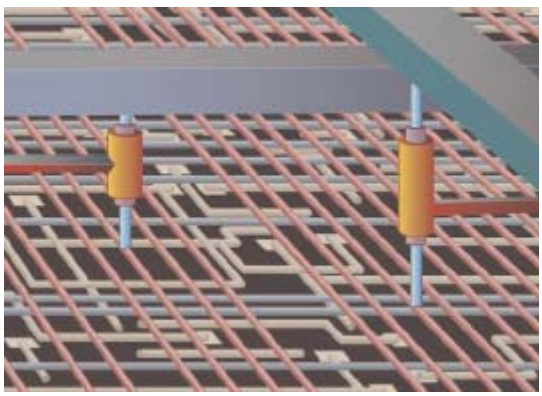

Fig. 1.11. Schematic, conceptual view of introducing a vertical nanowire or nanotube in a planar chip architecture. Taken from reference 28.

1.3.5. Quantum computation

The rapid miniaturization of nanoelectronics will suppose, in some point, a crossover where quantum mechanics will govern completely the physics of the processes, giving rise to the so called quantum computation. Quantum computers process information in a completely different way than microprocessors, using quantum algorithms that do not have classical analogues. From a physical point of view a bit is a two-state system, in which one of two distinguishable states, representing two logical values, is occupied. A qubit (quantum bit), the information unit in quantum computers, can not only be in the state "0" or "1," it may also be in a superposition of the two, just as a photon or an electron in a two-slit experiment can be in a superposition of passing through one slit or the other. In a sense, a qubit carries both values at the same time. Even more counterintuitive, two or more qubits can be quantum entangled, which means that neither of them carries any well-defined information on its own; rather, all information is stored in joint properties. This leads to nonlocal correlations, with measurement on one qubit instantly defining the state of the others, no matter how far they are apart. The use of this property supposes massive parallel computation, solving unapproachable problems up to date, in minutes.

In principle, any two-level system can be used as a qubit. The main problem occurs in the transmission of the quantum information, where decoherence, i.e. the destruction of the entanglement due to non-controlled interactions with the environment, must be avoided. For example, a tunneling process between normal metallic junctions is incoherent, ruling these systems out as possible candidates [74]. Various systems have been demonstrated to be possible components for quantum computers: trapped ions, neutral atoms, photons, nuclear magnetic resonance in liquids, or superconductor components [74-79].

1.4. Nanostructures studied in this thesis

We have studied basically tree types of nanostructures in this thesis, if we take into account geometrical effects:

1- Thin films (of Fe_3O_4: chapter 3): Nanometric in one dimension, macroscopic in the rest.

2- Nanowires (of Pt-C: chapter 5, of W-C: chapter 6, of Co: chapter 7): Nanometric in two dimensions (thickness and width), macroscopic in one (length).

3- Atomic nanoconstrictions (of Cr and Fe, chapter 4): Macroscopic electrodes are connected for a few atoms.

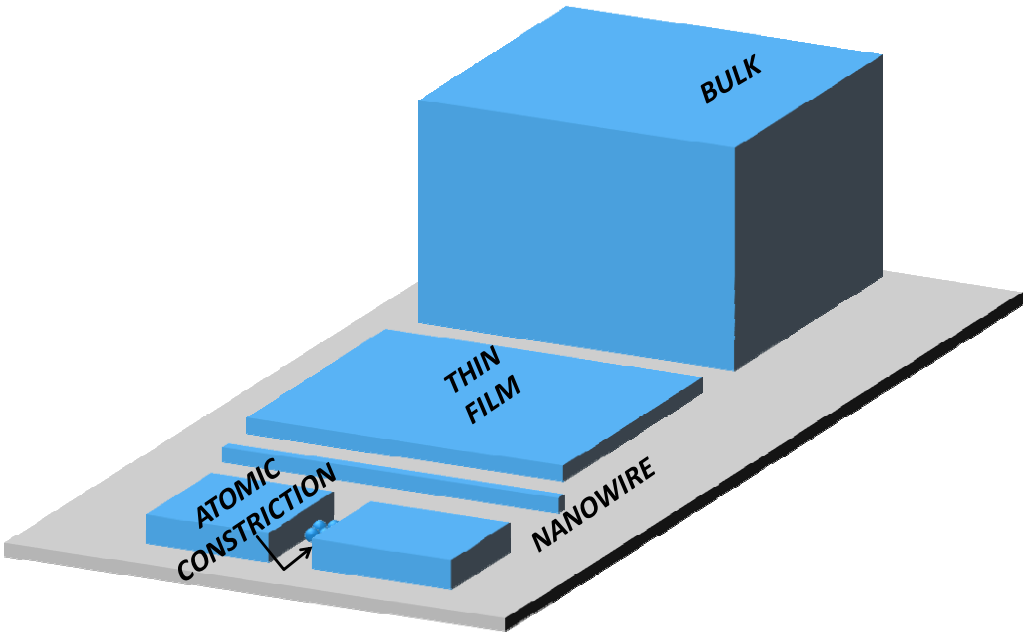

Fig. 1.12. Schematic cartoon, where the different nanostructures studied in the thesis are shown, for comparison of their dimensions. Thin film is thickness-nanometric, nanowires are thickness-and-width-nanometric, whereas an atomic constriction is formed by bulk electrodes joined by a few atoms.

We can do a rough comparison of how many atoms are contained in a 10 μm× 10 μm × 10 μm cube for all these geometries considered, by assuming a typical size of 0.1 nm for an atom, and using common sizes of the materials studied. Thus, whereas a bulk material would contain 10^{15} atoms, a thin film (thickness=20 nm) would have 2×10^{12} atoms. In the case of a nanowire (thickness= 50nm, width=100 nm), 5×10^{10} would be contained. For nanoconstrictions, although we would calculate 10^{13} atoms (and the response of them would be measured by a macroscopic probe), the electrical conduction is dominated by a few tens of atoms, those forming the constriction and a few neighbors in the electrodes. In this case, besides, superficial atoms are approximately the 100%, whereas it is of the order of $\sim10^{-3}$% in the other geometries. The scaling shown here when reducing dimensions is still more spectacular if nanometric dimensions would approach the nanometer. Surface effects, defects, confinement effects, etc get importance versus intrinsic properties as a smaller amount of atoms plays a role in the phenomenon studied. Some of the effects studied in this thesis are, in some way, manifestations of it.

Chapter 2

Experimental techniques

In this chapter we report on the experimental techniques used during this thesis both in the sample patterning and characterization. An important part will be focused in the lithography techniques and processes (micro and nano) used for the creation of structures with a well defined geometry in these scales. The setup of an experimental installation for the study of magnetotransport properties as a function of temperature, as well as that for electrical measurements inside a Dual Beam chamber will be also exposed. Spectroscopy (EDX and XPS), magnetometry (MOKE) and microscopy (SEM and AFM) techniques used along the work are included in this chapter. Most of the instruments described are located, in the Institute of Nanoscience of Aragón and in the Institute of Science Materials of Aragón (ICMA). Spatially-resolved MOKE and AFM were done in a two-month stage in the Imperial College in London, in the group of Prof. Russell P. Cowburn.

2.1. Lithography techniques

Lithography is the group of techniques used to transfer previously-determined patterns on a substrate. The typical size of these structures is micro- and nano-metric. Depending on the type of lithography technique used, the transfer is performed in a different way, which defines the resolution that can be attained. In this thesis, we have used two big groups of lithographies, both of them inside the top-down approximation:

(i) Optical lithography: These techniques have been used in a clean room environment. By far, this is the most common lithography technique in microelectronic fabrication. It permits the fabrication of micrometric structures

(ii) Lithography using focused electron and ion beams: This technique has been used in a Dual Beam system. With these techniques, nanostructures below 100 nm can be patterned.

We should remark that the equipments used were installed in the Institute of Nanoscience of Aragón (INA) premises, in Zaragoza, during the first two years of this thesis. Thus, the protocols for a big amount of the processes that will be shown here were carried out by myself, together with the technical staff of the Lithography Laboratory (R. Valero, I. Rivas, and R. Córdoba), and Doctor Javier Sesé.

2.1.1. Optical lithography

All the photolithography processes have been performed in a 10,000 class-clean room, in the INA. Clean rooms are special rooms, with well-controlled ambient conditions. Temperature, humidity, differential pressure and flux of air, as well as lightning and electrostatic protection have to fulfill determined standards. Class=10,000 means that the number of particles of size=0.5 μm per cubic meter should not be higher than 10^4. A deviation of these parameters can alter the processes, as well as modify their quality.

We will give a short overview of the equipments and processes used, by explaining one particular example patterned in this thesis: lithography in Fe_3O_4 thin films, whose results will be presented in chapter 3.

The starting point is to create a computer layout for the specific application. We have used the program Clewin® for it. In figure 2.1. we show the mask designed, where the different colors symbolize different layers. Since we desire to have two materials on top of the substrate (in this case MgO) with different shapes, it will be necessary to perform two lithographic processes. For both patterns to be well oriented one with respect to the other, lithography marks are added to the design (see figure 2.1(c))

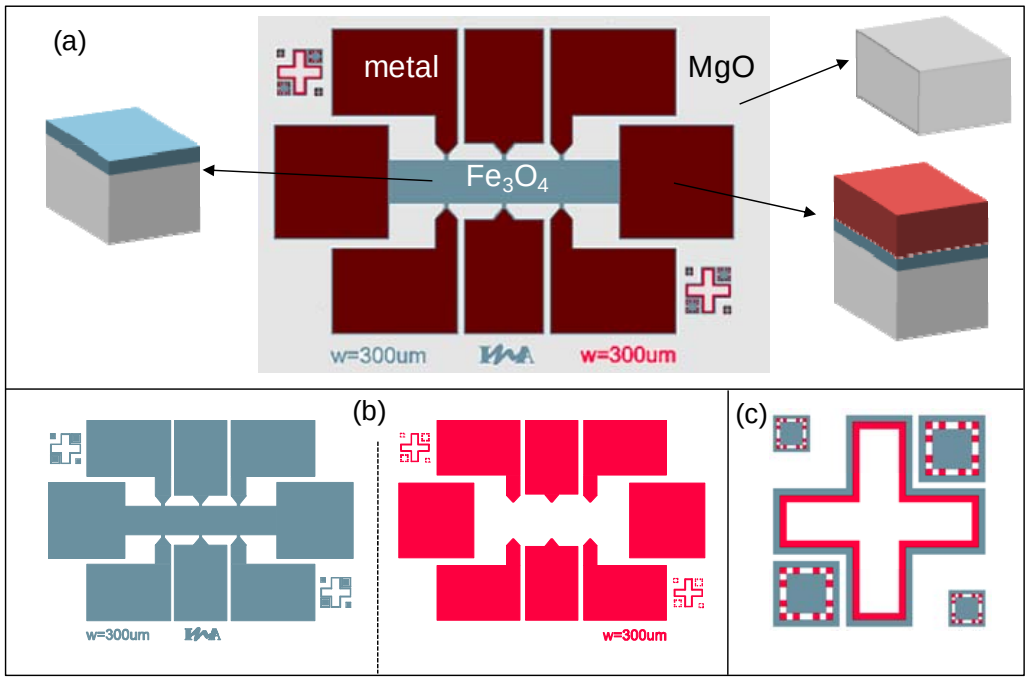

Fig. 2.1. Lithography mask designed by computer. **(a)** Top and 3D view of the mask. The red, blue and grey symbols symbolize a metallic material, Fe_3O_4 and the substrate MgO, respectively. **(b)** The two patterns included in the design. Each pattern requires a separated complete lithography process. **(c)** Marks used, which are necessary for the good alignment of the two steps.

Once the pattern is done, two photolithography masks (one for each step) are fabricated. These masks consist on a glass plate having the desired pattern in the form of a thin (~100 nm) chromium layer. The masks were fabricated by a company located in the Netherlands.

As shown in figure 2.2, the lithography process involves the following steps:

(i) *First step:* After it, a Fe_3O_4 film on top of MgO has the shape shown in figure 2.1(b)-left. The involved processes are:

(a) A thin film of Fe_3O_4 is epitaxially deposited on MgO (001) by Pulsed Laser Deposition. This work is part of the thesis of Julia Orna [1].

(b) The Fe_3O_4 thin film is spin coated with a photoresist. This is a polymeric photosensitive material that can be spun onto the wafer in liquid form. The spinning speed and photoresist viscosity will determine the final resist thickness. For the first step, we used a typical thickness of 2.4 μm.

(c) The substrate is soft-baked during 50 s at 100ºC in a hot plate, in order to remove the solvents from the resist, minimizes the stress, and improve the adhesion.

(d) The mask is aligned to the wafer, using a mask aligner by *Karl Suss*®, and the photoresist is exposed to a UV source, passing through the photomask (Hg light source, h-line: λ=405 nm), during 50 s. The areas of the mask with chromium are completely opaque to the light and complementary areas are transparent. The light passes through the mask, continuing through the lenses. The zones of photoresist which are exposed to light undergo a

chemical reaction upon exposure to light. As the resist used is positive, exposed zones become more soluble in the used developer.

(e) The resist is developed, leaving regions that are covered by photoresist and complementary regions that are not covered (as the resist is positive, it takes the shape of the structure designed, blue structure in figure 2.1(b)-left).

(f) The remaining resist is hard baked (125ºC, 50s in a hot plate) to harden it for next processes.

(g) The sample is introduced in an ion etching equipment by *Sistec*®, where ~300 eV argon ions impinge on the sample, etching it. As the Fe_3O_4 films have a maximum thickness of 40 nm, unprotected parts are removed, whereas those which have resist on top remain unharmed from this process. By the use of an electron neutralizer gun, the ions are neutralized ($Ar^+ \rightarrow Ar^0$) before arriving at the sample, avoiding charging effects at the surface of the insulator MgO substrate, which would eventually spoil the etching process after a certain point.

(h) The remaining resist is removed, by acetone immersion.

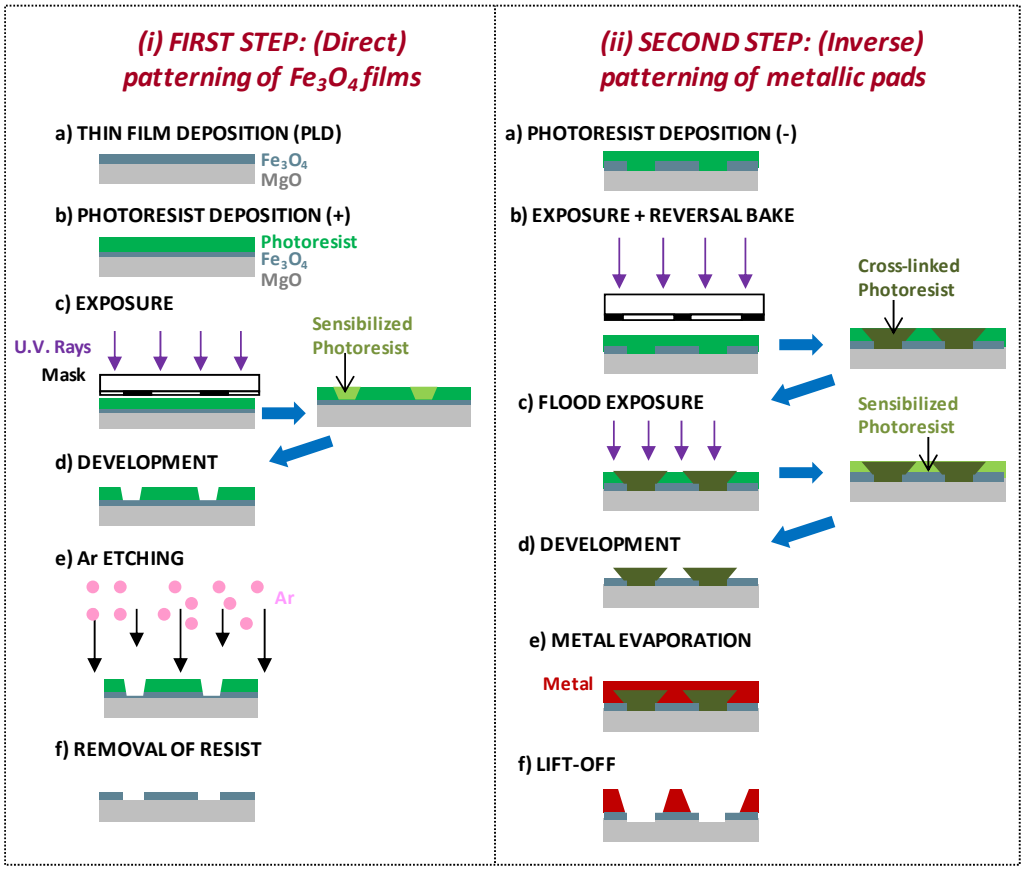

Fig. 2.2. Photolithography of Fe_3O_4 thin films. The two layers are patterned in two separated processes. In this scheme baking steps, explained in the text, are skipped. The photoresist profiles are exaggerated for pedagogical reasons.

Second step: Metallic pads are deposited on top of the Fe_3O_4, with the shape of figure 2.1(b)-right. Processes

(a) The sample is spin coated with an image-reversal (negative) photoresist. The thickness chosen was of 1.4 µm

(b) The resist is soft-baked during 50 s at 110 ºC in a hot plate.

(c) The mask is aligned to the wafer, using a mask aligner, and the photoresist is exposed (t=10 s). In principle, the exposed zones

become more soluble. Marks shown in figure 2.1(c) are used for a good alignment of both structures.

(d) A reversal bake is done, at 120º C during 2 min. This process crosslinks the exposed photoresist, becoming insoluble in the developer. The unexposed areas still behave like a normal unexposed positive resist

(e) A flood exposure, without mask, is done (15 s). Thus, zones which were first exposed (step (c)) are much more insoluble in comparison with those which were not.

(f) The resist is developed, leaving regions in the sample that are covered by photoresist and complementary regions that are not covered (as the resist is negative, resist forms the complementary structure of that designed, figure 2.2(b)-right).

(g) The sample is introduced in an electron-gun evaporator by *Edwards*®. A 100 nm thick metal layer (typically polycrystalline gold or aluminum) is evaporated. Usually a thin layer (around 10 nm) of chromium is deposited before, for the good adhesion of the metallic layer.

(h) The sample is immersed in acetone. The profile of the negative resist, contrary to the positive one (see in detail resist profiles in figure 2.2), favors the complete removal of those parts of metal with resist behind it. This type of process is called "lift-off".

An optical image of the sample, with gold as metallic layer, is shown in figure 2.3. We should remark that MgO substrates get cracked when immersed in an ultrasound bath. This makes this lithography process a bit more complicated than when using, for example, normal silicon substrates.

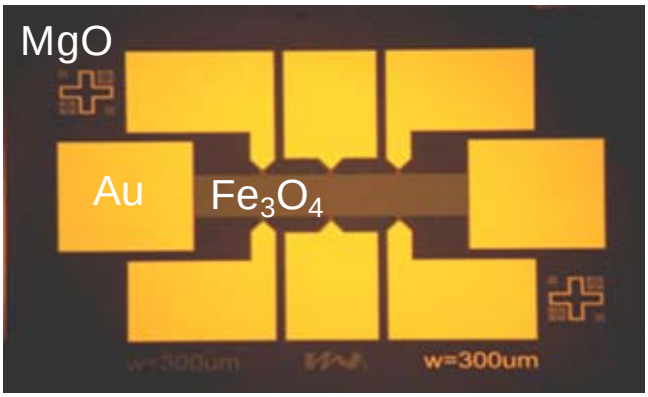

Fig. 2.3. Optical image of one Fe_3O_4 bar with gold pads on top, which is the result of a two-step lithography process.

The pads are finally connected by ultrasonic wire bonding to a chip carrier, with an instrument by *Dicing Systems*®. The chip carrier has macroscopic connections, which can be manipulated in a conventional way.

The lift-off process explained has been used in other types of designs, for applications using the Dual Beam system (see section 2.1.2). In this case, metallic circuits are patterned by photolithography, consequently nano-lithographied by the Dual Beam equipment. The substrate chosen for these applications is a silicon wafer, with a 150-250 nm thick insulator on top of it (either Si_3N_4 deposited by Plasma-Enhanced-Chemical-Vapor-Deposition, PECVD equipment by *Sistec*®, or thermally oxidized SiO_2). This layer insulates electrically the metallic pads, and, at the same time, electrons or ions can be partially evacuated thorough the Si substrate, avoiding charging effects, which ruin the nanolithography process.

An image of the equipments used for photolithography is shown in figure 2.4. The minimum line width obtained routinely in our laboratory in these processes is around 3-4 μm (better in the case of positive resist). The final resolution in an optical process is given by the diffraction limit ($\lambda/2$, λ being the light wavelength), although other effects such as optical aberrations of the system, the exposure mode and the chemical process linked to the resistance are actually whom dictate the limits. In semiconductor industry, critical dimensions below 100 nm are nowadays routinely

patterned in integrated circuits [2, 3]. Huge steppers working in projection mode, KrF or ArF lasers and immersion lens to increase the numerical aperture are used to push the limits of this technology [2, 3]. For a more detailed explanation of these processes, as well as of general aspects of lithography, see references 4 and 5.

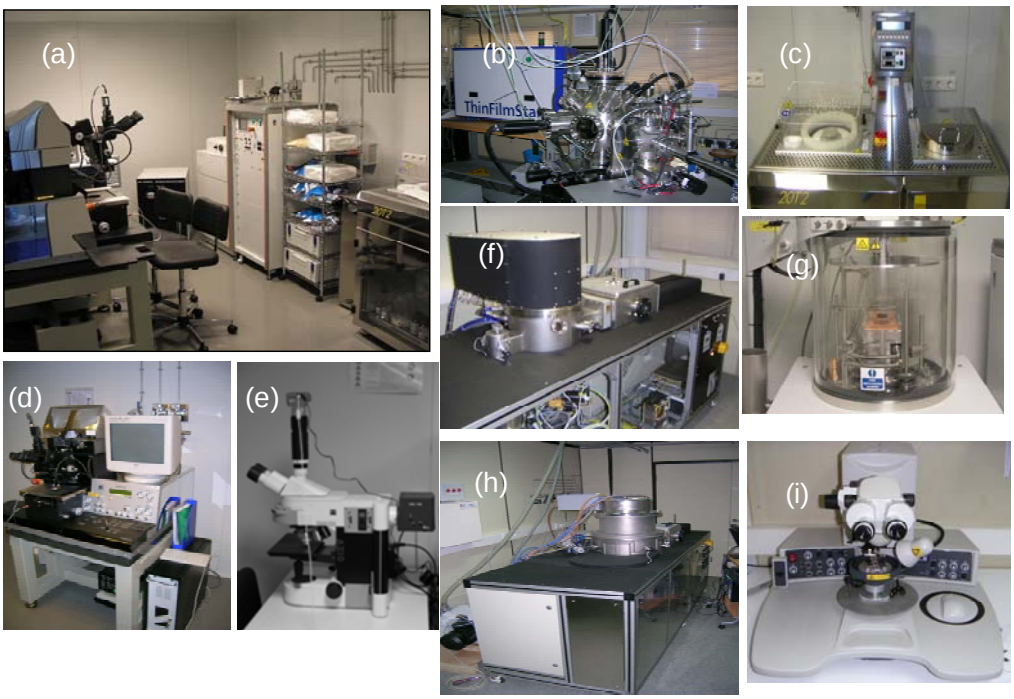

Fig. 2.4. Images of the instruments used for photolithography. **(a)** General view of the clean room. **(b)** Pulsed-Laser-Deposition equipment. **(c)** Spin coater and hot plate. **(d)** Mask aligner. **(e)** Optical microscope. **(f)** Plasma-Enhanced-Chemical–Vapor-Deposition equipment. **(g)** Electron-gun evaporator. **(h)** Ion milling equipment. **(i)** Wire bonding equipment.

2.1.2. Dual beam system

2.1.2.1. Introduction

A "dual beam" incorporates a focused ion beam (FIB) column and a scanning electron microscope (SEM) column in a single system. This combination makes this equipment a very powerful nanolithography tool, with important advantages over a single-beam SEM or FIB system. The typical dual-beam column configuration is a vertical electron column with a tilted ion column. Figure 2.5. shows such a configuration with the ion beam at 52° tilt to the vertical direction. In this case, the sample will be tilted to 0º and 52° for a SEM or FIB, respectively, processing normal to the sample surface. To enable ion milling and electron imaging of the same region, dual beams typically have a coincident point where the two beams intersect with the sample. This is the normal operating position for the system.

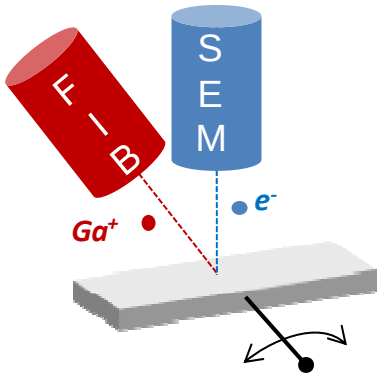

Fig. 2.5. Scheme of the Dual Beam configuration. SEM and FIB column form an angle of 52º. Both beams are focused in a coincidence point. The stage rotates depending on the process.

Some of the main applications of dual beam systems are [6]:

1. FIB etching and simultaneous SEM imaging.

2. Imaging with both beams: Although the electron beam is the primary imaging tool in a dual beam, the imaging from the ion and electron beams is often

complementary. The collection of primary ions is possible when using FIB.

3. Cross section fabrication and analysis.

4. Local deposition of materials by introducing precursor gases inside the chamber. This application will be explained in detail below.

5. Lamella preparation for TEM analysis. Thin specimens, transparent to high-energy electrons can be fabricated. Before the etching, a protective layer is deposited. After several progressive thinning processes, a micromanipulator takes the lamella to the TEM grid. This method is becoming popular in the microscopy laboratories as an alternative method to the manual one.

In figure 2.6. images of the experimental system, the *Nova Nanolab 200* by FEI® are shown. Together with the columns, detectors, manipulator, needles for gas injection (GIS) etc are shown. The processes are carried out in a chamber at high vacuum (turbo-molecular pump), whereas both columns need ultra-high vacuum (ionic pumps).

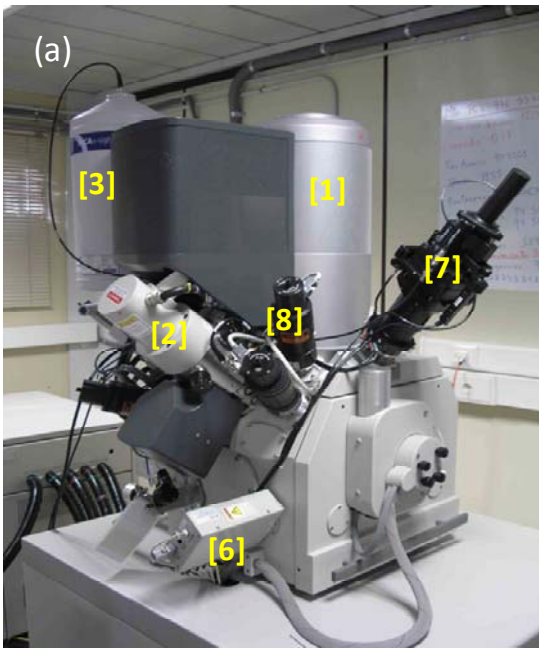

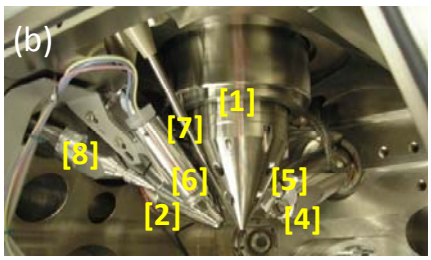

[1] FEG 30 keV electron column
[2] 30 keV Ga^+ ion column
[**3**] EDX detector *(Oxford Instruments)*
[4] ETD detector
[5] TLD detector
[6] CDEM detector
[Not visible] STEM detector
[7] Nanomanipulator *(Omniprobe)*
[Not visible] EBL Lithography *(Raith Elphy Plus)*
[8] 5 gas injectors
[9] Vacuum chamber

Fig. 2.6. Dual Beam equipment used. **(a)** General overview of the system. **(b)** View inside the chamber **(c)** Names corresponding to the numbers indicated in (a) and (b).

2.1.2.2. Focused electron beam (FEB)

The column used is a Field-Emission-Gun Schottky source, where electrons are emitted from a field sharp-pointed emitter, held several kilovolts negative potential relative to a nearby electrode, causing field electron emission. Schottky emitters are made by coating a tungsten tip with a layer of zirconium oxide, which has the unusual property of increasing in electrical conductivity at high temperature. The FEG produce an electron beam smaller in diameter, more coherent and with up to three orders of magnitude higher brightness than conventional thermionic emitters such as tungsten filaments. The result is a significant improved signal-to-noise ratio and spatial resolution.

The electron optics shares similarities with to that of light optics. The FEB column typically has two lenses, i.e., a condenser lens and an objective lens. The condenser lens is the probe forming lens, and the objective lens is used to focus the beam of electrons at the sample surface. A set of apertures of various diameters also helps in defining the probe size and provides a range of electron currents that may be used for different applications. Big apertures give high currents and low spatial resolution. For SEMs the acceleration beam energy is usually in the 1–30 keV range and the minimum beam diameter is near 1 nm.

To form an image, the beam is scanned, by means of magnetic lenses, along the sample, row by row. As the electron beam hits each spot on the sample, particles are emitted by the specimen surface, collected by the detectors to form the SEM image when convoluting all the spots. Several types of detectors are available in the equipment. We will only mention the most commonly used: the Everhart-Thornley SE detector.

As a consequence of the interaction of primary electrons (PE) with matter, both electrons and photons are emitted by the specimen surface. In figure 2.7(a) we show those used in our equipment to obtain information. In this section we will only center

in two main types of electrons generated (Auger electrons, X-Rays and cathodoluminescence will not be commented here):

- Secondary electrons (SE): These electrons are produced due to inelastic collisions with weakly bound outer shell valence electrons of semiconductors and insulators, or weakly bound conduction band electrons of metals. They are generated along the entire trajectory path of the PE. However, only a few of these created secondary electrons can escape up to the substrate surface. They have exit energies situated around a peak of a few eV.

- Backscattered electrons (BSE): These kinds of electrons are reflected primary electrons due to elastic collisions, having energy peaks situated near the primary electron energy and "escape" from a much larger volume.

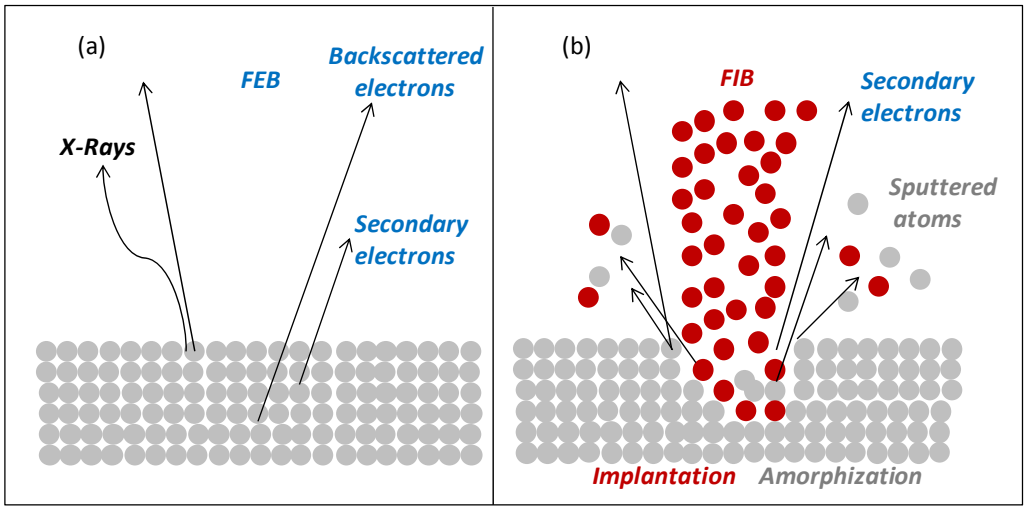

Fig. 2.7. Interactions between a Focused electron **(a)** or ion **(b)** beam and a substrate. The main effects in both cases are schematically shown.

2.1.2.3. Focused ion beam (FIB)

The FIB apparatus is very similar to a SEM. It is composed of three main parts: the source, the ion optics column, and the stage and beam control. The FIB optics and stage and beam control are very similar to those for FEB, explained in previous section. The ion source is a liquid metal source (LMIS), consisting of a reservoir of liquid gallium, which feeds the liquid metal to a sharpened needle, made of tungsten. The LMIS has the ability to provide a source of ions of ~ 5 nm in diameter [6], with a high brightness, typically ~10^6 A/cm^2 sr. The heated Ga flows and wets the W needle. An electric field applied to the end of the wetted tip causes the liquid Ga to form a point source on the order of 2-5 nm in diameter at the sample surface. The extraction voltage can pull Ga from the W tip and efficiently ionize it. Once the ions are extracted from the LMIS, they are accelerated through a potential (5-30 kV) down the ion column.

Figure 2.7(b) shows a schematic diagram illustrating some of the possible ion beam/material interactions that can result from ion bombardment of a solid. Milling takes place as a result of physical sputtering of the target, when the sputtered particle receives enough kinetic energy to overcome the surface binding energy of the target material. Sputtering occurs as the result of a series of elastic collisions where momentum is transferred from the incident ions to the target atoms within a collision cascade region. A portion of the ejected atoms may be ionized and collected to either form an image or be mass analyzed. Inelastic interactions also occur as the result of ion bombardment. Inelastic scattering events can result in the production of phonons, plasmons (in metals), and the emission of secondary electrons (SE). Detection of the emitted SE is the standard mode for imaging in the FIB. If the ion is not backscattered out of the target surface, it will eventually come to rest, implanted within the target at some depth below the specimen surface. As a consequence of the high energy of ions, the amorphization of the material is an important consequence of the FIB process. For details see reference 7.

2.1.2.4. Focused electron/ion beam induced deposition (FEBID/FIBID)

Anyone using an SEM will probably have observed that the surface becomes contaminated when the beam exposes for some time the same place. This film is formed from rest of hydrocarbons present in the vacuum system. This undesired effect can be, however, used to deposit locally a material, if the appropriate gas is adhered to the surface. This technique is one major application of a Dual Beam system, called Focused-Electron-Beam-Induced-Deposition (FEBID) and Focused-Ion-Beam-Induced-Deposition (FIBID), depending on the beam used.

FEBID and FIBID allow local deposition in the targeted place with controllable lateral size (typical size from 15 nm to 10 µm) and thickness (typically ranging from 10 nm to 10 µm). Amongst applications of FEBID and FIBID deposits, one can cite the reparation of optical masks and integrated circuits [8], fabrication of three-dimensional nanostructures [9], deposition of protection layers for lamella preparation [6], creation of electronic nanodevices [10], fabrication of nanoelectrodes and nanocontacts [11], transport studies of nanowires [12], deposition of magnetic [13] or superconductor materials [14], etc. This technique possesses unique advantages to fabricate nanostructures with respect to more conventional techniques (such as Electron Beam Lithography, for instance). It is a one step mask-less process, with resolution around 15 nm (determined by the volume interaction of the beam with the substrate). Sophisticated structures can be created, on principle on any surface, in a routine way. To illustrate the advantages with respect to techniques where resist is necessary, we show in figure 2.8. a comparison between EBL and FEBID/FIBID. Chapters 5, 6 and 7 in this thesis are dedicated to applications using these techniques.

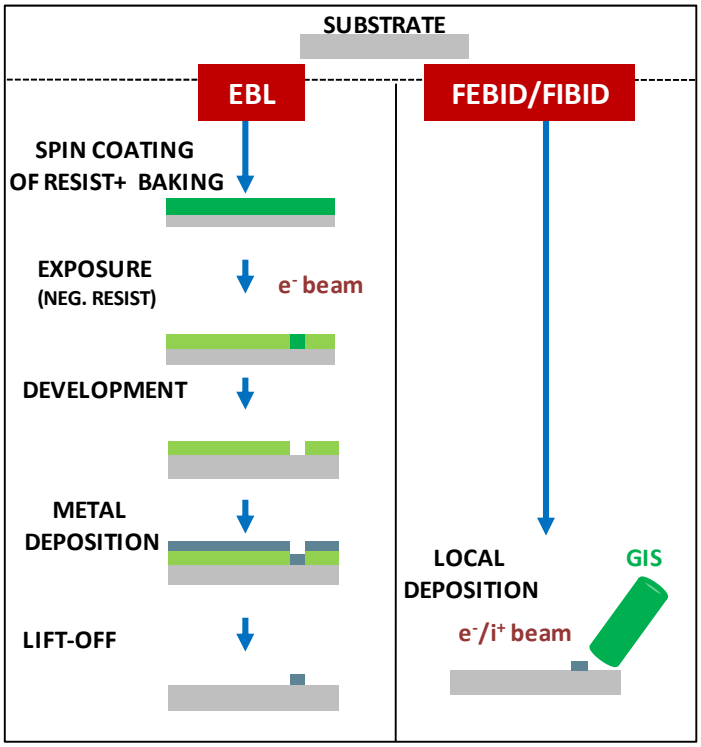

Fig. 2.8. Scheme comparing an EBL (lift-off) and an FEBID/FIBID process.

FEBID and FIBID involve a chemical vapour deposition process that is assisted by electron and ion beams respectively (for recent review articles, see references 15 to 17). The basic principle is simple: A Gas-Injection-System needle (GIS) is inserted near the substrate. Gas is injected into the chamber, getting adsorbed on the surface. The beam electrons/ions interact with these gas molecules, decomposing them. As a consequence, the volatile fragments are evacuated from the vacuum chamber, the rest getting deposited (see a scheme of the process in figure 2.9.).

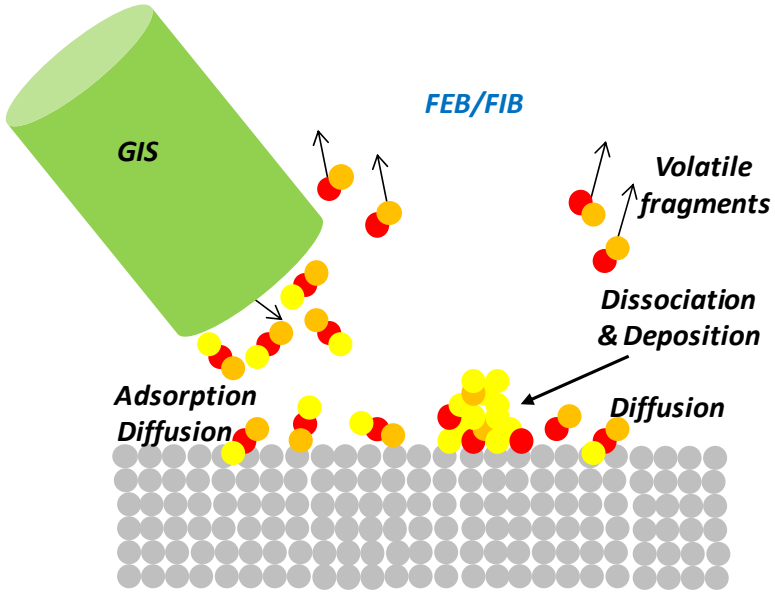

Fig. 2.9. Scheme for FEBID and FIBID. Molecules are injected by the GIS, get adsorbed, and diffused at the surface. Some of them are decomposed. The non-volatile fragments get deposited, whereas the volatile fragments are pumped away.

In order to get deeper understanding of this growth technique, three main physical-chemical processes should be taken into account:

- The first one is the substrate-precursor molecule interactions: Mechanisms such as diffusion, adsorption and desorption have to be taken into account.

- The second one is the electron/ion-substrate interaction. A primary beam of electrons/ions is focused onto the substrate. Some of these electrons collide and are deflected from their initial trajectory whereas other ones undergo inelastic collisions transferring the energy to other electrons/ions.

- The third one is the electron-precursor molecule interaction. The probability that an electron induces the scission of a bond in a precursor molecule depends on the electron energy and is generally expressed as a cross-section (cm^2). It depends on the energy of the bonds within the molecule and, in general, electrons with energy a few eV are able to produce the molecule dissociation.

Furthermore, three clear deposition regimes have been identified [15-17], which depend on all the factors described before:

- Electron-limited regime: the growth is limited by the current density and is independent of the gas flux.

- Precursor-limited regime: the growth is limited by the number of molecules, coming from the GIS, and arriving on the irradiated area,.

- Diffusion-enhanced regime: the supply of gas molecules for deposition is dominated by the surface diffusion.

The physical phenomena involved in the deposition are thus complex and models trying to explain the experimental results take into account factors such as the electron flux as well as their spatial and energy distribution, the cross section of the precursor as a function of electron energy, the precursor residence time, the electron-beam induced heating, etc. An important piece of information has been gained through Monte Carlo simulations [15-17]. Those simulations have highlighted the important role played by the generated secondary electrons in the deposition rate and also in the spatial distribution and resolution of the nanodeposits.

A typical situation for these techniques is to use an organo-metallic gas precursor for the local deposition. In general, these gases are not fully decomposed, and a carbonaceous matrix is also present in the deposits. The typical metal content for deposits by FIBID is around 30-40% atomic, with the rest being mainly carbon, whereas for FEBID the metal content is usually only around the 15-20 %. Thus, the main drawback when creating metallic nanostructures with these techniques is the high carbon percentage present in the deposits, which can influence dramatically the properties of these nanostructures. Post-growth purification processes are sometimes used to increase the metallic content [18, 19]. In the case of FIBID, the damage induced by ions is also an important issue to take into account. These aspects, together with a higher yield for FIBID with respect to FEBID, are the most relevant differences between depositing with one or other column. In this thesis we have used three

precursors, shown in figure 2.10.: methylcyclopentadienyl-trimethyl platinum [$(CH_3)_3Pt(CpCH_3)$], whose results are shown in chapter 5, tungsten hexacarbonyl [$W(CO)_6$], chapter 6, and dicobalt octacarbonyl [$Co_2(CO)_8$], chapter 7.

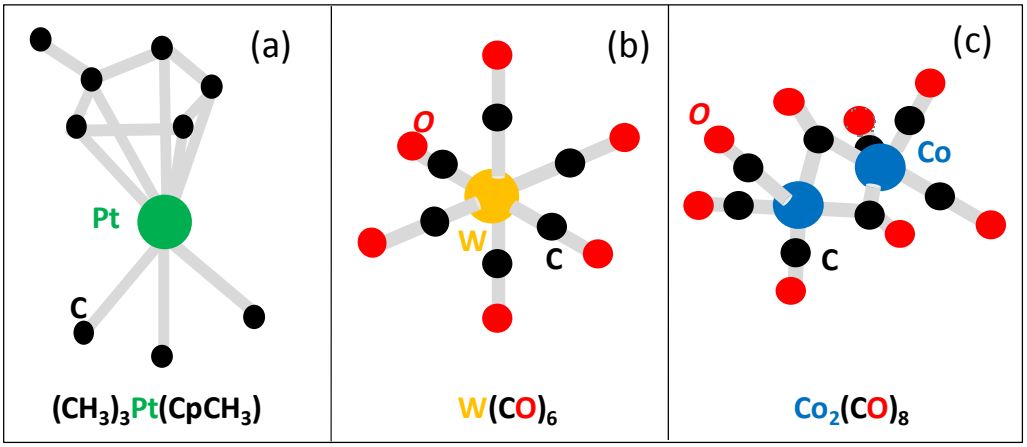

Fig. 2.10. Chemical structure of the three metal-organic gases used in this thesis. **(a)** $(CH_3)_3Pt(CpCH_3)$. **(b)** $W(CO)_6$. **(c)** $Co_2(CO)_8$

2.2. Electrical measurements

2.2.1. Magnetotransport measurements as a function of temperature

For the study of the electrical transport measurements of samples, as a function of temperature and magnetic field, we have used the combination of several equipments belonging to the Institute of Materials Science of Aragón (ICMA) (see in figure 2.11. some pictures):

- Combined Keithley® system, composed of a 6220 DC current source, and a 2182A nanovoltmeter. By injecting a constant current (DC), the voltage of the device under test is measured. A wide range of resistances can be measured, from 10 nΩ to 1GΩ.

- Closed-Cycle-Refrigerator (CCR) by Cryocon®. By means of the thermodynamic cycle in He gas, the cryostat can lower the temperature of the sample down to 25 K. The control of temperature is performed by standard PID parameters.

- Electromagnet by Walker Scientific®, delivering maximum magnetic fields of 11kOe.

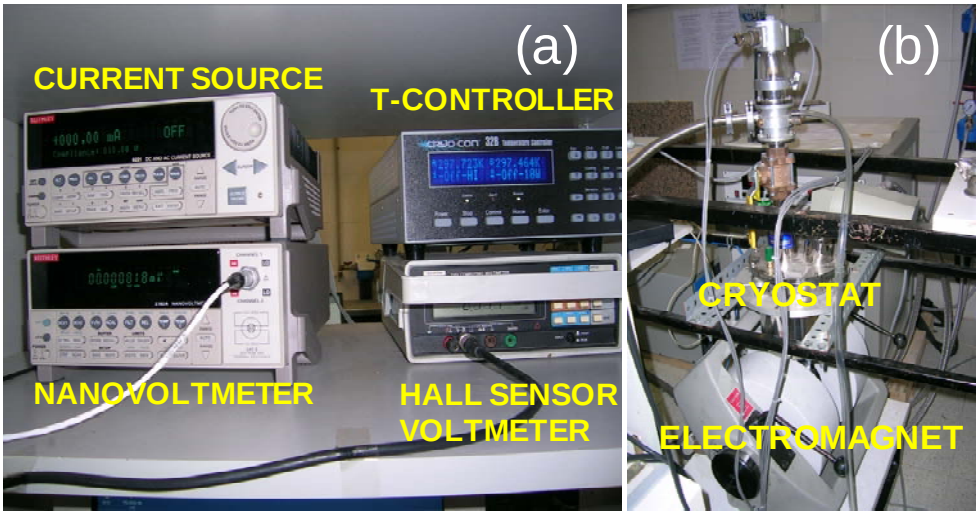

Fig. 2.11. Images of the system used for magnetotransport measurements as a function of temperature. **(a)** Equipments for electrical measurements, as well as for the control of temperature and magnetic field. **(b)** General view of the system.

A scheme of the system is shown in figure 2.12. The control of all equipments via PC was done by the design of Labview® programs. All this work was done together with Dr. Jan Michalik.

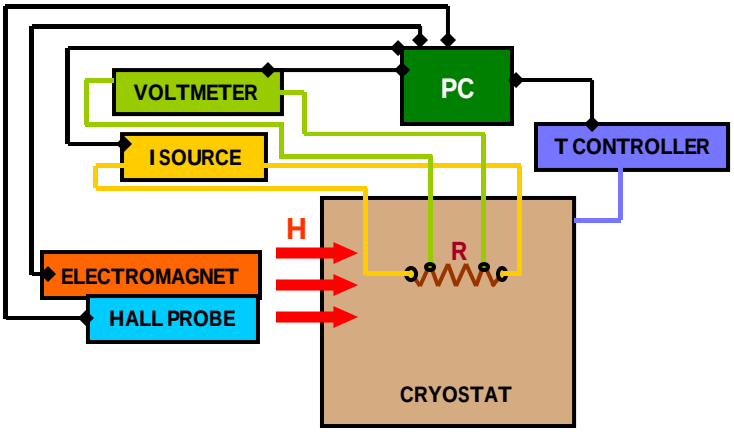

Fig. 2.12. Scheme of the system for magnetotransport measurements as a function of temperature.

The electrical measurements are normally done in a 4-probe configuration, to avoid the contact resistance in measurements. This geometry of measurement is schematized in figure 2.12.

The Keithley system has been used in two modes of measurements:

- Normal DC mode: A constant current is applied, and voltage is measured.

- *Delta* mode: The voltage is measured with alternating positive and negative test current. This allows the cancelling of constant thermoelectric voltages by alternating the test current. It significantly reduces white noise, resulting in more accurate low resistance measurements when it is necessary to apply very low power.

Some few electrical measurements in this thesis were done in a commercial Physical Properties Measurement System (PPMS) from Quantum Design, in the Service of Instrumentation of the University of Zaragoza. It was used when high magnetic fields (maximum field of 9 Tesla) or low temperatures (minimum

temperature of 300 mK) were necessary, for resistances below ~1MΩ.

2.2.2. "In situ" electrical measurements

Some of the results obtained in the thesis have been done by the combination of the nanolithography techniques with electrical measurements. The usual approach followed consists on a study of the devices after having been created or modified. However, in our case we have also done, in some cases, simultaneous electrical measurements while the nanostructure was being patterned. For it, two types of special stages were inside the Dual Beam system (see figure 2.13.):

(i) Four electrical microprobes by Kleindiek®. They are separately moved by a motor or piezoelectric, till contacted to pads. They are made of tungsten, have a final diameter of around 1 μm.

(ii) Home-made stage, with eight connections, with the sample contacted by wire-bonding to a chip carrier, which is loaded in the stage.

The electrical wires are transferred outside the chamber by a port, and connected to the same Keithley system explained before.

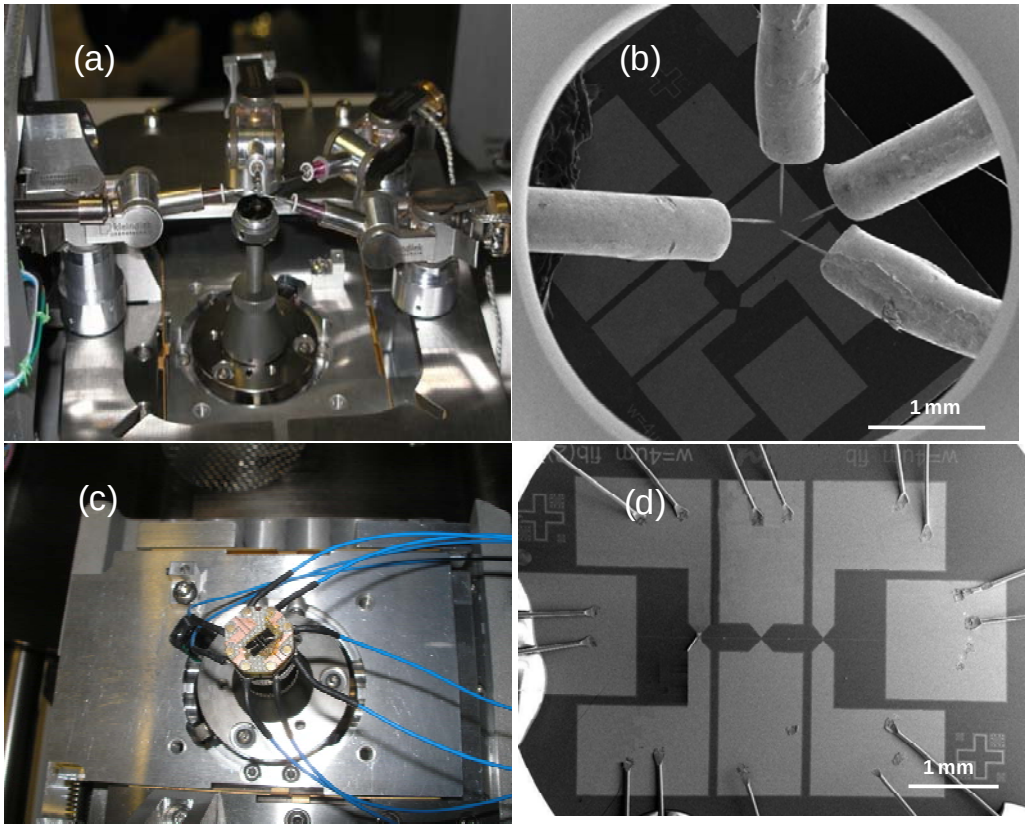

Fig. 2.13. Images of methods for electrical measurements inside the Dual Beam chamber **(a)** Electrical microprobes stage **(b)** SEM image of the microprobes inside the chamber, with a sample in a plane below **(c)** Stage for electrical measurements. A sample is mounted in the image **(d)** SEM image of a sample with microcontacts connected to the

2.3. Spectroscopic techniques

We have mainly used two different spectroscopy techniques to characterize he composition and chemical nature of the samples studied: Energy Dispersive X-Ray spectroscopy (EDX) and X-Ray Photoelectron spectroscopy (XPS).

2.3.1. Energy Dispersive X-Ray spectroscopy (EDX)

We showed in figure 2.7(a), that as a consequence of the interaction of electrons with matter, in the keV range, X-Ray photons are produced. The PE produce the emission of inner electrons, which create a hole in an atomic level. An electron from an outer, higher-energy shell can fill that hole, emitting an X-Ray, with a characteristic energy equal to the difference between the higher and the lower energy shell. As the energy of the X-rays are characteristic of the difference in energy between the two shells, and of the atomic structure of the element from which they were emitted, this allows the elemental composition of the specimen to be measured. See a scheme of the process in figure 2.14.

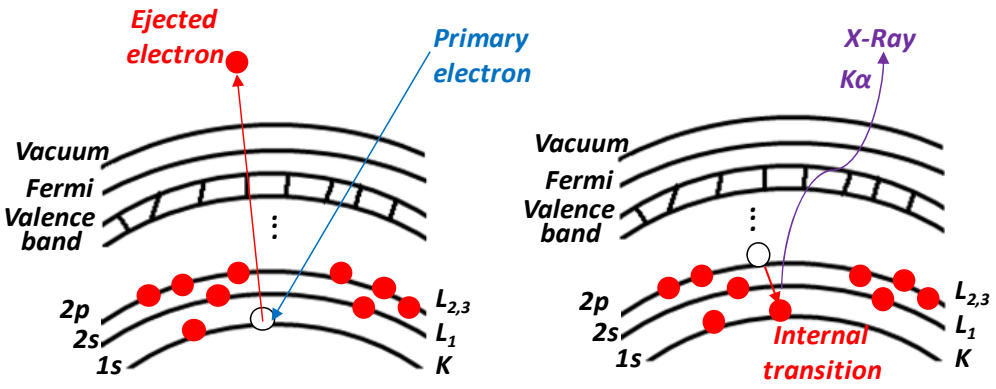

Fig. 2.14. Schematic diagram of the EDX process. Relaxation of the ionized atom results in photon radiation, characteristic for each element.

An EDX by Oxford Instruments® was used, incorporated in the Dual Beam system, for in situ compositional characterization (see figure 2.6.). The interaction volume of the electron beam with the sample determines both the lateral resolution and the depth of analysis; this is a function of the primary beam energy, invariably of

the order of one micrometer. The energy resolution is ~ 150eV. This permits to do a compositional quantification of the sample probed.

2.3.2. X-Ray Photoelectron Spectroscopy (XPS)

XPS (traditionally called ESCA) is a spectroscopic technique based on the photoelectric effect, i.e., the ejection of an electron from a core level by an X-Ray photon of energy hv. The energy of the emitted photoelectrons is then analyzed by an electron spectrometer. The kinetic energy (E_K) of the electron is the experimental quantity measured by the spectrometer, but this value will depend on the X-Rays energy. The binding energy of the electron (E_B) is the parameter which identifies an element specifically. The equation which describes the process is:

$$E_B = h\nu - E_K - W \qquad (2.1.)$$

where W is the spectrometer work function. Albert Einstein received the Nobel Prize in Physics in 1921 by the interpretation of the photoelectric effect. Figure 2.15. shows a scheme of the XPS process.

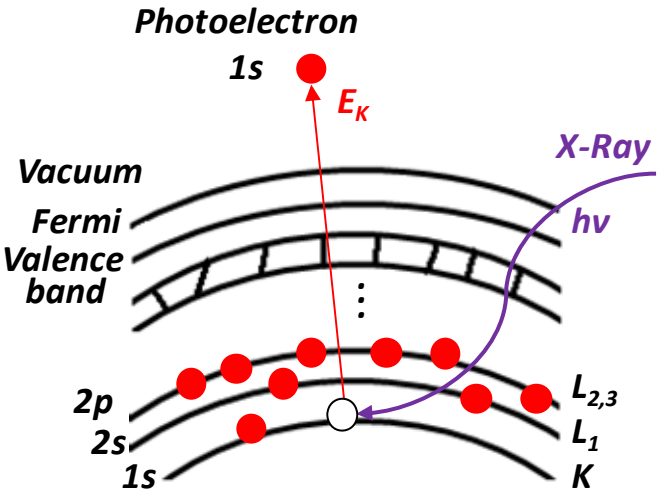

Fig. 2.15. Schematic diagram of the XPS process, showing the photoionization of an atom by the injection of a 1s electron

For these experiments we used an Axis Ultra DLD equipment by Kratos® , in the INA. A monochromatic Al kα X-Ray source was used, with exciting energy hν=1486.6eV. The sampling depth of X-ray is in the micrometric level, while only those photoelectrons from the outermost, ~10 nm or less, escape without energy loss. These electrons are those used for quantitative quantification; XPS is, thus a surface-sensitive technique. An in-depth study can be performed since the equipment incorporates a 5kV- Ar^+ gun, which progressively etches layers of material, which are consequently probed by XPS. A hemispherical detector analyzes the electron energy. The experiments require ultra-high vacuum conditions (ionic pump).

Due to the difficulty in focusing X-Rays, the effective minimum area probed in the equipment is approximately 30 × 30 μm^2. The high resolution of the equipment (maximum = 0.25 eV) permits to distinguish the valence state of the atoms composing the sample.

2.4. Spatially-Resolved MOKE magnetometry

The main magnetometry technique used in the thesis is a magneto-optic technique: the spatially resolved Longitudinal Magneto-Optical-Kerr-Effect (MOKE). These measurements were done in the Imperial College in London, in the group of Prof. Russell P. Cowburn.

The Kerr effect consists on the rotation of the plane of polarization of a light beam when reflected from a magnetized sample. We show in figure 2.16. the geometry for the longitudinal Kerr-effect (L-MOKE). Radiation from a light source is first passed through a polarizer. The resulting plane-polarized light is then incident on a sample. The L-MOKE is sensitive to the in-plane magnetization component of the sample, and thus it is in the incidence plane of light. The magnetization changes the angle of polarization of light, as well as induces an ellipticity in the initially linearly-polarized light. The thickness probed is typically of 20 nm. In the example of figure 2.16., the sample contains two domains magnetized in opposite directions. The light incident on one domain is rotated in the opposite direction from that incident on the other domain. Therefore, if the analyzer is oriented such that the light from the first domain is maximum, then the plane of polarization of the light reflected from the other domain is not aligned with the analyzer, and the signal is reduced.

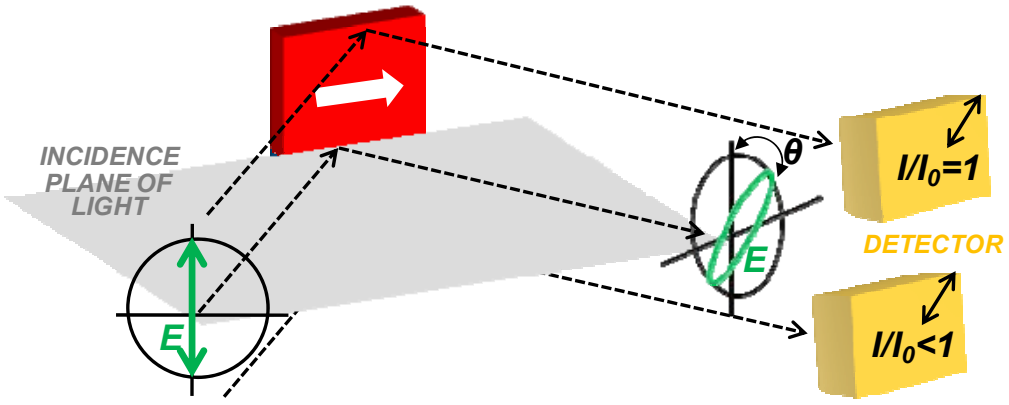

Fig. 2.16. Geometry for the Longitudinal-MOKE (see text). In the central ray of light, the polarization of the electric field changes from linear to elliptical polarization, with a change in the angle of polarization, θ. In the top ray, the detector is aligned to make the signal maximum. Thus, due to the contrary angle rotation in the bottom ray, due to an opposite magnetization direction in the sample, the signal collected by the detector is smaller.

Linearly polarized light can be decomposed in two oppositely circular polarizations. The angular number of both is equal to 1, but in right circularly polarization (+), m_L= +1, whereas left circularly light (-) has m_L= -1. Using the simple example of a magnetic material with atomic spin S=1/2, the exchange interaction splits its energy levels in two sub-levels, with total spin m_S= +1/2 and m_S= -1/2.

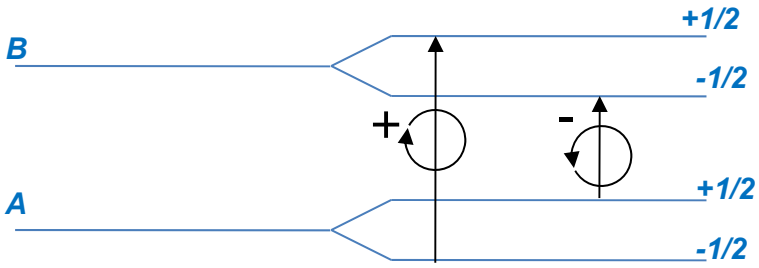

Fig. 2.17. Absorption of light in a ferromagnet, with S= 1/2.

Both energy and angular momentum must be conserved when a photon excites an electron from one sub-level in A to one in B. Selection rules dictate that $\Delta m_L = \pm 1$, implying that only transitions drawn in figure 2.17. are possible. Thus, oppositely polarized photons correspond to different electronic transitions in the atom. If the electronic population in B sub-levels differ one from the other, the absorption of one polarization is greater than the other (phenomenon called circular dichroism). When the resulting circular polarizations are recombined again, the plane of polarization is rotated compared with the incoming beam. The resulting phase difference between the initial and final planes of polarization is called circular birefringence.

The magneto-optical effects do not directly provide absolute values for the magnetization. The MOKE rotation depends on the angle of measurement and wavelength of light, as well as on the magneto-optic constant, which is material dependent at a determined temperature. Thus, MOKE measurements provide hysteresis loops in intensity (arbitrary units) as a function of the magnetic field. The Kerr effect is normally used for measurements of hysteresis loops in magnetic thin film layers, or for the imaging magnetic domains. However, this experimental setup [20, 21], now commercial by Durham Magneto Optics® is suitable for the

measurement of magnetic nanometric structures. A diode-pumped solid state laser (λ=532 nm) with a diameter of about 5 μm (FWHM) is used as probe. A CCD camera is used for pre-alignment of the nanometric structure, located on a substrate. The final alignment is done by performing a reflectivity map of the zone of interest. A motor permits to move the stage with a resolution of 50 nm. A quadruple is used for applying AC magnetic fields (1-27Hz), with H_{max}~400 Oe. The system is the state-of-the-art-MOKE instrument, having, for instance, a sensitivity for permalloy $S=6\times10^{-12}$ emu at room temperature [21] (in a SQUID magnetometer S ~10^{-8}- 10^{-9} emu). This high sensitivity permits to measure hysteresis loops in sub-micrometric & sub-λ nanomagnets. As the diameter of the laser is bigger than, at least, one of the dimensions of the nanostructure probed, a dilution factor is present in the MOKE signal with respect to the bulk material.

2.5. Atomic Force Microscopy

In previous sections we have cited two main microscopy techniques used for this work: the optical microscope, allowing the observation of structures with sizes slightly below one micron, and the scanning electron microscope, which can resolve objects around 1 nm in size.

In this section, we will comment some aspects of another microscope used, with resolution of fractions of a nanometer: the Atomic Force Microscope (AFM). AFM is a type of scanning probe microscope (as its father, the Scanning Tunneling Microscope), based on the interaction of a sharp tip with the surface sample, when it is brought into proximity to the surface. The tip is the end of a microscopic cantilever, used to scan the specimen surface. The cantilever is typically silicon or silicon nitride with a tip radius of curvature on the order of nanometers. The forces between the tip and the sample lead to a deflection of the cantilever, which can be modeled with the Hooke's law. The typical AFM forces are mechanical contact force, Van der Waals force, capillary forces, electrostatic forces, magnetic force (MFM) etc. Typically, the deflection is measured using a laser spot reflected from the top surface of the cantilever into an array of photodiodes.

The AFM images were performed in the Imperial College in London, with a Veeco® AFM. The PHD student Liam O'Brien, whose thesis director is Prof. Russell P. Cowburn, did a part of the measurements. Contact mode was used for imaging, where the force between the tip and the surface is kept constant during scanning by maintaining a constant deflection. The tip deflection is used as a feedback signal, which is used to form an image of the structure probed.

Some clear advantages of AFM with respect to the SEM can be named, such as a better spatial resolution, the measurements do not require vacuum conditions, a true three-dimensional surface profile is obtained, and there are not charging-effects problems with insulator samples. However, there exist important disadvantages of AFM compared with SEM. The SEM can image an area on the order of mm × mm,

with a depth of field on the order of mm. The AFM can only image a maximum height on the order of microns, and a maximum scanning area of a few μm^2. Besides, image artifacts are common, especially if an incorrect choice of tip for the required resolution is done. The significant lower speed in the image is also an important drawback, as well as the possible hysteresis in the piezoelectric. We should cite for completeness that AFM is also used as a tool for nano-patterning, by local oxidation, dip-pen nanolithography, etc.

2.6. Other techniques

In the thesis, some results will be presented with other techniques different from those explained before, and should also be mentioned. The person in charge of the measurements is cited in the text when a particular result is presented, in following chapters.

Pulsed Laser Deposition, PLD (INA): Fe_3O_4 thin films were epitaxially grown on MgO (001) substrates. A KrF pulsed laser produces an ablation in a Fe_3O_4 target, depositing stochiometrically the iron oxide on the substrate.

High Resolution X-Ray Diffraction, HR-XRD (INA): Structural characterization of thin films. Determination of the degree of crystallinity of a film grown on a substrate.

Superconducting quantum interference device, SQUID magnetometer (Scientific services of University of Zaragoza): A constant current passes through two in-parallel Josephson junctions. The applied voltage oscillates with the changes in the phase of the two junctions, which depend upon the change in magnetic flux. This results in a highly sensitive magnetometer.

High-Resolution Transmission Electron Microscope, HRTEM (Scientific Services of the University of Barcelona): 200 kV- electrons are accelerated, being transmitted through a thin sample (~100 nm). The image formed, consequence of the diffraction of electrons with the material, can be transformed to the real space, resulting in an image of the crystallographic structure of a sample at an atomic scale.

Scanning-Tunneling-Spectroscopy, STS (University Autonóma of Madrid, group of Prof. Sebastián Vieira): The local density of electronic states of a surface is probed at the atomic scale, by measuring the tunneling differential conductance between a STM tip and a sample at low temperatures.

Chapter 3

Magnetotransport properties of epitaxial Fe_3O_4 thin films

In this chapter we will show the magnetotransport properties of epitaxial Fe_3O_4 thin films [grown on MgO (001)]. A broad characterization has been performed, studying systematically, for several film thicknesses and as a function of temperature, the resistivity, magnetoresistance in different geometries, Hall effect and Planar Hall effect. Most of the measurements are substantially influenced by the presence of the Antiphase Boundaries, especially for ultra-thin films. In the case of the Anomalous Hall effect, an experimental evidence of the universal character of this phenomenon was demonstrated.

The growth of the films was performed by J. Orna, being matter of her Ph. D. Thesis.

3.1. Introduction

3.1.1. General properties of Fe_3O_4

Magnetite, Fe_3O_4 is the first magnetic material referred in the history of humankind. Its magnetic properties were reported in the *Chinese book of the Devil Master*, in the 4th century BC. This iron oxide is the magnetic mineral contained in lodestone, from which first compasses for navigation were made. In spite of this long perid, physics of magnetite still has a lot of open unresolved aspects.

Magnetite is magnetic at room temperature, being ferrimagnetic, with a Curie temperature of 858 K [1]. It belongs to the cubic ferrite family: $Fe^{2+}O^{2-}\cdot(2Fe^{3+}3O^{2-})$, with an inverse spinel crystallographic structure (lattice constant=8.397 Å). This structure (Fd3m space group) consist of a face-centered-cubic (FCC) oxygen lattice, with Fe^{3+} ions filling 1/8 of the available tetrahedral sites (A sites), and equal amounts of Fe^{2+} and Fe^{3+} ions filling half of the available octahedral site (B sites), see figure 3.1(a).

The spin moments of all the Fe^{3+} ions on B sites are ferromagnetically aligned and in opposite direction to the Fe^{3+} occupying the A sites. Therefore the magnetic moments of all Fe^{3+} cancel out, resulting in a zero contribution to the overall magnetization of the solid. However, all the divalent ions are ferromagnetically aligned parallel, providing a net magnetization of approximately 4 μ_B/f.u. Several magnetic exchange interactions are present in Fe_3O_4, which are detailed in figure 3.1(b).

The conduction in magnetite has been extensively studied and modeled. In a simple picture, as a consequence of the double-exchange (ferromagnetic) interaction existing between Fe^{2+} and Fe^{3+} in B sites, the additional spin-down electron can hop between neighboring B-sites, resulting in a high conductivity, and an intermediate valence of $Fe^{2.56+}$. Around 120 K (T_v), a first-order phase transition occurs, the so called Verwey transition [2]. At this transition, the structure distorts from cubic symmetry [3, 4], and a charge ordering occurs at the B sites, reducing the conductivity

two orders of magnitude [3, 4]. Conduction is, however, much more complex. We could cite the models developed by Ihle and Lorentz [5] and Mott [6], as those that are currently better established.

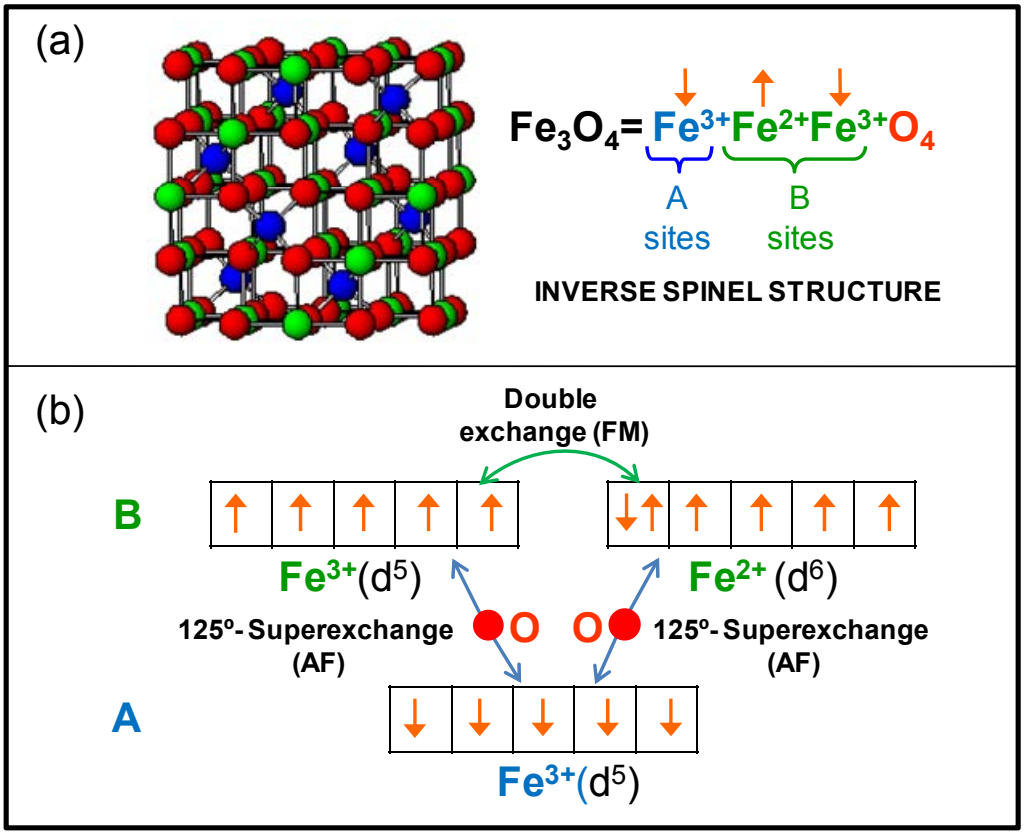

Fig. 3.1. (a) The inverse spinel structure of Fe_3O_4, consisting on a FCC oxygen lattice, with octahedral (B) and tetrahedral (A) sites, filled by Fe^{2+} and Fe^{3+} cations (see text for details). **(b)** Scheme of the exchange interactions present in magnetite. The strong antiferromagnetic (AFM) superexchange interaction between A and B ions, mediated by oxygen ions, forces the parallel alignment of ions in A sites. The ferromagnetic (FM) double-exchange interaction between Fe^{2+} and Fe^{3+} permits the hopping of electrons between B sites.

3.1.2. *Half-metal prediction for Fe_3O_4*

The spin polarization P can be defined as

$$P = \frac{N_{\uparrow}(E_F) - N_{\downarrow}(E_F)}{N_{\uparrow}(E_F) + N_{\downarrow}(E_F)} \qquad (3.1.)$$

where $N_{\uparrow}$ and $N_{\downarrow}$ are the density of states (DOS) with up and down spins, respectively. Spin polarization is, then, a measurement of the net spin of the current flowing through the material. If only one type of electron is responsible for conduction, |P|= 1, and the material is referred as "half-metal". In figure 3.2. a scheme of bands in a non-magnetic, a normal ferromagnetic (such as iron, for example) and a half-metal material, is shown.

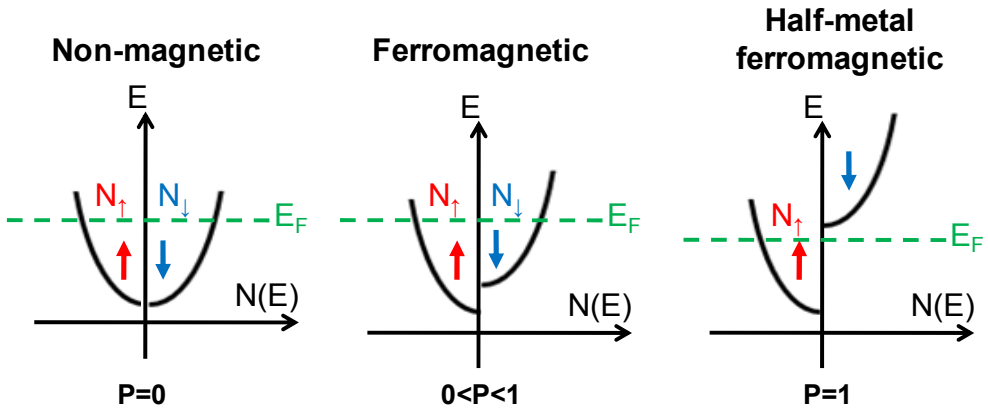

Fig. 3.2. Bands scheme of a non-magnetic, a ferromagnetic and a half-metal ferromagnetic material. In a half-metal, all the electrons responsible for conduction (those at the Fermi level) have only one spin direction.

In accordance with the qualitative description for conduction explained in the previous section, band calculations [7, 8] predict that the conduction in magnetite above T_v is fully polarized, with P = -1. In practice, photoemission [9, 10], tunneling magnetoresistance [11] or STM [12] measurements have evidenced a high negative spin polarization.

An enormous technological interest exists in studying half metal materials, due to its importance in spintronic devices, since magnetic tunnel junctions (MTJ) composed of two half-metal electrodes will exhibit high magnetoresistance (TMR) signals. Considering the model developed by Jullière [13] for TMR:

$$TMR(\%) = 100\frac{2P_1P_2}{1-P_1P_2} \qquad (3.2.)$$

TMR will diverge if $P_1=P_2=1$. We should, however, remark that in this simple model the DOS of the electrodes alone defines the tunneling current, but in reality the insulator barrier is also fundamental for the TMR signal [14] since it can act as a symmetry filter for the wave functions of tunneling electrons [15, 16].

Apart from magnetite, other compounds have been predicted as half-metals [17, 18]: CrO_2, manganites, double-perovskites and heusler alloys. For a possible application of in real spintronic devices, these materials should be grown in a form of highly crystalline thin films.

3.1.3. Properties of epitaxial Fe_3O_4 thin films

Many groups have worked during the last years in growing epitaxial Fe_3O_4 thin films by Molecular Beam Epitaxy (MBE) and Pulsed Laser deposition (PLD) [19-27]. The most commonly chosen substrate is single crystal MgO (001), because its cubic lattice parameter, 4.21 Å has a small lattice mismatch with bulk Fe_3O_4, permitting the epitaxial growth of films.

The most important aspect to remark in Fe_3O_4 thin films with respect to the bulk material is the presence of structural defects, caused by the growth mechanism, called Antiphase boundaries (APBs) [20, 21, 27]. APBS form when islands of Fe_3O_4 coalesce and neighboring islands are shifted with respect to each other. In figure 3.3. a scheme of an APB is shown. There exist different types boundaries, depending on the

vector shift present. For details of APBs see references 21 and 27.

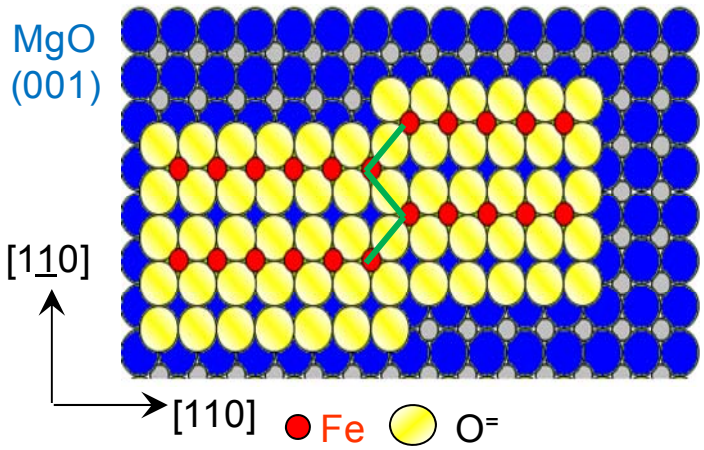

Fig. 3.3. Schematic representation of an APB in Fe_3O_4 formed in a MgO (001) substrate. When right and left iron oxide islands coalesce while growing, a loss of periodicity can occur, forming a boundary.

These structural defects play a major role in the properties of magnetite thin films, mainly due to the superexchange AF interactions between spins surrounding the boundary. The important increase of resistivity [22], the lack of saturation in the magnetization [27], or a higher magnetoresistance effect than in single crystals [20, 26, 28], as a consequence of the spin-polarized transport, are caused by APBs. It is important to point out that spin-resolved photoemission studies in thin films, show that APBs do not seem to reduce significantly the spin polarization in films [29].

3.2. Experimental details

3.2.1. Growth of the films

The Fe_3O_4 target was prepared from Fe powder by solid-sate reaction [30]. Fe_3O_4 thin films were grown [31] on MgO (001) substrates by PLD using a KrF excimer laser with 248 nm wavelength, 10 Hz repetition rate and 3×10^9 W/cm^2 irradiance. The base pressure in the deposition chamber was lower than 10^{-8} Torr, and the substrate was kept in vacuum at ≈400 ºC during laser ablation of the target.

3.2.2. Types of electrical measurement: Van der Paw and Optical lithography

The magnetotransport measurements were performed in the combined closed cycle refrigerator- electromagnet-Keithley system explained in section 2. Basically, all the work that will be exposed below comprises two types of measurements:

- As a function of the thin film thickness, at room temperature: 5 × 5 mm^2 samples were deposited, being measured by the Van Der Pauw technique [32] (current // [001] or // [110], depending on if longitudinal or transversal resistivity components is measured) after wire-bonding to the corners of the sample (see figure 3.4(a_1) and (a_2))

- As a function of temperature, for selected thicknesses= 40 and 20 nm: An optical lithography process was carried out in 0.5 × 0.5 inch^2 samples (current // (001), see figure 3.4(b) and section 2.1.1.), since the big resistance values for Fe_3O_4 at low temperatures (especially below T_v) would do unfeasible the measurements of transversal voltages (Hall and Planar Hall effect) with the Van Der Paw method.

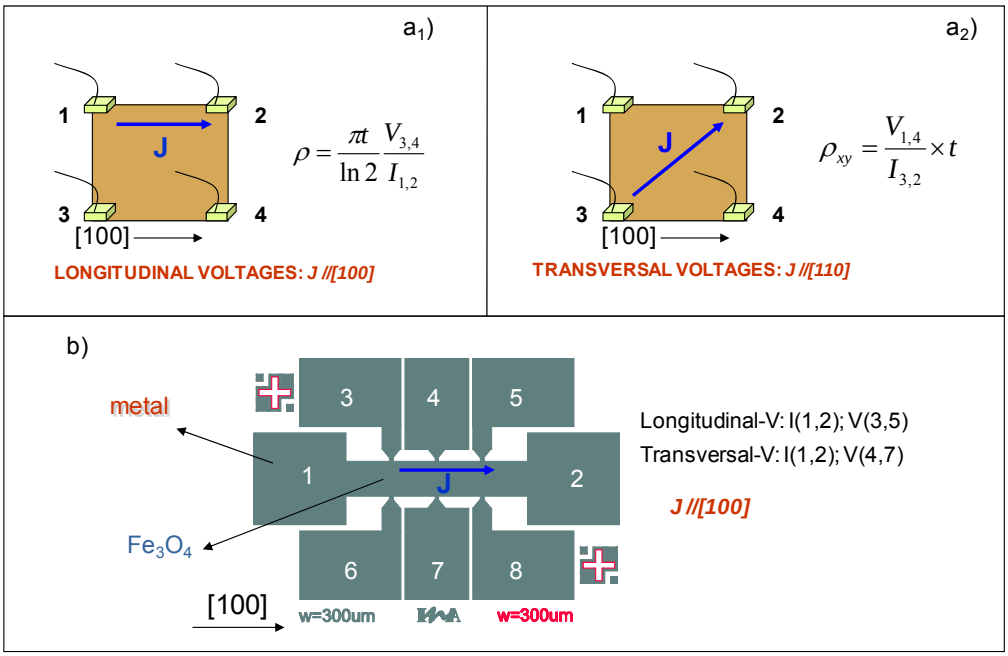

Fig.3.4. Geometry for the two types of measurements done in Fe_3O_4 thin films. **(a)** Van der Pauw measurements at room temperature, as a function of film thickness. Configuration for longitudinal (a_1) and transversal (a_2) voltages. The explicit expression for the components of the resistivity tensor are shown. **(b)** Sample for temperature-dependent measurements. Several equivalent pads were designed, for more flexibility in the measurements. Metal was deposited on these pads, on top of magnetite, to minimize the contact resistances.

3.3. Structural and magnetic characterization

Together with the thorough transport characterization explained in next sections, the films were characterized structural and magnetically [31], to prove the epitaxy of the films.

In figure 3.5. we show x-ray diffraction data taken on a 40 nm thick. The symmetrical θ/2θ scan around the 002-Bragg peak from the MgO substrate shows the 004-reflection from the Fe_3O_4 film, which gives the expected orientation Fe_3O_4 (001) // MgO (001). The Fe_3O_4 out-of-plane lattice parameter extracted from the peak position is a_{out} = 8.38 Å. This value, lower than the bulk Fe_3O_4 lattice parameter, indicates that the film is tensile strained in the plane, due to the slight differences in the lattices parameters between film and substrate, and therefore, is compressively strained in the out-of-plane direction. Moreover, the periodicity Δq of the observed Laue oscillations gives a coherence length $\xi = 2\pi/\Delta q = 39\pm1$ nm, which indicates the existence of crystalline coherence along the full thickness of the film. The observation of Laue oscillations, up to 10^{th} order, is normally taken as an indication of a very high crystalline coherence.

Magnetic measurements in a SQUID magnetometer revealed saturation magnetization at room temperature of M_s =440 emu/cm^3. As commented previously, the decrease of M_s with respect to bulk (M_s=480 emu/cm^3) is associated to the AF coupling in APBs [27].

Direct visualization of the APBs network in our samples was achieved through plane-view TEM measurements [33]. Figure 3.6. shows the dark-field image of a plane-view TEM specimen (40 nm thick film) collected by selecting a (220)-type reflection. The APBs are located where there is darker contrast. The mean size of domains between boundaries (APDs: Antiphase domains) for this sample is 24.4 nm with a standard deviation of 13.9 nm. This average domain size is comparable to other reported results for this film thickness [20, 21].

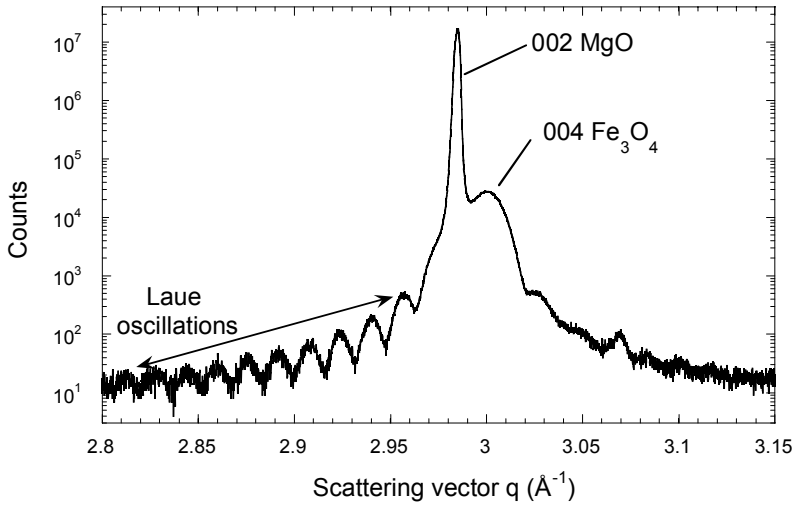

Fig. 3.5. Symmetrical θ/2θ scan as a function of the scattering vector q, around the 002 Bragg peak from the MgO substrate, showing the 004 reflection from the Fe_3O_4 film along with its Laue oscillations. The small peak at q = 3.07 $Å^{-1}$ is a reflection from the silver rest used to fix the substrate during deposition. Experiments performed by J. Orna and J.A. Pardo.

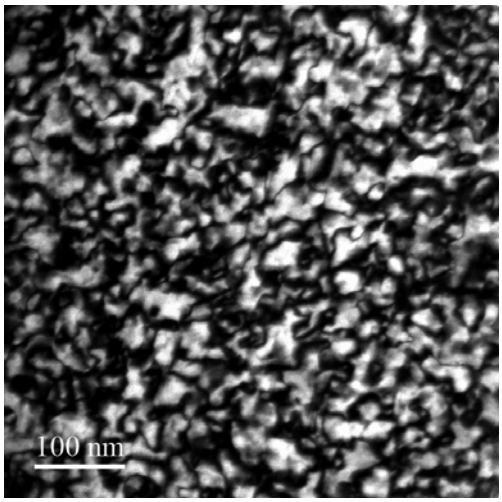

Fig. 3.6. TEM planar-view image of the 40nm-thick film, where the APBs network can be observed. The (220)-type reflection has been selected close to a two-beam condition, in which only the direct beam and one (220)-type reflection are strongly excited, near the [001] zone axis. Image taken by C. Magén in CEMES, Toulouse.

3.4. Resistivity

3.4.1. Resistivity as a function of thickness (room temperature)

The longitudinal resistivity ($\rho_{xx} \equiv \rho$) values at room temperature for films of thickness (t) ranging from 150 down to 3 nm are shown in figure 3.7. , compared with other works in literature [19-22, 26]. The good accordance in the data confirms the high quality of the films. The resistivity enhancement as the films get thinner, apart from the normal increase due to surface scattering, is a direct consequence of the increase in the density of APBs ($\rho \propto \text{thickness}^{-1/2}$) [20, 21].

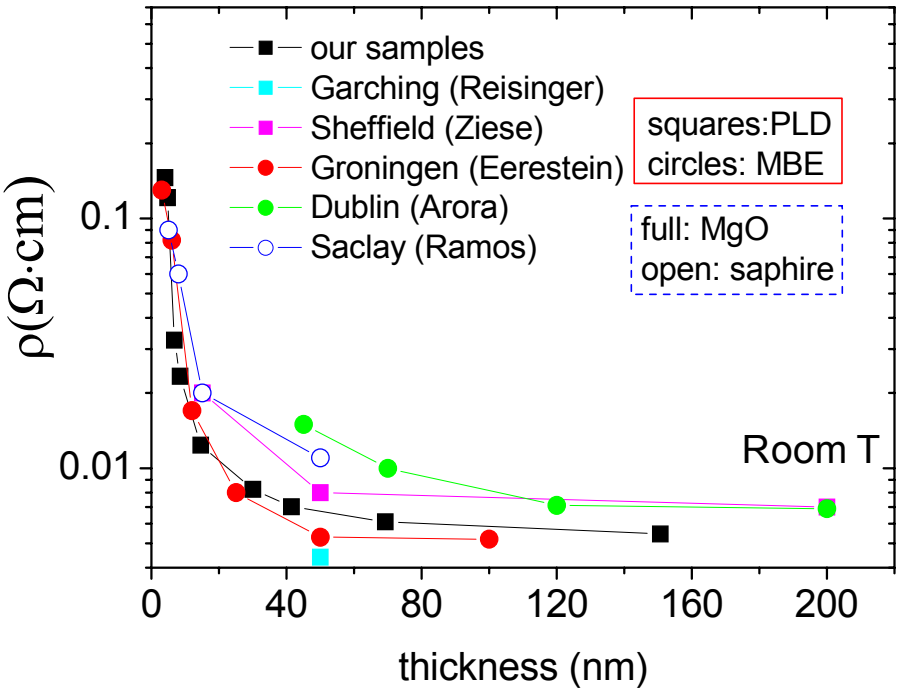

Fig. 3.7. Rom temperature resistivity measurements in a wide range of film thickness. Our data are compared with several groups, in good agreement. The data symbolized as squares or circles refer to samples grown by PLD or MBE, respectively. All these films were grown on MgO, except for the work in Saclay, where they used sapphire.

3.4.2. Resistivity as a function of temperature

Selected samples were measured as a function of temperature. Semiconducting behaviour of the resistivity is observed in the film as a function of temperature, as occurs in the bulk samples (see figure 3.8.). The Verwey transition is observed as a significant increase of ρ. As the films get thinner, the transition gets smoother and smoother, becoming imperceptible for t= 5nm. The Verwey temperature for films is lower than in single-crystals (T_v~120 K). The decrease of T_v with respect to the bulk value has been observed in epitaxial thin films for thickness below 100 nm The two effects observed as films get thinner: decrease of T_v and disappearance of the transition have been associated to the stress caused by the substrate [34] and the inhibition of long range order for very thin films, as a consequence of the big density of APBs [21, 35].

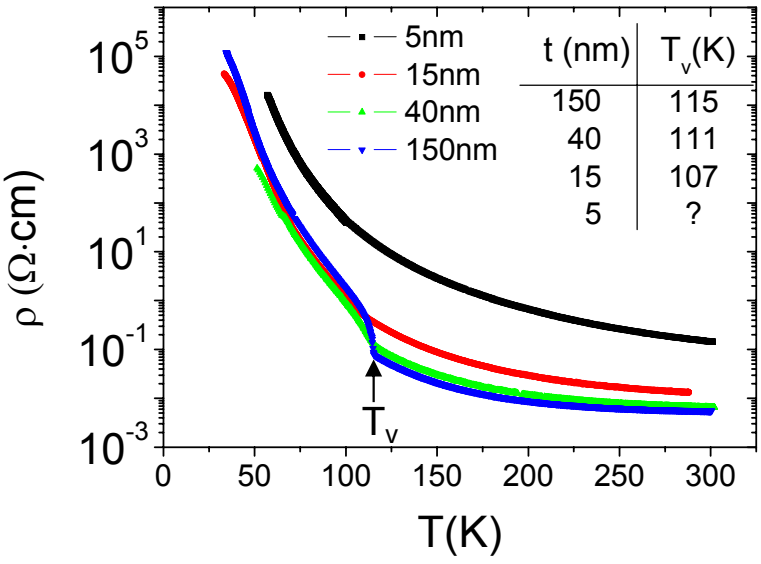

Fig. 3.8. Resistivity as a function of temperatures for four thicknesses. The Verwey transition is indicated with an arrow. As the films get thinner, the transition becomes less abrupt, and T_v is shifted towards lower temperatures.

3.5. Magnetoresistance and anisotropic magnetoresistance

As it was explained in the introductory section, epitaxial Fe_3O_4 thin films present higher (although moderate) magnetoresistance (MR) values than single crystals, due to the spin-polarised transport across sharp antiferromagnetic boundaries [26, 28]. We have used the convention, for the definition of MR:

$$MR(\%) = 100\frac{[(R(H) - R_0)]}{R_0} \qquad (3.3.)$$

3.5.1. Geometries for MR measurements

We have measured the MR up to 11 kOe in 3 geometries, depending on the relative direction of the magnetic field H with respect to the current and substrate plane (see figure 3.9.): H perpendicular to the thin film plane (perpendicular geometry: PG), H in plane and parallel to the current I (longitudinal geometry: LG), H in plane and perpendicular to I (transversal geometry: TG). Measurements in the perpendicular geometry were also done up to 90 kOe in a PPMS by Quantum Design.

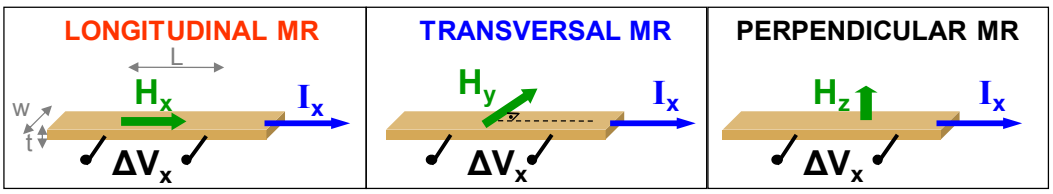

Fig. 3.9. MR geometries ($\rho_{xx} = \frac{\Delta V_x}{I_x}\frac{wt}{L}$). See text for details.

3.5.2. MR as a function of thickness (room temperature)

In figure 3.10. a typical example of the measurements performed is shown for a 40 nm thick film, for the three geometries. The magnetoresistive effect, in all cases, is small (a few percent) and negative. The shape of the magnetoresistance curves is linear for the LG and TG in the range of fields measured, and parabolic for fields lower than the anisotropy field, and linear for fields higher, for the PG. In references

20 and 28, this behaviour is modelled.

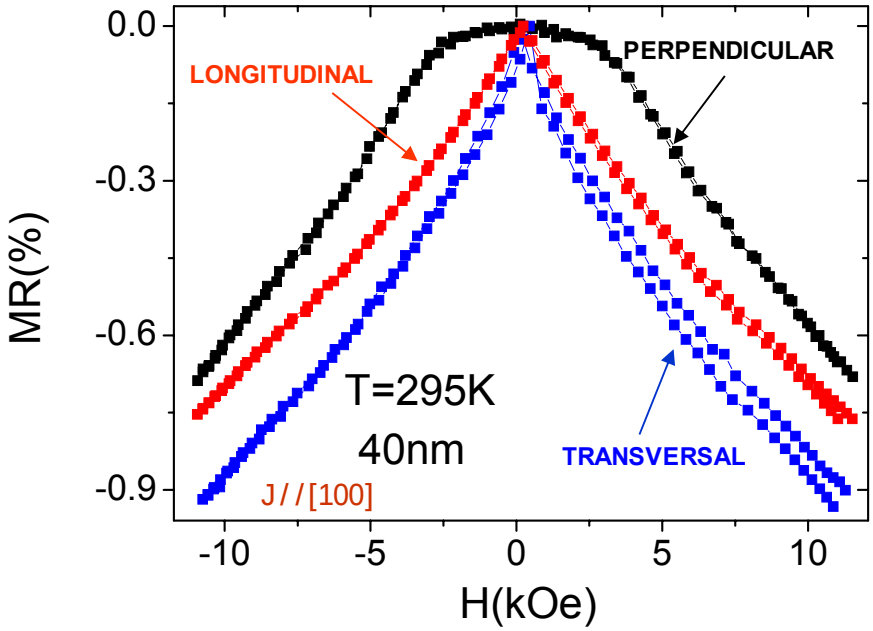

Fig. 3.10. MR measurements for a 40 nm thick film, at room temperature, in 3 geometries. The MR effect is thought to be caused by the spin-polarized transport though APBs.

In figure 3.11. the MR value in the LG, at maximum H, is shown for all thickness studied, together with the coercive field (H_c) derived from the measurements (field where MR presents peaks, see figure 3.12.). As the films get thinner, the MR first increases, reaching a maximum at around 40 nm, and decreases abruptly for t < 30 nm. The increase of MR as t decreases can be understood by the presence of a higher density of APBs in the films, since the MR effect is mainly due to the transport though them. However, the decrease in the size of the APDs for thinner films, results in a tendency of the domains to behave superparamagnetically [36], decreasing the MR effect. This superparamagnetic behavior is manifested by the evolution of H_c with thickness, and has been widely studied in Planar Hall measurements (see section 3.6.).

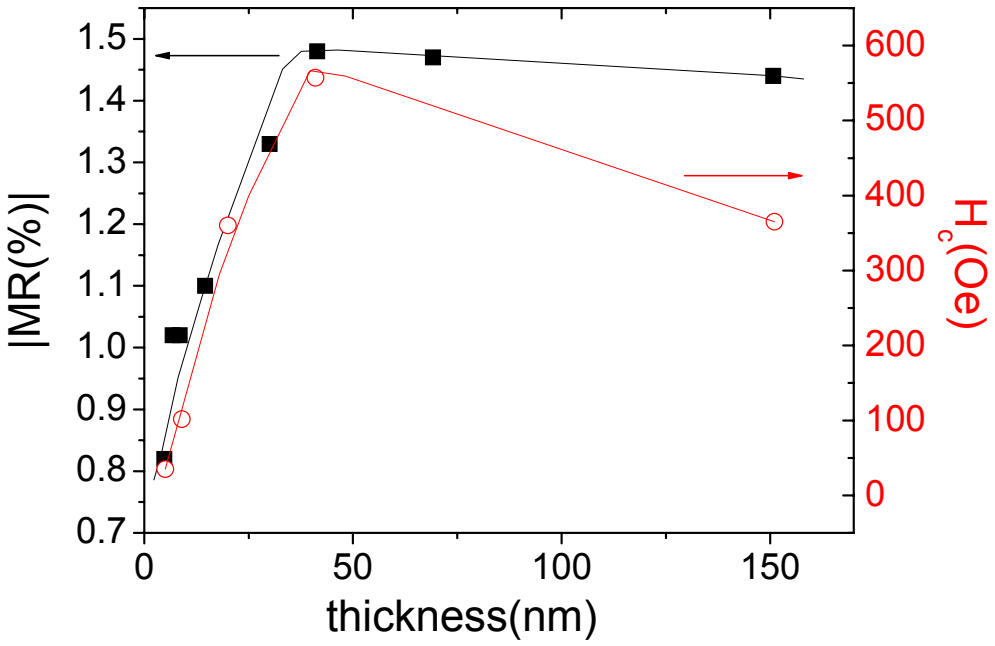

Fig. 3.11. MR value at 11 kOe in the LG for all the films studied, at room temperature (squares). The evolution of MR with thickness is well correlated with the behavior for H_c (circles). Both behaviors are understood by the increase of the density of APBs as the films get thinner (see text for details). Lines are guides to the eye.

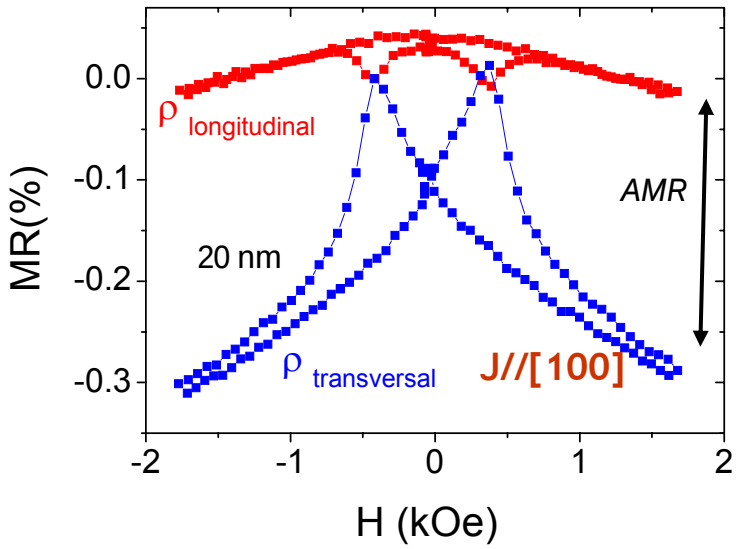

Fig. 3.12. MR measurements at room temperature for a 20 nm thick film. The anisotropic MR effect is evidenced, with AMR >0, in this case. Peaks in the MR are associated to the coercive field.

In figure 3.12. the MR measurements for a 20 nm thick film, at room temperature, are shown for a low range of fields (-1.5 kOe < H < 1.5 kOe). The difference in resistance between the LG and the TG is the so called anisotropic magnetoresistance (AMR). The AMR is defined as

$$AMR(\%) = 100\frac{\rho_{//} - \rho_{\perp}}{\rho_0} \qquad (3.4.)$$

where $\rho_{//}$ and $\rho_{\perp}$ are the resistivities when current and magnetization are parallel (LG) and perpendicular (TG), respectively, and ρ_0 is the resistivity at the coercive field. The origin of the AMR lies in the spin-orbit coupling, and was first explained by Kondo in the early-1960s [37]. Briefly, the s electrons, which are responsible for the conduction, are scattered by the unquenched part of the orbital angular moment of the 3d electrons. As the spin magnetization direction rotates in response to the applied magnetic field, the 3d electron cloud deforms, due to the spin-orbit coupling, and changes the amount of scattering of the conduction electrons. The process is schematically shown in figure 3.13. In magnetite, the AMR sign depends on the direction of current with respect to the crystallographic direction [26]. AMR has been studied in detail in the PHE measurements (section 3.6.).

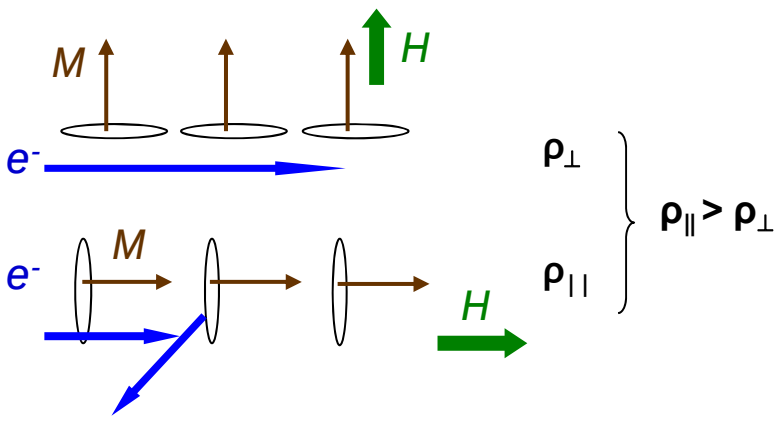

Fig. 3.13. Schematic representation of the origin of AMR

3.5.3. MR as a function of temperature

In figure 3.14(a) the results of MR in the PG are shown, for a 40 nm thick film, at several temperatures (T), with magnetic fields up to 90 kOe. The MR ranges as a function of T from 0.5-3.5 % or 2.5-8% at 11 and 90 kOe, respectively. The evolution at 11 kOe for two samples as a function of T is shown in figure 3.14(b). A maximum is observed (for all geometries-here we show the TG) in T_v. This behavior has been previously observed in Fe_3O_4 single crystals [38], polycrystalline [39] and epitaxial [25] thin films. This evidences that an intrinsic effect is superimposed to the APBs effect for the MR.

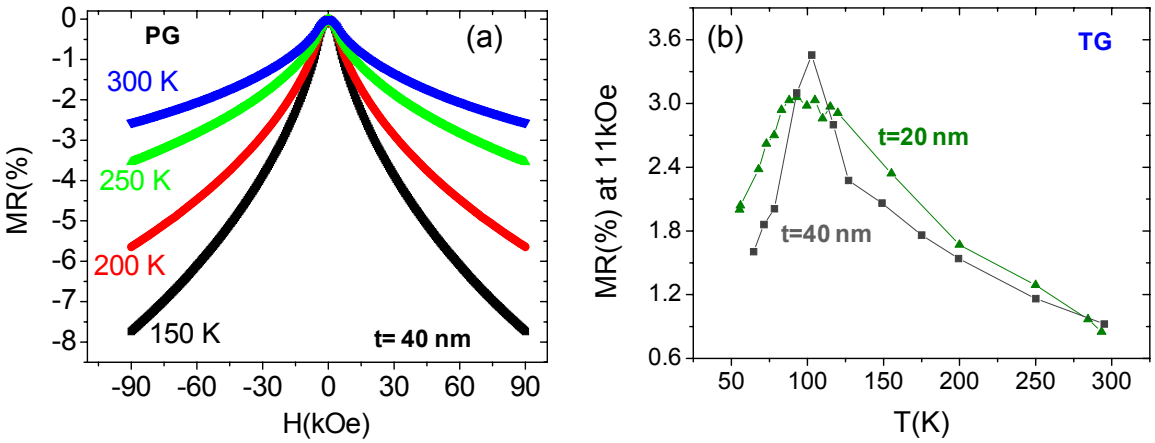

Fig. 3.14. (a) MR in the PG for a 40 nm thick film, up to 90 KOe, for $T>T_v$. **(b)** MR for two films, with 40 and 20 nm thickness. The maximum in the MR at T_v is observed.

3.6. Planar Hall effect (PHE)

3.6.1. Introduction to the Planar Hall effect

In general, in a magnetic material where a current density (**J**) is flowing, an electric field (**E**) is established, proportional to J by means of the resistivity tensor (***ρ***) [40]:

$$\vec{E} = \tilde{\rho}\vec{J} = \sum_j \rho_{ij} J_j \qquad (3.5(a))$$

$$\vec{E} = \rho_{\perp}(B)\vec{J} + \left[\rho_{//}(B) - \rho_{\perp}(B)\right]\left(\vec{m}.\vec{J}\right)\vec{m} + \rho_H(B)\vec{m}x\vec{J} \qquad (3.5(b))$$

where **m** is the normalized magnetization, **m**=**M**/M_0. The second term gives account of the AMR and the PHE, and the third term is the Anomalous Hall effect.

In the geometry of measurement of the PHE, both the magnetic field and the current are applied in the film plane. This is in contrast to the standard Hall effect, where the magnetic field is applied perpendicular to the film plane, and the physical origin is different (see section 3.7.). In a simple but common situation with a single-domain sample showing in-plane magnetization (**M**), when a current density **J** is applied along the x direction, and **M** forms an angle θ with the x direction, an electric field appears given by

$$E_x = J\rho_{\perp} + J(\rho_{//} - \rho_{\perp})\cos^2\theta \qquad (3.6.)$$

$$E_y = J(\rho_{//} - \rho_{\perp})\sin\theta\cos\theta \qquad (3.7.)$$

The longitudinal component of this electrical field gives rise to the AMR effect, with resistivity $\rho_{xx}= E_x/J$, whereas its transversal component gives rise to the PHE effect, $\rho_{xy}= E_y/J$. Thus, the PHE is a different manifestation of the same physical phenomenon that originates the AMR effect, explained in section 3.5. However,

instead of resulting in a change of the longitudinal voltage measured, when changing the angle between the magnetic field and the current, the PHE is a transversal (to the current) voltage. In figure 3.15. a scheme of configurations for AMR and PHE measurements is shown.

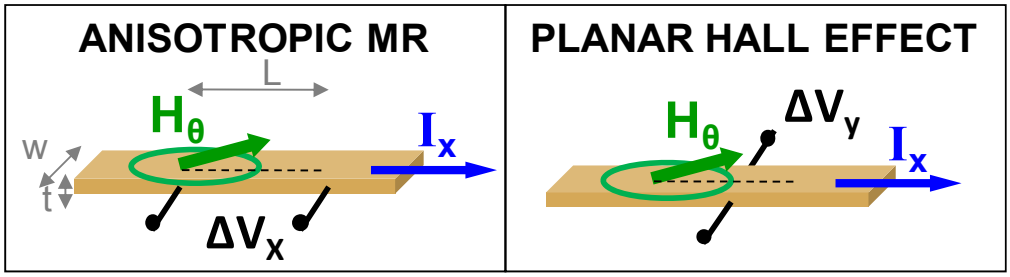

Fig. 3.15. Geometries for AMR ($\rho_{xx} = \frac{\Delta V_x}{I_x}\frac{wt}{L}$) and PHE ($\rho_{xy} = \frac{\Delta V_y}{I_x}t$) measurements. See text for details.

Due to the link between the magnetization direction and the PHE, the PHE has been used in thin films as a sensitive tool to study in plane magnetization processes when transport measurements are more suitable than direct measurements of the magnetization [41, 42]. The PHE can be also used for sensing low magnetic fields, showing advantages with respect to AMR sensors in terms of thermal drift [43, 44]. Recently, the discovery of the so-called giant planar Hall effect (GPHE), found in the ferromagnetic semiconductor $(Ga_{1-x}Mn_x)As$ [45], has attracted much interest. The effect at liquid helium temperature for this compound is four orders of magnitude higher than the one existing in ferromagnetic metals, reaching values for ρ_{xy} of a few mΩcm (in FM metals is of the order of nΩcm). The discovery has resulted in a thorough study of the magnetization properties of the material by means of this effect [46-48], and as a tool to investigate the resistivity of an individual domain wall [49, 50]. The system $(Ga_{1-x}Mn_x)As$, with T_C below 160 K, is restricted for applications of the GPHE in magnetic sensing at low temperatures. In the search for giant PHE at room temperature, promising results have been found in Fe_3O_4 [51, 52] and manganites [53, 54]. In these films, Bason *et al* have even proposed the use of PHE-based MRAM devices [52-54] as an alternative to the more-established MTJ-based

technology.

3.6.2. PHE as a function of film thickness (room temperature)

At room temperature the PHE has been studied in films with thickness of 5, 9, 15, 40 and 150 nm. For the study of the PHE, all measurements were done with the applied magnetic field forming a fixed angle with the current, θ=45º, since the signal will be maximum in this geometry when saturation in magnetization is reached. From equation 3.7.:

$$E_y^{(45^\circ)} = \rho_{xy}^{(45^\circ)} J = \frac{\rho_{//} - \rho_{\perp}}{2} J \qquad (3.8.)$$

(For simplicity in notation, we will refer $\rho_{xy}^{45^\circ}$ as ρ_{xy} from now on). From these measurements, the AMR can be directly derived:

$$AMR(\%) = 200 \frac{\rho_{xy}}{\rho_{xx}} \qquad (3.9.)$$

To confirm that the even response measured at 45º was caused by the PHE, we also measured with a 135º configuration ($\rho_{xy}^{135^\circ} = -\rho_{xy}^{45^\circ}$), see equation 3.7.). After subtracting the common offset, signals with opposite sign were obtained (see the particular case for the 40 nm-thick film at room temperature in the figure 3.16(a)). In figure 3.16(b) the results of the PHE for the 40 nm-thick film with current applied in two different directions, **J**//[110] and **J**//[100], are compared (van Der Pauw and optically-lithographed bar, respectively). The sign is different, which indicates that the AMR is positive ($\rho_{//}>\rho_{\perp}$) if **J**//[100] whereas it is negative ($\rho_{\parallel}<\rho_{\perp}$) if **J**//[110]. Such a difference in the sign of the AMR in Fe_3O_4 has been explained by Ziese and Blythe with a phenomenological model in which the AMR is expressed as a function of the magnetocrystalline anisotropy constants [26]. As discussed in such reference, the AMR sign and its absolute value have an intrinsic origin related to the spin-orbit coupling via the magnetocrystalline anisotropy constants.

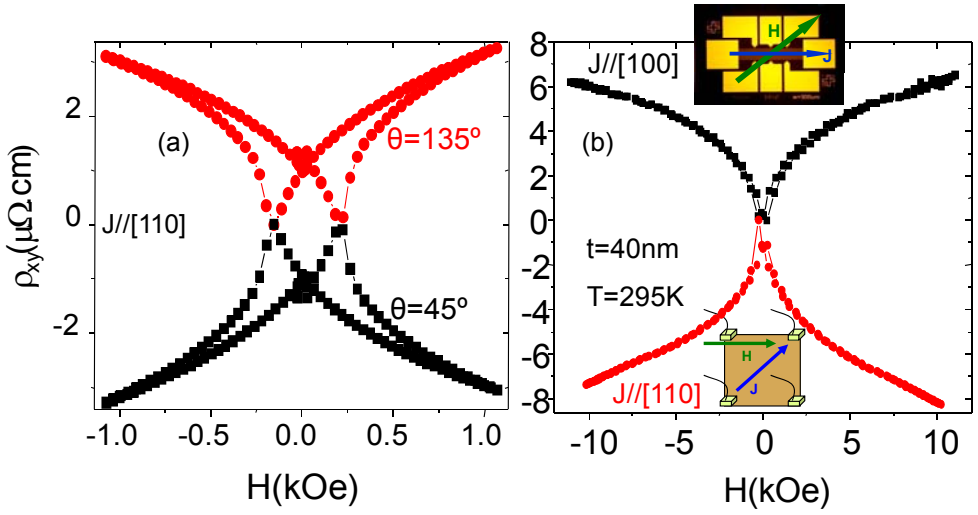

Fig. 3.16. Transversal resistivity as a function of the magnetic field for a 40nm-thick film at room temperature. **(a)** Comparison between measurements with the magnetic field applied forming either θ=45º or θ=135º with current. **J** //[110] in both cases. **(b)** Comparison for PHE measurements with two different current directions: **J**//[110]-Van der Paw, and **J**//[100]-optically lithographed bar. The origin of the differences of sign in (a) and (b) is discussed in the text.

In figure 3.17. we show the transversal resistivity as a function of the applied magnetic field for all the studied thin films with **J** //[110]. The obtained values are of the same order as in references 51 and 52 for Fe_3O_4, where 100 nm and 9 nm films were respectively studied. The values for ρ_{xy} at maximum field are listed in table 3.I., where a continuous decrease in magnitude with increasing film thickness is observed, as is the case for ρ_{xx}. The maximum value of ρ_{xy}=-59.4 μΩcm is obtained for the 5 nm-thick film. A low-field slope of about 200 μΩcm/T is found in this film, corresponding to a sensitivity of 400 V/AT, indeed a very large value.

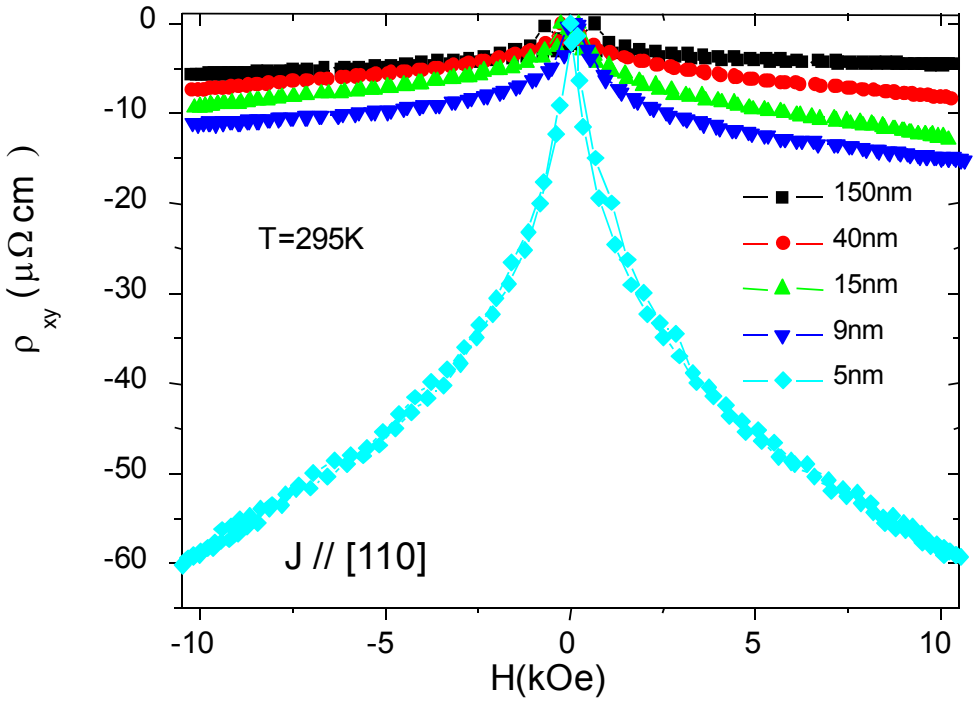

Fig. 3.17. Transversal resistivity ρ_{xy} as a function of the magnetic field (θ=45º) for several thin film thickness at room temperature with current direction **J** // [110].

thickness (nm)	150	40	15	9	5
ρ_{xx} (mΩ·cm)	5.5	7.0	12.4	23.4	121.4
ρ_{xy} at 11kOe (μΩ·cm)	-4.5	-8.3	-12.9	-15.3	-59.4
AMR(%)=200ρ_{xy}/ρ_{xx}	-0.18	-0.24	-0.21	-0.13	-0.1

Table 3.I.. Longitudinal (ρ_{xx}) and transversal (ρ_{xy}) resistivity (at maximum field) for the studied thin films at room temperature. Measurements were done with **J** applied in the [110] direction. The values for the transversal resistivity are obtained with θ=45º.

An important issue to point out is the evolution of the films towards superparamagnetic (SP) behaviour as the films decrease in thickness, due to the reduction of the ferrimagnetic exchange coupling existing between spins surrounding the APBs [36]. As explained before, the density of APBs varies as $t^{-1/2}$ [20, 21]. The APDs for ultrathin films have sizes of a few unit cells, and their magnetic moments start to fluctuate due to the thermal energy. The progressive shift towards zero field found for the peaks associated with the coercive field in our PHE measurements, as well as the increase of the slope for ρ_{xy} at high fields suggest the occurrence of this phenomenon. These features influence the possible applications of the PHE observed in these films. The SP tendency is also reflected when the AMR is calculated from PHE measurements (see table 3.I). The AMR has an approximately constant value of -0.2% for films above 10 nm, in agreement with bulk results and thin films in this range of thickness for **J**//[110] (ref. 26). Below 10 nm, an important decrease in magnitude occurs, compatible with the absence of anisotropy found for SP samples [36]. This behavior is the same as MR measurements shown in section 3.5.2. Thus, for very thin films (below 5 nm), the PHE will be limited in magnitude by the difficulty in magnetizing the sample and the decrease in the AMR value. Therefore, thinner films than the studied here are not expected to present higher PHE values than the reported ones. It should be also noticed the difficulty to use the GPHE in very thin Fe_3O_4 films for magnetic storage since an improvement in signal magnitude with decreasing thickness also implies a decrease in coercive field. On the other hand, the superparamagnetic tendency implies a less-hysteretical GPHE effect, which is welcomed for magnetic sensing.

3.6.3. PHE as a function of temperature

In figure 3.18. we show the ρ_{xy} isotherms from room temperature down to 70 K for a 20 nm-thick film. The longitudinal offset makes unfeasible measurements at lower temperatures. ρ_{xy} increases moderately when cooling from room temperature down to 200 K, changing its sign at about 150 K. When approaching the Verwey transition, a huge increment in the magnitude of ρ_{xy} occurs, as is also observed in the longitudinal resistivity. *Colossal* values, one order of magnitude bigger than the highest reported previously at 4.2 K in $(Ga_{1-x}Mn_x)As$ [49] are found for $T<T_v$. Thus, ρ_{xy} is about 16 mΩcm at T=73 K in this film.

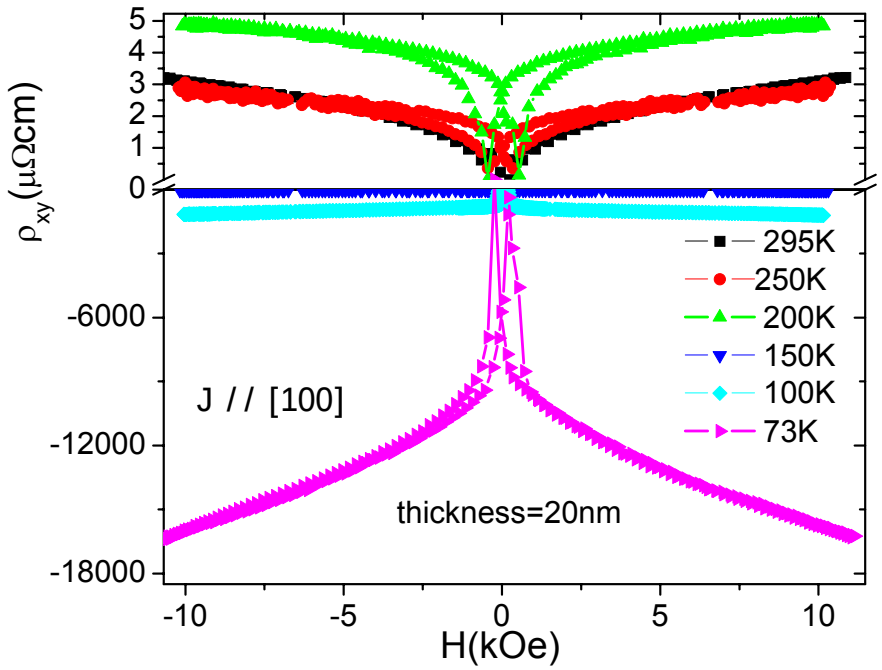

Fig. 3.18. Transversal resistivity isotherms as a function of the magnetic field (θ=45º) for a 20 nm-thick film. A change in sign for T<150 K is observed. Colossal values are found for $T<T_v$. Measurements done with **J**//[100].

In the case of a 40 nm-thick film, two changes in sign are observed between room temperature and 70 K. A huge increment in the absolute value of ρ_{xy} is also observed when crossing Tv, giving as a result ρ_{xy} about 15 mΩcm at T=70 K. In order to gain more insight in the mechanisms responsible for the dependence with temperature of the PHE, AMR ratios calculated from the PHE at 11 kOe in both samples are shown in figure 3.19. The obtained values are in agreement with previous studies for the AMR in magnetite thin films [26], with **J**//[100].

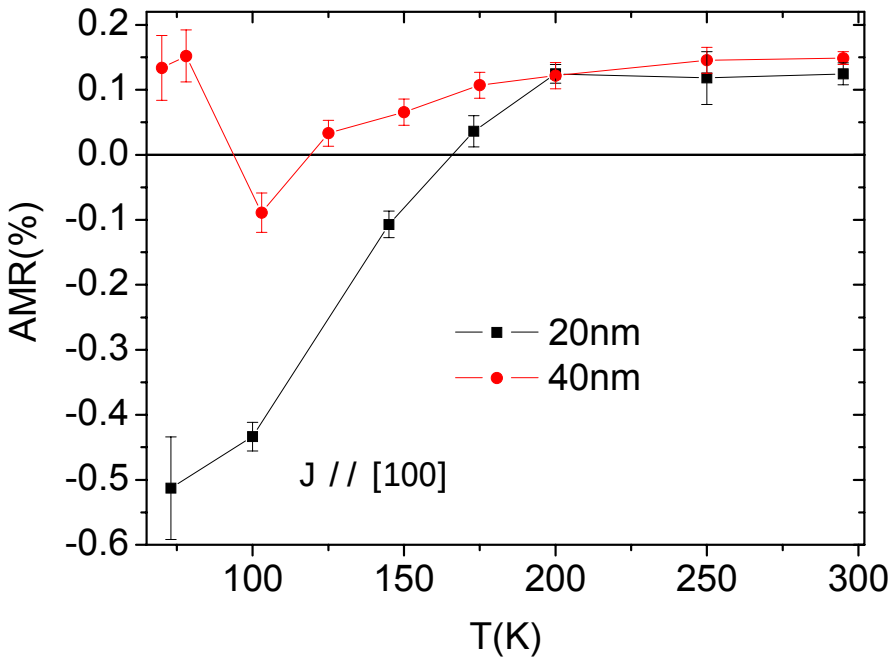

Fig. 3.19. AMR ratio as a function of temperature for a 20 nm and a 40 nm-thick film at 11 kOe. The AMR ratio is calculated from PHE measurements at 45º (equation 3.9.). Measurements done with **J**//[100].

For both films, AMR≈0.2%, independent of temperature, is found for temperatures above 150 K. Different tendencies are followed in each thin film below this temperature. Whereas in the case of the 20 nm-thick film, a change in sign occurs, giving as a result negative values for T<150K, for the 40 nm film ρ_{xy} is positive except in the surroundings of T_v. The changes of sign in the AMR are likely related to intrinsic changes in the magnetocristalline anisotropy in this temperature range as previously observed in bulk single crystals [55]. Such changes will dramatically modify the anisotropy constants, which correspondingly will vary the AMR/PHE value as demonstrated in the phenomenological model presented in ref. 26. The magnetic anisotropy in these films is expected to depend strongly on the film thickness and detailed magnetic studies beyond the scope of the present study would be required to clarify the quantitative relationship between the magnetic anisotropy changes and the AMR/PHE.

One important result inferred from the obtained AMR temperature dependence is that the absolute value of the AMR is large below the Verwey transition. The ground state of Fe_3O_4 below the Verwey transition is still a matter of debate [56]. Recent experiments indicate that pure electrostatic models do not seem to be able to explain the ground state below the Verwey transition and the electron-lattice coupling must play a key role in order to stabilize it [56]. The large values of the AMR below the Verwey transition observed by us give evidence for a substantial magnetocrystalline anisotropy of the ground state caused by a significant spin-orbital coupling. This suggests that the claimed strong electron-lattice coupling could arise from a large spin-orbital coupling.

3.7. Anomalous Hall effect (AHE)

3.7.1. Introduction to the Anomalous Hall effect

In non-magnetic materials, when a magnetic field is applied perpendicular to the film plane (H_z), a transversal voltage (V_y) is established when a current is injected in the x direction. This effect, called Ordinary Hall effect (OHE) is proportional to the applied magnetic field, and it originated by the Lorentz force acting on moving charged carriers, deflecting its trajectory, and establishing a stationary voltage (see figure 3.20.).

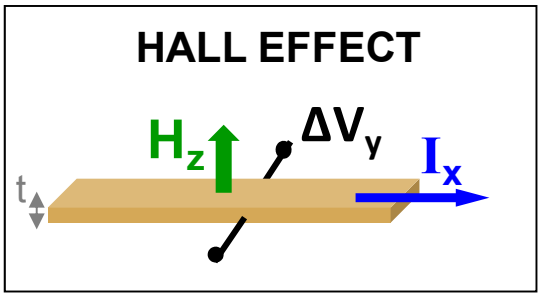

Fig. 3.20. Geometry for Hall effect measurements ($\rho_{xy} = \frac{\Delta V_y}{I_x} t$). See text for details.

In magnetic materials, an additional term to the OHE, the so called Anomalous or Extraordinary Hall effect (AHE) appears, as a consequence of the spontaneous magnetization the material possesses. The last term in equation 3.5(b) gives account of the AHE. Thus, the Hall (transversal) resistivity can be written as

$$\rho_{xy} = \rho_H = \mu_0 \left(R_0 H + R_A M \right) \qquad (3.10.)$$

The first term, proportional to the applied magnetic field, is the OHE, and the second one, in general much larger than the first one, is the AHE, which is proportional to the magnetization of the material. The origin of the AHE has been a controversial issue for decades, where different theories have tried to explain this effect. Different dependences between the Hall and the longitudinal resistivity, ρ_{xx}, are

given, depending on which origin is associated:

- Extrinsic mechanism, based on the asymmetric interaction of carriers with the scattering centers in the system (see figure 3.21.). The asymmetries require spin-orbit coupling and spin polarization of carriers to happen. There are two types of mechanisms proposed:

  - *Skew scattering* [57]: Asymmetric scattering, with $\rho_H \propto \rho_{xx}$ ($\sigma_H \propto \sigma_{xx}$).

  - *Side-jump scattering* [58]: Spin-dependent lateral displacement (~0.1 Å) of the incident electron wave during the scattering. $\rho_H \propto \rho_{xx}^2$ (σ_H constant).

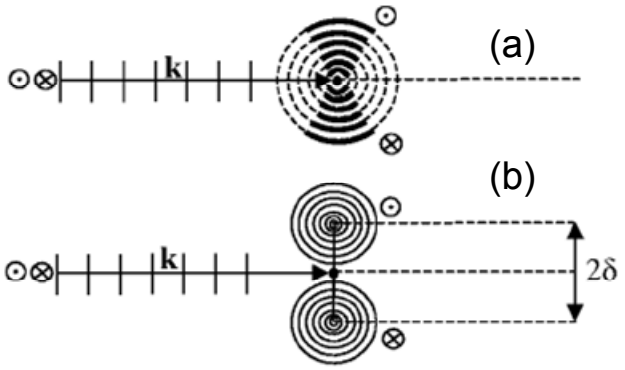

Fig. 3.21. Schematic picture of the two extrinsic mechanisms for the AHE. **(a)** Skew scattering. **(b)** Side-jump scattering. The point and cross circles symbols up and down spins, respectively. Taken form Crépieux *et al* [59].

- Intrinsic mechanism, independent of the scattering of electrons, based on the *Berry phase* of Bloch waves [60, 61]. An additional term to the group velocity of electrons appears, mediated by the Berry phase $\Omega(\mathbf{k})$:

$$v_g(\mathbf{k}) = \frac{1}{\hbar}\nabla_k \varepsilon(\mathbf{k}) - e\mathbf{E}\times\Omega(\mathbf{k}) \qquad (3.11.)$$

  The AHE, via the spin-orbit interaction, can be expressed in terms of this geometrical curvature in momentum space, giving a dependence $\rho_H \propto \rho_{xx}^2$ (σ_H constant).

A recent theory [62] based on multi-band ferromagnetic metals with dilute impurities seems to have solved this complex scenario, where three regimes can be distinguished as a function of the longitudinal conductivity (see figure 3.22.):

- In the clean regime, with extremely high conductivity, the skew scattering causes the effect ($\sigma_H \propto \sigma_{xx}$).

- An extrinsic-to-intrinsic crossover occurs at lower conductivities (σ_{xx}=10^4-10^6 Ω^{-1}cm^{-1}), where σ_H becomes constant.

- In the dirty regime (σ_{xx}<10^4 Ω^{-1}cm^{-1}) a relation $\sigma_H \propto \sigma_{xx}^{1.6}$ is predicted, caused by the damping of the intrinsic contribution.

Recently, this crossover has been experimentally found for a series of itinerant ferromagnets [63] and a compilation of an appreciable amount of low-conductivity compounds reveal the expected dependence in the dirty limit, regardless of hopping or metallic conduction [64].

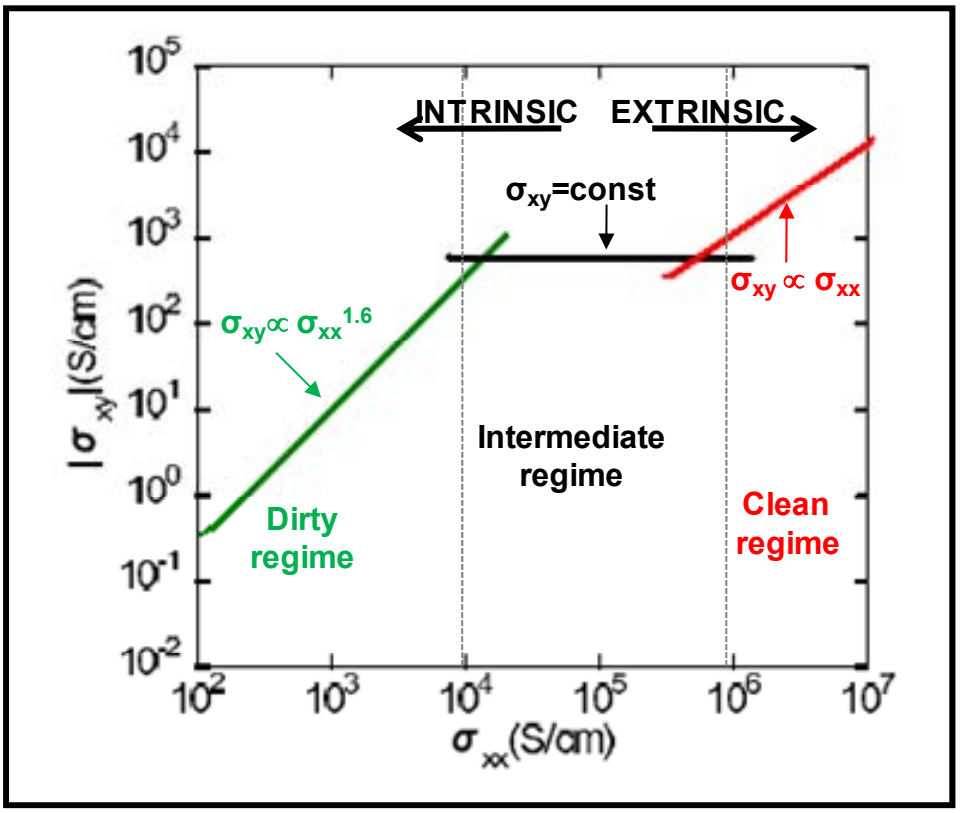

Fig. 3.22. Schematic diagram for the three AHE regimes, classified as a function of the longitudinal conductivity: **Clean** ($\sigma_{xx}>10^6\ \Omega^{-1}cm^{-1}$), dominated by the skew scattering: $\sigma_{xy}\propto \sigma_{xx}$, **Intermediate** ($10^4<\sigma_{xx}<10^6\ \Omega^{-1}cm^{-1}$), dominated by an intrinsic mechanism: constant σ_{xy}, and **dirty**, where the damping of the intrinsic contribution results in $\sigma_{xy}\propto \sigma_{xx}^{1.6}$. [Hall conductivity: $\sigma_H = -\rho_H/(\rho_{xx}^2+\rho_H^2)$; longitudinal conductivity: $\sigma_{xx} = \rho_{xx}/(\rho_{xx}^2+\rho_H^2)$.

3.7.2. AHE as a function of the film thickness (room temperature)

In figure 3.23. we represent the Hall resistivity ρ_H at room temperature as a function of the film thickness. For all samples, ρ_H is negative, increasing in modulus as the films get thinner. The value for the 40nm-thick film at 11kOe is 13.9 μΩcm, in excellent agreement with that obtained in reference 19 at the same field (13.75 μΩcm), as expected for similar high-quality films. The maximum Hall slope is found for the 5nm-thick film, reaching 125 μΩcm/T, which corresponds to a sensitivity of 250 V/AT. This sensitivity at room temperature is only higher for ferromagnetic materials such as Co_xFe_{1-x}/Pt multilayers [65]. It is important to remark that in the range of magnetic fields measured with the system available in our laboratory (H_{max}=11 kOe), the contribution of the AHE dominates completely the Hall effect, being unrealistic to determine the ordinary part from the Hall slope at the highest measured magnetic field. This impossibility to saturate the film in moderate magnetic fields is due to the antiferromagnetic coupling between spins at the neighborhoods of APBs [27]. This fact can explain the dispersion in values for the ordinary Hall constant R_O obtained by different authors [19, 66]. Therefore, there should exist a perfect proportionality between ρ_H and the magnetization perpendicular to the plane of the film. This is clearly seen, e.g. for the 40nm-thick film at room temperature in the inset of figure 3.23.

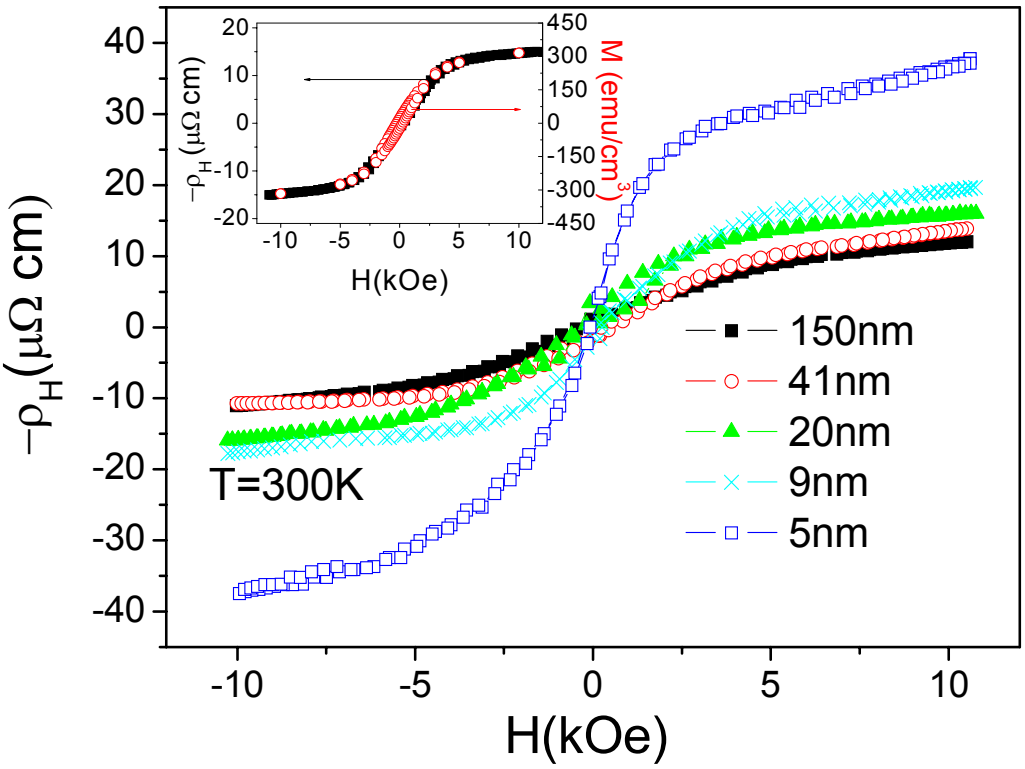

Fig. 3.23. Hall resistivity at room temperature as a function of thickness for a series of samples. The field is applied perpendicular to the plane of the film. The inset shows a comparison of the Hall resistivity at 300K for a 40 nm thick-film together with the perpendicular magnetization at that temperature for another sample of the same thickness grown in the same conditions. The perfect proportionality between both evidences that the AHE dominates the measurement in the range of field measured.

3.7.3. AHE as a function of the temperature

In order to account for the thermal dependence of ρ_H we have measured the 20 nm and 40 nm films as a function of the temperature. In figure 3.24. we show the ρ_H isotherms for the 40 nm-thick film at temperatures above the Verwey transition. For both samples ρ_H increases in modulus monotonously when the temperature

diminishes, presenting a huge enhancement as the temperature approaches the transition (see figure 3.25.). This abrupt change in ρ_H at T_V is a general behavior for Fe_3O_4, also found in single crystals [67] and polycrystalline films [39], which seems to be related with changes in the electronic structure and the spin-orbit coupling that occurs at the transition [3, 68]. In both samples the values for ρ_H increase by a factor higher than 100 from room temperature down to 60K, reaching values above 1mΩ·cm at that temperature.

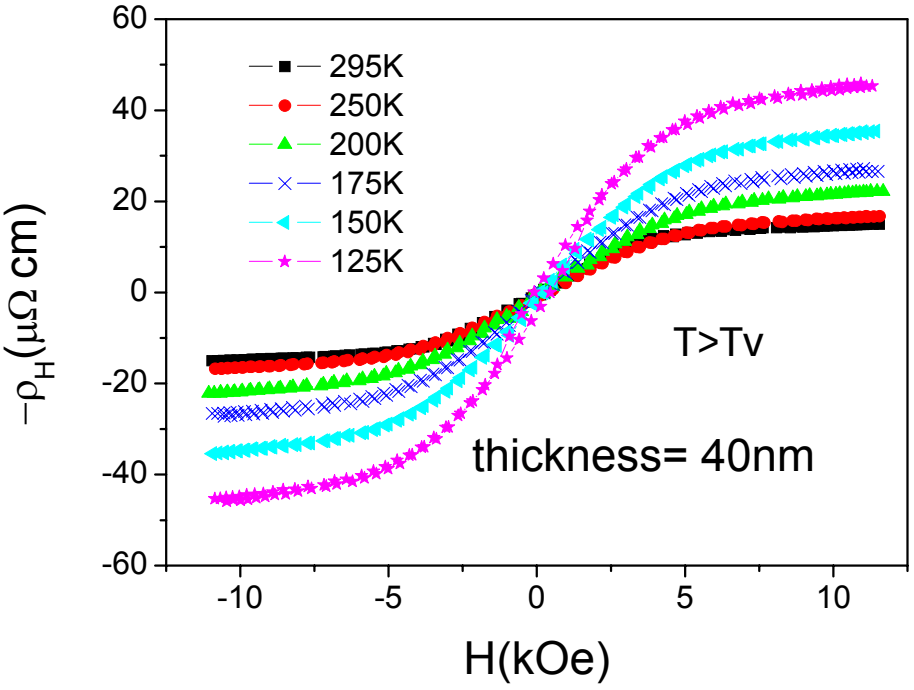

Fig. 3.24. Hall resistivity isotherms in a film of 40 nm for temperatures above the transition. The Hall resistivity increases as the temperature is diminished, reaching in this case 45μΩ·cm at 125K.

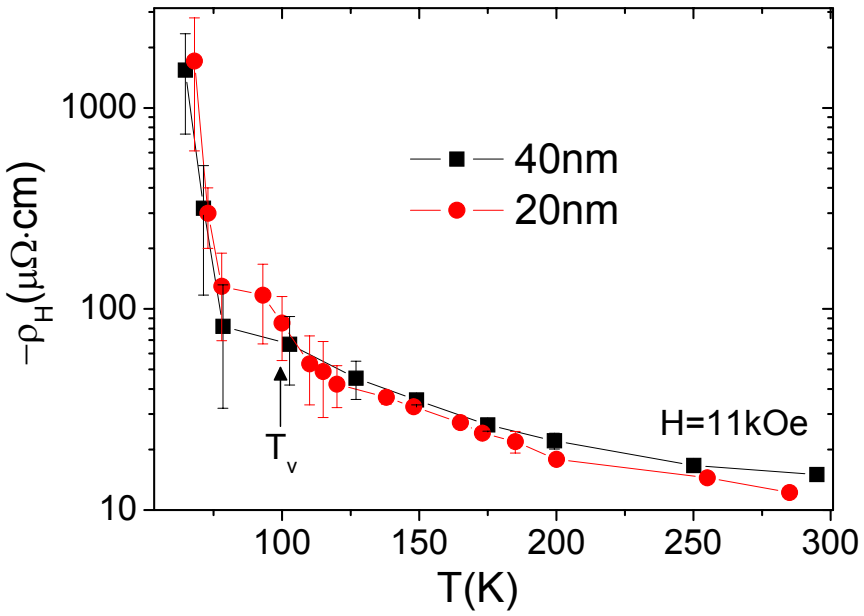

Fig. 3.25. Hall resistivity at 11 kOe as a function of temperature for both samples.

3.7.4. AHE in Fe_3O_4. Universal behavior.

In figure 3.26. we show the absolute value of the Hall conductivity at maximum field (11kOe) as a function of the longitudinal conductivity for all the samples measured, at room temperature and as a function of temperature. In spite of the different thicknesses and measurement temperature, the relation $\sigma_H \approx 10^{-4} \cdot \sigma_{xx}^{1.6}$ (dashed line) is followed in all cases. The increase in the value of the error bars for σ_H at temperatures below the transition ($\sigma_{xx}<1.5\ \Omega^{-1}\cdot cm^{-1}$) is due to the fact that residual contributions to the voltage measured, such as the longitudinal resistivity, increase substantially. Another relevant source of errors due to slight unavoidable misalignments in the experimental setup is the contribution of the Planar Hall effect, that, as we have shown in section 3.6., reaches colossal values in our films for $T<T_v$, and could be at the origin of previous results yielding a different sign of ρ_H [69] in this temperature range. Together with our results, other measurements found in the

literature for the AHE in magnetite have also been plotted. Specifically, another 45nm-thick film epitaxial thin film at room temperature [19], a polycrystalline 250nm-thick film at temperatures below 300K [39] and single crystals [67, 70] in the range 150K<T<500K have been included. These data approximately converge with ours, revealing the same physical origin in all cases.

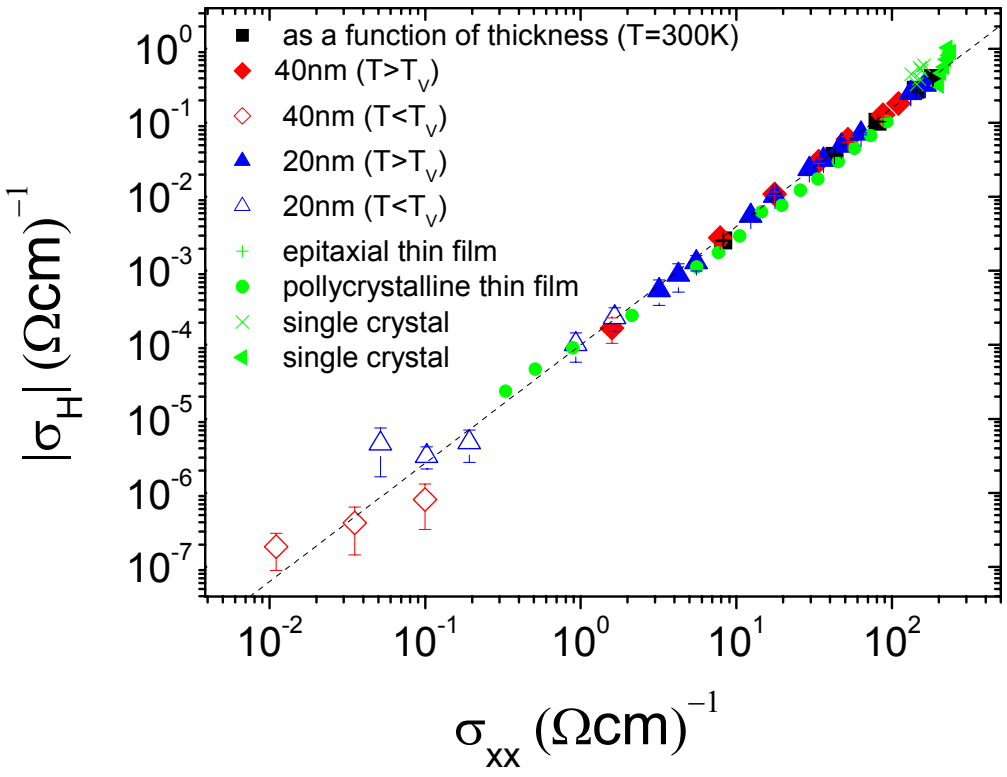

Fig. 3.26. Relationship between the magnitude of the Hall conductivity at 11kOe and the longitudinal conductivity for our films and data taken from references [19, 39, 67, 70]. Dashed line is the function $f(\sigma_H)=10^{-4}\ \sigma_{xx}^{1.6}$.

We explained in section 3.1.3 some effects appearing in epitaxial Fe_3O_4 thin films, associated with the presence of APBs. These effects become more evident the thinner the films are. In previous sections we have shown how the APBs influence the magnetotransport properties measured: resistivity, MR and PHE. However, in this section, we have shown that the AHE in Fe_3O_4 thin films presents a universal behavior. First, the enhancement in the Hall resistivity as the temperature is diminished seems to be related with the increase in the longitudinal resistance, as a consequence of the broadening that occurs in the band gap as T_V is approached. This results in huge Hall resistivities of the order of mΩ·cm at low temperatures. Second, the dependence $\sigma_H \propto \sigma_{xx}^{1.6}$ found over four decades of longitudinal conductivity is in accordance with the recent unifying theory for the AHE presented in section 3.7.1. [62]. This relation is followed by samples in a wide range of thicknesses and irrespective of the measurement temperature. Furthermore, the same dependence for σ_H is found in other samples of magnetite taken from the literature, regardless they are single crystals or polycrystalline thin films. The theory [62] explains that the magnitude of the AHE is determined by the degree of resonance caused by the location of Fermi level around an anticrossing of band dispersions. Besides, it assumes metallic conduction. From our results we can infer that the Verwey transition, associated with a cubic-to-monoclinic structure transition, does not play an important role in this behavior. It was pointed out before that this dependence is also followed in hopping conduction [64]. In the case of Fe_3O_4, our results suggest that this dependence also takes place irrespective of the different conduction mechanisms occurring above and below T_V [3]. Other important issue is related with the presence of APBs. As was mentioned before, some magnitudes such as the resistivity or magnetization are subjected to important changes from the bulk material to the thin films, due to the presence of these structural defects. The moderate magnetoresistance ratios in films are explained by the spin-polarized transport through them. However, the AHE is again not affected by the density of APBs, which decreases with film thickness. Finally, it should also be remarked that the presence of stress in epitaxial thin films caused by the substrate could eventually have an influence in the band structure in comparison with the bulk material, but the convergence of all data reveals that this is

not an important issue for the AHE. All these facts support the belief that the relation $\sigma_H \propto \sigma_{xx}^{1.6}$ is universal for this low-conductivity regime.

3.7.5. Fe_3O_4 inside the AHE dirty regime of conductivities.

Finally, for completeness, we show in figure 3.27. a wide compilation of results for the AHE found in the literature for magnetic compounds, together with those for Fe_3O_4 previously shown in figure 3.26., all of them in the dirty regime of conduction. We include data for metals, oxides, and magnetically-doped semiconductors, with completely different crystallographic structure, magnetic density when doping, and electrical conduction. The Hall conductivity follows the universal relationship $\sigma_H \propto \sigma_{xx}^{1.6}$ over six decades of longitudinal conductivity in all cases. The different proportionality constants in the fits are explained in theory to be caused by a different impurity potential [62]. The universal scaling is followed in spite of the big differences between these compounds. The theory developed in reference 62 was done for metallic conduction, with the band playing a vital role in this effect, so it is surprising the good convergence of all these results.

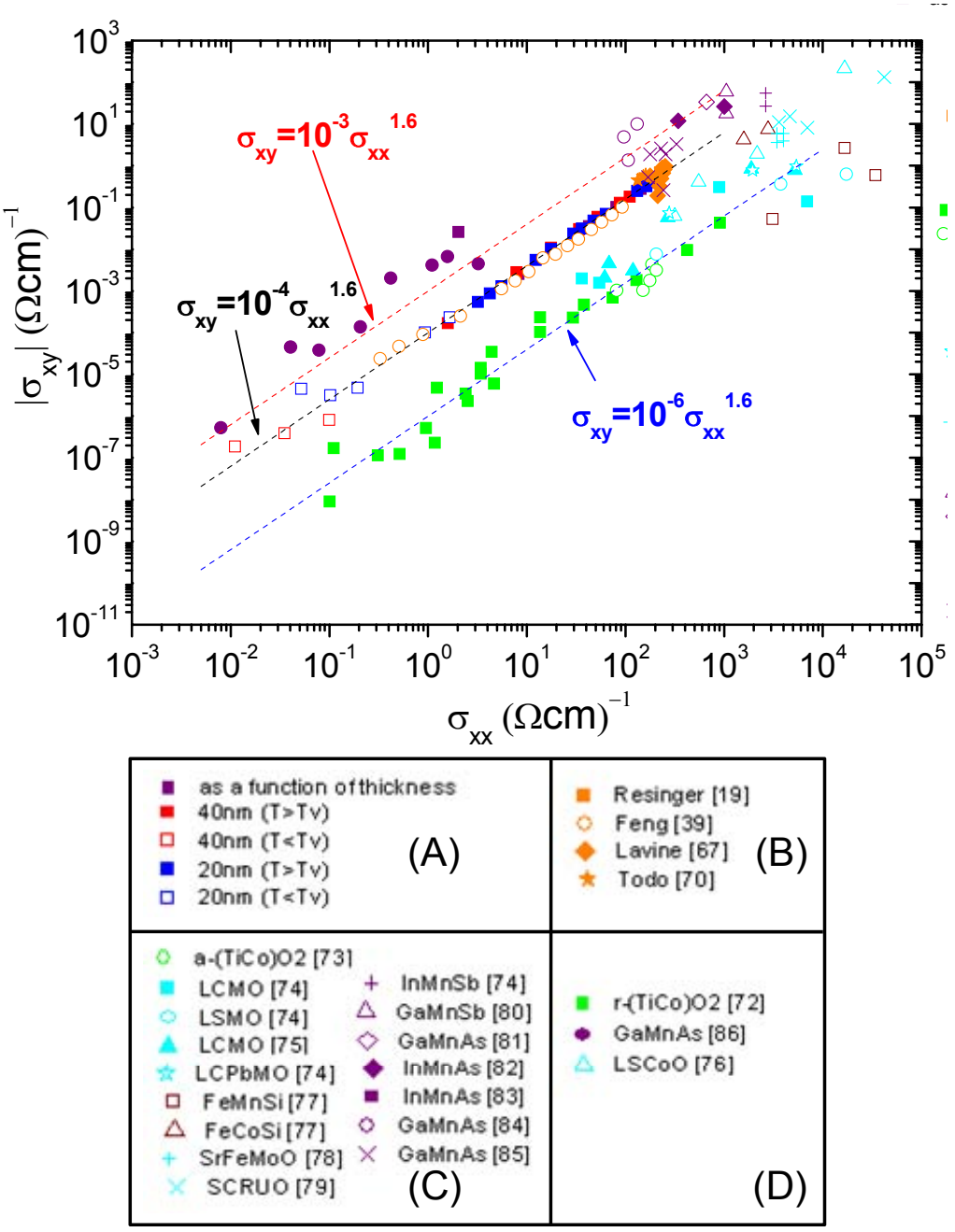

Fig. 3.27. Anomalous Hall conductivity as a function of the longitudinal conductivity for a wide amount of magnetic oxides, metals and semiconductor ferromagnets, all in the dirty regime of conductivities. All data are well fitted to $\sigma_H \propto \sigma_{xx}^{1.6}$. Most of the data are taken from reference 64. In the table below, the compounds are shown, together with its reference (between brackets). **(A)**: Our measurements. **(B)**: Other Fe_3O_4 results. **(C)**: Compounds with metallic conduction. **(D)**: Compounds with hopping conduction.

3.8. Conclusions

We have grown high-quality epitaxial Fe_3O_4 films on MgO substrates and studied systematically their magnetotransport properties. A complete optical lithography process was successfully performed for the films, allowing technically difficult measurements, below the Verwey transition.

Resistivity measurements show a perfect agreement with previous results of other groups. ρ follows the relation $t^{-1/2}$, as a consequence of the increase of the APBs when film thickness decreases. Measurements as a function of temperature show a decrease of T_v as films get thinner, together with a smoothing of the Verwey transition, becoming undistinguishable for $t<10$ nm.

Magnetoresistance measurements reproduce previous results in the literature, and can be understood by the spin-polarized transport through APBs. The tendency towards the superparamagnetic behavior of the APDs is evidenced for ultra-thin films. An intrinsic peak for the absolute value of the MR at T_v indicates that an intrinsic phenomenon is superimposed to the extrinsic effect caused by APBs.

Thickness and temperature dependences of the giant planar Hall effect in the films have been studied. Samples with moderately-high APBs density show higher PHE signals due to the induced increase in the absolute value of the resistivity anisotropy, making them interesting candidates for magnetic sensing and non-volatile memories, as well as for magnetization studies through transport measurements. A record value of the planar Hall effect at room temperature of $|\rho_{xy}|\approx 60$ $\mu\Omega$cm was obtained for the 5 nm-thick film. As a function of temperature, the PHE increases in magnitude, reaching colossal values below the Verwey transition, in the range of a few mΩcm. The anisotropic magnetoresistance values inferred from these measurements indicate that the ground state below the Verwey transition likely bears a substantial spin-orbit coupling.

Anomalous Hall effect measurements in the films show that the dependence $\sigma_H \propto \sigma_{xx}^{1.6}$ is fulfilled over four decades of longitudinal conductivity, irrespective of

thickness or measurement temperature. Comparison with literature confirms this behavior is general for this compound, as well as for others in the same (low) regime of conduction. This result supports a recent theory developed to explain the anomalous Hall effect, indicating the universality of this relation in the dirty regime of conductivities.

Chapter 4

Conduction in atomic-sized magnetic metallic constrictions created by FIB

This chapter reports the study of electron conduction in metallic constrictions, with sizes in the atomic range. First, a novel technique for the fabrication of nanoconstrictions at room temperature in metallic materials will be presented, based on the potentialities that the dual-beam equipment offers.

We will show that it is possible to create atomic-sized constrictions inside the vacuum chamber where the sample is fabricated. Second, this method has been used for experiments in a magnetic metal as iron, where phenomena such as ballistic magnetoresistance and ballistic anisotropic magnetoresistance have been investigated.

4.1. Theoretical background for atomic-sized constrictions

4.1.1. Introduction

In the macroscopic world, the nature of the electrical conduction in metals does not depend of its size. However, when this size approaches the atomic regime, electrons can be conducted without being scattered, and Ohm's Law is not fulfilled anymore. In this regime, called ballistic, the normal concept for conduction is changed, being necessary to invoke the wave nature of the electrons in the conductor for a proper description. The energy scales involved are so large than quantum effects are visible at room temperature [1].

The creation of constrictions with these dimensions is a hard task, and laboratory techniques which manipulate in the molecular and atomic scale are necessary, normally under highly strict environmental conditions

4.1.2. Conduction regimes for metals

Let us imagine two big metallic electrodes, connected by a constriction (also denoted as contact) of length L, through which electrons flow.

If this contact has macroscopic dimensions, the electrons are scattered when passing, since $L > l$ (where l is the elastic mean free path, typically a few tens of nanometers in metals at low temperatures). In this case, Ohm's law is fulfilled, and the conductance of this constriction is given by the classical expression:

$$G = \sigma S/L \qquad (4.1.)$$

where σ is the conductivity of the material, and S is the section of the contact. We call this regime of conduction *diffusive*.

When the dimensions of a contact are much smaller than l the electrons will pass through it without being scattered. This regime is called *ballistic*. In such contacts there will be a large potential gradient near the contact, causing the electrons to

accelerate within a short distance. This problem was first treated semiclassically by Sharvin [2], obtaining for the conductance:

$$G = \frac{2e^2}{h}\left(\frac{\pi a}{\lambda_F}\right)^2 \qquad (4.2.)$$

where a is the radius of the contact. In this case, the resistance is not proportional, as it was the case in the diffusive regime, to the number of scattering events. The resistance of the ballistic channel tends to zero, and it is the boundaries between the leads and channel which are responsible of the resistance of the system. In Sharvin's formula, G depends on the electronic density through the Fermi wavelength λ_F, and it is independent of σ and *l*. Quantum mechanics are only introduced in this treatment by Fermi Statistics.

This semiclassical approach is, however, not valid, when the contacts are atomic-sized, with a few atoms contributing to the conduction of electrons. In this case $L \sim \lambda_F$ (from a few to fractions of Å) and we enter into the *full quantum limit*. This problem was treated by Landauer [3], reaching for the value of the conductance:

$$G = \frac{2e^2}{h}\sum_{i=1}^{N}\tau_i \qquad (4.3.)$$

where τ_i is the transmission coefficient of the channel i. The conductance is proportional to the value

$$G_0 = \frac{2e^2}{h} \qquad (4.4.)$$

which is called the "quantum of conductance", and whose corresponding resistance value, the quantum of resistance, is R_0=12.9 kΩ. Thus, the wave nature of electrons is manifested by the quantization of the conductance. This result is analogous to the propagation of waves through wave guides, when the channel width is of the order of the incident wavelength.

The existence of conduction channels is related to the presence of wavefunctions at the Fermi energy. For the simplest 1D case, the number of conduction channels

results from the number of intersecting branches of a 1D dispersion curve with the Fermi energy. For metallic systems, the occurrence of single channel conduction is thus expected in monovalent metals. Moreover, realistic geometries for atomic-size contacts can deviate significantly from a periodic 1D system, resulting in non-perfect transmission factors. It has indeed been shown theoretically and experimentally that perfect single-channel conduction is rather rare, exclusively limited to monovalent metals like Au [4]. The full atomic orbital overlap and bonding has to be considered in describing realistic atomic-sized contacts. When doing so, it appears that the number of conducting channels is roughly of the order of the number of valence electrons. Transmission factors can also depend sensitively on the exact geometry of the contact and the orbitals considered. Hence, it should be underlined that conductance quantization in an integer number of G_0 is only obtained for idealized 1D systems. In fact, it can be shown that transmission factors vary continuously with orbital overlap: if it were possible to continuously change the interatomic distance between two central atoms of an atomic chain, the conductance would smoothly decrease. Thus, it is likely that conductance steps that are experimentally observed when creating atomic contacts are associated with the stability of some specific atomic configurations rather than a signature of quantized transport [1].

4.1.3. Typical methods for the fabrication of atomic contacts

As it was commented in the introductory part, the methods for creating atomic contacts are mainly laboratory techniques, normally working at Helium liquid temperature, and in ultra-high vacuum conditions. These experiments have led to huge advances in the understanding of electron conduction in atomic-sized metal structures. Between the most commonly used we should cite:

(i) Mechanical break junctions (MBJ) [5]: A metallic film is broken in a controllable way, by bending a flexible substrate on which the material has previously been deposited. This is clearly the most documented method for fabricating atomic contacts.

(ii) Use of STM [6]: The tip is contacted to a surface, and the distance between the tip-sample distance is varied at a constant low bias voltage (~10 mV), recording the current.

(iii) Electrical Break Junctions [7]: Atoms are electromigrated by the appliance of large current densities on a previously (usually by EBL) patterned neck of a metallic thin film.

(iv) Electrochemical junctions [8]: In an electrochemical bath, a previously patterned (EBL) gap is filled by electrodeposition.

4.2. Atomic constrictions in magnetic materials

4.2.1. Introduction

Due to the spin degeneracy of the conduction electrons in magnetic materials, the quantum of conductance includes a factor of two. Due to the strong exchange energy, magnetic materials have their band structure split. Conducting channels are therefore spin dependent and the conductance quantum in magnetic materials is

$$G_0^{\,M} = \frac{e^2}{h} \qquad (4.5.)$$

Hence, in the case of single-channel conduction, electronic transport would be fully polarized and the material would become (locally) a half-metallic conductor.

4.2.2. Ballistic magnetoresistance (BMR)

Since the conduction in metals in the ballistic regime is governed by the band structure, the magnetoresistance properties of magnetic materials should therefore be affected, due to the absence of spin-dependent diffusion. In the case of GMR, this fact was studied theoretically by Schep *et al* [9], although experimental results in this issue were unsuccessful [10].

The topic was revived with spectacular results, when MR values of a few hundred per cent were measured in Ni contacts formed by approaching wires mechanically [11]. These results were also obtained in nanocontacts of other ferromagnetic materials by using different techniques, by several groups [12-16]. The effect proposed, coined as Ballistic Magnetoresistance (BMR), was associated to the presence or non-presence of a domain wall in the contact, blocking or letting the electrons pass through the contact. When the magnetizations in the electrodes are parallel, the conductance is of the order of the conductance quantum, but in the antiparallel case, electrons are partially reflected because the majority spin channel changes its spin direction in the contact. Hence, magnetoresistance would be expected to reach extremely large values when the sample resistance is of the order of 10 kΩ.

These results supposed a high impact in the Spintronics community, since new devices based on this effect, higher than GMR, could be performed. However, next experiments [17-19] trying to reproduce previous results revealed that actually mechanical artifacts, such as atomic reconfigurations or magnetostriction (change of volume in a magnetic material when its magnetization changes), were responsible for this high effect, and actually BMR would be only of the order of a few tens per cent [20]. The high controversial scenario lived in these years had its maximum point in 2004, in the "Symposium on the Controversy Over Ballistic Magnetoresistance' at the Ninth Intermag Conference (Anaheim, CA, January 5–9, 2004)". Currently, the scientific community has basically concluded that the impressive BMR is a consequence of spurious effects [20], although it should be also remarked that it is still unclear if magnetic nanocontacts of high transmission factors can be made [1]. This would require making a 1D wire, without imperfections, with a diameter smoothly increasing when connected to the diffusive reservoirs.

4.2.3. Ballistic anisotropic magnetoresistance (BAMR)

Another different finding in atomic-sized contacts was a large anisotropy in the MR of the contacts, whose magnitude and angular dependence were found to be very distinct from bulk materials, the so called ballistic anisotropic magnetoresistance (BAMR).

Anisotropic magnetoresistance in bulk ferromagnetic materials (diffusive regime) was introduced in chapter 3. In a few words, in a FM it is possible to describe its conductance in two separated channels, for spin up and down directions [21]. When adding to the energy of the system the spin-orbit coupling (L-S), the wavefunctions of electrons have to be recalculated, not being anymore eigenstates of S_z, since the L-S mixes spin states. This mixing is anisotropic, giving as a consequence an anisotropy of the resistance [22, 23]:

$$AMR(\%) = 100\frac{\rho_{//} - \rho_{\perp}}{\rho_0} \qquad (4.6.)$$

The sign of the AMR depends on the band structure of the FM, normally being positive in metals ($\rho_{//} > \rho_{\perp}$).

The dependence of the AMR with the angle θ formed by the current and the magnetization is:

$$\rho(\theta) - \rho_{\perp} = (\rho_{//} - \rho_{\perp})\cos^2\theta \qquad (4.6.)$$

In ballistic transport, the AMR has to be recalculated, since the structural, electronic and magnetic properties of atoms change. For instance, the quenching of the orbital moment will not be as quenched as in bulk [24], and the spin-orbit coupling will increase substantially [20]. Theoretical studies of BAMR in chains of Ni and Co [25, 26] indicate that the effect would be much higher than in bulk, of the order of G_0, and with an angle dependence much more abrupt.

Some experimental measurements support these theories. Specifically, we can cite the work by Sokolov *et al* [27], where in Co contacts made by electrodeposition, changes in the AMR of the order of the quantum of conductance were found, and the work by Viret *et al* [28], where iron contacts fabricated by mechanical break junction were systematically studied, finding even higher effects for samples in the tunneling regime than in the metallic (ballistic) regime. However, critical voices have claimed that atomic reconfigurations in the contact, rather than an intrinsic electronic effect, are the most feasible reason for this behavior [29].

4.2.4. Objective of this work

After having exposed the interesting effects appearing in magnetic atomic-sized constrictions, together with the polemics associated to these high-impact results, it seems crucial the creation of magnetic nanocontacts free from spurious effects, to

clearly discriminate whether these effects are intrinsic, or not, in magnetic materials. The typical techniques used for this purpose (see section 4.1.3.) control extraordinarily well the reduction of the contacts to the atomic regime. However, the constrictions fabricated by these methods are not tightly attached to a substrate, favoring the mechanical artifacts to be present. Besides, the realization of real devices using BMR or BAMR with those methods is not possible, due to its incompatibility for integration. Therefore, nanolithography techniques have been used aiming to create stable nanoconstrictions at room temperature, which could lead to immense applications. However, the resolution of techniques such as EBL or FIB makes really challenging the creation of contacts smaller than 100 nm. Some results can be cited using these techniques [30-35], but MR effects found are, in general, similar to those for bulk, and the lack of reproducibility is evident.

Thus, the work presented in this chapter has had as objective the creation of magnetic nanoconstrictions in the ballistic regime of conduction by means of FIB, trying to systematically study the BMR and BAMR. The work has been successful in the realization of an approach that creates atomic-sized contacts, although the study of MR effects in magnetic nanoconstrictions has, on the contrary, been less satisfactory.

4.3. Experimental procedure. Example for a non-magnetic material: Chromium

For the realization of atomic-sized constrictions we have designed an experimental procedure basically consisting in the following steps (see details of the equipments in section 2):

1. Optical lithography process via lift-off to define a 4 μm metallic path connected by macroscopic pads

2. FIB etching process in the Dual Beam system, controlling the resistance → creation of metallic constriction

3. If the process is done with iron, chamber venting and measurement of the MR as a function of temperature in a CCR

In order to illustrate the procedure, the creation of a controlled atomic-sized constriction based on chromium/aluminium electrodes is described (see a scheme of the process in figure 4.1.). The experiments were made at room temperature in the Dual Beam system. Two electrical microprobes were contacted on the pads (see figure 4.2.). These conductive microprobes were connected via a feedthrough to the Keithley system explained in section 2, located out of the chamber. The lead resistance is about 15 Ω, which guarantees no significant influence on the measured resistance at the stages where the conductance steps occur, which corresponds to resistances of the order of 10 kΩ.

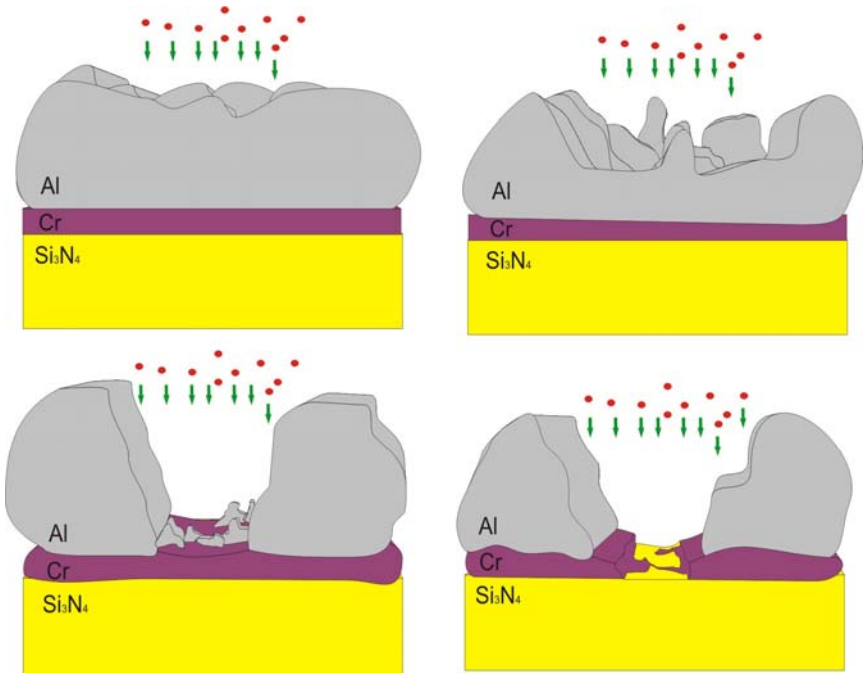

Fig. 4.1. Schematic cartoon of the etching process. Electrical transport measurements are simultaneously measured. The inhomogeneous etching in Al favours clear images of the formed nanoconstrictions in Cr when Al is fully removed.

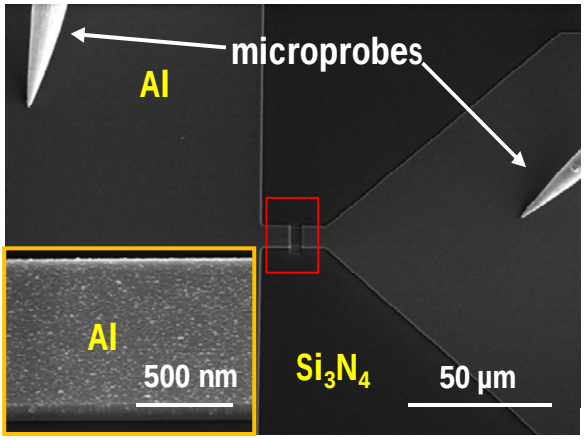

Fig. 4.2. SEM image of the electrical aluminium pads patterned by optical lithography. The two microprobes are contacted for real-time control of the electrode resistance. The red square indicates the area of etching. The inset is an SEM image of the Al/Cr electrode prior to the Ga etching.

The Ga-ion etching proces was done in two consecutive steps. First, starting from 15 Ω, with the ion-column set at 5 kV and 0.12 nA, aiming to shorten the time of the experiment. The etching was stopped when the resistance reached 500 Ω, still far from the metallic quantum limit. In the second step, the ion-column was set at 5 kV and 2 pA, for about 12 minutes. During this period we monitored the variation of the resistance and simultaneously 10 kV-SEM images were collected. This allowed us the correlation between resistance and microstructure. In other experiments, the milling was stopped at determined resistance values, at which current versus voltage curves were measured. The maximum bias current was selected in order to avoid the deterioration of the device due to heating effects.

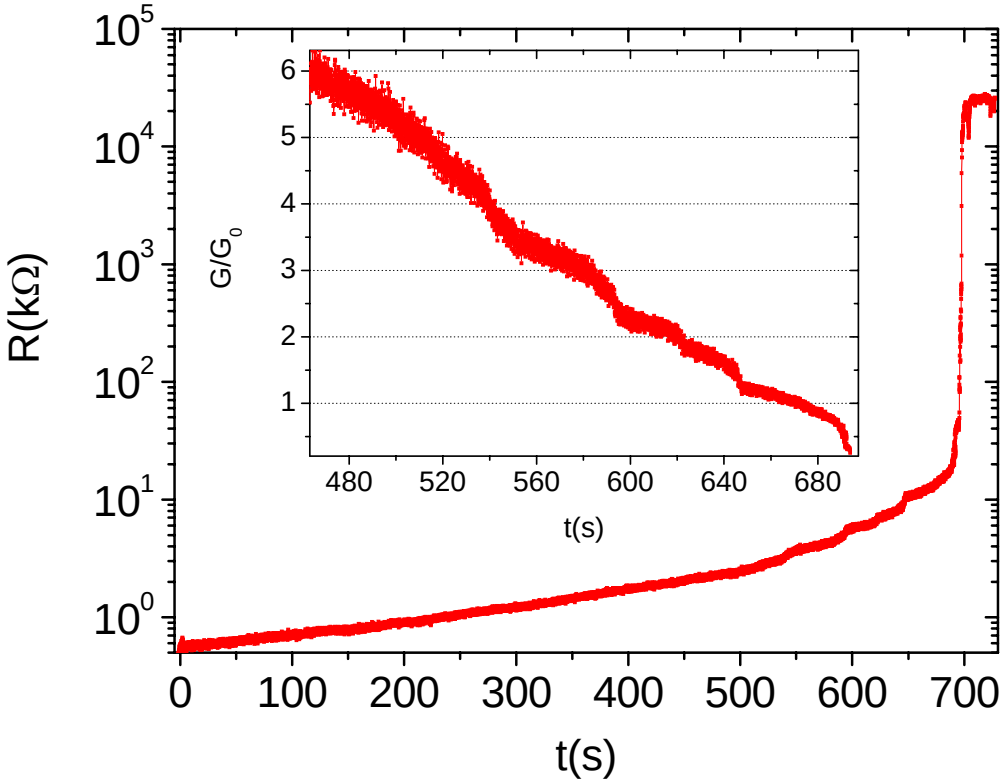

Fig. 4.3. Resistance versus time in a typical ion etching process for Cr/Al. Conductance (in $G_0=2e^2/h$ units) versus etching time of the nanoconstriction whose results are shown in the inset. In this stage of milling, steps of the order of G_0 are seen, corresponding to discrete thinning of the contact area of the order of one atom. The last step is followed by a sharp decrease of conductance, corresponding to the crossover to the tunnelling regime.

In figure 4.3. we show a typical resistance-versus-etching time result at a starting value of 500 Ω. The resistance increases continuously for about 10 minutes, up to a point, in which a 3 orders of magnitude jump is seen. Just before this abrupt change, the resistance shows a discrete number of steps. We can see in the inset that, for this particular case, plateaus with a small negative slope for the conductance are roughly located near integer multiples of G_0. This step-wise structure is a clear indication of the formation of point contacts in the metal electrode before the complete breaking of the formed nanowires. This is similar to what it is seen in experiments done with the other techniques explained in section 4.1.3. [1]. The long experimental time to create one of these constrictions (hundreds of seconds) compared to other techniques such as STM or MBJ (tens of microseconds) does not favor the building of histograms with enough statistics to assign the observed step-wise behavior to conductance quantization. From tens of experiments, we can conclude the reproducible existence of steps in the conductance in the verge of the metal-tunneling crossover and certain dispersion in the specific values of the conductance plateaus, which we always observe below 4 G_0. Anyhow, previous studies indicate that conductance histograms are more irregular in transition metals nanoconstrictions [1, 36] than in the case of monovalent metals like Au [4]. This is due to the fact that the number of conducting channels in a single-atom contact is determined by the number of valence electrons and its orbital state. Theoretical works show that the conductance in non-monovalent metals strongly depends on the specific atomic configurations of the constriction [37-39], which suggests that strong dispersion in the specific values of the conductance plateaus are expected in a reduced number of experiments. To determine the values where steps in conductance occur, numerical differentiation of the G(t) curve was done. Peaks with approximately zero maximum value are observed where plateaus in G occur. In the particular case of figure 4.3., the fit of these peaks to a Gaussian curve gives the maximum at the values (1.02 ± 0.01) G_0, (1.72 ± 0.01) G_0, (2.17 ± 0.01) G_0, and (3.24 ± 0.02) G_0. The broadness of the found steps is a typical feature of room temperature measurements [1, 36, 40].

In figure 4.4., SEM images taken during the etching process are shown. The etching by Ga ions in the first stages of milling is highly inhomogeneous due to the presence of an Al layer deposited on purpose on top of the Cr layer. The granular morphology presented by the evaporated aluminium favors this phenomenon, known as “channelling”, in which preferential sputtering of some grains with respect to others with different crystalline orientation occurs [41]. At this milling-time, numerous micrometric channels conduct the current. The progressive thinning during the process as well as the fracture of some of them involves a progressive and continuous increase of resistance. Around 1 kΩ one can clearly distinguish how the Al layer has been fully removed from the constriction zone. The chromium is now the only responsible for conduction. The Cr grain size is smaller than in Al, and a more homogeneous etching process takes place from that moment on. The plateaus found for the conductance correspond with images where only one metal nanowire is not fractured, reaching atomic-sized contacts just before the final breaking and the crossover to the tunnelling regime. When this finally occurs, an abrupt jump occurs in the resistance, reaching values in the MΩ range, associated with a tunneling conduction mechanism.

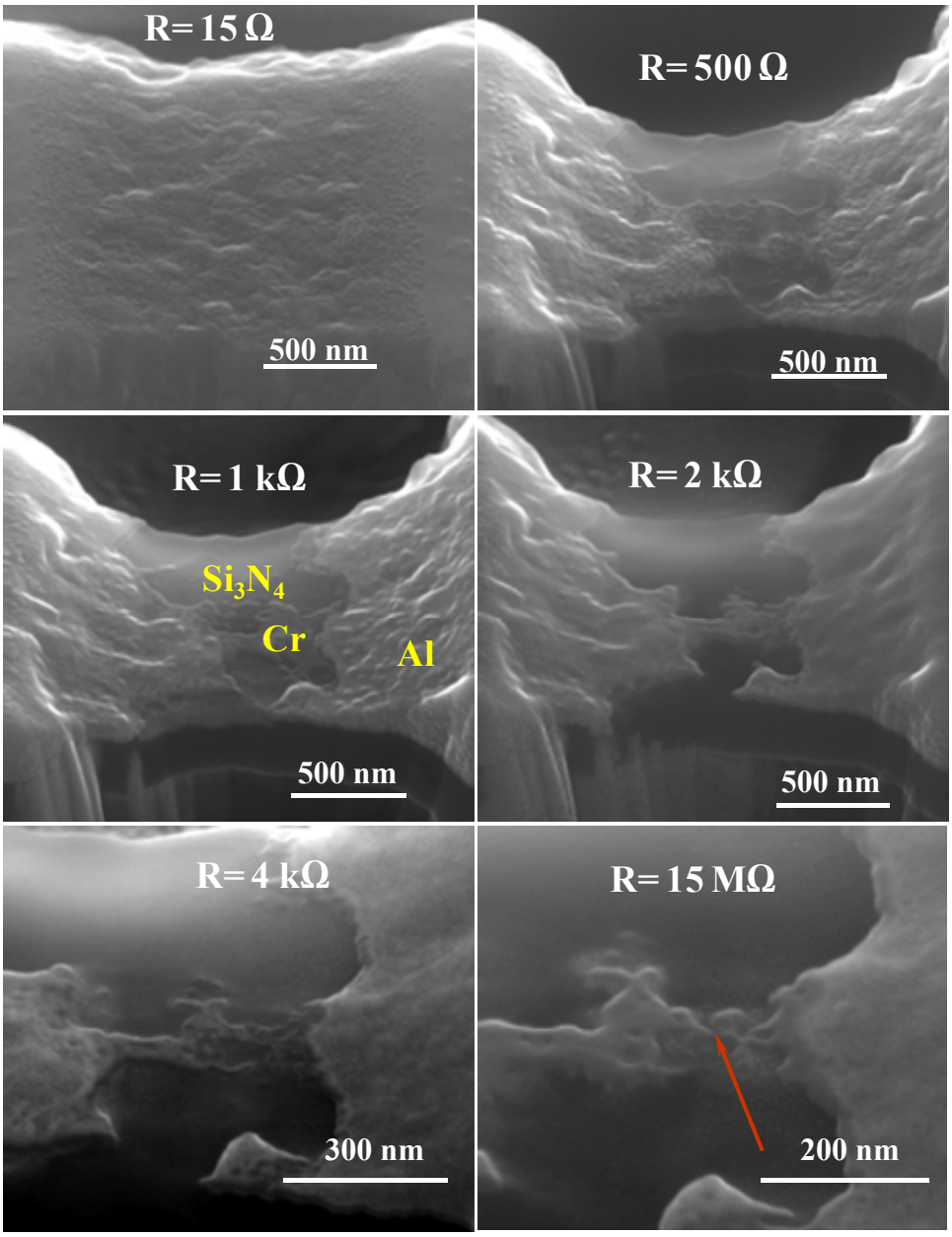

Fig. 4.4. SEM images at different stages of milling (view at 52º tilt angle), showing the change of the microstructure of the Al/Cr electrode as a function of time. The high magnification used in the images allows the visualization of the evolution of the material under ion bombardment at a sub-micrometric scale. The resistance value in each case is shown. In the verge of the metal-tunnel crossover (image corresponding to R=4 kΩ) the current flows through a single nanoconstriction and atomic-sized-conduction features are observed. When the last nanoconstriction gets fractured (image corresponding to R=15 MΩ), the resistance jumps to MΩ range values. The arrow signals the breaking point of the constriction.

In some constrictions, the etching was stopped at different moments, measuring I-V curves. As it can be seen in figure 4.5., the linear I-V behavior indicates metallic conduction, and consequently that the constriction is not broken. Once the constriction breaks, a non-linear I-V behaviour is found, as expected in tunnelling conduction. Fitting the I-V curves for tunnelling conduction to the Simmons model for a rectangular tunnel barrier [42] gives as a result a barrier height of the order of 4.5 V, a junction effective area of 300 nm^2 and a barrier width of the order of 0.65 nm. The found barrier height corresponds with the work function for chromium [43] and the other parameters seem reasonable, evidencing the adequacy of the fit in spite of the simplified assumptions of the model. Even though re-sputtering of some Al atoms towards the contact area could be possible, the value found for the barrier height in the tunneling regime seems to indicate that the electronic transport through the nanocontact is governed by the Cr atoms.

We have not observed degradation during the measurement time (tens of seconds) since the substrate under the formed metal constriction guarantees a robust and stable structure. We have found that when the constriction shows resistance values of the order of the conductance quantum, a limiting maximum power of 0.3 nW is required to avoid degradation, which constrains the maximum applied voltage to values below ~6 mV. Considering a contact area of 0.3x0.3 nm^2, a $5.5x10^7$ A/cm^2 current density is obtained, which is around three orders of magnitude larger than the maximum current bearable by a macroscopic metallic wire. This huge current density is understood in terms of ballistic transport through the contact [1].

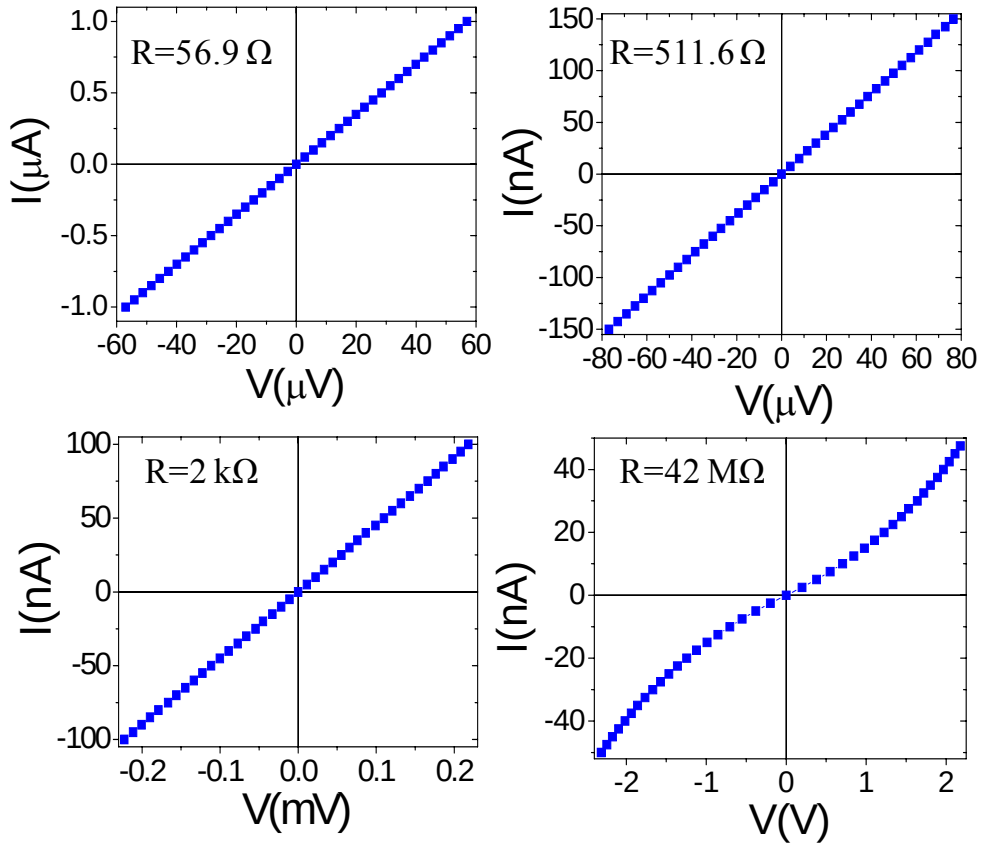

Fig. 4.5. I-V curves measured at fixed resistance values. A linear dependence, as expected for metallic conduction is observed except for the last stages of milling, where the tunnelling regime has been reached.

With the available data, it is not possible to discard that, due to the moderate vacuum level (10^{-6} torr) and the Ga-assisted etching process, some impurity could be in the surroundings of the nanoconstriction and could exert some influence in the conduction properties. However, the obtained linearity in the I-V curves in the metallic regime seems to confirm the presence of clean contacts, because only the presence of adsorbates and contaminants produce non-linear curves in the low-voltage regime [23, 24]. In our case, the use of low ion energy (5 kV) and current (2 pA) is expected to minimize the role of Ga damage and implantation. We have carried out a chemical analysis of the surroundings of the created nanoconstrictions by means of EDX measurements. The results give a typical composition for Si/O/Cr/Ga/C (in

atomic percentage) of 30/45/23/1/1. If the substrate elements (Si and O in this case) are discarded, the Cr and Ga atomic percentages are found to be around 96% and 4%, respectively. However, one should be aware that this technique has a very limited resolution in depth and lateral size.

We would like to remark that ion-etching processes are commonly used in micro/nano-fabrication steps in laboratory and industrial processes without affecting the device properties. Thus, it is reasonable to assume that for many types of devices the use of suitable ion energy and dose won't affect the device properties. This issue is deeply studied in section 4.4.2.2.

Finally, we must point out the importance of the chosen parameters, crucial to see the transition from the ohmic to the tunneling regime in a detailed way (this is not the case in other conditions).

4.4. Iron nanocontacts

4.4.1. Creation of Fe nanoconstrictions inside the chamber

The procedure used in this case is approximately the same as that exposed in section 4.4.1. for chromium, but in this case a 10 nm-thick iron layer was deposited before optical lithography and etching, once it was checked that the etching process was inhomogeneous enough to create appropriate structures which favor the formation of constrictions.

In figure 4.6. we show a typical example performed in iron. During the first 2 min, the Ga etching process is performed using 5 kV and 70 pA, the resistance

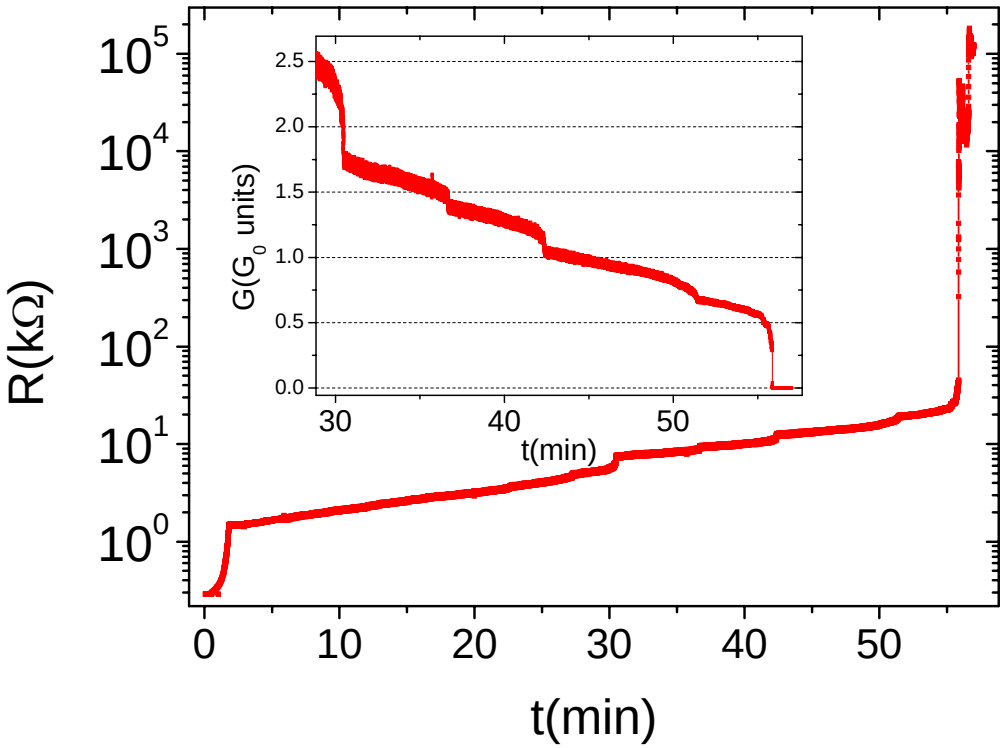

Figure 4.6. Resistance versus time in a typical ion etching process of an Fe electrode, where discrete jumps are observed before the tunneling regime is reached. The inset shows the corresponding conductance (in $G_0 = 2e^2/h$ units) versus etching time. In this stage of milling, steps of the order of some fraction of G_0 are seen, corresponding to discrete thinning of the contact area of the order of one atom. The last step is followed by a sharp decrease of conductance, corresponding to the crossover to the tunneling regime.

approaching 2 kΩ at the end. Then, we continue the Ga etching process using 5 kV and 0.15 pA. The process is slower and allows the detection of step-wise changes in the resistance before the jump to the tunneling regime, similar to the observed behavior in the case of the Cr-based electrodes. The inset shows a close-up of the same results representing the conductance (in units of G_0) versus time. Clear steps are observed which are also interpreted as evidence of the formation of atomic-size metallic contacts just before entering the tunneling regime. These same features were observed for tens of samples, indicating that the process is suitable for iron. The constrictions are found to be stable inside the vacuum chamber. Next step was to measure MR effects of the created constrictions, what implies to open the vacuum chamber and put the sample in contact with atmosphere.

4.4.2. Measurement of one constriction in the tunneling regime of conduction

As an example of the typical problems found when Fe contacts are exposed to ambient conditions, we show in this section the MR results for one sample.

4.4.2.1. Creation of the constriction

In this particular case, the Ga-FIB etching was done in a region of around 2×6 μm^2 (red square in figure 4.7(a)), with a beam acceleration voltage of 5 kV and a beam current of 10 pA, constant through the process. The etching process took a few minutes time, roughly corresponding to a total ion dose of 10^{17} ions/cm^2. In figure

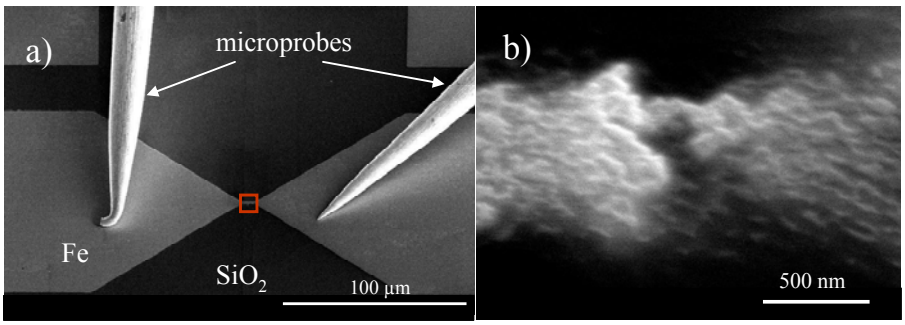

Fig. 4.7. 52º tilted-view SEM images of the fabricated constriction. **a)** Experimental configuration, with the two microprobes contacted to the Fe pads for the *in situ* control of the resistance while the process is taking place. The red square indicates the etched zone. **b)** Microstructure of the iron after etching. A constriction is formed as a consequence of the ionic bombardment.

4.7(b) the microstructure of the constriction after the milling is shown.

In figure 4.8. we show the evolution of the resistance with the process time. Since the initial resistance of the iron electrode is R_i ~3 kΩ, the resistance corresponding to the etched part (R_c) is the measured value minus R_i ($R=R_i + R_c$). After 2 minutes of etching, R starts to increase abruptly, and the FIB column is stopped when $R_c \approx 8$ kΩ. The R is measured during several minutes, finding that the constriction, in the metallic regime, is stable under the high vacuum conditions of the chamber (P~10^{-6} mbar). To avoid the possible deterioration when exposed to ambient conditions, a ~10 nm-thick layer of Pt-C was deposited by electrons (FEBID) on top of the etched zone (one single deposition, at 0º), using $(CH_3)_3Pt(CpCH_3)$ as gas precursor. The high resistance of this material, because of the high amount of carbon, guarantees a resistance in parallel to the constriction of the order of tens of MΩ [44], which is confirmed by the negligible change of R while the deposit is done.

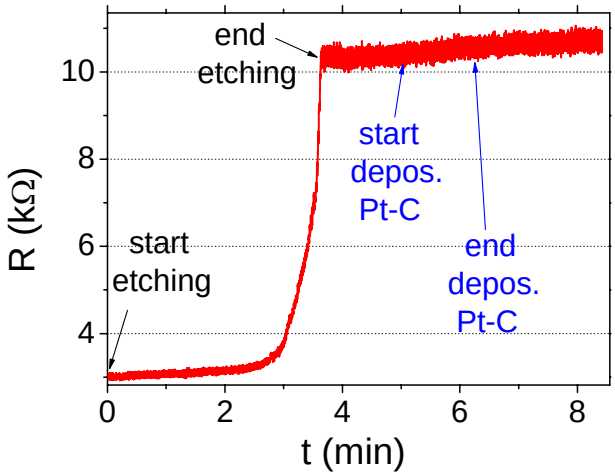

Figure 4.8. Resistance of the iron electrode as a function of the process time. The FIB etching is stopped when the resistance reaches 11 kΩ (R_c~8 kΩ). The constriction is covered by a thin layer of Pt-C, deposited by FEBID. The fabricated nanostructure is stable inside the vacuum chamber.

4.4.2.2. Magnetoresistance measurements

Once the constriction had been fabricated, the sample was exposed to ambient conditions over a few minutes, and transferred to the CCR-electromagnet system explained in chapter 2. The measurements of the resistance at room temperature showed an increase of the resistance by a factor of 10 (R≈100 kΩ), evidencing the departure from metallic conduction in the nanoconstriction. This value is significantly above the resistance corresponding to the quantum of conductance ($R_0=1/G_0=12.9$ kΩ). The non-linearity of the current-versus-voltage curves (not shown here) indicates that the constriction is not anymore in the metallic regime, but in the tunneling one. The high reactivity of the nanostructure due to its large surface-to-volume ratio seems to be the most reasonable explanation of this effect. The resistance increased up to 120 kΩ at T=24 K.

We measured the magnetoresistance at low temperatures with the magnetic field (H) parallel to the current path. In figure 4.9. the evolution with H at several temperatures is shown. MR ratios of the order of 3.2% are obtained. This value is a factor 30 times higher than in Fe non-etched samples, used as reference, where we observed a MR = -0.11 % in this configuration (note the different sign). As it is schematically explained by the arrows in the graph, the evolution of R is understood by a change from a parallel (P) to an anti-parallel (AP) configuration of the ferromagnetic electrodes, separated by an insulator. More in detail, starting from saturation, a first continuous increase in R is observed, of the order of 0.8 %. This seems to be caused by a progressive rotation of the magnetization (M) in one of the electrodes. At around H=700 Oe, an abrupt jump of the resistance occurs (MR =2.5%), since the magnetization of one electrode switches its direction, and aligns almost AP to the M of the other electrode (intermediate state: IS). The MR becomes maximum at H=1 kOe, when the magnetization in both electrodes is AP. At H≈2 kOe, the M in the hard electrode also rotates, resulting again in a low-R state (P). As T increases, the IS, previously explained, disappears. IS is probably caused by the pinning of the M by some defects present in the soft electrode. Thus, the increase of the thermal energy favors the depinning of M. When the temperature was increased

above 35 K, the nanoconstriction became degraded, likely due to the flow of the electrical current.

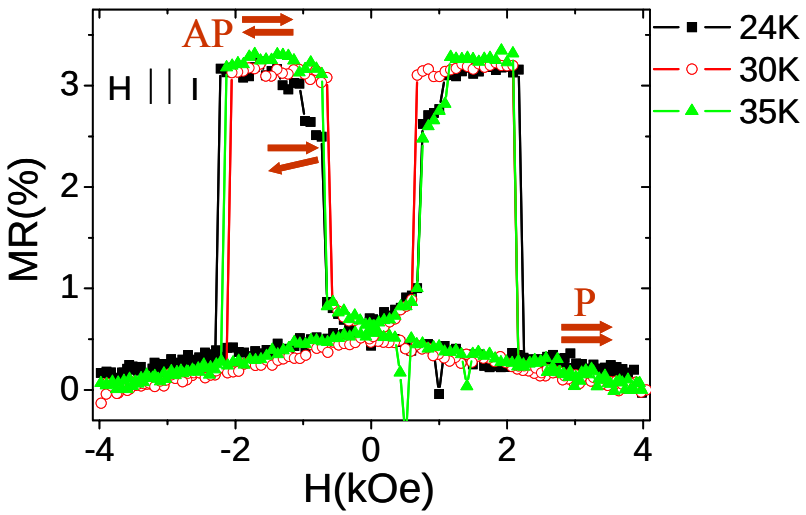

Figure 4.9. Magnetoresistance as a function of the magnetic field at low temperatures. The MR is positive, with a value of 3.2% at 24 K, and can be understood by the decoupling of the magnetic electrodes separated by a tunneling barrier.

In figure 4.9. the dependence of the MR at 24 K as a function of the applied voltage is shown, for the P and AP configurations. The diminishment of the resistance with the voltage is a typical feature of tunnel junctions, attributed to several factors such as the increase of the conductance with bias, excitation of magnons, or energy dependence of spin polarization due to band structure effects [45]. As the magnetostrictive state of parallel and antiparallel electrodes is the same, it seems that magnetostriction is not the cause of the observed TMR effect.

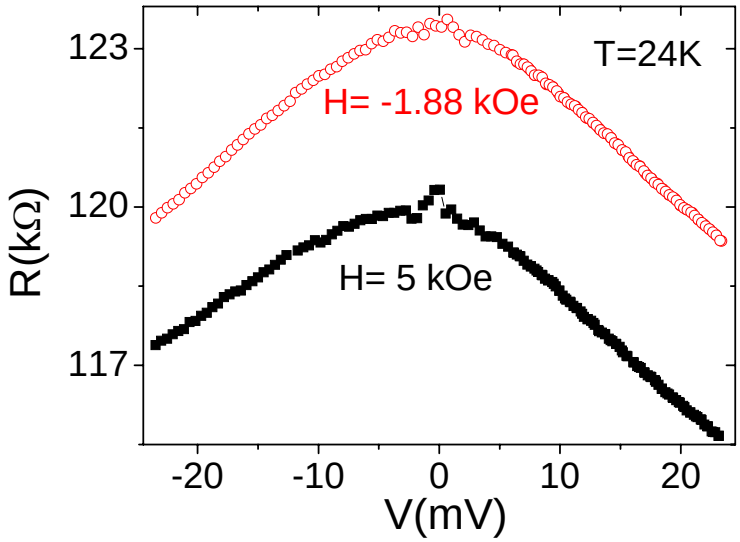

Fig. 4.10 . Bias dependence of the magnetoresistance at T= 24K for AP (H= -1.88 kOe) and P (H= 5 kOe) configurations.

We have also studied the dependence of the anisotropy of the MR with the field angle at saturation, by rotating the sample at the maximum field attained, H=11 kOe. In figure 4.11. the evolution of MR is shown as a function of θ, the angle formed between H and the substrate plane. An AMR effect (AMR) is present in the tunneling regime (TAMR). This effect is around 2% at 24 K, higher and of different sign from the AMR occurring in the bulk material (~ -0.3%). As remarked in section 4.2.3., a TAMR has been previously observed in iron nanocontacts fabricated by MBJ [28], and implies that the evanescent wave functions maintain a strong atomic orbital character. The angle dependence is found to be more abrupt than the normal one for the AMR, proportional to $\cos^2\theta$. This behavior is typical for BAMR [27, 28], and can be understood by considering the details of orbitals overlap [25, 26].

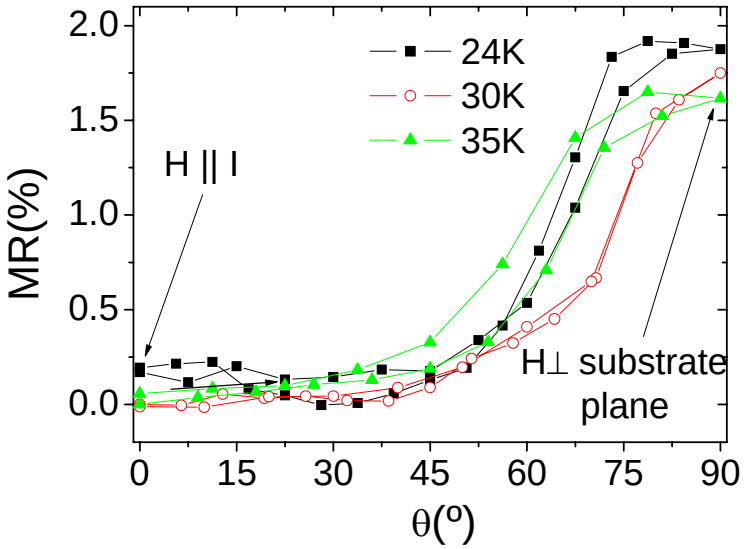

Fig. 4.11. Angle dependence of the MR for low temperatures. A fixed field, H=11 kOe, is applied.

The experiments as a function of angle are also helpful to discard that magnetostriction effects are responsible of the observed MR. The magnetostriction in iron is given by:

$$\frac{\Delta l}{l} = \frac{3}{2}\lambda_S(\cos^2\theta - \frac{1}{3}) \qquad (4.7.)$$

with $\Delta l/l = -7 \times 10^{-6}$ for $\theta = 0º$, and $\Delta l/l = 3.5 \times 10^{-6}$ for $\theta = 90º$.

Thus, the increase of the MR as a function of θ has a contrary sign that if it was caused by magnetostriction, where the minimum resistance would be expected when H is perpendicular to the substrate plane.

The results for this sample are an example of the behavior of all samples we have created. Although it is possible to fabricate Fe nanoconstrictions near the ballistic regime of conductance by the method developed, which are stable inside the FIB chamber, they are degraded when exposed to ambient conditions, breaking or oxidizing, changing to the tunneling regime of conductivities. For the sample shown

here, the TMR ratios at low temperature are 30 times higher than non-etched samples. We also observe a TAMR effect at low temperatures, of the order of 2%, and with an angle dependence different from the $\cos^2\theta$ expected for bulk AMR. From these experiments we also assure that magnetostriction is not playing any role in the measurements.

This result also evidences a crucial point for FIB fabrication: under low voltages etching, and with a moderated ion dose, the FIB procedure does not destroy the magnetic properties of the devices, although more research is required to investigate at what extent they are affected.

4.5. Conclusions

A new approach to obtain stable atomic-sized contacts at room temperature under high vacuum has been performed. The combination of the FIB etching, with simultaneous electrical measurements allows a fine control of the resistance. The steps in the conductance just prior to the crossover to the tunnelling regime are an indication of atomic reconstructions. The plateaus at different conductance values are associated with different atomic configurations in the constriction. The simultaneous imaging of the etching process via the electron column allows following the formed structure in real-time.

The constrictions are stable at room temperature and under high vacuum conditions, proved for Cr and Fe. The possibility of establishing point contacts in a wide variety of materials under similar conditions is expected with the exposed methodology. This is not the case for other techniques, which are less flexible with respect to the used materials and protocols. In our case, the sputtering rate of the material under etching at the used ion energy seems to be the most relevant factor together with the ion column current, which influences the ion beam width and the etching rate. We can forsee great potentialities of this method for the creation of functional devices in the field of Spintronics.

In the case of Fe nanocontacts, the difficulty to have stable nanocontacts when exposed to ambient conditions has been shown. In spite of the protective covering, the constrictions are either completely degraded, or in the tunneling regime when they get in contact with air.

We have shown an example of one iron contact presenting tunneling conduction. It has TMR ratios at low temperature 30 times higher than non-etched samples. We also observe a TAMR effect at low temperatures, of the order of 2%, and with an angle dependence different from the $\cos^2\theta$ expected for bulk AMR. From these experiments we also assure that magnetostriction is not playing any role in the measurements. This result shows that under low voltages etching, and with a

moderated ion dose, the FIB procedure does not destroy the magnetic properties of the devices, although more research is required to investigate at what extent they are affected. The high stability expected for these constrictions in comparison with other suspended atomic-size structures, makes this result promising for future research. A systematic study of the MR is currently under progress to improve the stabilization of constrictions in the metallic range of resistances, and investigate if high BMR and BAMR values can be attained at room temperature, which would have high impact in the field.

We should also remark that a different approach has been developed in our laboratory during this thesis [46], following the same philosophy that the method exposed in this chapter. The main advantage is the well-defined current direction attained, suitable for anisotropic magnetoresistance measurements. However, it is performed at 30 kV, inducing a higher amount of amorphization [41], with a possible increase of the degree of deterioration of the magnetic properties. For details see reference 46.

Chapter 5

Pt-C nanowires created by FIBID and FEBID

In this chapter we will present a thorough characterization of the electrical properties of Pt-C nanowires created by FIBID and FEBID. The same methodology as in chapter 4 will be used, where the resistance of the NWs is probed as the NW is being grown, getting a perfect control of the process. The electrical properties are studied at room temperature, “in situ”, and as a function of temperature, “ex situ”. These results are correlated with chemical and microstructural characterization, and can be understood within the framework of the theory by Mott and Anderson for disordered materials.

The chapter is mainly devoted to the study of wires created by FIB. By depositing NWs with different thicknesses, we study deposits in different ranges of conductivity. These NWs present a metal-insulator transition as a function of thickness, with the metal-carbon proportion as the key parameter that determines the mechanism for electrical conduction.

Besides, this same methodology has been used to compare NWs grown by FIBID in the metallic regime of conduction with wires grown by FEBID. The deposits induced by electrons are orders of magnitude more resistive than those induced by ions for all thicknesses, resembling Pt-C FIBID NWs in the insulating regime of conduction. The substantial differences in the electrical transport measurements between both types of deposits can be understood by means of the theories detailed for FIBID-NWs, giving rise to a complete picture for Pt-C deposits grown by focused beams.

5.1. Nanowires created by Focused-Ion-Beam-Induced-Deposition (FIBID)

5.1.1. Previous results in Pt-C nanodeposits grown by FIBID

One of the most commonly deposited metallic materials using FIBID is Pt. A lot of work has been done regarding its electrical transport properties, with a wide range of reported results on the resistivity at room temperature (ρ_{RT}), as well as on the thermal dependence of the resistance, as pointed out in reference 1. We show in table 5.I. the results compiled in that work, together with additional references [1-12]. In addition to the value for ρ_{RT}, we also include, when reported, the thermal coefficient of the resistivity ($\beta=d\rho/dT$), the residual resistivity ratio (RRR= ρ_{RT}/ρ_{lowT}), the electronic mechanism proposed for conduction, the character of current-versus-voltage curves, the chemical composition of the deposits, and the gas precursor used. As revealed by Transmission Electron Microscopy, the microstructure found rather inhomogeneous, with crystalline metallic inclusions (around 3-10 nm) embedded in an amorphous carbon matrix [1-5, 9] (see section 5.2.2.3). An important point that is usually missed when comparing these results is the two types of precursors used for Pt deposition. We can see that in two groups [3-5 and 10], the nanowires (NWs) are deposited with cyclopentadienyl-trimethyl platinum, $(CH_3)_3PtCp$, whereas in the rest of groups [1, 2, 6-9, 11, 12] methylcyclopentadienyl-trimethyl platinum, $(CH_3)_3Pt(CpCH_3)$ is used. Deposits using the first precursor (one carbon less present in the molecule) have the lowest resistivity reported (only about 7 times higher than that of bulk Pt) and a positive β. At low temperatures they present deviations from the behavior expected for pure Pt NWs, such as weak antilocalization and quasi-one- dimensional-interference effects [3-5]. On the contrary, with the second precursor, β is always negative, either with an appreciable thermal dependence, associated with variable-range hopping (VRH) [2, 12], or an almost-negligible dependence [1, 9, 10], resembling the conduction of a dirty metal, with metallic [9] or tunneling conduction [1]. In this work, we center our study on NWs created with the second precursor, of more extended use in the scientific community, with the aim to clear up the, in principle, contradictory reported results.

Report	ρ_{RT} ($\mu\Omega$ cm)	β= dρ/dT	RRR= ρ_{RT}/ρ_{lowT}	Conduction	I-V curves	Atomic % C:Pt:Ga:O	Gas precursor
Lin *et al* [3-5]	61.5-545	> 0	≈ 1.3	Disordered metal	Linear	67:30:3:0	$(CH_3)_3PtCp$
Tao *et al* [6]	70-700	---	---	---	---	24:46:28:2	$(CH_3)_3Pt(CpCH_3)$
Puretz et al [7]	400-2100	---	---	---	---	47:37:13:0	$(CH_3)_3Pt(CpCH_3)$
Telari *et al* [8]	500-5000	---	---	---	---	70:20:10:0	$(CH_3)_3Pt(CpCH_3)$
De Teresa *et al* [9]	800	< 0	0.8	Disordered metal	Linear	70:20:10:0	$(CH_3)_3Pt(CpCH_3)$
Peñate-Quesada *et al* [1]	860-3078	< 0	≈ 1	Inter-grain tunneling	Non-linear	Similar to [12-14]	$(CH_3)_3Pt(CpCH_3)$
Tsukatani *et al* [10]	1000	≈ 0	≈ 1	---	---	---	$(CH_3)_3PtCp$
Dovidenko *et al* [11]	1000-5000	---	---	---	---	63:31:4:2	$(CH_3)_3Pt(CpCH_3)$
De Marzi *et al* [12]	2200	< 0	≈ 0.7	VRH	---	---	$(CH_3)_3Pt(CpCH_3)$
Langford *et al* [2]	1000-10^6	< 0	0.6	VRH	Linear	50:45:5:5	$(CH_3)_3Pt(CpCH_3)$
Present study	**700-10^8**	**< 0**	**Thickness dependent**	**MIT**	**Thickness dependent**	**Thickness dependent**	**$(CH_3)_3Pt(CpCH_3)$**

Table 5.I. Compilation of reports for Pt-C NWs created by FIB. All deposits are done at 30kV, except in [6] (30-40 kV) and [7] (25kV). In these two references the atomic percentage is obtained by Auger spectroscopy, whereas the rest are EDX measurements. Contradictory results are found for the transport properties and composition. The present work can explain the differences in terms of a different compositon with thickness. In reference [1], the non-linear I-V characteristics were observed for a 3078 $\mu\Omega$ cm NW.

5.1.2. Experimental details

5.1.2.1. Deposition parameters

The Pt-C NWs were grown using the FIB column integrated in the Dual Beam system, together with the automatic Gas Injection System (GIS) to introduce the gas into the process chamber, all explained in detail in section 2. The SEM was used for imaging the sample, minimizing the ion dose in the deposits. The deposition parameters are: $(CH_3)_3Pt(CpCH_3)$ precursor gas, (T_G) = 35 ºC precursor temperature, (V_{FIB}) = 30 kV beam voltage, (I_{FIB}) = 10 pA beam current, substrate temperature = 22 ºC, dwell time = 200 ns, chamber base pressure = 10^{-7} mbar, process pressure = 3×10^{-6} mbar, beam overlap = 0 %, distance between GIS needle and substrate (L_D) = 1.5 mm . Under these conditions, a dose of 3×10^{16} ion / cm^2-min roughly irradiates the sample. We must emphasize that the values for T_G (about 10 ºC below the usual operation temperature) and L_D (~1.35 mm higher than usually) were chosen to decrease the deposition rate, allowing detailed measurements of the evolution of the resistance as the deposit was realized. This is required to get fine control, especially during the initial stages, where a very abrupt change in the resistance occurs in a very short period of time (see section 5.3). We obtained approximately the same final resistivity when depositing NWs using normal conditions (see section 5.2.1), so these changes do not seem to affect substantially the properties of the NWs. Thermally-oxidized silicon (~200 nm of SiO_2) was used as substrate, and aluminium pads were previously patterned by optical lithography (see lift-off process in section 2.1.1. for details). The studied NWs (top-bottom deposit in figure 5.1(b)) are length (L) = 15 µm, width (w) = 500 nm, thickness (t) = variable with process time.

5.1.2.2. "In situ" measurement of the resistance during the growth process

The electrical resistance was measured inside the process chamber using the experimental setup explained in detail in section 2.2.2. In figure 5.1(a), a SEM image shows the experimental configuration for the deposition, where the 4 microprobes are contacted to the pads, and the GIS needle is inserted near the substrate. By applying a constant current between the two extremes of the NW, and measuring the voltage drop

in two of the intermediate pads, we are able to measure the resistance of the NW which is being grown, once it is below 1 GΩ. This method is similar to others reported in literature [13, 14]. The probe current (I_{probe}) was changed during the measurement, in order to optimize the signal-to-noise ratio, and trying to minimize heating effects of the device while it was created. Typical values for I_{probe} range from 5 nA at the beginning of the monitoring (R ~1 GΩ) up to 10μA at the end (R ~1 kΩ). All these measurements have been done at room temperature

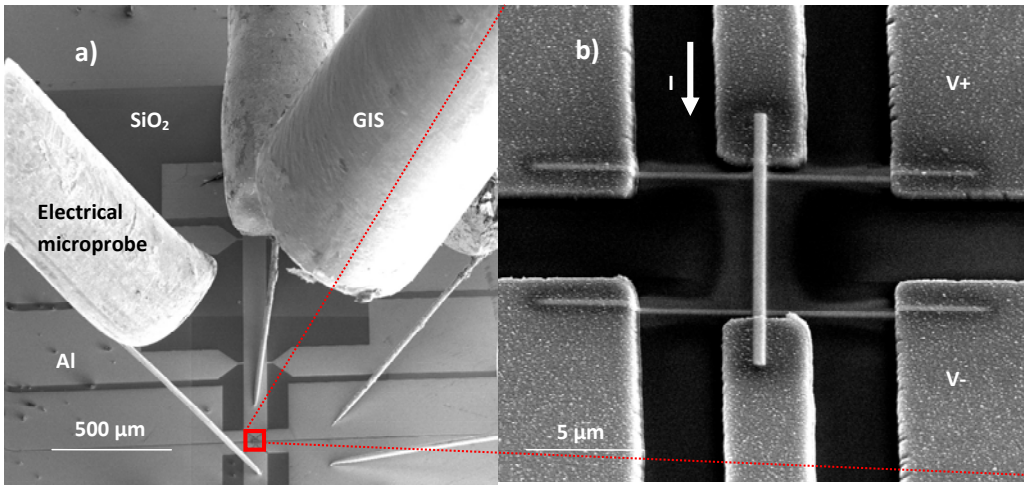

Fig. 5.1. (a): SEM image of the experimental configuration for 4-wire electrical measurements. The 4 microprobes are contacted to Al micrometric pads, while the deposit is carried out. For deposition, the GIS needle is inserted near the substrate. **(b)**: SEM image of one deposited Pt-C NW (vertical line). The additional two horizontal lines are done before the vertical NW, to perform 4 wire measurements (see text for details).

In figure 5.1(b) the vertical deposit is an example of a studied NW. Before its deposition, additional "perpendicular-to-the-nanowire" deposits were performed (horizontal deposits) for 4 wire measurements, avoiding non-linear effects associated with the resistance of the contacts [15, 16]. These extra-connections were done using several growth parameters, finding no differences in the resistance measurements of the NWs. This avoids any influence of the associated halo to the deposition in the results, which could be the source of spurious effects [11, 17].

5.1.2.3. Compositional analysis by EDX

For the study of the composition by Energy Dispersive X-Ray (EDX), we performed deposits on SiO_2 of the same lateral dimensions as those used for electrical measurements, and varying thickness. The EDX measurements were done by means of a commercial Oxford INCA 200 EDX setup whose detector is driven in the vicinity of the sample. The selected energy for the microanalysis is 20kV. Prior to each EDX experiment, energy calibration by means of a Co calibration sample was done.

5.1.2.4. Structural analysis via Scanning-Transmission-Electron-Microscopy

Cross-section lamella of selected NWs was performed with the dual beam equipment by means of Ga ion thinning initially at 30 kV and finally at 5 kV. An Omniprobe nanomanipulator was used to perform in-situ lift-out and placing of the lamella on a Cu grid. The STEM images were obtained inside the same experimental setup, in Dark Field mode, under 30 kV and 0.15 nA conditions.

5.1.2.5. XPS measurements

In order to study the chemical nature of the deposits, we have done depth-profile X-ray Photoelectron Spectroscopy (XPS) measurements in an Axis Ultra equipment by Kratos, at a base pressure of 3×10^{-10} Torr. Because of the limited spatial resolution of the X-ray probe, this deposit was much larger in comparison with all the others: length = 100μm × width = 100μm × thickness = 200nm. Under the chosen conditions, previously detailed, this would imply a process time of about 25 hours, so we changed the I_{BEAM} to 3 nA, reducing significantly the deposition time. The dose rate, $\sim 10^{16}$ ions/cm^2-min, was approximately the same in both types of experiments. A 5 kV-argon etching, with current densities of the order of 0.15 A/m^2 was done, to obtain a XPS depth profile of the deposits (probing every 30 nm).

For the quantitative analysis of the XPS spectra, a Shirley-type background was subtracted, using pseudo-Voigt peak profiles with a 10-30 % Lorentzian contribution in all edges, except for the Pt 4f. In this case, because of the asymmetry of the peaks,

the spectra were analyzed using the Doniach - Sunjic function [18]:

$$I(\varepsilon) = \frac{\Gamma(1-\alpha)}{(\varepsilon^2+\gamma^2)^{(1-\alpha)/2}} \cos\left(\frac{1}{2}\pi\alpha + \theta(\varepsilon)\right) \tag{5.1.a}$$

$$\theta(\varepsilon) = (1+\alpha)\tan^{-1}\left(\varepsilon/\gamma\right) \tag{5.1.b}$$

where ε is the energy measured relative to Fermi energy, Γ is the gamma function, γ is the natural linewidth of the hole state corresponding to its lifetime, and α is the line asymmetry parameter. The function was convoluted with a Gaussian curve with FWHM = 0.3 eV, to take into account the experimental broadening (instrumental resolution, sample inhomogeneity, etc) [19].

5.1.2.6. Transport measurements as a function of temperature

The measurements of the electrical resistance as a function of temperature were performed in the closed-cycle refrigerator detailed in section 2.2.1.

5.1.3. Results

5.1.3.1. Compositional (EDX) and structural (STEM) analysis of the deposits

We performed chemical analysis by EDX on NWs with different thicknesses. The composition was found to be homogeneous over the entire deposited surface, but

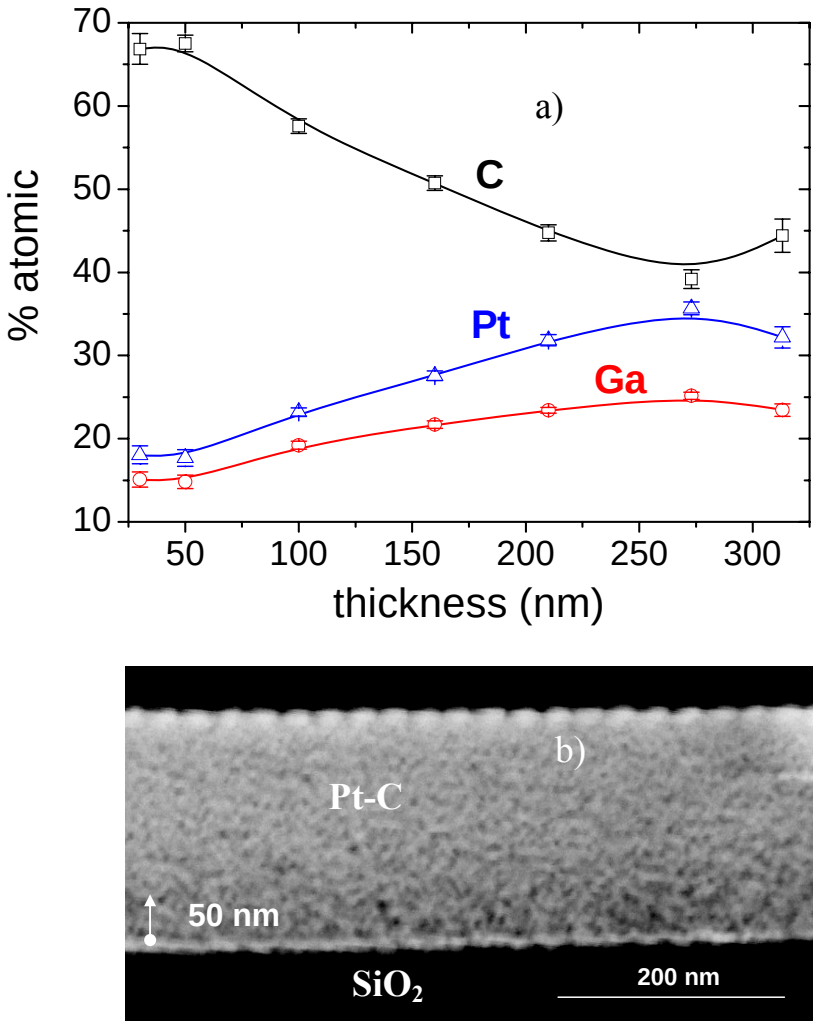

Fig. 5.2. (a): Atomic percentage compositions of Pt-C nanowires as a function of their thickness, determined by EDX. We observe a clear difference in composition for the NWs smaller than 50 nm in comparison with the others, where a higher metallic content is present. Oxygen is always below 1%. **(b)**: STEM dark-field image of a 200 nm-thick lamella prepared from a NW. Approximately, the first deposited 50 nm have a darker contrast in comparison with upper layers, indicating a higher carbon concentration at the initial stages of growth.

strongly dependent with deposition time.

The results are shown in figure 5.2(a). For t = 25 nm and 50 nm, the deposit is highly rich in carbon: ~ 68 %, with Pt ~ 18 % and Ga ~ 14 % (atomic percentages). A residual fraction of oxygen (less than 1%) is also present. For higher thickness, the metal content increases gradually, till approximately saturated values: C ~ 40-45 %, Pt ~ 30-35 %, Ga ~ 25 %.

We have fabricated 200 nm-thick lamellae for STEM imaging inside the chamber. We can see an example in figure 5.2(b), where the difference in dark–bright contrast indicates a gradient in composition as a function of thickness. For the initial deposited nanometers (roughly 50 nm), the image shows a higher C concentration than in the upper part of the deposit, where a higher metal content is present. This agrees perfectly with the former EDX analysis, and was previously found in TEM images by Langford et al [2].

We can understand the gradient in composition with thickness taking into account two possible factors. First, an important decrease in the secondary electrons yield in SiO_2 that occurs when this oxide is irradiated with ions in the keV range [20], because of the large energy gap present in SiO_2. The SE are considered to be the main cause of the dissociation of the precursor gas molecules [21, 22]. Thus, at the beginning of the growth process, a smaller amount of SE is emitted in comparison with the subsequent stages, when the effective substrate becomes the initial C-Pt-Ga deposit. This argument is in agreement with the penetration range of Ga at 30 kV in a SiO_2 and Pt-C substrate (of the order of 30-50 nm), as SRIM calculations indicate [23]. A second explanation can be related to heating effects present during the deposit, which is a crucial point in a FIBID and FEBID process [21, 24, 25]. As the structure grows in height the heat flow would pass from a 3–dimensional regime to a pseudo 2–dimensional regime. Thus, the higher Pt percentage for the top of the structure could be associated with heat dissipation that is less effective than at the beginning of the growth [21, 25]. The gradient in metal-carbon concentration with thickness gives rise to a broad phenomenology in the transport properties of the NWs, as will be described later in this work.

5.1.3.2. XPS measurements

In order to gain a more detailed insight into the nature of the FIBID-Pt, we have performed a depth profile XPS analysis in a micrometric sample, which remained in contact with the atmosphere for 1 day after deposition. Survey spectra show the presence of carbon, platinum, gallium and oxygen, with concentrations similar to those obtained by EDX. A detailed analysis was done by studying the evolution of the absorption edges: C 1s, Pt 4f, Ga 3d and O 1s, as a function of thickness.

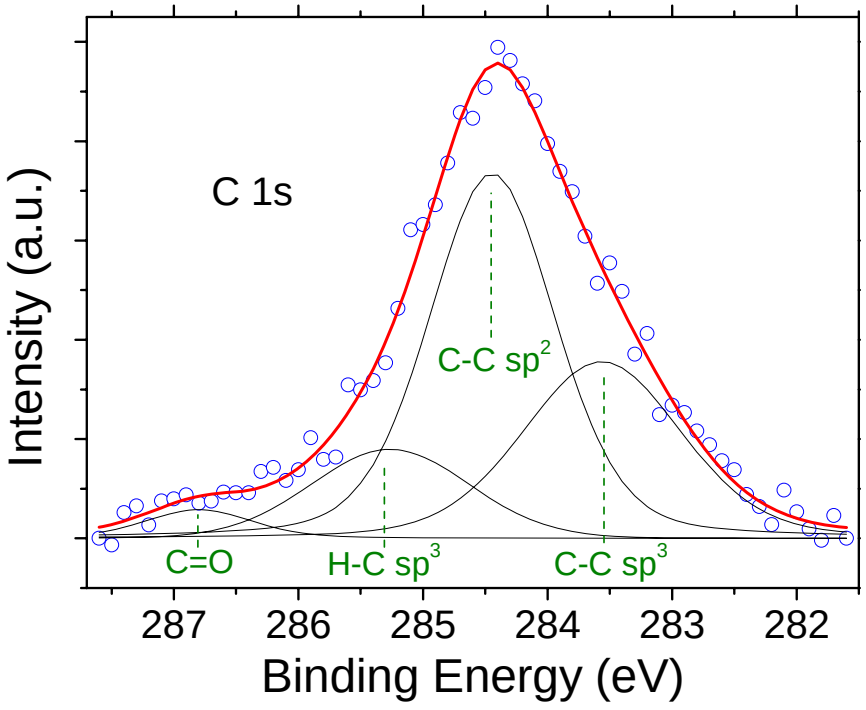

Fig. 5.3. C 1s XPS core level for the 170 nm-thick layer (corresponding to a 30 nm in-depth etching). The solid lines are the components in which the spectrum is decomposed. The resulting fit is superimposed on the experimental data (open circles). The energies found for the peaks are associated with C-C sp^3, C-C sp^2, C-H sp^3 and C=0 (see text for details). The carbon present in the deposit has approximately 50% sp^2 hybridization through all the deposit thickness.

i) Analysis of the C 1s edge:

The C 1s spectra have a constant profile through all the thickness. In figure 5.3., we can see the particular case for thickness = 170 nm (30 nm ion-etched), where four chemical components are used to fit the spectrum. These components are, in order of binding energy: sp^3 carbon with carbon-carbon bonds (C-C sp^3, 283.6 ± 0.1 eV) [26], sp^2 carbon with carbon-carbon bonds (C-C sp^2, 284.3 ± 0.1 eV) [26, 27], sp^3 carbon with hydrogen-carbon bonds (C-H sp^3, 285.3 ± 0.1 eV) [26, 27], and a C=0 contribution, at 286.2 ± 0.1 eV [28]. This last minor peak is compatible with the O 1s spectra (not shown here), where a peak is found at 531.8 ± 0.1 eV. All the peaks have a full-width-at-half-maximum of 1.3 ± 0.3 eV [27]. Thus, we find that the carbon present in the deposit has a sp^2 hybridization of around 55%. This percentage is slightly lower than in previous results obtained by Energy Electron Loss Spectroscopy in suspended Pt nanostructures grown by FEBID, where an approximately 80 % ratio has been reported [29].

ii) Ga $3d^{5/2}$ edge (not shown here):

A peak is present at 18.7 ± 0.1 eV, corresponding to metallic gallium [30].

iii) Analysis of the Pt $4f^{7/2}$ edge:

In figure 5.4. we show the Pt 4f depth profile. Paying attention to the $4f^{7/2}$ edge, all the spectra can be fitted by one single peak, associated to metallic Pt. This is true in all cases except for the top layer (200 nm), which is much broader, where an extra peak is necessary to fit the spectrum. This extra contribution is located at 72.5 ± 0.1 eV, indicating the presence of oxidized Pt in the external surface, in the form of an oxide or hydroxide form [28]. In the O 1s edge, a peak at 531.2 ± 0.1 eV gives account of it. This oxidation seems to be of outstanding relevance for the transport properties of the NWs with small thickness (lower than 50 nm) when exposed to ambient conditions (see section 5.1.3.4).

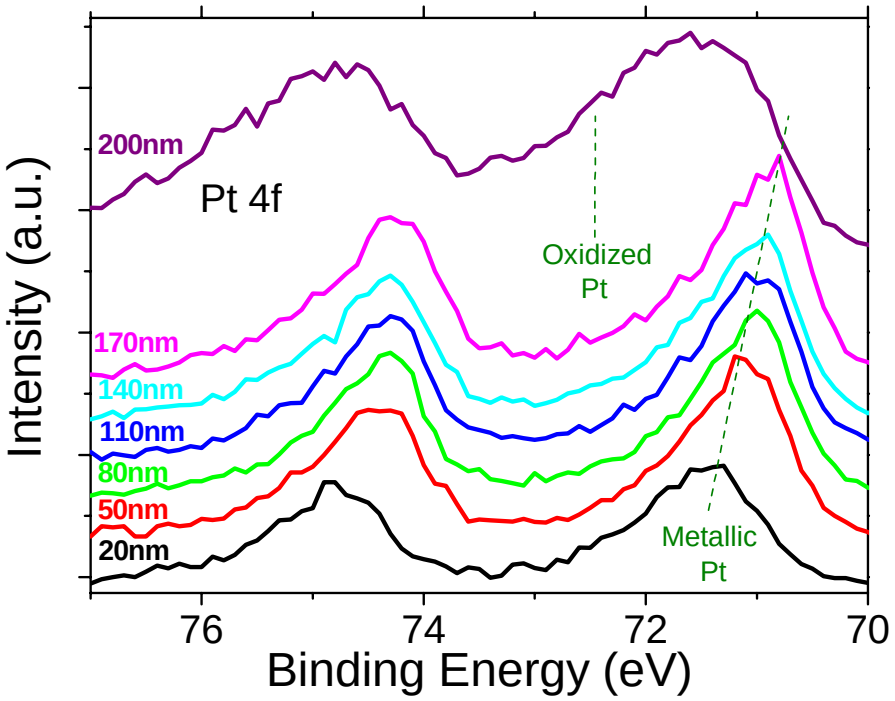

Fig. 5.4. Pt 4f core level XPS depth profile. Successive spectra were obtained after a 30 nm argon etching process. The numbers in the figure refer to the remaining sample thickness. The external surface of the deposit presents a broader spectrum than the rest, as a consequence of an extra peak present, associated with platinum oxide or hydroxide (left dashed line). For the rest of surfaces, the spectra can be fitted by only one contribution, associated to metallic platinum. This peak presents a shift towards lower binding energies as the probed layer is increasingly internal (oblique, right dashed line), as well as a decrease in the asymmetry of the Pt 4f peak. We correlate this evolution with thickness with a progressive increase of the cluster sizes as the deposit gets thicker

For the rest of Pt 4f spectra, we can see substantial differences with thickness. First, a progressive shift towards higher binding energies (BE) occurs from the more external part of the deposit (170 nm) to the more internal one (20 nm) (see oblique line). For the 170 nm spectrum, the maximum is located at 70.7 ± 0.1 eV. This BE matches the range typically found at the surface of Pt crystals [31]. For the 20 nm spectrum, the maximum shifts in BE to the value of 71.2 ± 0.1 eV. The second

important thickness-dependent feature is associated with the asymmetry of the peaks. The asymmetry in XPS peaks for metallic systems is caused by the screening of the core–hole by low energy electron–hole excitation at the valence band [19]. By fitting the peaks with the line shape proposed by Doniach and Sunjic [18] to describe this effect (equations (5.1.a) and (5.1.b)), we find that whereas the outer surfaces present an asymmetry factor $\alpha = 0.18 \pm 0.04$, matching perfectly with the value for bulk Pt [19], the more internal surfaces have $\alpha = 0.10 \pm 0.06$. This lower value for the asymmetry is presumably caused by a decrease in the local density of d-states at the Fermi level [32, 33]. The lifetime width of the core hole created by photoemission is almost constant through the entire thickness, $\gamma = 0.56 \pm 0.05$. This value is higher than for bulk Pt, which is typical for small metal clusters [32, 34]. The two features found as the deposited thickness increases (enhancement in the degree of asymmetry and shift towards lower BE) would be compatible with an increase in size of the Pt clusters [32, 34] with thickness.

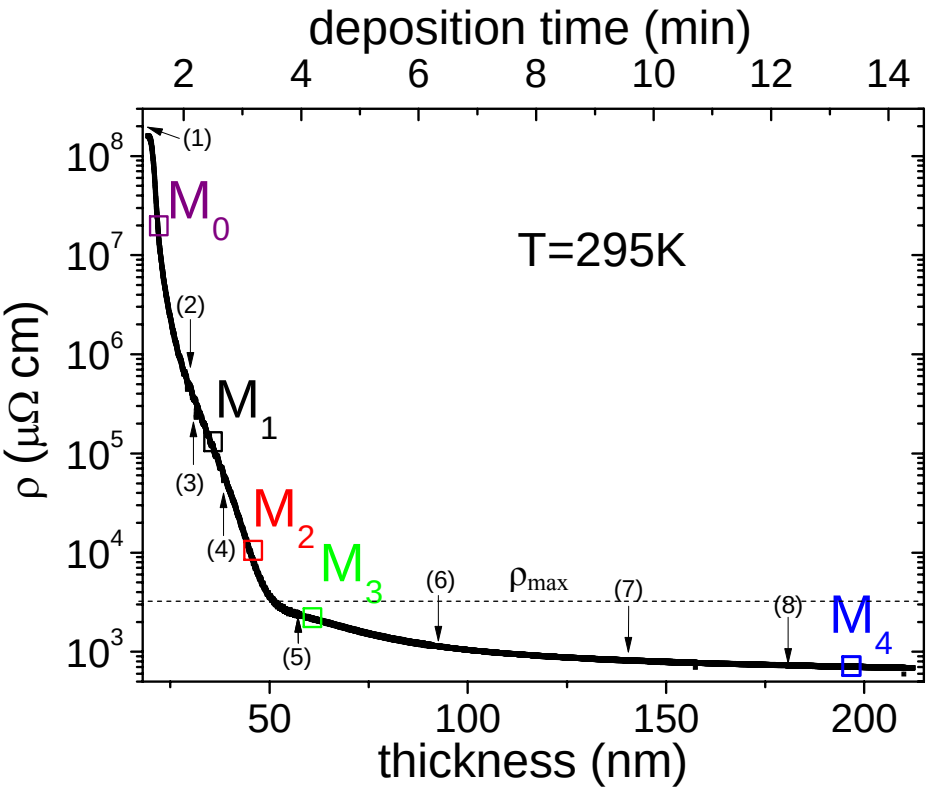

Fig 5.5. Resistivity as a function of deposition time and thickness for a typical process. The resistivity varies by more than four orders of magnitude as a consequence of a change in composition. A thickness of 50 nm marks the transition between a non-metallic conduction (t<50 nm) and metallic one (t>50 nm). The resitivity saturates to a constant value for t>150 nm, ρ≈ 700μΩ cm (about 65 times higher than bulk Pt). The maximum resitivity for metallic conduction in non-crystalline materials (ρ_{max}), as calculated by Mott, is marked. This line separates the insulator NWs from the metallic ones. The numbers in parentheses correspond to different probe currents during the measurements. (1): 5 nA, (2): 10 nA, (3): 30 nA, (4): 100 nA, (5): 1 μA, (6): 3 μA, (7): 5 μA, (8): 10 μA.

5.1.3.3. "In situ" measurements of the resistance as the NWs are grown

As we explained in previous sections, we have measured the resistance of the NWs as the growth process is performed. In figure 5.5. we show how the resistivity (ρ) of a NW evolves as a function of deposition time in a typical experiment. The

results were reproduced over several experiments.

The highest value for ρ corresponds to ~1 GΩ in resistance, and to ~1 kΩ for the lowest value. We have correlated the process time (T_p) with the deposited thickness by doing cross-section inspections of NWs created at different times. Thus, we can also express the results in terms of resistivity, by using the relation:

$$\rho = R\frac{w \times t}{L} \qquad (5.2.)$$

We can see that under these conditions the resistivity of the NWs starts from a value above 10^8 μΩ cm. An abrupt decrease is produced as the thickness increases, lowering its resistivity in 4 orders of magnitude when the thickness reaches 50 nm. From that moment on, ρ decreases slightly, saturating to a constant value of ~ 700 μΩcm (around 65 times higher than the value for bulk Pt) for t> 150 nm. The negligible thickness dependence of ρ for thickness >50 nm was previously evidenced in reference 15. We have not observed any increase in ρ for long T_p as a consequence of the disorder created by ions, such as that reported for W and Pd-FIBID [13]. This procedure has been repeated many times (~10), the behavior being the same in all cases. From these experiments, we conclude that the resistivity at room temperature is highly dependent on the NW thickness. This result explains the large diversity of values for ρ_{RT} of FIBID-Pt NWs reported in the literature [1-12]. We must emphasize that the chosen parameters are of great importance in the particular values of the resistivity for a given thickness, since effects such as heating, diffusion, interaction of the beam with substrate, etc, can differ depending on the conditions. We are not able to reach resistivities as low as the ones reported by Lin *et al* [3-9]. The different precursor gas used for deposition, as it was pointed out in section 5.1.1., seems to be the most probable reason for it. The resistivity as a function of thickness crosses the value reported by Mott for the maximum metallic resistivity for a non-crystalline material, $\rho_{max} \approx$ 3000 μΩcm [35] at ≈50 nm (see dashed line in figure 5.5). Taking into account this criterion, we would roughly expect a non-metallic conduction for samples with $\rho > \rho_{max}$, and a metallic conduction for $\rho < \rho_{max}$.

To study the nature of the conductivity in deposits having different thickness, we have fabricated several NWs, by means of stopping the growth process when a determined value of the resistivity is reached. Hereafter these NWs will be generically referred to as: M_0 (~10^7 μΩ cm), M_1 (~10^5 μΩ cm), M_2 (~10^4 μΩ cm), M_3 (~2×10^3 μΩ cm) and M_4 (~700 μΩ cm), see squares in figure 5.5. The resistance in all cases is stable under the high vacuum atmosphere, once the deposit has stopped. Current versus voltage (I-V) measurements have been performed "in situ", at room temperature. In figure 5.6. we show examples of the differential conductance (G = dI/dV, obtained numerically) as a function of voltage. For M_4 (figure 5.6(e)) and M_3 (figure 5.6(d)), I-V is linear (G constant), so a metallic character is inferred. However, for M_2 (figure 5.6(c)), G(V) is slightly parabolic. This result agrees perfectly with reference 8, where this behavior is observed for a deposit of ρ= 3078 μΩ cm. The same non-linear effect is even much stronger for M_1 (figure 5.6(b)). A different

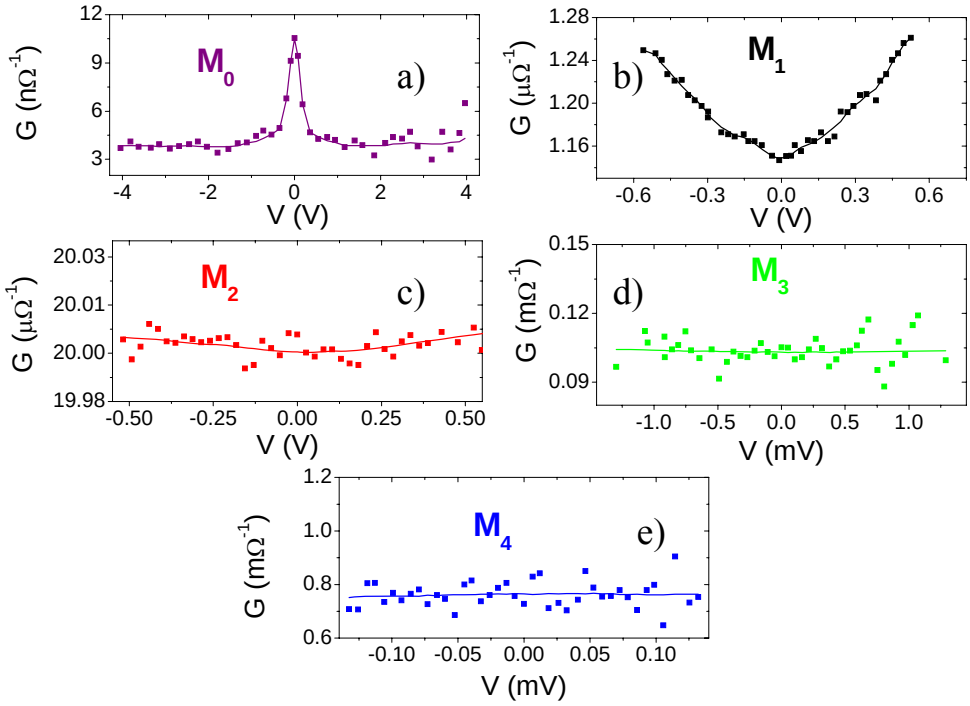

Fig. 5.6. Differential conductivity versus voltage for samples in different regimes of conduction, marked in the ρ(t) curve (figure 5.5.). G(V) has been obtained by a numerical differentiation of current versus voltage curves. In M_0, an exponential decrease in the differential conductance is present. In M_1, a positive tendency for the G(V) curve is observed, being hard to see for M_2. In M_3 and M_4, G(V) is constant (see text for details).

behavior in G(V) occurs for the most resistive sample, M_0 (fig. 5.6(a)), where a peak in the differential conductance is found at low bias, decreasing from ~ 10 $n\Omega^{-1}$ to a constant value of 4 $n\Omega^{-1}$ for voltages higher than 0.5 V. G(V) measurements confirm Mott's criterion for the maximum resistivity for metallic conduction in non-crystalline materials [35]. We discuss in detail the evolution of G(V) with thickness in sections 5.1.3.3 and 5.1.4.

We can understand these strong differences for the electrical transport properties at room temperature taking into account the results obtained in section 5.1.3.1., where a gradient in composition is observed for the NWs as a function of thickness. For NWs thinner than approximately 50 nm, the metal (Pt + Ga) content is lower than 33% (atomic), resulting in resistivity values orders of magnitude higher than those for pure Pt, together with non-linear features in the I–V curves. For NWs thicker than 50 nm, the metal content is higher than 33 %. In this case, the resistivity reaches a minimum value (about 65 times higher than for Pt), and metallic I–V characteristics are observed. A more detailed discussion will be presented in section 5.1.4.

5.1.3.4. Temperature dependence of the electrical properties

For a better understanding of the transport mechanisms in the Pt-C NWs, we have measured the thermal dependence of the resistance, as well as I–V curves at different temperatures. We have studied NWs in the representative ranges shown in section 5.1.3.3.: M_0, M_1, M_2, M_3 and M_4. The first substantial difference between samples is related to the modification of the resistance when the NWs come into contact with ambient atmosphere. For M_4, M_3 and M_2, we did not observe important changes in R, whereas for M_1 the resistance was roughly doubled, and for M_0 it became higher than 1GΩ. These changes are clearly associated with the oxidation effect for Pt at the top part of the deposits after exposure to ambient conditions (see section 5.1.3.2).

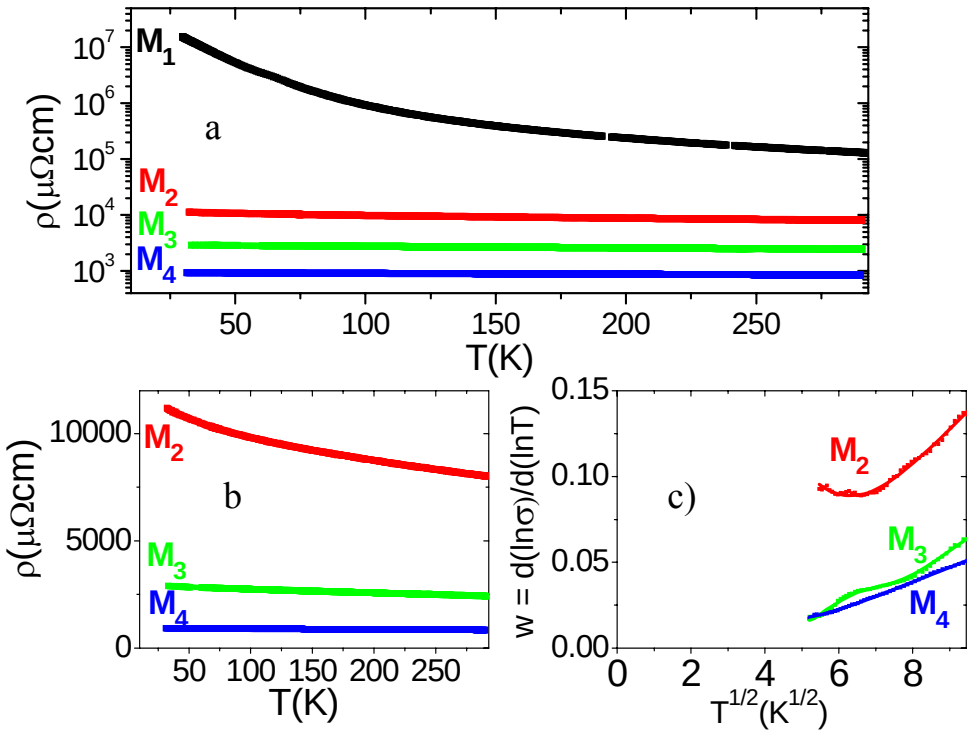

Fig. 5.7 (a): Resistivity as a function of temperature for NWs in four selected regimes of resistivity (note the logarithmic scale). The thermal dependence is radically different depending on the value of ρ at room temperature, indicating a metal-insulator transition as a function of thickness (therefore as a function of composition). **(b):** ρ(T) curves of M_2, M_3 and M_4 in normal scale, to observe in detail the variations in resitivity for these samples. **(c):** *w* (equation 5.3. in text) as a function of $T^{1/2}$. From this analysis, together with the I-V behavior, we deduce that for NWs in the regime of M_3 and M_4 the conduction is metallic, being insulator for the rest of the selected regimes

In figure 5.7(a) we show the resistivity versus temperature [ρ(T)] curves for M_1, M_2, M_3 and M_4). We can see a radically different behavior depending on the resistivity at room temperature. In the case of M_1, a highly negative thermal dependence is found, increasing more than two orders of magnitude when T= 25 K (RRR= $\rho_{RT}/\rho_{25K} \approx 9\times10^{-3}$). Nevertheless, in the rest of the samples (see their evolution with temperature in detail in figure 5.7(b)) a minor dependence on temperature is found, with RRR slightly lower than 1 (≈ 0.7 for M_2, ≈ 0.8 for M_3, ≈ 0.9 for M_4). This is a clear evidence of the important role played by the disorder created by the Ga ion irradiation

during the growth, as well as by the inhomogeneous nature of the deposit. We must remark again that a positive thermal coefficient for FIBID-Pt has been shown in literature [10-12], but using a different gas precursor.

We have used the ρ(T) measurements to determine if the NWs series presents a metal-insulator transition (MIT) with thickness, by calculating the variable:

$$w(T) = \frac{d\left(\ln \rho^{-1}\right)}{d\left(\ln T\right)} \qquad (5.3.)$$

The dependence of *w* upon T is far more sensitive for determining the transition than ρ(T), as has been stressed by Möbius et al [36]. $w(T \rightarrow 0) = 0$ implies a metallic character of the conduction, whereas either a diverging or finite value for $w(T \rightarrow 0)$ indicates that the sample is an insulator. In our case, the lowest temperature attainable is too high (25 K) to apply this criterion strictly. However, in M_2, as shown in figure 5.7(c), *w*(T) is far from tending to zero, whereas in M_3 and M_4 the behavior of *w*(T) has this tendency. We could then infer that M_3 and M_4 have metallic conduction, being insulators for the rest. This is in perfect agreement with the results obtained at room temperature (see section 5.1.3.2.) and, as will be shown below, with the I-V study done as a function of temperature. Therefore, the results support a scenario where the Pt-C NWs grown by FIB present a MIT as a function of thickness (metal/carbon composition). If a low metal content is present, the conduction is attributable to carrier hopping into localized states, whereas a high enough amount of metallic inclusions guarantees that transport will take place by carriers in extended states. This explains the diversity of results found in literature for the dependence of Pt-FIBID resistivity with temperature. It should be noticed that amorphous carbon by itself is well known to present a MIT by tuning the sp^2-sp^3 ratio [37, 38], but in our case the amount of metal present in the deposits is the key parameter for determining the mechanism responsible for conduction.

We have studied in detail ρ(T) in the non-metallic sample M_1. By fitting the curve using an activation dependence:

$$\rho(T) = \rho_{\infty} \exp^{\left(\frac{T_0}{T}\right)^N} \quad (5.4.)$$

it is found that the best exponent N is 0.5. Variable-range hopping (VRH) of electrons between localized states, as predicted by Mott, has the same functional dependence, but with N=0.25 [35]. Efros and Shklovskii demonstrated that a VRH process when the Coulomb interaction between sites is taken into account (ES-VRH) results in a Coulomb gap, yielding an exponent of 0.5, instead of 0.25 [39]. There exists a critical temperature T_c above which Mott-VRH is fulfilled, whereas below T_c, Coulomb interactions become important, and the conduction is by ES-VRH. As discussed in reference 40 for FEBID-Pt nanostructures, a T_c higher than room temperature is expected if reasonable assumptions are made for the values of two unknown quantities in this material: the density of states at the Fermi energy, and the dielectric constant. The observed thermal dependence of M_1 suggests that the same arguments are valid in this case. We should also mention that ρ(T) in M_2 also follows this dependence in the low T-regime.

We have also performed I-V curves as a function of temperature for all the samples and, as in the case of measurements inside the chamber, differentiated numerically the curves to obtain the differential conductance G. First, for M_4 and M_3, I-V curves are linear for all temperatures (not shown here), indicating a metallic character in all the range of T studied. This is not the case for M_2 and M_1. The results are in perfect agreement with the *w*(T) analysis done before.

In the case of M_2, we show in figure 5.8. the normalized conductance G/G_0 versus voltage for selected temperatures, where G_0 is the lowest value for G. The non-linearity effects increase as T diminishes, reaching 2 % [$100\times(G/G_0-1)$] at 25 K. We can see that the dependence for this sample is the same as that for the one reported in reference 1, where the increase in the differential conductance with voltage was understood in terms of the Glazman-Matveev model [41] for multi-step tunnelling occurring between the Pt-Ga nanocrystals embedded in the C-insulator matrix. We will discuss this dependence in section 5.1.4.

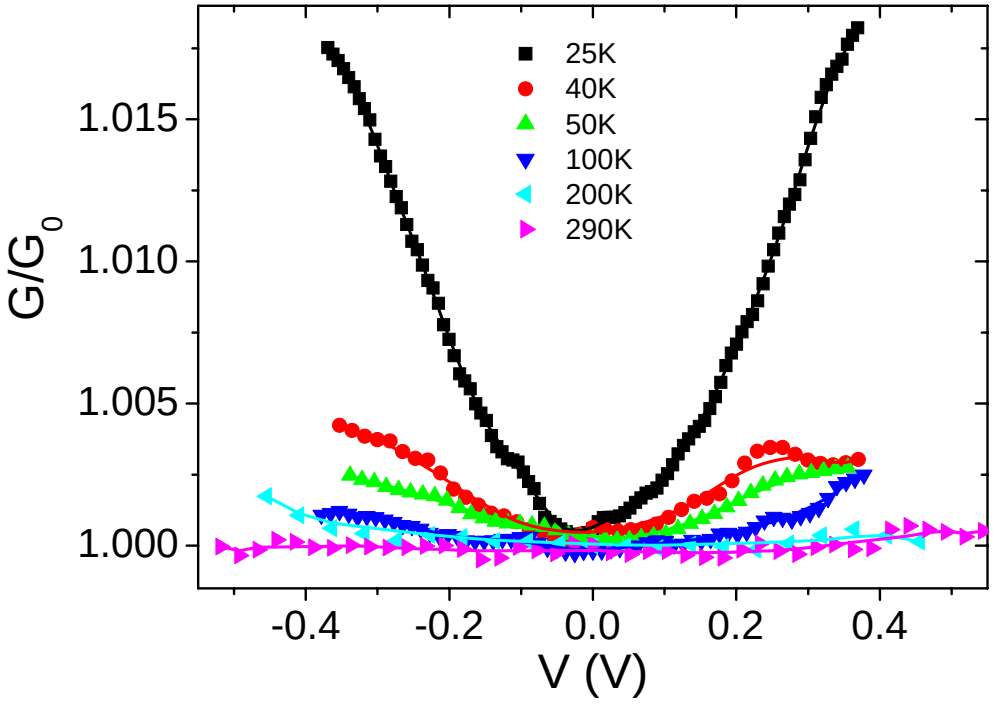

Fig. 5.8.: Normalized differential conductance (G/G_0) as a function of voltage for M_2. A positive differential conductance is observed, increasing the non-linearity as T is lowered

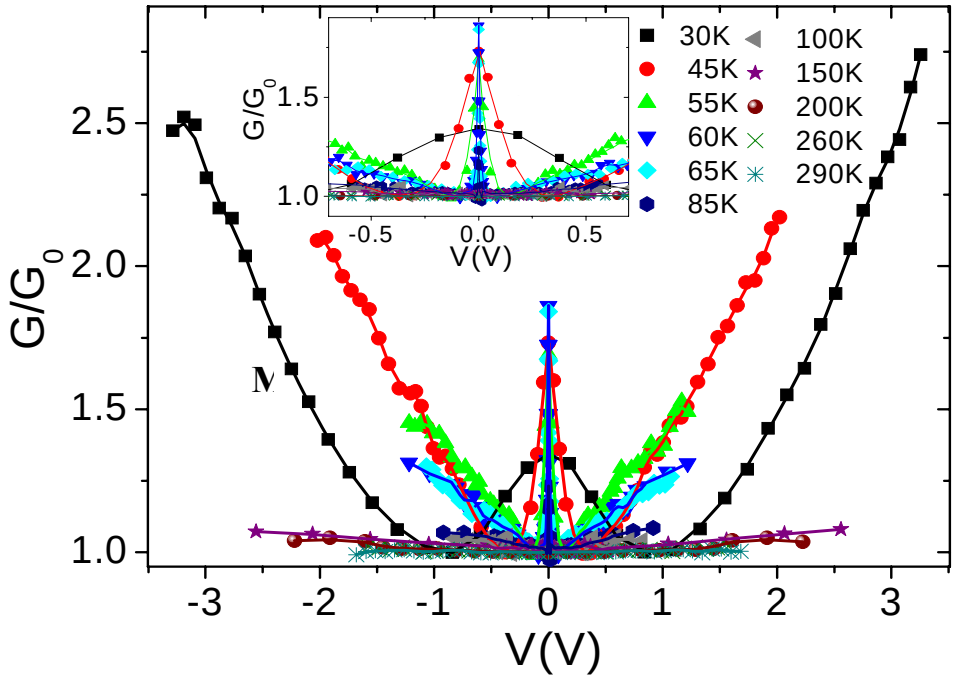

Fig. 5.9.: Normalized differential conductance (G/G_0) as a function of voltage for M_2. The positive differential conductance, also observed in M_2, is present in M_1 for high bias. Superimposed to this effect, a decrease in the differential conductance occurs for T< 100 K. The evolution of this phenomenon is shown in detail in the inset.

In figure 5.9. we show the normalized conductance for M_1. For temperatures higher than 100 K, the same dependence as in M_2 is exhibited. This sample is much more insulating than M_2, so the non-linearity at 100 K, for instance, is around 5%. A richer behavior is found for temperatures below 100 K. As can be observed, a peak in G(V) appears at zero bias, as a consequence of a decrease of the conductance for low voltages. It is the same behavior found for the sample M_0 for "in situ" measurements, and we will show in section 5.2. that this behavior is also present in NWs grown by FEBID. For higher V the same non-linear dependence for G(V) as in sample M_2 is observed. We can see in detail the thermal evolution of the peak in G(V) as a function of temperature in the inset of figure 5.9. The height of the peak increases in magnitude as the temperature is lowered, reaching its maximum at 60 K (around 80 % at V=0). For lower T, the peak becomes broader and smaller in height. On the other hand, the non-linear effect at high voltages (increase of the differential conductance) is above 150 % at 30 K. We interpret in detail all these results in the following section.

5.1.4. Discussion of the results

As has been shown in previous sections, the methodology we have used to study the resistivity of Pt-C NWs created by FIB, using "in situ" measurement of the resistance while the deposit is being performed, has allowed us to determine substantial differences in the electrical transport properties with thickness, i.e., with composition. In this section we discuss the different mechanisms for conduction existing in the NWs, and their temperature dependence, which depend on their composition.

The MIT we observe in the NWs as a function of thickness can be understood under the Mott-Anderson theory for non-crystalline materials [3]. Amorphous carbon (a-C) is a disordered semiconductor. The gap when the hybridization is partially sp^2, as we have determined by the XPS analysis, is typically around 1- 2.5 eV [42, 43]. Because of the intrinsic disorder present in the nanodeposits, band tails appear inside the gap as localized states, with the so called mobility edge separating localized and non-localized states inside the band. If inside a matrix composed by a-C, metallic

inclusions are introduced in a low percentage (M_0 and M_1), this will mainly result in the incorporation of localized defects within the band gap. The conductivity, especially at low temperatures, will be due to hopping conduction between these defects. As the deposit induced by ions continues (M_2), two effects occur: an increase of disorder favored by the continuous ion irradiation, and the incorporation of a higher percentage of metal, as we showed by EDX characterization. The disorder will result in a decrease of the gap by an enlargement of the band tails, resulting in a partial delocalization [42]. Therefore, the hopping will not be only between the impurity states within the gap, but also by means of the localized states inside the band, below the mobility edge. An even higher percentage of metallic inclusions will create a continuum of levels, inducing a transition to the metallic regime when the concentration is above the percolation edge (M_3 and M_4). Under this scenario, we can understand the different results reported in literature regarding the transport properties of Pt-C deposits grown by FIB (see section 5.1.1. and table 5.I.). Depending on the carbon concentration, the conduction will be metallic, by means of extended states, or insulating, by a hopping process between localized states.

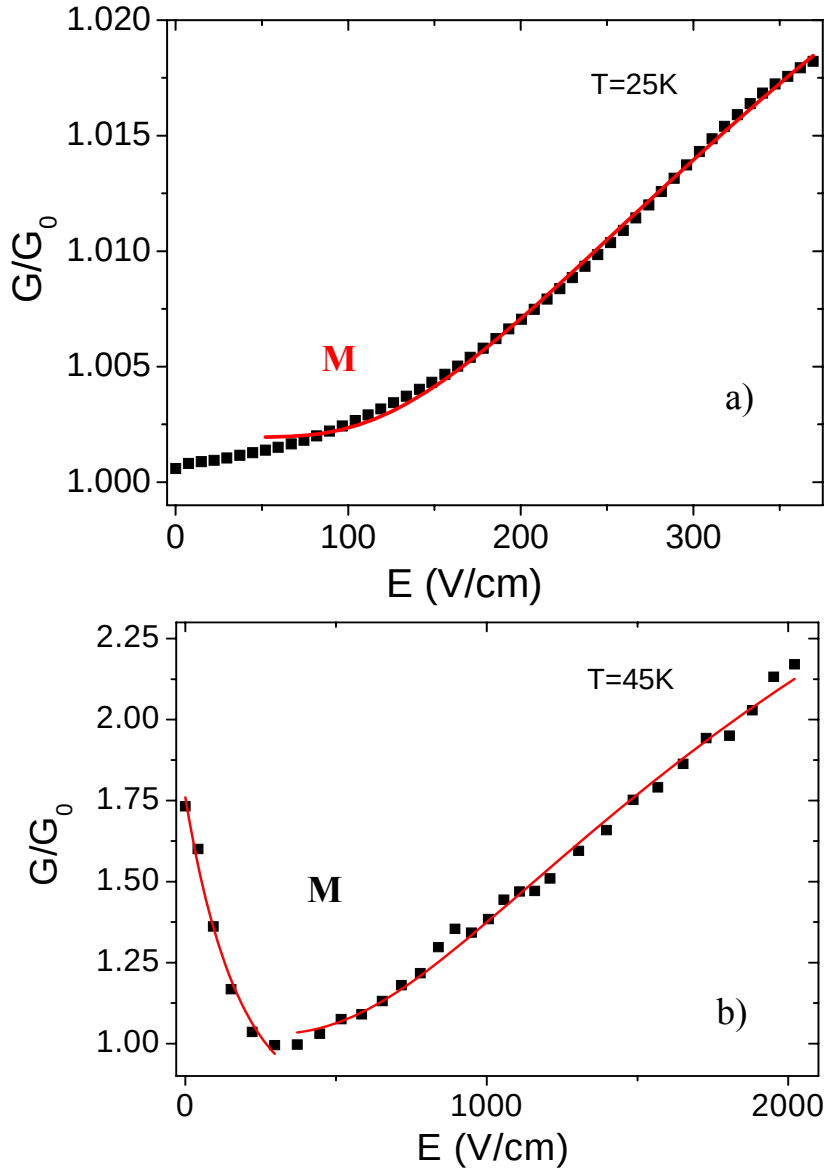

Fig. 5.10.: Normalized differential conductance (G/G_0) as a function of the electric field, for M_2 at T= 25 K **(a)**, and M_1 at T=45 K **(b)**. Red solid lines are fits to the experimental data. In **(a)**, the fit is done for E> 50 V/cm to the ES-VRH model for $E>E^*$ (see equations 5.5. in text). In **(b)**, the same model is used for the fit if E> 350 V/cm. If E<350 V/cm, the Shklovskii theory to describe an exponential decrease in the hopping conductivity is used (equation 5.6. in text).

To understand the mechanisms for conduction in the insulating regime we now focus our discussion on the voltage dependence of the differential conductance for the

samples M_0, M_1 and M_2 (figures 5.6(a), 5.8. and 5.9.). We will first interpret the G(V) behavior for the less resistive sample, M_2 (figure 5.8.). As we previously commented, the thermal dependence at low temperatures is associated with an ES-VRH. In this theory, above a critical electric field E^*, the hopping is field-dominated, and the conductance is expressed by [44]:

$$G = G(0)\exp\left(-\sqrt{\frac{E^*}{E}}\right) \qquad (5.5.a)$$

$$E^* \approx \frac{1.4e}{4\pi\varepsilon_0\varepsilon\xi_L^2} \qquad (5.5.b)$$

where E is the applied electric field, ε is the dielectric constant, and ξ_L is the localization length. We show in figure 5.10(a) a typical fit performed for M_2 at 25 K. In this case, the data fit quite well to the dependence of (5.5.a.) for fields above 100 V/cm. From (5.5.b.), and assuming a dielectric constant ε ≈ 4 for an a-C rich Pt NW [40, 45], we can estimate the localization length as a function of temperature, for T<125 K (figure 5.11.). Thus, $\xi_L(M_2)$≈ 80 nm for this range of temperatures.

The same treatment has been done for the differential conductance of M_1 (figure 5.10 (b)), but in this case the ES-VRH dependence in fulfilled in the whole range of temperatures measured. The fit has been done to the part of G(E) where the conductance increases with the electric field. An example for T=45 K is shown in figure 5.10(b), where the positive exponential dependence predicted by (5.5.a.) is fitted to the experimental data for fields E> 350 V/cm. The localization length derived for the fits is shown in figure 5.11. ξ_L ≈ 30-50 nm for high temperatures, decreasing to a value of about 20 nm for low temperatures. The lowest temperature attained in the setup is quite high (25 K), and could explain why ξ_L is significantly bigger than the size of the metallic crystals in the carbon matrix (around 3 nm), in terms of a thermal effect [2, 3, 9].

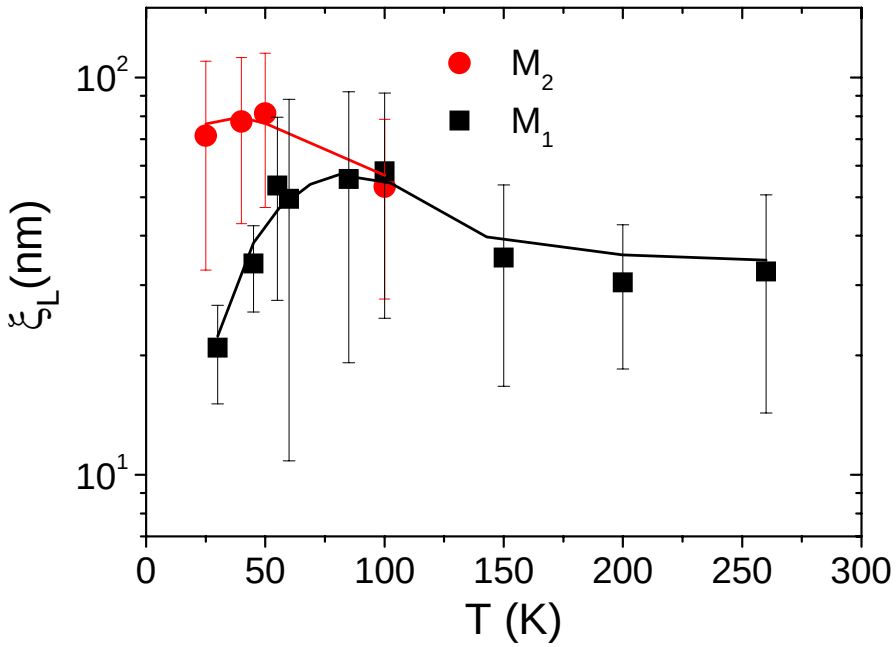

Fig. 5.11.: Localization length as a function of temperature derived from the ES-VRH theory (equations 5), describing the positive tendency of G(E) for M_2 and M_1.

We should now discuss the origin of the low-bias decrease of the differential conductance found for the most resistive sample in the series (M_0) at room temperature, as well as for M_1 for T<100 K. Bötger and Bryksin [45] and Shklovskii and co-workers [46, 47] developed analytical models for the hopping conduction in disordered systems under strong electric fields. Those models predict that in certain conditions an exponential decrease of the hopping conductivity with the electric field occurs, even producing a negative differential conductance in certain cases. Experimentally, this was demonstrated in lightly doped and weakly compensated silicon [48, 49]. Recently, numerical simulations confirm that this behavior of the conductance as a function of the applied voltage is inherent to the hopping transport in this conduction regime [50]. The theory developed predicts an exponential decrease of the conductance with the electric field in the following form:

$$G(E) \approx G(0)\exp\left(\frac{-eEL_0}{2kT}\right) \tag{5.6.a}$$

$$L_0 = \frac{R}{3}\left(\frac{1.74R}{\xi_L}\right)^{0.88} \tag{5.6.b}$$

where $R=N^{-1/3}$ is the mean inter-impurity distance, ξ_L is the localization length, and L_0 is the typical length of the region where the electron gets "trapped". This equation is valid if $eEL_0>>kT$. To understand the essence of the effect, let us think of a cluster composed of impurities, responsible for the hopping conduction. In a hopping process at moderate fields, the electron hops from one site to other, opposite to the electric field. In this process, there exists the possibility that the electron arrives at a "dead-end", i.e. an impurity centre whose neighboring sites are distant enough to make it energetically unfeasible that the electron to continue its way. If this happens, the electron tries to move in the direction of the field to escape from this "trap" to further continue hopping again opposite to E. However, if the conduction occurs under a strong electric field, some of these backward movements are forbidden. Thus, electrons get trapped in such dead–ends, and consequently the current density decreases with E. For a detailed description of the phenomenon see references 45-47 and 50. We associate the decrease in G(V) found in M_0 and M_1 to this effect, in complete agreement with the previous interpretations done for other ranges of resistivities and fields. As observed experimentally in figures 5.6(a) and 5.9, after the drop in G(V) at low bias, a change to positive slopes appears at even higher fields, which is a direct consequence of the high value of the field, which provides enough energy to overcome the traps in the system, resulting in the dependence of VRH with field described by equation 5.6 [49].

We have used the equations (5.6.) to fit the experimental G(E) data of M_0 and M_1. In figure 5.10 (b), the example for M_1 at 45 K is shown, where the fit is done for $0<E<350$ V/cm. For $T>50$ K, the criterion $eEL_0>>kT$ is not fulfilled, resulting in unphysical values for L_0 (≈ 10 μm), and consequently for the localization length (below the nanometer). We therefore centre our study for $T<50$ K, where $L_0\approx$ 100 nm.

If we assume an impurity concentration similar to that which exists in silicon when the exponential decrease in G(V) is observed, N≈ 10^{16} cm^{-3} [47, 49], an estimate of the ξ_L can be made. For low temperatures, $\xi_L \approx 10$ nm. This value approaches the one estimated by the ES-VRH fits for the higher-bias increase of G(E), of around 20 nm. The non-perfect agreement between both values seems logical, since assumptions regarding the dielectric constant and the concentration of impurities are done in both models. Nevertheless, the values are in the same order of magnitude, evidencing the consistency of the analysis performed. If we apply the same procedure for M_0 at room temperature, we obtain $L_0 \approx 200$ nm, resulting in a localization length $\xi_L \approx 6$ nm if an impurity concentration $N = 5 \times 10^{15}$ cm^{-3} is assumed.

5.2. Comparison of NWs created by FEBID and FIBID

The aim of this section is to compare the electrical conduction properties of Pt-C NWs grown by FEBID and by FIBID. The deposits are compared for thicknesses high enough so that FIBID-NWs have metallic conduction (in the range of M_4).

5.2.1. Experimental details

We detail the parameters different from those exposed in section 5.1.2.

5.2.1.1. Deposition parameters

The deposition parameters for FEBID-NWs are: $(CH_3)_3Pt(CpCH_3)$ precursor gas, (T_G) = 45 ºC precursor temperature, (V_{FEB}) = 10 kV beam voltage, (I_{FEB}) = 0.54 nA beam current, substrate temperature = 22 ºC, dwell time = 1 µs, chamber base pressure = 10^{-7} mbar, process pressure = 3×10^{-6} mbar, beam overlap = 0 %, distance between GIS needle and substrate (L_D) = 1.35 mm. For FIBID-NWs, the parameters are the same as in section 5.1.2.1., except for T_G = 45ºC, and L_D=1.35 mm.

5.2.1.2. "In situ" electrical measurements

The procedure is identical to that described in section 5.1.2.2, except that the resistance-versus-time measurements were done in a two-probe configuration, by connecting the conductive microprobes via a feedthrough to a Keithley 2000 multimeter located out of the dual beam chamber, which allows measuring the deposit resistance by two-probe measurements provided that its value is below 120 MΩ. A constant current of value 700 nA was applied. The lead resistance, only about 13 Ω, guarantees no significant influence on the measured resistance of the deposit, which is at least two orders of magnitude larger as will be shown later.

5.2.1.3. High Resolution Transmission-Electron-Microscopy (HRTEM)

The high-resolution TEM (HRTEM) study was carried out using a Jeol 2010F equipment operated at 200 kV (point to point resolution 0.19 nm) on Pt deposits grown on Cu TEM grids with a supporting carbon membrane

5.2.2. Results

5.2.2.1. "In situ" measurements of the resistance as the NWs are grown

In figure 5.12 we compare Pt samples by FEBID and FIBID with similar thickness in order to give evidence for the strong difference in the resistance of the deposits. Three FEBID and FIBID deposits are shown to illustrate the reproducibility of the results. In the case of FEBID (FIBID) deposits, after 6.3 (1.5) minutes, the resistance reaches 120 MΩ and we start the resistance monitorization. After additional deposition time of 14.6 (10.7) minutes, the final resistance is found to be 23.5 MΩ (1 kΩ). Even though the final thickness of all the deposits is roughly the same (~160 nm), measured by conventional cross-section inspection, the resistance is four orders of magnitude lower for FIBID-Pt than for FEBID-Pt. Thus, in the case of Pt by FEBID the resistivity is about 10^7 μΩcm, whereas it is about 800 μΩcm cm in the case of Pt by FIBID, in any case much higher than for bulk Pt, of 10.8 μΩcm. EDX analysis reveals that a higher metallic/carbon content in the case of FIB-deposits is responsible for the important differences in resistivity (In atomic percentage, FEBID-NWs: C(%)=87.81 ± 0.21, Pt(%)=12.19 ± 0.2; FIBID NWs: C(%)=71.80 ± 0.22, Pt(%)=17.40 ± 0.22, Ga(%)=10.80 ± 0.21).

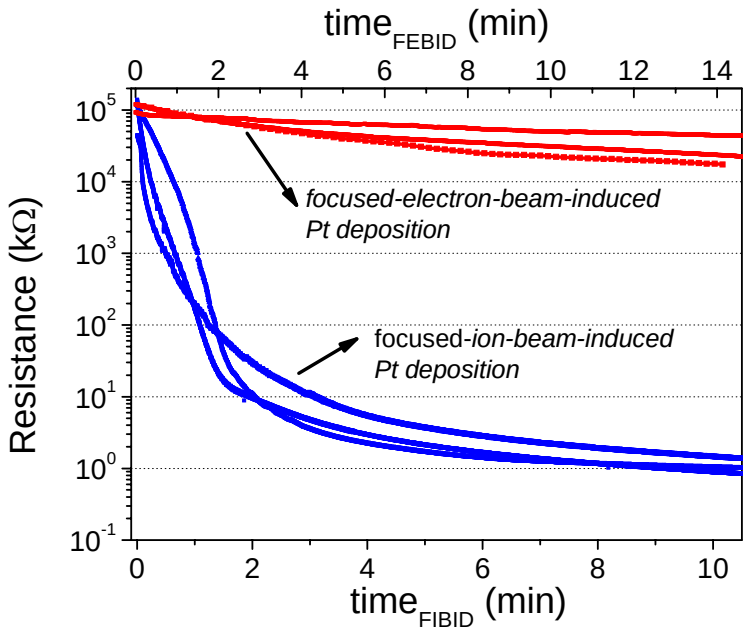

Fig. 5.12. Resistance versus time measurements, comparing several Pt samples grown by FEBID and FIBID. The result gives account of the big differences in the conduction mechanism for both types of deposits, as a consequence of the distinct types of interactions in both cases. For the sake of clarity, zero time is the starting point of the resistance

We must notice that in spite of slightly different parameters for the growth of FIBID-NWs than those selected in section 5.1, the final resistivity is approximately the same. Thus, after the profuse discussion of the previous section, we conclude that the FIBID-Pt NW used for comparison with those deposited by electrons, are in the metallic regime of conduction (samples in the range of M_4).

In figure 5.13., still in-situ, we compare the four-probe current-versus-voltage dependence after finishing the growth of one FEBID and one FIBID Pt deposit of similar thickness to those of figure 5.12. Whereas the FIBID deposit shows the expected linear dependence, the FEBID deposit, with $\rho \approx 10^7$ $\mu\Omega$cm, shows a non-linear dependence. The differences between both types of behavior lie on the different metallic content of the nanodeposits. The linear behavior of the FIBID Pt is the expected response for a metallic or quasi-metallic system. On the other hand, the non-

linear behavior observed in the FEBID Pt deposit can be explained on the basis of the relevant role played by the semiconducting carbonaceous matrix. Interestingly, as the behavior for the conductance of the FEBID-Pt wire decreases up to ≈0.6 V and then starts to increase for higher voltages (see inset in figure 5.13(b)). This dependence is qualitatively the same as the most resistive FIBID-NWs studied in section 5.1. (M_0). The high electric fields produce the trapping of electrons, inducing a decrease in the conductance for low bias [45-47] (see section 5.1.4. for details).

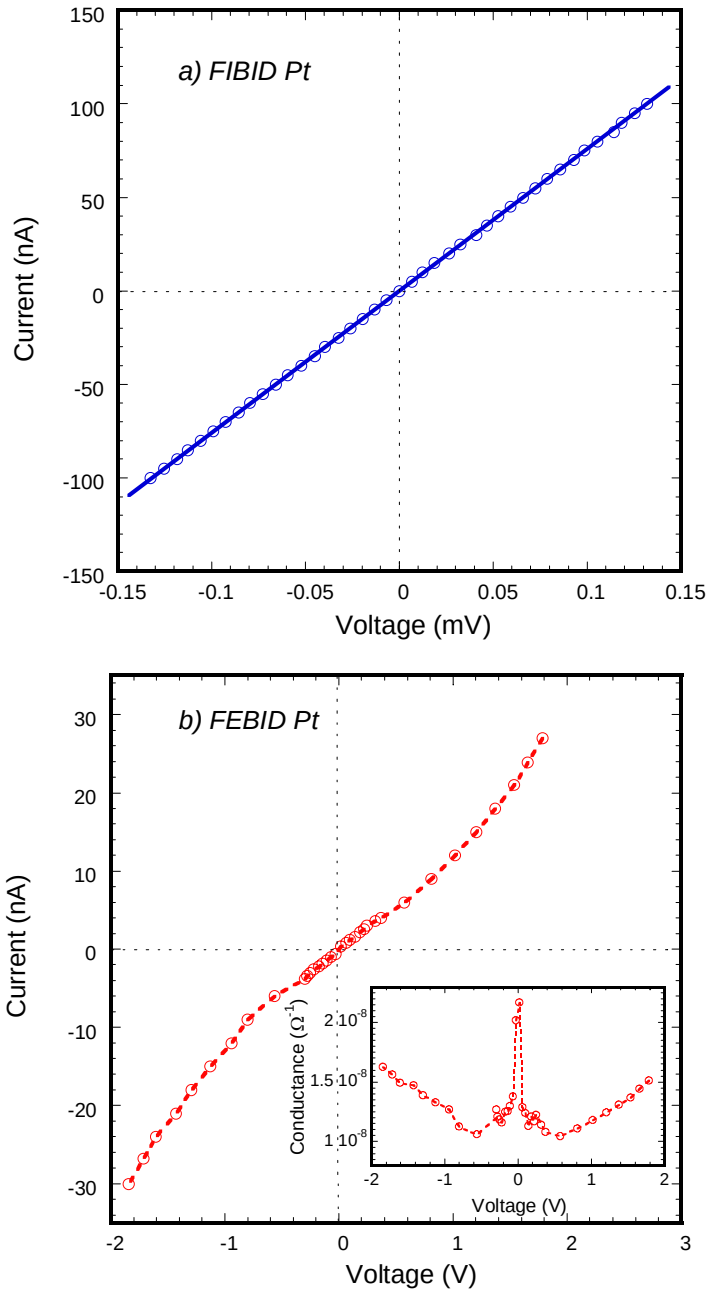

Fig. 5.13. In-situ four-probe current-versus-voltage measurements of FEBID and FIBID Pt deposits with thickness ~160 nm. The measurements in the FIBID Pt nanowire indicate linear dependence between current and applied voltage **(a)** whereas those in the FEBID Pt nanowire indicate non-linear dependence **(b)**. The inset shows the anomalous dependence of conductance versus voltage, understood by the trapping of carriers in sites under strong electric fields

5.2.2.2. Temperature dependence of the electrical properties

In figure 5.14. the dependence of the resistance with temperature for the FEBID deposit is shown (the behavior of the FIBID NW is almost negligible, as M_4 in section 5.1.). R(T) shows a strong semiconductor behavior, and at T=150 K the resistance is of the order of 1 GΩ, the maximum resistance that our experimental setup can measure (a factor of 5.5 compared to 300 K). In the inset of figure 5.14., the representation of ln(G) versus $T^{-1/2}$ indicates that below 200 K the conduction mechanism fits the ES-VRH [4] (equation 5.4., with N=0.5). The same temperature

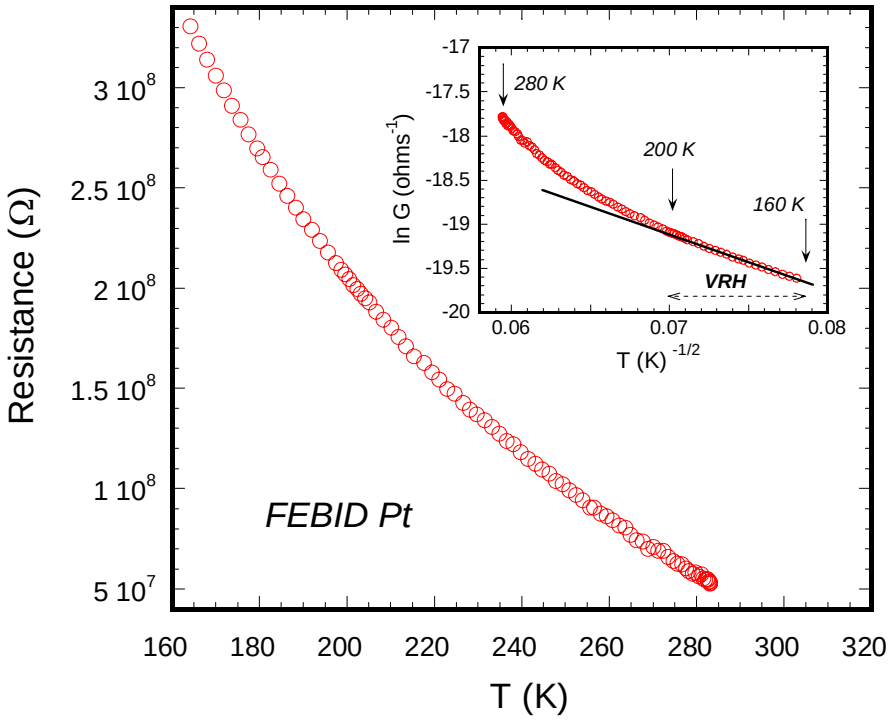

Fig. 5.14. Temperature variation of the resistance of a FEBID Pt nanowire, showing a semiconducting dependence. The inset shows the analysis of data in the form of ln(G) versus $T^{-1/2}$. An ES-VRH is deduced from this fit, for T >200 K

dependence has been previously found in FEBID-Pt deposits by Tsukatani et al. [51]. Above 200 K, the thermal energy is high enough to allow other electronic processes to be involved such as hopping via thermal activation [35], leading to a deviation from the $T^{-1/2}$ law.

As a result of this comparison, and taking into account the conclusions of section 5.1:

(i) The mechanisms for conduction of Pt by FEBID and FIBID for thicknesses roughly higher than 100 nm are different, with a metallic conduction for deposits induced by ions, and by an activation mechanism for those induced by electrons. By changing process parameters such as the beam energy or current, within accessible ranges, we do not find significant differences in the transport results, FEBID-Pt always being several orders of magnitude more resistive than the FIBID one

(ii) It is evident the big similarities between FEBID deposits and highly resistive FIBID deposits, in spite of the different mechanisms for deposition, the presence of Ga ions for FIBID, and the increase of disorder by the interaction of ions. As in the study performed in this thesis, previous reports comparing both materials mainly focus on the differences found between low-ρ-FIBID-Pt and FEBID-Pt [9, 16, 46]. Further work is necessary to study the similarities and differences between both systems in the range of resistivities where the coincident features appear.

5.2.2.3. HRTEM images

For completeness, we include HRTEM images of both deposits [52] that illustrate the reason for the different mechanisms of conduction.

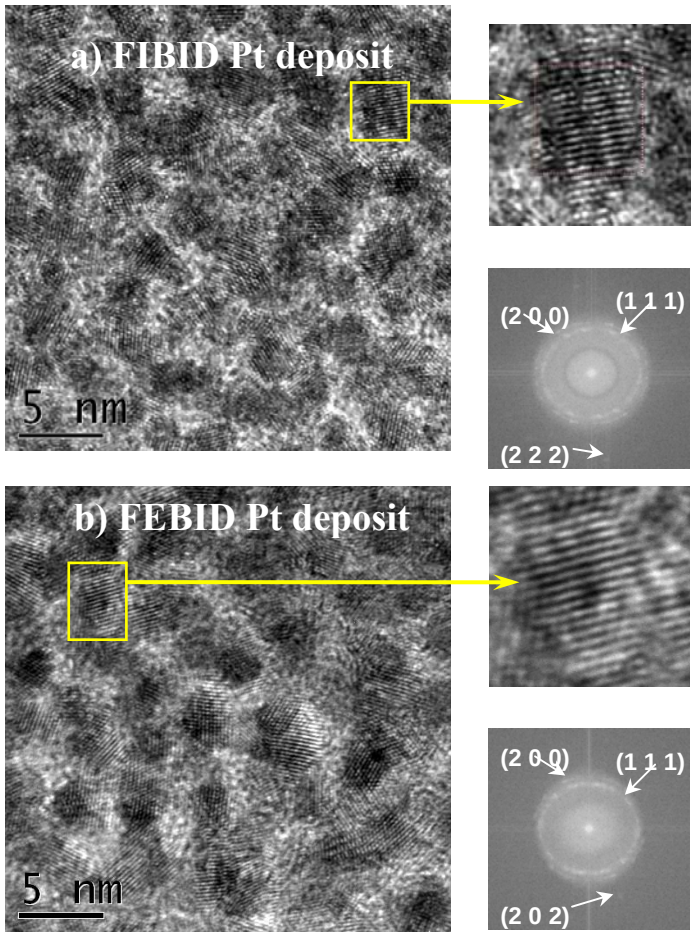

Fig. 5.15. HRTEM images of a Pt nanodeposit by FIBID **(a)** and FEBID **(b)**, in both cases grown at 30 kV beam energy on top of a TEM Cu grid covered with a thin supporting holey carbon membrane. One Pt grain has been selected in each case for magnification and clear observation of the corresponding atomic planes. The Fast-Fourier-Transform of the full image gives diffraction spots that correspond to the (200), (111), (222) and (202) atomic planes of fcc Pt.

As can be observed in figure 5.15., the FEBID and FIBID Pt-C wires consist of ellipsoidal crystalline Pt grains embedded in an amorphous carbonaceous matrix. The crystalline Pt grains are easily identified due to the clear observation of Pt atomic

planes with the expected planar distances. Thus, fast-Fourier transforms of the images give as a result the presence of diffraction spots corresponding to the planar distances of 0.2263 nm, 0.1960 nm, 0.1386 nm, and 0.1132 nm, which correspond respectively to the (111), (200), (202) and (222) atomic planes of fcc Pt, with lattice parameter of 0.3924 nm. An average size of Pt crystallites has been obtained from the measurement of about 50 individual grains in each image through the counting of the number of atomic planes. It is found that no matter the used beam energy and current, in all the FEBID and FIBID deposits the average Pt crystallite size is about 3.2±0.8 nm. Thus, from these HRTEM images, the microstructure of the FEBID and FIBID Pt deposits is similar. The higher percentage of Pt in deposits by FIB brings about the percolation of grains, inducing metallic characteristics in the electrical transport.

5.3. Conclusions

We have performed a detailed study of the transport properties of Pt-C NWs grown by Focused-Ion/Electron-Beam induced deposition. By controlling the resistance as the deposit is done, we can see the different regimes for the resistivity existing in this material.

In the case of FIBID, we have deposited NWs with five different thicknesses, that is, in five different regimes of (over 5 orders of magnitude) conductivity. By studying NW resistivity as a function of temperature, as well as the dependence with voltage on the differential conductivity, we observe a metal-insulator transition in the NWs as a function of thickness (carbon-metal content). This transition is interpreted under the theory of Mott-Anderson for non-metallic disordered materials. As the NW increases in height, a higher concentration of metal is introduced in the semiconducting carbon matrix. This gives rise to the appearance of impurity levels in the band gap, together with the localization of states in the formed band tails. As the growth continues, the introduction of metal clusters finally results in a delocalization of the electron wave-functions, and NWs above 50 nm present metallic conduction.

This work explains the discrepancy existing for previous Pt-C nanostructures created by FIB, where in some cases a metallic character was reported, in contrast to others, where insulating conduction was observed. It also gives a counterpoint to the traditional work when growing metal nanostructures by FIB, since we demonstrate the possibility to deposit materials with different conduction characteristics, making it, in principle, feasible to fabricate insulator or metal nanowires with the same technique and precursor, just by controlling and changing the growth parameters. This is of special relevance because of its potential extrapolation to other materials grown by FIBID and FEBID, since most of the gas precursors used by these techniques use organo-metallic gases, as it is the case here.

The comparison of metallic-FIBID and FEBID wires can be explained by the different composition of both types of deposits, as a consequence of the different mechanism responsible for deposition, with a lower metallic doping for deposits induced by focused electrons. The common features between FEBID-NWs and low

metallic FIBID-NWs are also evidenced by electrical, spectroscopic and imaging measurements.

The discovery of an exponential decrease in the differential conductance behavior in low-metallic doped carbon NWs constitutes an experimental evidence in a nanometric structure of the validity of the theories developed for hopping conduction in strong fields. The existence of this trend in both types of deposits (grown by FEB and FIB) indicates that this conduction process naturally appears in Pt-C NWs grown with focused-beam methods.

Chapter 6

Superconductor W-based nanowires created by FIBID

In this chapter the results obtained for W-based nanowires grown by Focused-Ion-Beam-Induced-Deposition will be shown. This material is superconductor for temperatures below ~5K

The first part of the chapter shows the characterization of the microstructure and chemical composition, by High-Resolution-Transmission-Electron-Microscopy and X-Ray Photoelectron Spectroscopy studies. The second part consists of the study of the electrical measurements of wires, studying if the superconducting properties are preserved for wire width in the nanoscale. Finally, and for completeness, spectacular measurements by Scanning-Tunneling-Spectroscopy will be shown, as a result of collaboration with the group of Prof. Vieira and Dr. Suderow (UAM, Madrid).

6.1. Introduction

6.1.1. Nanoscale superconductors

Since the discovery of the superconductivity in 1911 by Kamerling Onnes [1], superconductor materials (SCs) have been one of the main research subjects in condensed-matter physics over the last 100 years. As a result, lots of important findings have been done, with the Fe-based SCs [2] as maybe the last hottest topic in the field. As important applications of SCs, we could cite, among others, the production of high magnetic field coils, applied in Magnetic Resonance Imaging, or SQUID magnetometers. Nowadays, large effort is being made in the search of better SC properties, by finding new materials, or by the modification of existing ones, as well as their behavior at the nanoscale. Basic studies regarding one-dimensional superconductivity [3], vortex confinement [4, 5], vortex pinning [6], etc. have been tackled recently. The fabrication of nanoSQUIDS is one of the most appealing applications of such nano-superconductors [7, 8] as well as being supporting material for superconducting quantum bits [9, 10]. As in other branches of Nanoscience based on a top-down approximation, complex nanolithography techniques such as electron-beam lithography, involving several process steps, are used to create such superconducting nanostructures.

6.1.2. Previous results in FIBID-W

Sadki *et al* [11] discovered in 2004 that W-based nanodeposits created by 30kV-FIBID, using $W(CO)_6$ as gas precursor, were superconductors, with a critical temperature around 5 K, substantially higher than in metallic crystalline W (T_c = 0.01 K) [12]. This high T_c was associated to the amorphous character of the material, as determined by X-Ray diffraction measurements, as well as by the presence of C and Ga inside the deposits (in atomic percentage, determined by EDX: W/C/Ga =40/40/20%). Values for the critical field (Bc_2=9.5 T) and current density (J_c= 0.15 MA/cm^2) were deduced from electrical measurements in wires of 10 µm (length) × 300 nm (width) × 120 nm (thickness).

A few more results can be found in the literature after this important result. The most relevant references are:

(i) Luxmoore *et al* [13]: analogous W-based deposits by electrons (FEBID) do not present SC transition down to 1.6 K, suggesting the importance of Ga in the SC properties in FIBID-W, by getting implanted and creating amorphization.

(ii) Spodding *et al* [14]: Measurement of resistance during the growth of 500 nm-wide W-C wires, and study of Bc_2 and J_c, with similar results to those of reference 11.

(iii) Li *et al* [15]: It is claimed that T_c can be tuned from 5.0 to 6.2 K by varying the FIB current. This is explained by the modulation of disorder created by ions near the metal-insulator transition, in accordance with the theory developed by Osofsky *et al* [16].

(iv) Kasumov *et al* [17, 18]: An interesting application of these W-nanodeposits is its use as resistance-free leads, for the electrical characterization of contacted single organometallic molecules.

6.2. Experimental details

The FIBID superconducting nanodeposits were fabricated at room temperature in the dual-beam equipment detailed in section 2., which uses a 5-30 kV Ga^+ FIB. The $W(CO)_6$ precursor gas is brought onto the substrate surface by a GIS, where it becomes decomposed by the FIB. Common parameters for this deposition process are: Precursor gas temperature=50 ºC, Vol/dose=8.3 × 10^{-2} μm^3/nC, dwell time=200 ns, beam overlap= 0%, chamber base pressure = 10^{-7} mbar, process pressure = 6 × 10^{-6} mbar, distance between GIS needle and substrate = 150 µm.

6.2.1. HRTEM analysis

The high-resolution transmission electron microscopy (HRTEM) study was carried out using a FEG-TEM Jeol 1010 equipment operated at 200 kV (point to point resolution 0.19 nm) on 20 nm-thick W nanodeposits directly grown on TEM grids for electron transparency in the experiment.

6.2.2. XPS measurements

A 100µm ×100µm ×100 nm sample was deposited on a Si wafer, using V_{BEAM}= 30 kV, I_{BEAM} =5 nA.

The measurements were done in the equipment detailed in chapter 2. A 5kV-argon etching, with current densities of the order of 0.15A/m^2 was done, to obtain a depth profile of the deposits (probing every 20nm). For the quantitative analysis of the XPS spectra, we used pseudo-Voigt peak profiles with a 10 to 20% Lorentzian contribution, subtracting a Shirley -type background.

6.2.3. Electrical measurement in rectangular (micro- and nano-) wires

Rectangular wires were deposited on previously-micropatterned SiO_2//Si, where Al or Ti pads were evaporated after an optical lithography process, to realize contact pads for the magnetotransport measurements (see details of lithography in section 2). The dimensions of the wires are: length=12 µm, variable width and thickness (2 types). The first type consists of microwires (M_i) with width ≈ 2 µm and thickness ≈ 1

μm, and the second type consists of nanowires (N_i) with widths in the range 100-250 nm and thickness of 100-150 nm. The different parameters used are detailed in table 6.I.

The transport measurements (up to 9 T magnetic fields) were done in a PPMS system (Quantum Design).

6.3. HRTEM analysis of FIBID-W

In figure 6.1. the HRTEM images of one selected FIBID-W nanodeposit (under 30 keV) is shown [19]. The microstructure is globally homogeneous at the scale of tens of nanometers. At the scale of about 1 nm, some contrast appears in the images likely due to local differences in the relative amount of the heavier W compared to the lighter C and Ga. No crystalline structure is observed anywhere by direct inspection of the images. This is confirmed by the Fast Fourier Transform (FFT) of the image, shown in the inset, which does not present any diffraction spot or ring. This is in contrast for example to FIBID-Pt, where metallic grains are embedded in an a-C matrix [20], but in good agreement with previous XRD [11] and HRTEM [13] experiments in FIBID-W nanodeposits. From these measurements we can infer the amorphous nature of the FIBID-W nanodeposits.

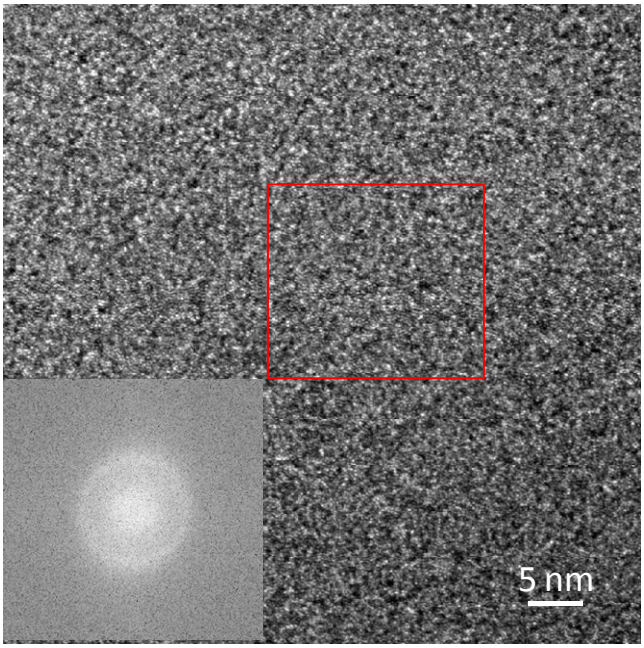

Fig. 6.1. High-resolution transmission electron microscopy image of the W nanodeposit grown under 30 keV Ga-ion beam and FFT of the selected area which indicates the amorphous nature of the deposit.

6.4. XPS study of FIBID-W

X-Ray photoelectron spectroscopy (XPS) measurements were performed to determine the chemical composition and the chemical state of the deposits.

In figure 6.2. the in-depth study (every 20 nm) shows a quite homogeneous deposit. The composition, in atomic percentage, is: W=(39.81±7.63)%, C=(43.23±3.69)%, Ga=(9.48±2.79)%, O=(7.47±1.52)%. Similar results were obtained with standard EDX characterization inside the chamber, and are in perfect agreement with reference 11.

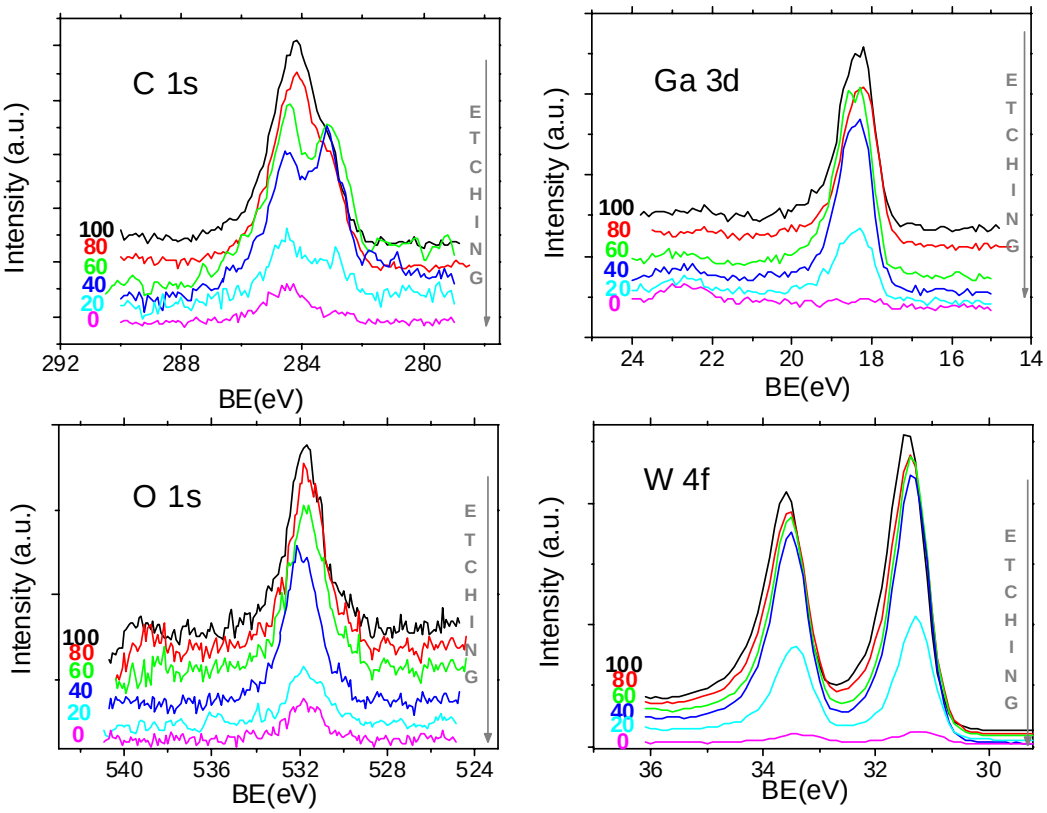

Fig. 6.2. XPS depth profile analysis of a FIBID-W microdeposit. The surface is probed every 20 nm by Ar etching (see vertical arrow on the right of the graphs). The composition is very homogeneous along the thickness, with the deposit composed of C, W, Ga and O. The numbers in every figure refer to the remaining sample thickness in nanometers.

In figure 6.3. typical fits for the W 4f and C 1s spectra are shown.

(i) W 4f: The main peak for the W4f$^{7/2}$ appears at 31.4eV, associated to metallic W [21, 22]. A minor peak at 32.1eV, corresponding to tungsten carbide (WC) [21, 22] is also present. A separation of 2.1eV between the 4f$^{7/2}$ and the 4f$^{5/2}$ components is found in all cases. The ratio between both species through the thickness is W^0/WC=5.17±0.53. In table 6.II. details of the fit are provided.

PEAK	BE (eV)	FWHM (eV)	% Lorentzian	Species
1	31.4	0.68	10	W (4f$^{7/2}$)
2	32.1	1.03	10	WC (4f$^{7/2}$)
3	33.6	0.68	10	W (4f$^{5/2}$)
4	34.3	1.03	10	WC (4f$^{5/2}$)

Table 6.II. W 4f components. The peak numbers appear in figure 6.6. The FWHM of the same species was fixed at the same value (same mean life time). The area between components was constrained to the relationship 4:3, taking into account the degeneracy of each level.

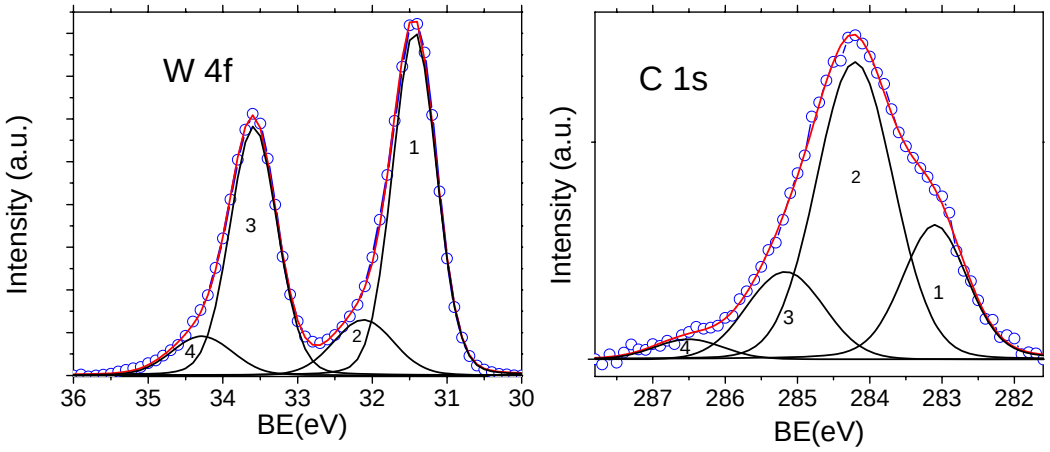

Fig. 6.3. Typical fits for W 4f (left) and C1s (right) spectra along the depth profile. Together with the experimental data (blue dots), the fit is superimposed (red line), result of the convolution of the different components (black lines). The details of the fit are shown in tables 6.II. and 6.III.

C 1s: The spectrum is significantly broad, and can be deconvoluted in three peaks. One at 283.1eV, due to WC [23, 24], and the others at 284.3 and 285.2eV, which correspond to amorphous carbon, sp^2 and sp^3 atoms, respectively [23, 24]. The proportion between both types of carbon (sp^2/sp^3) is found to be 3.45±0.15 through the profile.

PEAK	BE (eV)	FWHM (eV)	% Lorentzian	Species
1	283.1	1.06	20	WC
2	284.2	1.25	20	ac-sp^2
3	285.2	1.25	20	ac-sp^3
4	286.5	1.10	20	C-O

Table 6.III. C 1s components . The peak numbers appear in figure 6.6.

From the XPS analysis performed, we conclude that FIBID-W deposits are formed by metallic W filaments whose surface has bonding to carbon atoms, forming WC.

For completeness, we include in table 6.IV. different types of tungsten and tungsten species, with its superconducting transition temperature associated. We see that only amorphous W, in combination with other elements, presents transition temperatures similar to that for FIBID-W, $T_c \approx 5$ K.

Material	T_c (K)	Reference
Metallic W	0.01	Gibson *et al* [12]
β -W	3.2 - 3.35	Bond *et al* [25]
(Hexagonal) -WC	---	Willens *et al* [26]
(FCC) – WC	10	Willens *et al* [26]
W_2C	2.7	Willens *et al* [26]
Evaporated amorphous W + Re	3.5 - 5	Collver *et al* [27]
Sputtered amorphous W + Si, Ge (20-40%)	4.5 - 5	Kondo *et al* [28]
CVD amorphous W + C (40%)	4	Miki et al [29]
FIBID-W	**4.1-6**	[11, 13-15, 30, 31]

Table 6.IV. Different W and W- species found in nature, together with its SC transition temperature.

6.5. Superconducting electrical properties of micro- and nanowires

The aim of these experiments is first to characterize "bulk-type" W deposits in the micrometer range in order to investigate if narrow wires in the nanometer range still keep the same performance as the bulk ones. The best resolution obtained corresponds to width ~ 100 nm, determined by SEM inspection (see figure 6.4.).

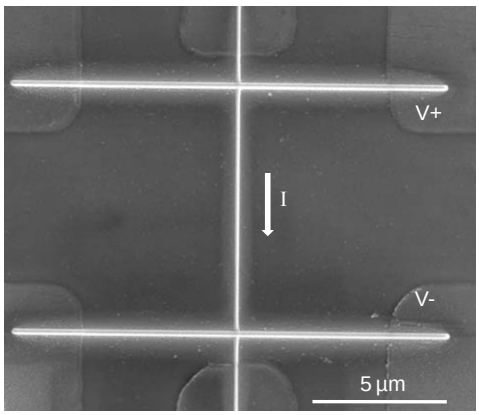

Fig. 6.4. SEM image of one deposited NW, (vertical line). The additional two horizontal lines are done to perform 4 wire electrical measurements.

In Table 6.V., some relevant data of the wires studied in the present work are summarized. Four microwires (μWs: M_1-M_4) and four nanowires (NWs: N_1-N_4) have been investigated.

Sample	V_{BEAM} (kV)	I_{BEAM} (nA)	Width (μm)	Section area (μm^2)	T_C (K)	ρ_{300K} (μΩcm)
M_1	5	1	2	1.97	5.3	163
M_2	10	1.1	2	1.62	5.4	147
M_3	20	0.76	2	2.10	4.7	209
M_4	30	1	2	1.64	4.9	229
N_1	30	0.01	0.24	0.036	5.1	309
N_2	30	0.01	0.17	0.017	5.0	295
N_3	30	0.01	0.11	0.016	4.8	533
N_4	30	0.01	0.15	0.015	4.8	633

Table 6.V. Data of the growth conditions (V_{BEAM}, I_{BEAM}), dimensions (width, section area), and physical properties (T_C and room-temperature resistivity) of all the wires investigated.

6.5.1. Critical temperature of wires

In figure 6.5(a), the temperature dependence of the resistivity of the M_3 microwire (grown at 20 kV/0.76 nA) is shown. It is found that T_C= 5.4 K, where the critical temperature is defined at 90% of the transition (ρ/ρ_n=0.9). From the measurements of the resistivity under several magnetic fields, the critical field, B_{C2}, has been estimated and shown in figure 6.5(b), being of the order of a few Tesla, with a typical temperature dependence. These results coincide perfectly with those by Sadki *et al* [11]. For all the microwires (grown at different conditions as shown in Table 6.V), the measured T_C ranges between 4.8 K and 5.4 K and seems to correlate with the room-temperature resistivity as proposed by Li *et al*. [15].

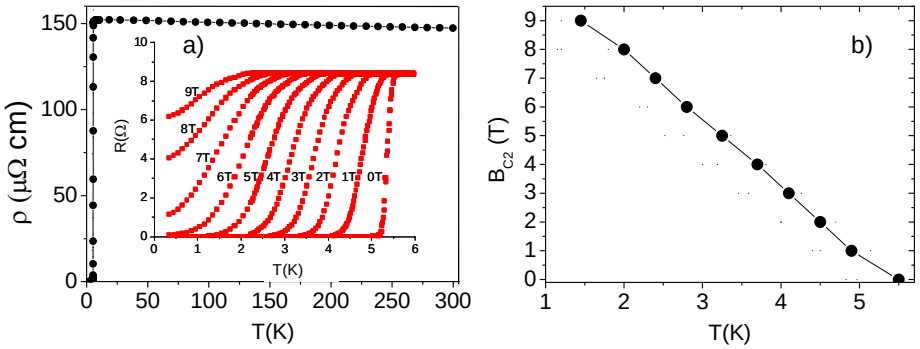

Fig. 6.5. For the M_3 microwire, **a)** Resistivity as a function of temperature. The inset shows measurements of the resistivity under various applied magnetic fields **b)** The critical field, H_{C2}, as a function of temperature.

In figure 6.6., the resistance-versus-temperature behaviour of one of the nanowires (N_2) is shown. The nanowire resistance starts to decrease at 5.2 K and becomes null at 4.8 K. The transition temperature (≈5 K) and transition width (≈0.4 K) are similar to those of microwires, indicating good sample stoichiometry and homogeneity. It is remarkable that a high T_C is maintained in the nanowires, which opens the route for the use of this superconducting material in nanodevices working at temperatures above liquid Helium.

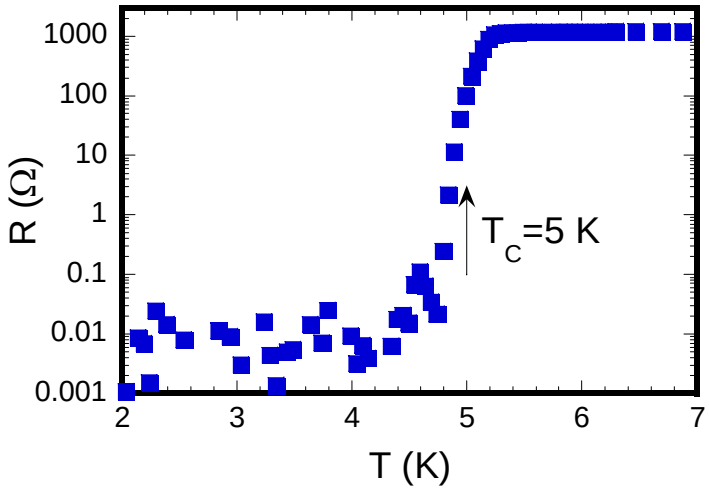

Fig. 6.6. Resistance (in log scale) versus temperature of N_2 (width=170 nm), indicating T_C=5±0.2 K.

The values of T_C and room temperature resistivity for all the wires (micro and nano) is indicated in figure 6.7. It is generally observed that the NWs show slightly higher resistivity than the μWs, but without evident influence on the T_C value. More work is needed to understand the correlation between the room-temperature resistivity and T_C.

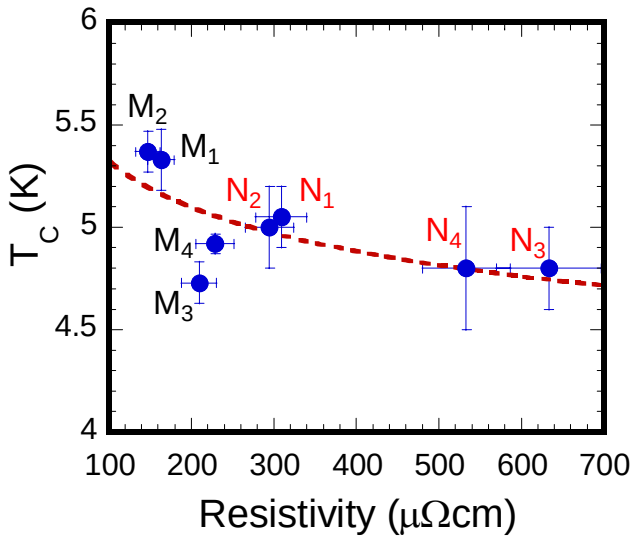

Fig. 6.7. T_C versus resistivity of all the microwires (M_1, M_2, M_3, M_4) and nanowires (N_1, N_2, N_3, N_4) studied in the present work. Whereas the nanowires show higher resistivity, T_C ranges in all cases between 4.7 and 5.4 K, with a slight tendency to decrease as a function of the resistivity.

6.5.2. Critical field of the nanowires

The resistance in the NWs has been studied at fixed temperature as a function of the applied magnetic field with the aim of determining the range of magnetic fields where the NWs can be used for superconducting applications. As an example of the obtained results, we focus on the behavior of the N_2 sample at T=2 K, represented in figure 6.8(a)). The resistance is null below H~2 T and increases continuously up to reaching the normal-state resistance. The value of B_{C2} is found to be ~8 T, which is the same as found in the μWs, as shown in figure 6.5(b) All the studied NWs show similar behavior to this, as can be observed in figure 6.8(b), where NWs N_1 to N_3 are compared normalizing the resistance to the normal-state value. These results demonstrate the good translation of the superconducting properties of FIBID-W deposits to the nanometric scale. A number of interesting features appearing in figure 3 will be discussed and systematically analyzed in the future. Here, we just highlight the onset of finite resistance at relatively low magnetic field, the non-linear resistance before reaching the normal-state resistance, and the dependence with the nanowire thickness of the starting magnetic field with non-zero resistance.

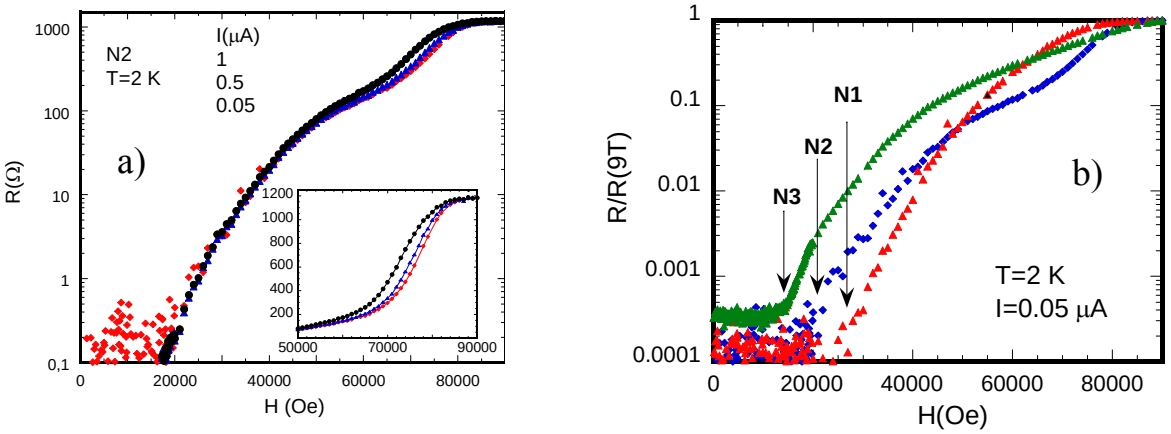

Fig. 6.8. (a) Resistance (in log scale) versus applied magnetic field at T=2 K of N_2. Three different currents have been used (1, 0.5, 0.05 μA, shown with symbols in black, blue and red color respectively) and the inset shows in linear scale the different behavior produced by the increasing current. (**b)** At T=2 K, resistance normalized to the value at H=9 T as a function of the magnetic field in nanowires N_1, N_2, and N_3 using 0.05 μA current in all cases.

6.5.3. *Critical current of the nanowires*

Another important issue to be studied in these NWs, having in mind certain applications, is the value and dependence of the critical current. The results obtained on the N_2 sample are shown in figure 6.9(a) to illustrate the found dependence. At T=2 K, the critical current in this nanowire is of the order of 20 μA, decreasing for higher temperatures. Focused studies would be required to investigate if these nanodeposits show the "peak effect" of the critical current observed in other superconductors [32, 33]. In figure 6.9(b) we represent the resistance at T=2 K normalized to the normal state as a function of the current density in several nanowires. At that temperature, the value of critical current density ranges between 0.6 MA/cm^2 and 0.9 MA/cm^2. One could think that the dispersion in the measured values are to be ascribed to slight differences in composition, the amount of defects, error in the determination of the sectional area, etc. On top of that, these results suggest that the critical current density decreases as the nanowire width decreases (from 240 nm for N_1 down to 170 nm for N_2 and 110 nm for N_3). This point should be addressed in more detail in future.

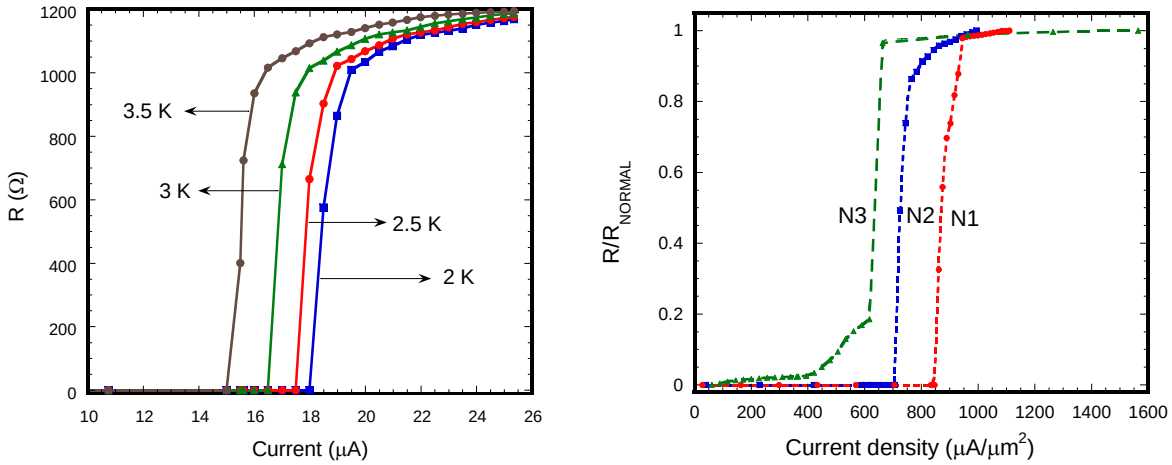

Fig. 6.9. (a) For N_2 sample, resistance versus applied current at different temperatures. As expected, the critical current decreases as T_C is approached. **(b)** For several nanowires, dependence of the resistance (normalized to the value in the normal state) with the injected current density at T=2 K.

6.6. Study of FIBID-W by Scanning-Tunneling-Spectroscopy

In this section we will show a brief summary of the results obtained as a consequence of the collaboration established between our group and Professor Sebastián Vieira, Dr. Hermann Suderow and Lic. Isabel Guillamón, at the Universidad Autónoma de Madrid [34]. The publications resulted from this collaboration are refs. 30, 35, and 36.

A FIBID-W micrometric sample (30 μm × 30 μm), deposited on a Au-Pd substrate, was studied by Scanning-Tunneling- Microscopy (STM) and Spectroscopy (STS). STS allows spectroscopy studies with a spatial resolution down to the atomic scale [37], allowing a direct mapping of the vortex lattice [38].

The first outstanding result was that tunneling experiments could be done in a FIBID-W sample that had been exposed to ambient conditions for one day (normally extremely clean surfaces are necessary for this kind of experiments), presenting a very homogeneous surface. By a detailed set of measurements, they found that the density of states of this superconductor could be perfectly fitted to the Bardeen–Cooper–Schrieffer (BCS) theory for superconductors (see figure 6.10.).

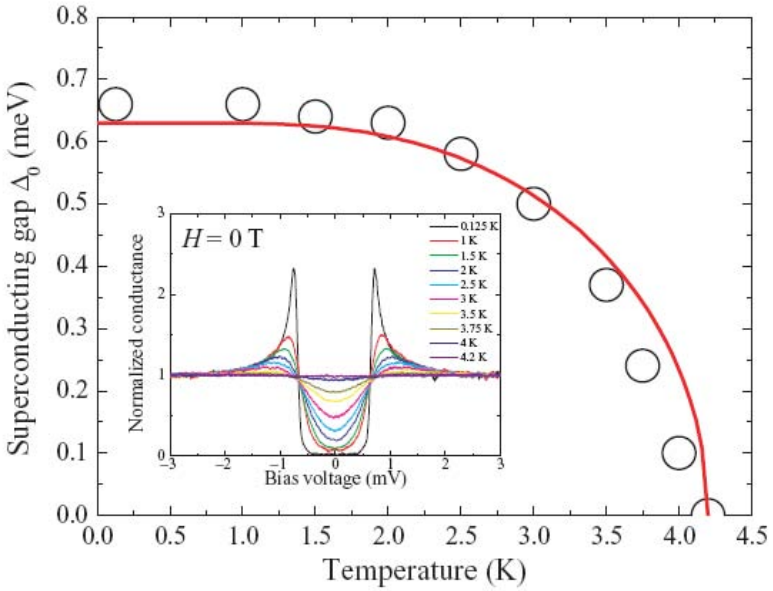

Fig. 6.10. Temperature dependence of the superconducting gap obtained from fits to the tunneling spectra shown in the inset. Red line is the BCS expression, taking $\Delta_0 = 1.76 k_B Tc$ and $T_c = 4.15$ K.

Up to the experiments performed in this material, atomic level STM/S experiment over large surfaces in a superconductor was still lacking. This work shows that the amorphous FIBID-W system is the first reference s-wave BCS this system, "the long sought paradigm for STM/S studies" [30].

Furthermore, under an applied magnetic field, a well defined Abrikosov lattice was observed, being systematically studied as a function of temperature and field, by STS. In figure 6.11. an example of the vortex lattice is shown, with the vortices appearing bunched close to some linear surface depressions observed in the topography. By direct STS imaging, it was possible to observe the melting of the 2D-lattice into an isotropic liquid [36].

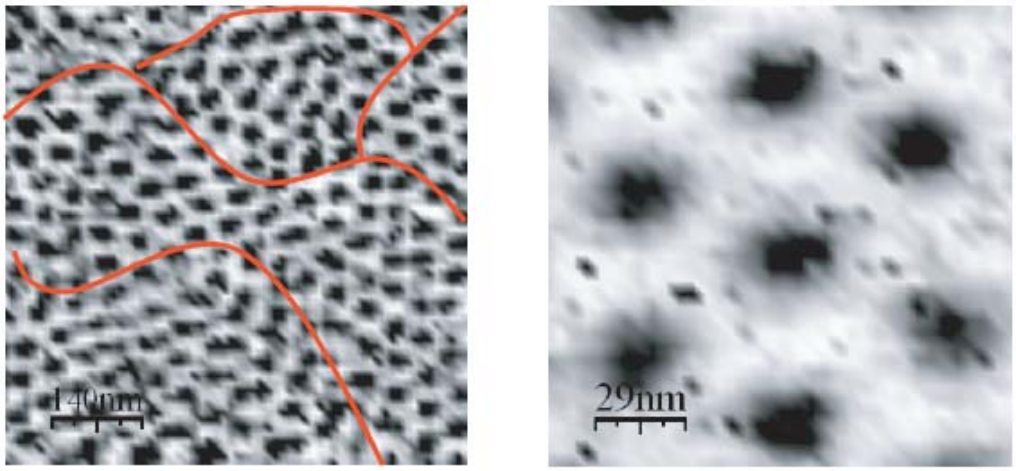

Fig. 6.11. Vortices lattice at 1 T, obtained from STS images constructed from the Fermi level conductance (shown as raw images, without any filtering or smoothing effects). Left panel shows a large STS image, and right panel shows a single hexagon. Small linear surface depressions found in the topographic images are marked as red lines. The STS images of the right panels are made far from surface depressions, and the corresponding topographic STM images are absolutely flat and featureless, with surface roughness below about 0.5 nm.

6.7. Conclusions and perspectives

The FIBID-W nanodeposits were characterized by HRTEM. The amorphous character of this material explains the high T_c.

XPS measurements show an homogeneous composition, formed by metallic W filaments, with its surface bonded to carbon atoms, forming WC.

From the electrical measurements in microwires and nanowires, we conclude that superconducting properties are retained by the narrowest wires, opening applications at the nanoscale. In particular, the values found for T_C, for the critical field H_{C2}, and for the critical current make these narrow wires promising for nanometric superconducting-based and hybrid devices.

Finally, the STS study done by the group of Prof. Sebastián Viera, shows outstanding properties for this material. The FIBID-W nanodeposit is the first fully isotropic s-wave superconductor that can be studied in detail down to atomic level, allowing the direct observation of the melting of the 2D-vortex lattice.

From these conclusions, it can be anticipated that FIBID-W could be feasibly used to build superconducting electronic devices, due to its unique characteristics and the controllable and flexible growth at the nanometric scale. For example, mesoscopic superconductors have been proposed to be used as logic elements in quantum computing by manipulation of a controllable vortex lattice [9, 10]. Application of these nanodeposits in the fabrication of micro/nano-SQUIDs [7, 8] at targeted places for high-resolution magnetometry at the nanoscale is straightforward and the first steps in that direction are being given. Fabrication of resistance-free nanocontacts for dedicated transport experiments can be also a major application of these FIBID-W nanodeposits [17]. A long-standing problem in the electrical characterization of nanodevices is the high contact resistance of wires required to make the connection to the macroscopic world and this problem can be solved by means of superconducting wires. Moreover, fabrication of hybrid metallic-superconductor nanocontacts using these superconducting W nanodeposits seems also feasible thanks to the

characteristics of FIBID W deposition. Such nanocontacts would enable the study of interesting phenomena like Andreev reflection [18] and measurements of the spin polarization of ferromagnets [39].

Chapter 7

Magnetic Cobalt nanostructures created by FEBID

This chapter includes the characterization of cobalt nanostructures created by Focused-Electron-Beam-Induced-Deposition (FEBID). Microstructural and spectroscopic measurements show that the deposits are extremely pure (>90 %), when relatively high beam currents are used, in sharp contrast with usual concentrations obtained using this technique (below 50%), which is ascribed to a heating effect. A wide range of magnetotransport measurements have been performed, evidencing the high Co percentage in these deposits. By using spatially-resolved Magneto-Optical-Kerr magnetometry, the reversal of the magnetization has been systematically studied in single wires and nanostructures with different aspect ratios. Besides, nanowires exhibiting good domain wall conduit behavior (propagation field much lower than nucleation field) have been created.

7.1. Previous results for local deposition of magnetic materials using focused beams

The capability of locally growing magnetic devices with high resolution is a longed-for result, since its realization would have a high impact in fields such as magnetic storage, or magnetic sensing, among others.

The possibility to create magnetic nanometric-sized structures using a focused technique (FIBID or FEBID) seems thus very attractive for this purpose, since these techniques posses a high flexibility and resolution, having a perfect compatibility with other lithography techniques. These are obvious advantages with respect to multi-step processes involving growth and subsequent patterning. However, these techniques have not been for the moment exploited as much as, for example, EBL or direct patterning by FIB for the growth of functional nanometric elements. The main reason for it is the low purity of the deposits (rarely exceeding the 50% atomic), as a consequence of the absence of the complete low dissociation rate of the gas precursor molecules, especially for FEBID [1, 2]. Organic precursors are usually employed, resulting in a big amount of carbon mixed with the metallic element. Thus, properties deviate radically from those ones desired [3]. Post-purification procedures have been reported to improve the metallic content [4, 5].

Some results can be found in literature concerning the deposition of magnetic nanostructures by these techniques. For iron, several gas precursors have been used: $Fe(CO)_5$ [6-8] , $Fe_3(CO)_{12}$ and $Fe_2(CO)_9$ (ref. 9). For cobalt, the same gas precursor is mainly used: $Co_2(CO)_8$ [10-15] (except reference 10, all the works cited were done with FEBID technique).

Due to the big fraction of carbon normally present in the deposits, it is crucial to explore the functionality of these nanomaterials, by means of a thorough magnetic characterization. Before this thesis, studies of the magnetism of single nanodeposits had been carried out, either in an indirect way, by electrical magnetotransport measurements [12, 15], or by local probes, such as Magnetic Force Microscopy [11, 13, 15] or electron holography [6-8].

7.2. Experimental details

The FEBID magnetic nanodeposits were fabricated at room temperature in the dual-beam equipment detailed in section 2., which uses a 5-30 kV FEG-Column. The $Co_2(CO)_8$ precursor gas is brought onto the substrate surface by a GIS, where it becomes decomposed by the FEB. Common parameters for this deposition process are: Precursor gas temperature=Room Temperature, Vol/dose=5×10^{-4} μm^3/nC, dwell time=1 μs, beam overlap= 50%, base chamber pressure = 10^{-7} mbar, process pressure = 3×10^{-6} mbar, vertical (horizontal) distance between GIS needle and substrate = 135 (50) μm.

7.2.1. Compositional analysis by EDX

Energy Dispersive X-Ray (EDX) measurements we performed in the setup detailed in section 2.1.2., for deposits created with beam energy and current in the ranges of 5-30 kV and 0.13-9.5 nA, respectively. The selected electron beam energy for the microanalysis is 20kV.

7.2.2. HRTEM

The high-resolution transmission electron microscopy (HRTEM) study was carried out using a FEG-TEM Jeol 1010 equipment operated at 200 kV (point to point resolution 0.19 nm) on 50 nm-thick Co nanodeposits directly grown on TEM grids for electron transparency in the experiment.

7.2.3. Electrical measurements of wires

Rectangular wires were deposited on previously-micropatterned SiO_2//Si, where Al or Ti pads were evaporated after an optical lithography process, to realize contact pads for the magnetotransport measurements (see details of lithography in section 2).

These measurements were done in two different equipments, depending on the

geometry of the applied magnetic field with respect to the thin film plane. For fields perpendicular to the thin film plane, a commercial PPMS from Quantum Design was used, with fields up to 9 T and in a temperature range 2 K<T<300 K. In this setup, perpendicular magnetoresistance and Hall effect were measured. For fields in the plane, the measurements were done in the CCR explained in section 2. In this case, different geometries between the current and the magnetic field were established.

7.2.4. Spatially-resolved MOKE measurements

The MOKE measurements were performed at the Imperial College (London), in the group of Professor Russell Cowburn. This setup (details in section 2.4.) measures the longitudinal–Kerr effect, with a laser probe of ~ 5μm, allowing to measure hysteresis loops measurements of single nano-objects, with for instance, sensitivities of around 10^{-12} emu in the case of permalloy [16].

7.3. Compositional (EDX) and microstructural (HRTEM) characterization

We have performed in-situ EDX microanalysis of several Co nanodeposits grown under different combinations of electron-beam energy and current, in order to study any correlation between the growth conditions and the nanodeposit composition. A summary of the results is displayed in Table 7.I. The set of results clearly demonstrates that the main parameter governing the nanodeposit content is the beam current. For beam currents above ~2 nA, the Co content in atomic percentage is around 90% or more, whereas for lower currents the Co content is typically around 80% or less. The rest of constituents of the nanodeposits are C and O.

E_{BEAM} (keV)	I_{BEAM} (nA)	% C (atomic)	% O (atomic)	% Co (atomic)
5	0.4	15.10 ± 0.33	2.00 ± 0.17	82.89 ± 0.51
	1.6	13.07 ± 1.74	3.66 ± 0.72	83.27 ± 1.02
	6.3	7.22 ± 1.00	1.43 ± 0.40	91.36 ± 0.64
10	0.13	8.90 ± 0.20	10.25 ± 0.20	80.87 ± 0.20
	0.54	5.34 ± 1.09	2.72 ± 0.69	91.94 ± 1.77
	2.1	3.87 ± 0.92	1.35 ± 0.65	94.78 ± 1.55
	8.4	5.21 ± 0.10	1.17 ± 0.23	93.62 ± 0.27
18	9.2	9.26 ± 0.63	2.40 ± 0.27	88.34 ± 0.66
30	0.15	19.23 ± 0.50	19.30 ± 0.20	61.50 ± 0.50
	9.5	3.22 ± 0.21	0.21 ± 0.12	96.57 ± 0.40

Table 7.I. EDX results of FEBID-Co nanodeposits grown under different conditions.

As an example, in figure 7.1., the Co, C, and O content is represented as a function of the beam current in deposits performed at 10 kV beam energy. The Co content increases monotonously from about 80% for a beam current of 0.13 nA to about 95% for beam currents above 2 nA.

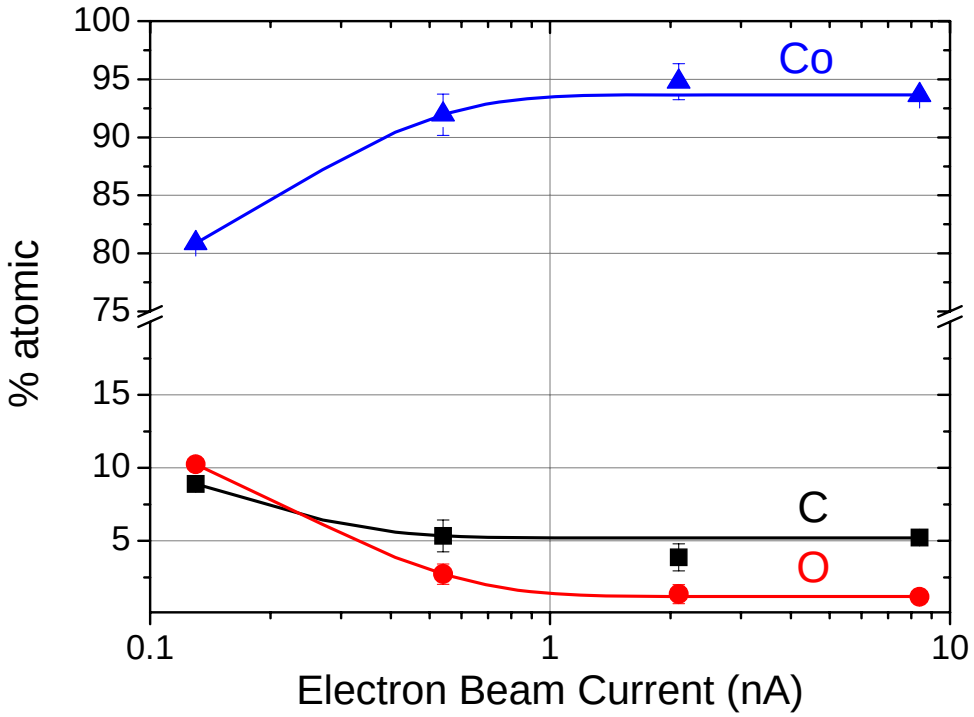

Fig. 7.1. Atomic percentage of Co (blue triangles), C (black squares), and O (red dots) as a function of the electron-beam current in nanodeposits grown with the FEBID technique at beam energy of 10 kV using $Co_2(CO)_8$ as the precursor gas. Details are given in the text. Lines are guides to the eye.

As far as we know, Co percentages above 90% have not been reported so far [11-15]. A previous study by Utke *et al* also found an increase in the Co content as a function of the beam current, as it is our case [14]. They reported a maximum Co concentration around 80%, but currents above 80 nA were necessary for this high concentration. For currents in the range of our study, Co percentages were always found to be below 60% (we must notice in this point that the beam current is a crucial parameter in the electron beam resolution). It has been argued that beam-induced heating is the main effect responsible for the increase of metallic content with current [1, 14]. The precursor gas molecule, $Co_2(CO)_8$, can be thermally decomposed at relatively low temperature, 60ºC [23]. As a consequence, the use of high current will favour local heating, enhancing the precursor molecule dissociation and the high Co

content. It should be pointed out that our electron beam source is a field-emission gun, which will likely produce smaller beam spots on the substrate than in the case of thermionic-tungsten-filament sources, employed for example in reference 14. Thus, the electron beam current will be focused on a smaller area, producing larger local heating effects. We put forward that this is the reason for the higher Co content in our nanodeposits compared to previous studies. Recent results in our group by R. Córdoba (unpublished) using a micro-heater during deposition confirm this hypothesis.

HRTEM measurements [17] indicate a high purity in the deposits. In figure 7.2. the microstructure of one deposit, grown at 5 kV/98 pA, is shown. FEBID-Co is formed by small cobalt crystalline grains, of size ~ 2-5 nm. The grains are randomly oriented, with HCP and FCC structures, as electron-diffraction patterns indicate.

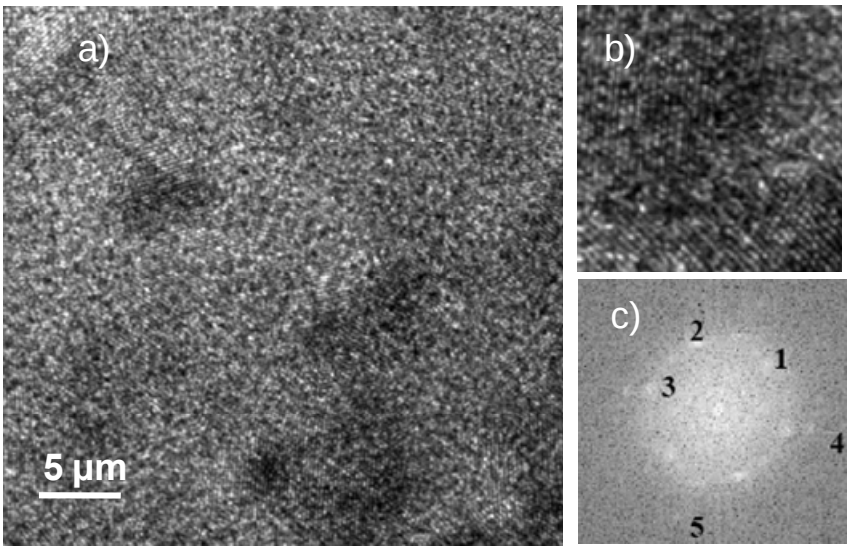

Fig. 7.2. (a) HRTEM images of one FEBID-Co deposit grown on a TEM grid, under 5 kV and 98 pA conditions. **(b)** Detail of the image, where crystallographic planes are well observed. **(c)** FFT of image (b), where crystallographic planes [1: (10-10) hcp, 2: (111) fcc, 3: (101) fcc, (10-12) hcp, (11-20 hcp)] are observed.

7.4. Magnetotransport measurements of FEBID-Co nanowires

In this section, we will demonstrate that a high content of Co is required to obtain high-quality magnetotransport properties. For this study, the Co-based deposits were designed to bridge a 12 μm gap (horizontal line in figure 7.3.). Typical dimensions for the deposits are length= 9 μm × width= 500 nm × thickness= 200 nm. Additional transversal deposits were designed to determine, by conventional 4-probe measurements, the longitudinal and transversal components of the resistivity tensor.

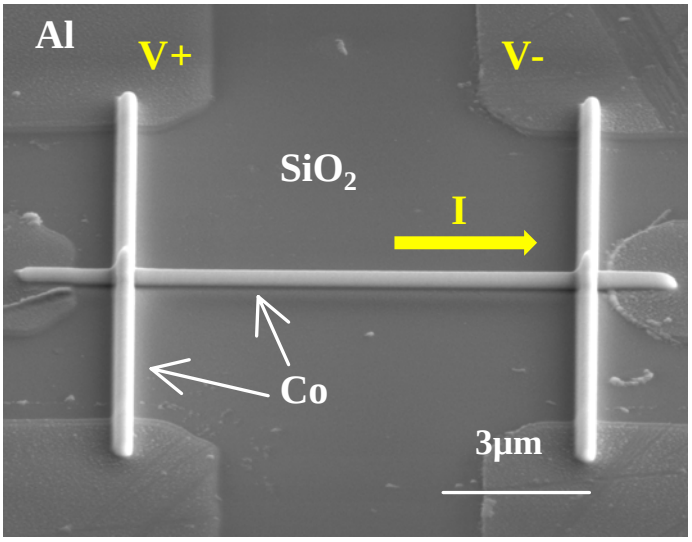

Fig. 7.3. SEM image of one of the created devices. The current flows through the horizontal deposit, whereas transversal deposits are performed for four-probe measurements. Deposits are done on top of a SiO_2 substrate in which Al pads were previously patterned by conventional optical lithography techniques.

The relevance of the surface oxidation of these cobalt nanowires for the magnetotransport properties has been evaluated by preparing some samples with a 5-10 nm FEBID Pt capping layer. This small FEBID-Pt thickness together with its high resistivity [18], guarantees a high resistance in parallel with the Co lines, assuring no perturbation in the Co conduction, as it was subsequently checked. After several days in air, no changes were found in the resistance of any nanowire (either if they were covered or not). We expect that only the usual passivation layer (~1-2 nm) at the

topmost surface will be present in the non-covered nanowires, without any significant influence on the obtained results. This is not the general case in other deposits created by focused beams [18].

7.4.1. Magnetotransport properties of cobalt NWs grown at high currents

As an example, we will show hereafter the results obtained on a NW grown with a beam energy of 10 kV and a beam current of 2.1 nA, thus having a high Co content (around 95%). A wide range of magnetic field-dependent transport measurements has been performed.

In figure 7.4. we can see a typical resistivity-versus-temperature measurement for this nanowire. The behaviour is not, as it is the general rule in FEBID deposits, semiconducting-like [18], but fully metallic, confirming that the residual amount of carbon in the sample is minimal. The resistivity at room temperature is of the order of 40 μΩcm, only a factor of 7 larger than in bulk polycrystalline cobalt. As will be discussed later, this value of resistivity is just related to the small grain size of the FEBID deposit. Another nanowire grown at 10 kV and 0.54 beam current, with Co content around 92%, also displays similar resistivity value. These FEBID-Co deposits are the most conductive ones found in literature. The Residual Resistivity Ratio ($RRR=\rho_{300K}/\rho_{2K}$) is about 1.3, in agreement with results for polycrystalline cobalt thin films [19].

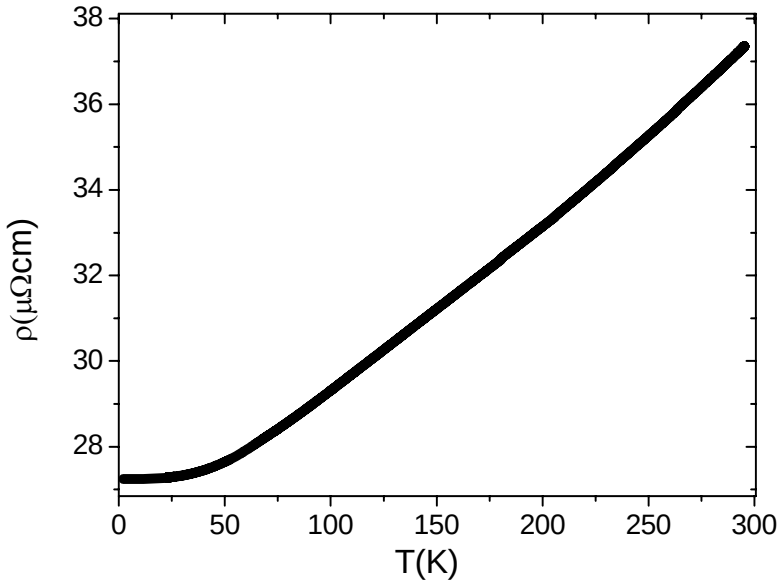

Fig. 7.4. Resistivity of a Co nanowire grown at 10 kV beam energy and high current, 2 nA, as a function of temperature. Fully metallic behaviour is observed.

In figure 7.5. we show the Hall effect resistivity:

$$\rho_H = \frac{V_H t}{I} \qquad (7.1.)$$

for the NW as a function of field for the maximum and minimum temperature measured. ρ_H increases at low fields until reaching magnetic saturation. For higher fields, only the ordinary part variation (ρ_{OH}) is observed, with contrary sign to the anomalous one (ρ_{AH}). This behaviour has also been observed in magnetron sputtered polycrystalline cobalt films [19]. The ordinary part is obtained by the standard method of fitting the slope at high fields, whereas the anomalous one is determined by extrapolating to H=0 the fit of ρ_{OH} (see figure 7.5.). From the different isotherms, we find that the relationship $\rho_{AH} \propto \rho^2$ holds in all cases, revealing an intrinsic origin of the Anomalous Hall effect, as it is expected in this conductivity regime [20, 21]. From the intersection of the linear regions of the ordinary and the anomalous Hall effect [22] (1.42 T at 300 K) and taking into account the demagnetizing factor for the created geometry, we find a saturation magnetization M_s=1329±20 emu/cm^3, corresponding to a 97% of the bulk Co value. We would like to remark that such high magnetization

has never been reported before for Co nanodeposits created by FEBID.

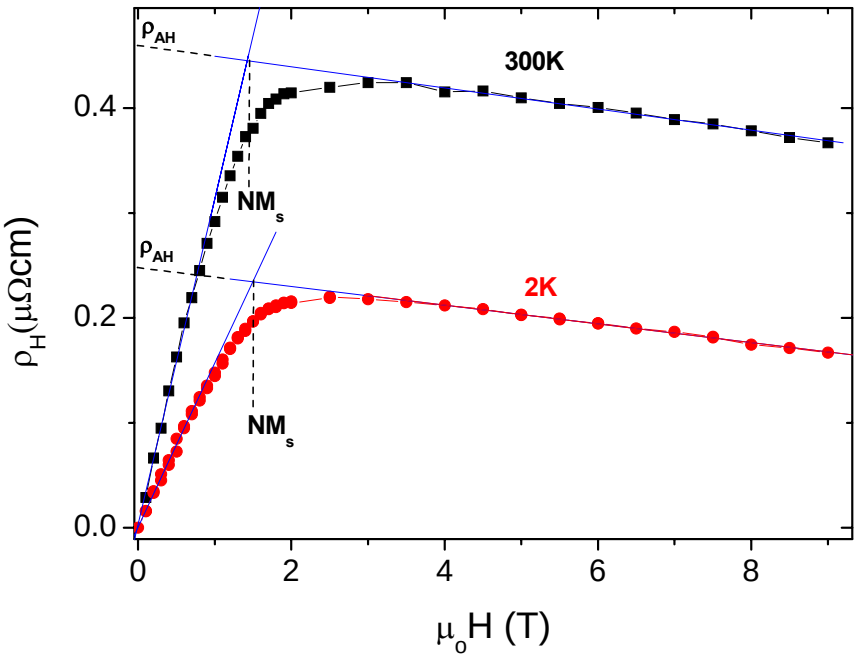

Fig. 7.5. Hall resistivity at 300 K and 2 K in the same Co nanowire shown in figure 2. The magnetic character is manifested by the presence of the anomalous Hall effect. The ordinary part is determined by the slope at high H, whereas the anomalous constant is calculated by extrapolating this slope at zero field. From the intersection of the linear regions of the ordinary and the anomalous Hall effect the value of NM_S (N=demagnetising factor, M_S=saturation magnetization) is obtained, which allows the determination of M_s (see text for details).

From the ordinary part at 2 K, the density of electrons is calculated to be $n_e=7\times10^{-28}m^{-3}$. Using this value and the experimental value of the resistivity at low temperature, $\rho(0)\approx27$ μΩcm, one can estimate the mean-free-path as in reference [22]:

$$l(0)=\frac{\hbar k_F}{n_e e^2 \rho(0)}\approx 4nm \qquad (7.2.)$$

This value is of the order of the grain size determined by high-resolution-transmission-

electron microscopy-images (see section 7.3.), suggesting that the scattering is mainly produced at the grain boundaries between crystalline grains.

In figure 7.6., MR measurements at 300 K are shown with three different geometries (see figure 3.9.): H perpendicular to the thin film plane (perpendicular geometry: PG), H in plane and parallel to the current I (longitudinal geometry: LG), H in plane and perpendicular to I (transversal geometry: TG). The measured MR in the three geometries is in perfect agreement with previous results in Co nanowires fabricated by an EBL process [23, 24]. The magnetization prefers to align along the NW axis due to the strong shape anisotropy (length ≈ 18 × width ≈ 45 × thickness). The differences in the saturation fields for TG and PG are due to the width-thickness ratio (>1). The slight decrease of the MR at high magnetic fields is caused by small misalignments of the wire with H. The different magnetoresistance observed between the LG and any of the others is caused by the anisotropic magnetoresistance, AMR=100($\rho_{//}$-$\rho_{\perp}$)/ρ (see section 3.5. for details of AMR). The value at 300 K is positive, around 0.65-0.7%, as previously found in Co nanowires [23, 24] and thin films [25]. Supposing coherent rotation when the field is applied in the PG, the anisotropy constant in this geometry, K_u^{PG}, can be estimated. From reference 23:

$$R(H) = R_{//} - (R_{//} - R_{\perp})\left(\frac{\mu_0 M_s H}{2K_U^{PG}}\right)^2 \qquad (7.3.)$$

where, $R_{//}$ and $R_{\perp}$ are, respectively, the resistances at zero field and after magnetic saturation along the perpendicular direction. At 300K, $K_u^{PG}=7.9\times10^5$ J/m^3 is obtained. In the TG, however, the dependence is far from being quadratic, and the same analysis cannot be performed. This suggests that the mechanism towards saturation in this configuration is not just by coherent rotation of the magnetization. Further experiments with specific magnetic techniques are requested to investigate in detail the exact mechanisms of magnetization reversal in these NWs.

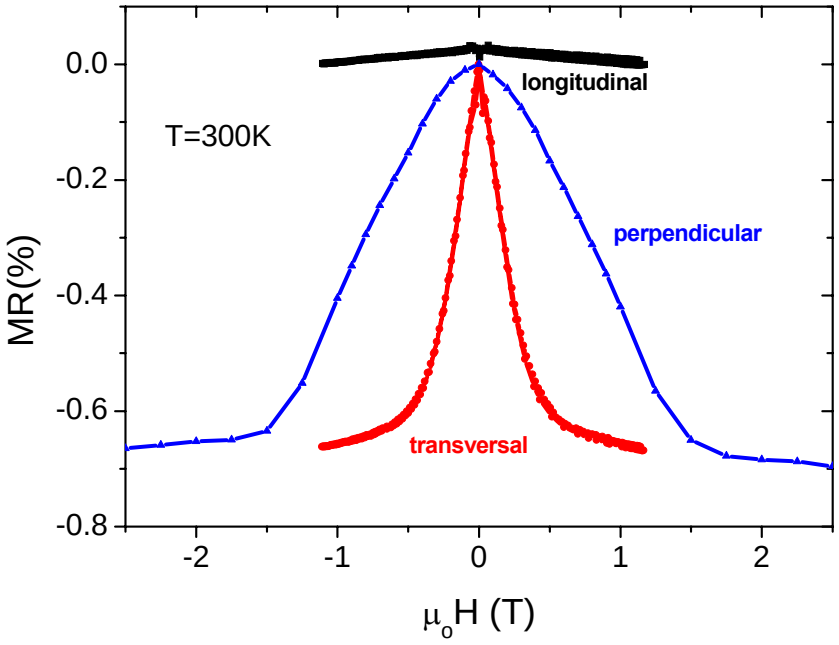

Fig. 7.6. Magnetoresistance measurements at 300 K in longitudinal, transversal and perpendicular geometries of the same Co nanowire as in figures 7.5. and 7.4.

The AMR was further studied as a function of temperature by means of the Planar Hall effect (PHE), in a 45º configuration between I and H, where the transversal voltage is maximum [26]. In figure 7.7(a) we can see the transversal resistivity ρ_{xy} in this configuration for several isotherms. From ρ_{xy} and under saturation, the AMR ratios can be calculated as

$$AMR(\%) = 200\frac{\rho_{xy}}{\rho} \qquad (7.4.)$$

The AMR slightly increases when lowering temperature, from 0.65% at 300 K to 0.8% at 25 K, in good agreement with EBL-fabricated Co nanowires [23, 24]. Figure 7.7(b) shows in detail ρ_{xy} in a low range of field in two selected isotherms. Abrupt switches occur around 150 Oe, the switching field increasing when temperature diminishes, as expected for an activation process [27].

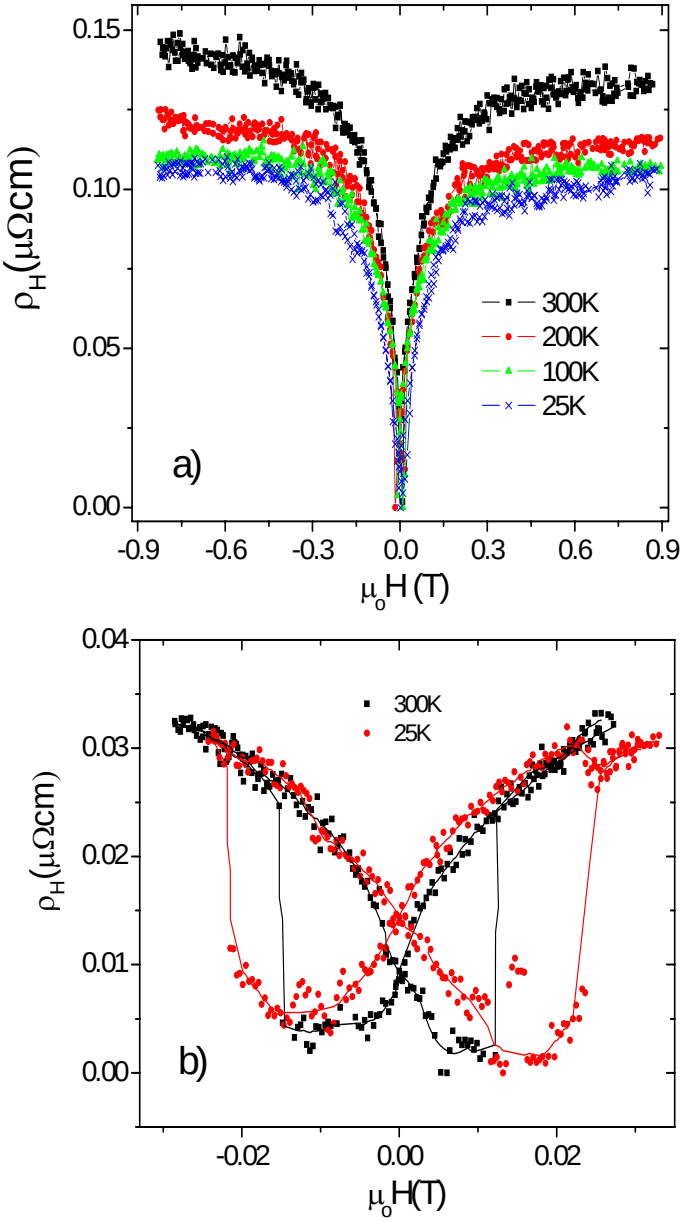

Fig. 7.7. (a) Planar Hall effect resistivity isotherms performed in the same Co nanowire shown in figures 2 to 4. The magnetic field is applied in the substrate plane, forming 45º with the current, where the PHE voltage is maximum. From these measurements, the AMR has been determined as a function of temperature (see text for details). **(b)** Detail of a) at low magnetic fields, showing abrupt magnetic switches as a consequence of the strong shape anisotropy and the magnetic field configuration. The lines are guides to the eye.

7.4.2. Magnetotransport properties of cobalt NWs grown at low beam currents

For the sake of completeness, we will show the results obtained in one nanowire grown at 10 kV and low current, 0.13 nA, with cobalt content around 80%. As shown in figure 7.8., such a low cobalt content precludes the achievement of high-quality magnetotransport properties. The room temperature resistivity value, 10800 μΩ cm, is more than 300 times larger than in the case of the nanowires grown under high currents. Besides, the study of the resistivity as a function of temperature indicates a slightly semiconducting behaviour, in sharp contrast to the full metallic behaviour found for the nanowires grown under high currents. The current-versus-voltage measurements performed at 25 K and 300 K are linear, indicating an ohmic behaviour. The MR measurements shown in the top inset of figure 6 indicate low MR ratios in the perpendicular and transversal configurations, about -0.08%, one order of magnitude smaller than those found for the nanowires grown under high currents and those expected in bulk polycrystalline Co. Summarizing, nanodeposits with high Co content are required to obtain high-quality magnetotransport properties.

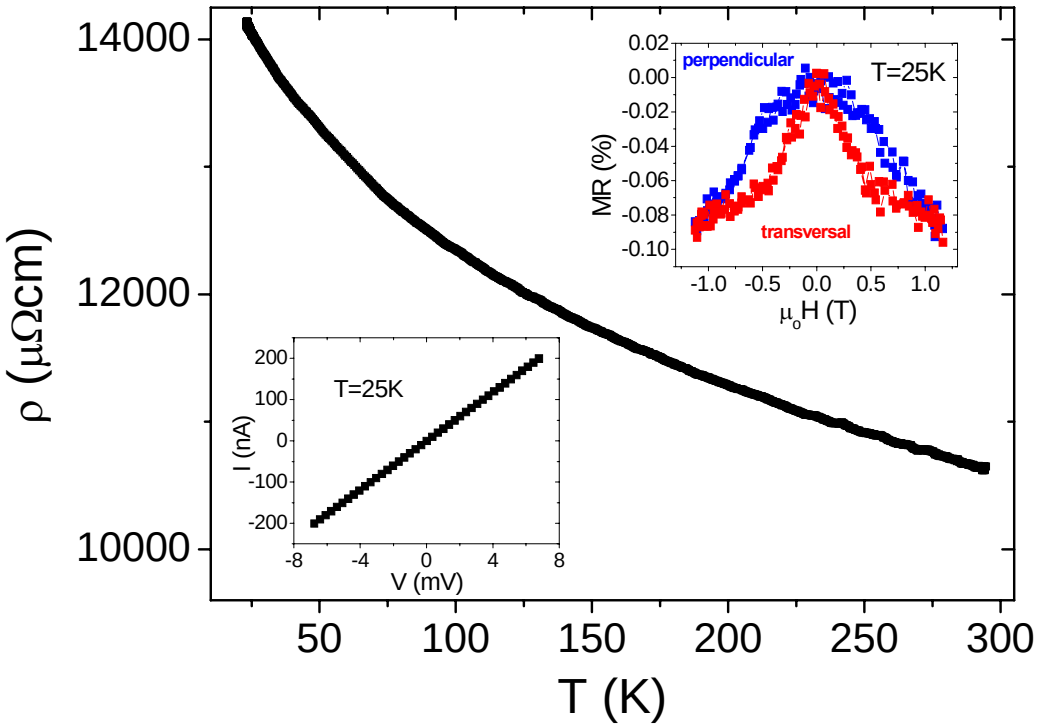

Fig. 7.8. Resistivity as a function of temperature of a Co nanowire grown at 10 kV beam energy and low current, 0.13 nA. The bottom inset shows the current-versus-voltage measurement at 25 K and the top inset displays magnetoresistance measurements at the same temperature. The high value of the resistivity, the semiconducting temperature dependence and the low MR values illustrate the degraded magnetotransport properties of nanowires grown at low current.

7.5. Systematic MOKE study of rectangular nanowires

After having demonstrated that FEBID-Co is really pure, in this section, we will show a systematic study, by means of spatially-resolved magneto-optical Kerr effect (MOKE), of the magnetic hysteresis loops of single wires in a wide range of aspect ratios, and grown under different beam currents. The dependence of the switching fields with the dimensions is studied, and compared with analogous structures fabricated by other techniques. This study tries to understand the mechanisms for the reversal of the magnetization for these structures. This has been under intense study for the last decade [23, 28-33], due to its relevance in Spintronics applications [34].

7.5.1. Types of structures grown. Maximum resolution obtained.

The rectangular deposits were grown at 5 kV, with beam currents (I_{FEB}) = 0.4, 1.6, 6.3 and 24 nA. Two types of substrates were used for these experiments: a silicon wafer (type I), and a 200 nm-thick SiO_2 layer on top of Si, created by a thermal oxidation process (type II). The dimensions of the rectangular lines were: length (L) = 8 or 4 μm (no difference was found for same aspect ratio), thickness (t) = 200 or 50 nm. The nominal widths (w) were chosen to have structures with aspect ratios (AR=L/w) varying from 1 up to 32 (16). The study was complemented by depositing single-pixel-line wires using the smallest beam current selected, I_{BEAM}= 0.4 nA. The aim to grow these lines was to determine the best resolution in width attained under conditions appropriate for reasonably high Co content (see table 7.I.). The wire width will presumably be bigger than the FEB spot size, as a consequence of the interaction volume of the electrons with the substrate [1, 2]. The minimum width was found to have a full width at half maximum of around 150 nm for a 40 nm-thick deposit (corresponding to an AR =26 for L=4 μm).

In figure 7.9., some examples of SEM images of lines deposited in both substrates are shown. Additionally to the main line, a parasitic deposit around the structure is present (ranging, in one y-direction, between 400 nm up to 1 μm, as

determined by SEM images, slightly larger in the case of the type II-substrate). This halo is caused by backscattered electrons (BSE) and their generated secondary electrons (SE) [1, 2], phenomenon similar to that existing in electron beam lithography, called "proximity effect". Previous works report a lower metal concentration in the halo, ~5 times smaller with respect to the main deposit, when

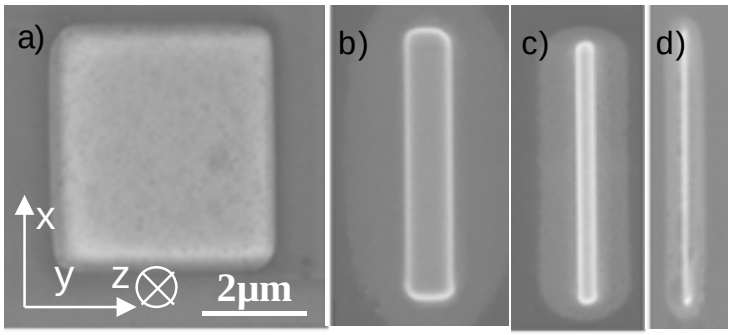

Fig. 7.9. SEM images of rectangular deposits with different aspect ratios. The scale bar is the same for all of them. Together with the main deposit, a micrometric-wide halo parasitic deposit is present (see text for details). The axis nomenclature is maintained during all the study.

using this gas precursor [15].

7.5.2. AFM investigation of the nanowires topography

In figure 7.10. the profiles of some lines are shown, measured by AFM, together with a 3-dimensional image of the corresponding wire. As it can be noticed, the profiles are highly dependent on the beam spot used for fabrication [1, 2]. In figure 7.10(a), a 8 µm × 8µm × 50 nm structure grown by a $I_{BEAM}^{(1)}$=24 nA shows a nonuniform distribution in height, being higher in the edges than in the centre. This effect has been previously observed when depositing residual carbon [35] and in C-Fe deposits [9] at high currents. The regime of deposition in this case is called *diffusion-enhanced regime* (DER). If the supply of gas molecules for deposition is exclusively by a direct adsorption from the gas phase, all parts under the beam spot have the same probability to be deposited, resulting in a constant-in-height structure. However, in the DER, the surface diffusion has a vital importance in the supply of gas molecules. The molecules come from outwards of the beam spot to inwards, being deposited at a

higher rate in the edges with respect to the central part of the deposit.

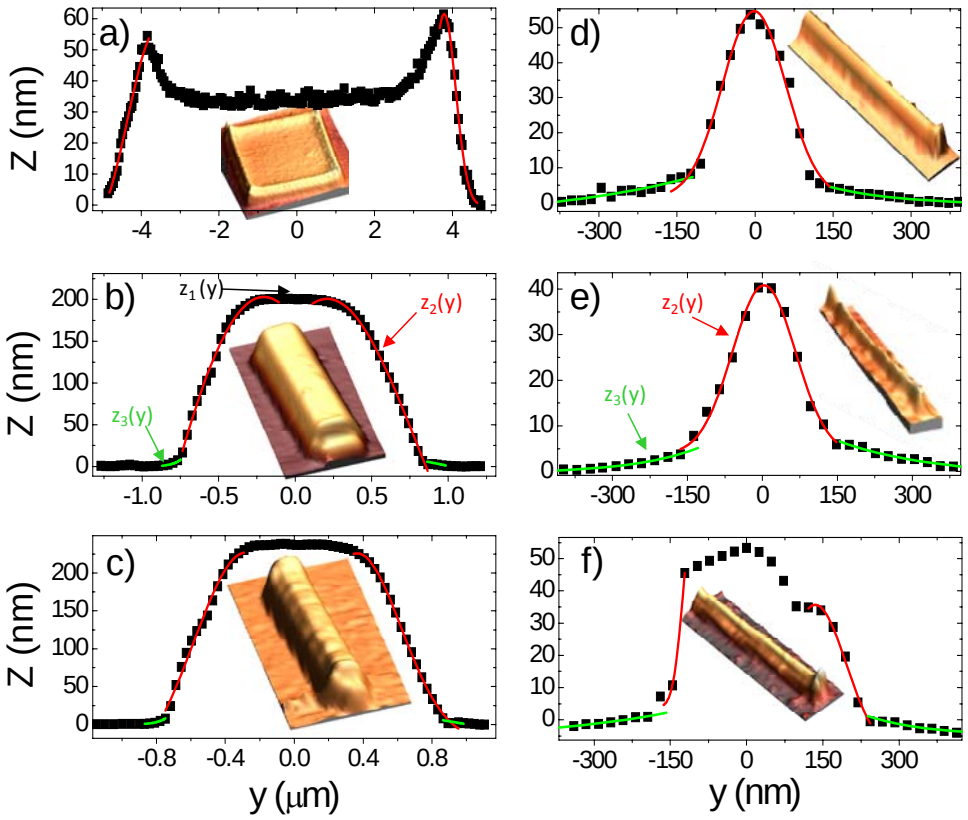

Fig. 7.10. AFM images of the wide variety of profiles attained by the wires, dependent on the growth parameters.Together with the profile, the 3D-image is inserted in every graph. Note the different axis scale to observe details in the y-direction. The beam currents used are: (a) I=24 nA (b) I=6.3 nA (c) I=1.6 nA, (d) and (e) I=0.4 nA. In **(a)** the profile is associated to a diffusion-enhanced regime for deposition, whereas the rest of profiles can be explained by a precursor-limited regime. In all, the different fits, to $z_2(y)$: red line and $z_3(y)$: green line, are shown (explicitly indicated in figures **(b)** and **(e)**). In **(f)**, a shift during the process, caused by a charging effect, produces a two-height profile wire.

For the rest of beam currents used this effect is not important, resulting in an approximately constant height in the central part of the structure. In this case, the regime for deposition is called *precursor-limited regime* (PLR), since the use of relatively high currents with a moderate gas pressure results in a deposition induced by a direct supply from the gas phase. In figure 7.10(b) and 7.10(c) lines deposited with $I_{BEAM}^{(2)}$=6.3 nA and $I_{BEAM}^{(3)}$=1.6 nA, respectively, are shown. Figures 7.10(d), (e) and (f) are profiles for structures with $I_{BEAM}^{(4)}$=0.4 nA. The wire in 7.10(e) was grown by a single-pixel-line process (in the rest, the beam defines a rectangular profile when scanning). The structural profiles along the y direction,were fitted to a general function:

$$z_1(y) = z_0 \qquad for \qquad |y| < y_1 \qquad (7.5(a))$$

$$z_2(y) = A\exp\left(\frac{-y^2}{2\sigma^2}\right) \qquad for \qquad y_1 < |y| < y_1 + \Delta \qquad (7.5(b))$$

$$z_3(y) = B\exp\left(\frac{-|y|}{y^*}\right) \qquad for \qquad |y| > y_1 + \Delta \qquad (7.5(c))$$

In the following, a deeper description of these profiles is given. Equation (7.5(a)) gives account of the constant height in the centre of the structure when fabricating wide structures, as a consequence of the good beam overlap (see for instance figures 7.10(b) and (c)). The bigger height in the edges in the DER is therefore not considered in this model. The mean roughness for this central part was found to be typically around 10 nm. Gaussian fits of the tails of the deposit (equation (7.5(b)) are shown in figure 7.10, as red lines. The full width at half maximum (FWHM) of them depends on the beam current, being approximately of 500 nm for $I_{BEAM}^{(1)}$, $I_{BEAM}^{(2)}$ and $I_{BEAM}^{(3)}$, and of 150 nm for $I_{BEAM}^{(4)}$. This dimension is several times higher than the gaussian primary beams used, and is caused by the generation of SE in the substrate in a larger volume than that targeted by the primary beam. Monte-Carlo simulations evidence this effect [1, 2]. The most external, exponential part of the

profile (equation 7.5(c)) corresponds to the halo deposit explained in the previous section, occurring as a consequence of the generation of BSE when irradiating the substrate. This picture can be understood using the Bethe stopping-power formula [12, 36]. The parameter y* was found to be of the order of a few hundreds of nanometers.

Lower currents than those used here would have resulted in a crossover to the *electron-limited regime* (ELR), where the replenishment rate of molecules would be higher than the dissociation rate of gas molecules. The profiles in this regime are sharper [1, 2], but we intentionally did not use small currents since the purity of the FEBID-Co is substantially smaller for low beam currents, as was deeply studied in sections 7.4.1 and 7.4.2.

It is interesting to include figure 7.10(f), where a deposit with a two-step height was imaged. This structure was grown on SiO_2, and as a consequence of the charging effect by the progressive accumulation of the irradiated charge, a beam shift occurred during its growth. The grounding of the substrate near the place of interest, by the contact of a commercial Omniprobe needle, was used to avoid this effect in most of the deposits. As we will show in next section, this has relevant influence in the magnetic properties, Magnetization hysteresis loops by MOKE measurements

7.5.3. Magnetization hysteresis loops MOKE measurements

In figure 7.11., some examples of hysteresis loops at room temperature of different deposits are shown, as determined by longitudinal MOKE. In all cases (blue continuous line), the magnetization refers to the x-component (principal axis of the line). In figure 7.11(a), the magnetization in the y-direction is also included for a structure with AR=2 (red dashed line). The order, (a) to (e), corresponds to a progressive increase in the aspect ratio of the wires (from 2 up to 26). For these structures, where the AR>1, the M_x loops are approximately square-shaped, indicating that the x-direction is the easy axis of magnetization, due to the shape anisotropy. Besides, the switching of the magnetization occurs in a field interval of a few tens of oersted. This has been reported to be a typical feature for the switching of M in cobalt wires mediated by nucleation of domain walls (DWs) plus propagation [23, 24]. No multidomain states seem, therefore, be present in the reversal of the magnetization in high-aspect ratio wires, since in this case the reversal of M occurs in a field interval of a few hundreds of oersted [24]. The thickness of our wires is above the limit found in reference 24 for single-domain behaviour of cobalt wires (t above ~20 nm). The reversal of M_y in figure 7.11(a) is clearly different, because in this case the magnetic field is applied along a hard magnetic axis. This seems to result in a progressive rotation of M, followed by a quite abrupt switch.

The MOKE loop in figure 7.11(f) corresponds to a structure analogous to that shown in figure 7.10(f), with a two-step height profile, caused by a shift during the growth. This profile results in a two-step switch of M.

Experiments devoted to determine the importance of the halo in the magnetism of the wires were done, by focusing the laser spot exclusively on that zone, out of the main structure, and performing hysteresis loops. We did not obtain a relevant magnetic signal in any case, indicating the low magnetic character of this second-order deposit. Thus, we conclude that although SEM images show a total structure extending for a few microns in the x-y plane, the structure grown is ferromagnetic only in the main wire. The reduced thickness (AFM images, figure 7.10.), more susceptible to a complete oxidation, together with a significant higher carbon+oxygen/cobalt ratio present in the halo with respect to the main deposit, as preliminary measurements with a STEM microscope indicate [37], are in perfect consonance with these conclusions obtained from MOKE measurements. This result is not general for FEBID processes, since for instance, the contrary effect has been reported in iron deposits grown by FEBID using $Fe(CO)_5$ as gas precursor [7].

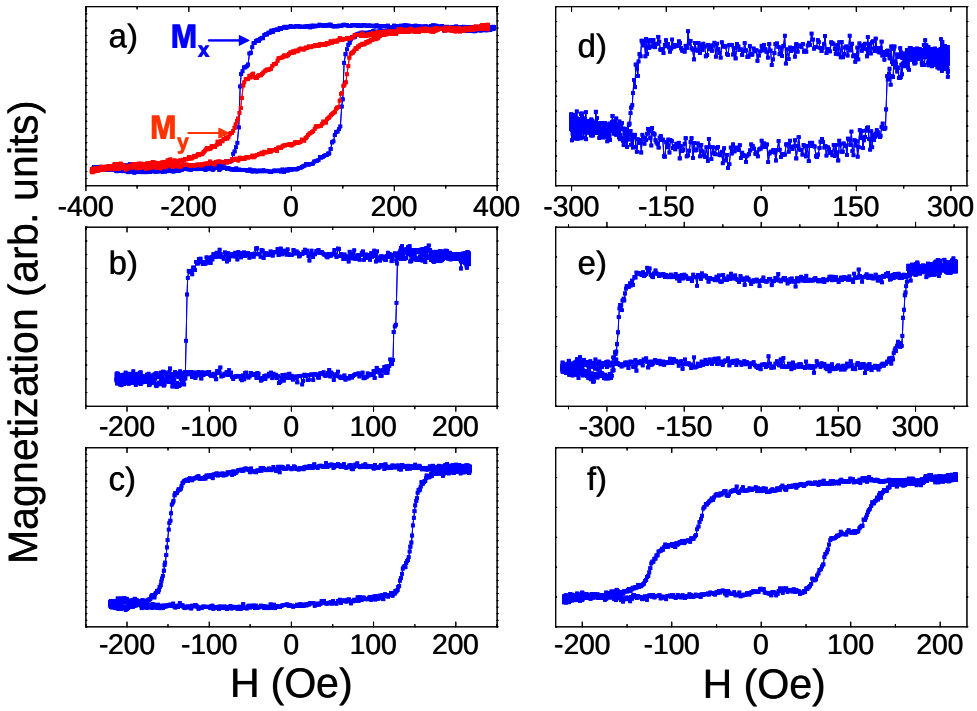

Fig.7.11. Examples of magnetization MOKE loops for different wires. All the magnetization results refer to the x-direction (easy magnetic axis), except for (a), where the magnetization in the y-direction is also included. The aspect ratio is in **(a)** AR=2, **(b)** AR=4, **(c)** AR=8, **(d)** AR=10, **(e)** AR=26, corresponding to a single-pixel-line growth process. In **(f)**, a two-step profile deposit, analogous to the one shown in 7.10(f), produces the switching of the magnetization in two steps.

The value for H_c was determined by a gaussian fit of the derivate of the hysteresis loop. The dependence of H_c with the wire width is plotted in figure 7.12., showing the dramatic effect of the sample geometry in the reversal of the magnetization thorough shape anisotropy effects. The coercivity decreases with width for all the samples studied, increasing with thickness. This trend has been previously observed in wires of different materials [23, 29, 30], and can be understood in magnetostatic terms, since the demagnetizing field depends in a first order approximation on the t/w ratio. By fitting H_c to an inversely proportional dependence with width ([$H_c=H_\infty+\beta/w$], see dashed lines in figure 7.12.), we obtain a coercive field for an infinitely-wide element H_∞= 90 (70) Oe for the 200 (50) nm thick wires, which

is a reasonable value for a cobalt polycrystalline thin film. If, on the contrary, the field derived from this fit is made equal to the coherent rotation switching field value, $H_c=2\pi M_s$ ~ 8350 Oe (M_s value determined by magnetotrasport measurements, see section 7.4.1), we obtain an equivalent width of 3.5 and 7 nm, for thickness of 50 and 200 nm, respectively. These widths are compatible with the expected lateral wire dimension, of the order of the exchange length value, ~ 5 nm in Co [30]. These results are in perfect agreement with ref. 23 and 30, where Co wires fabricated by EBL were analysed in the same manner.

On the other hand, Uhlig *et al* [30] described the dependence of H_c with shape in cobalt and permalloy nanolines as:

$$H_c = a + \frac{bM_s t}{w} \qquad (7.6.)$$

finding a universal dependence, since b=3 in all cases. This factor is related with the in-plane aspect ratio (L/w) of the volume in the wire responsible for the magnetization reversal, assuming coherent rotation in this critical nucleus, and applying a Stoner-Wolfharth analysis [38]. b=3 means that the in-plane area for the reversal is $1.25w^2$. From our results, we find that the area that induces the reversal of M in our wires is $(1.20 \pm 0.05)w^2$ for the 50 nm-thick deposits, and $(1.50 \pm 0.06)w^2$ for the 200 nm-thick structures. Thus, both dependences do not collapse exactly to the same value. Nevertheless, the lack of accuracy in the determination of the exact dimensions of the wires, the different profiles they have, as well as possible changes in the purity and microstructure of the deposits with the beam current can induce these small differences. The remarkable conclusion from this analysis is that the volume involved in the initial reversal of M is very different from the whole structure. The reversal process is dominated by the formation of domain walls at the surfaces of the wire width, near the edges (as it will be shown in section 3.3) or surrounding existing defects, which will be propagated trough the whole wire when a magnetic field is applied. The minimization of the magnetostatic energy, by avoiding surface magnetic charges, causes this behaviour. Thus, the ‘‘effective’’ volume appears to be a localized

surface-dominated mode, roughly independent of the element size [39]. This nucleus has a similar area to that reported for Co nanowires fabricated by EBL, evidencing that an equivalent mechanism for the reversal of M occurs in FEBID-Co wires, in comparison with structures fabricated with more conventional techniques.

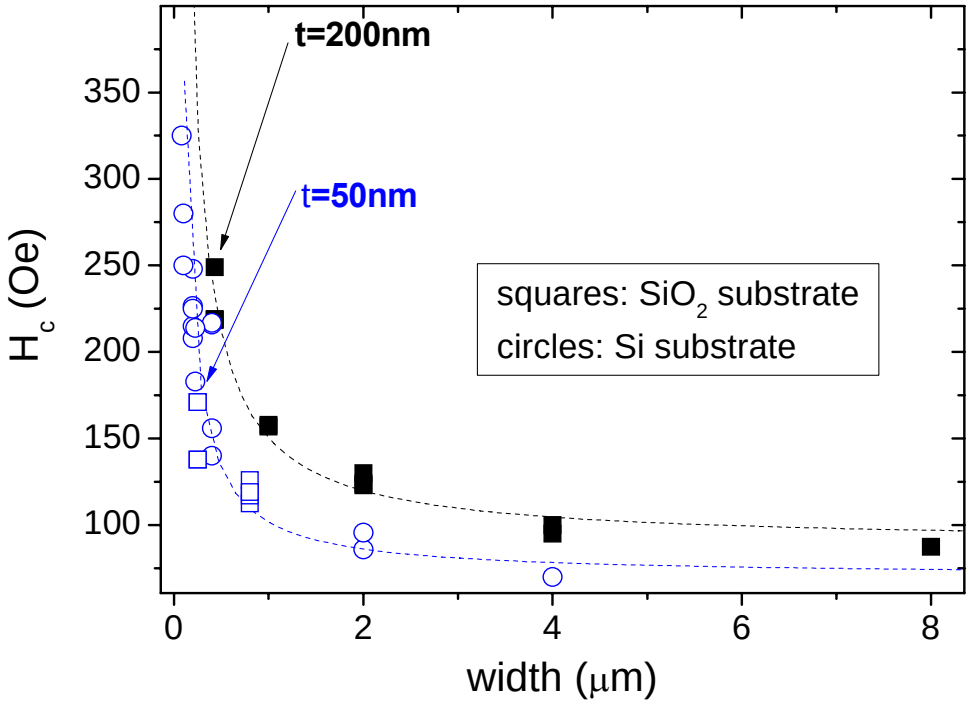

Fig. 7.12. Coercive field as a function of the deposits width. H_c is proportional to the t/w ratio, consequence of the dependence of the demagnetizing field with the wire dimensions. From the fits (dashed lines), a rough estimation of the coercivity for a Co film, the length for coherent rotation, as well as the in-plane area responsible for the reversal of the magnetization, is deduced (see text for details).

7.6. Domain wall conduit behavior in FEBID-Co

7.6.1. Domain wall conduit: The concept

Domain wall conduit behavior is the possibility to displace DWs at much lower fields than those needed to nucleate new domains [40]. If this occurs, DWs can be treated as particles moved in a controlled way along magnetic networks [41], by the application of an external magnetic field (or by a current, by means of the spin torque effect [42]). In figure 7.13. this concept is schematically explained.

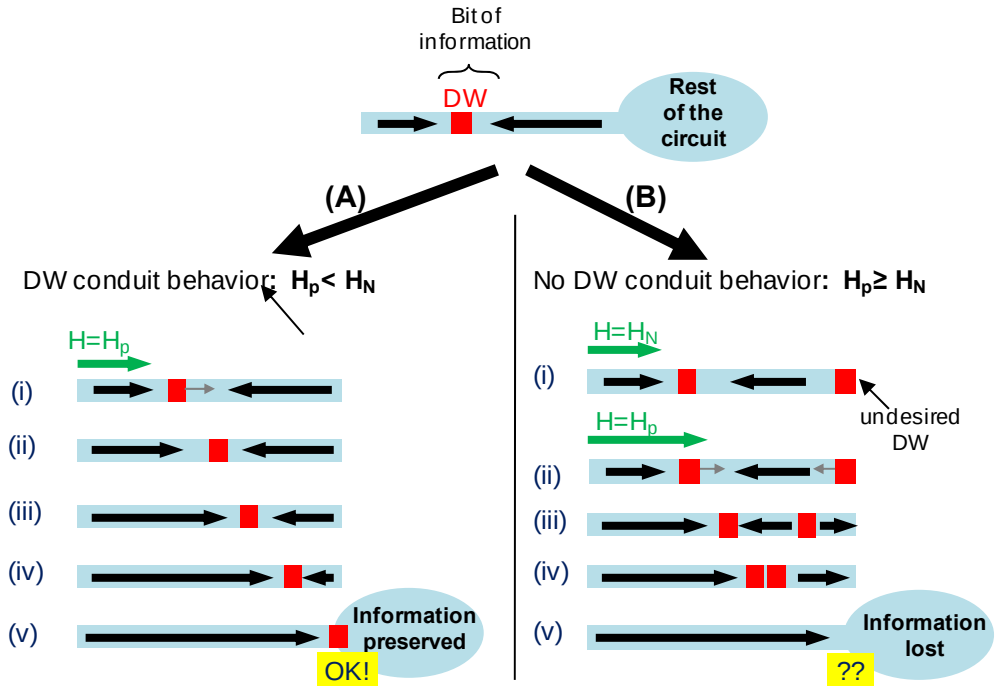

Fig. 7.13. Sketch of the concept of domain wall conduit behavior. The information stored, in the form of a DW, is preserved (A) or lost (B), depending if there exists good conduit behavior (A), or not (B). In (A), the DW is transmitted to the part of the circuit where it is needed when $H=H_P$. On the contrary, in (B) new DWs are created at $H=H_N$ (i-right), and therefore annihilate the pre-existing DW (iv-right) when propagated, at $H=H_P$.

This behavior can only occur in the nanoscale, where single-domain structures are feasible, since the magnetostatic energy is the dominating term controlling the magnetic configuration of the nanostructure. DW conduit has been exploited in the last years in planar permalloy NWs, where interesting applications have been proposed. The following references highlight the most important ones:

(i) D.A. Alwood, R.P. Cowburn *et al* [43]: creation of an arithmetic logic analogous based on semiconductors (CMOS technology), which relies on the movement of DWs in complex networks. Logical NOT, logical AND, signal fan-out and signal-cross-over were designed, all of them integrated in the same circuit (see figure 7.14(a)).

(ii) S.S. Parkin *et al* [44]: creation of the so-called horizontal *racetrack memories*, i.e. non-volatile memories composed of 2D-arrays of magnetic NWs where the information is stored by means of tens-to-hundreds of DWS in each NW (see figure 7.14(b)). Its analogous 3d-version has also been proposed.

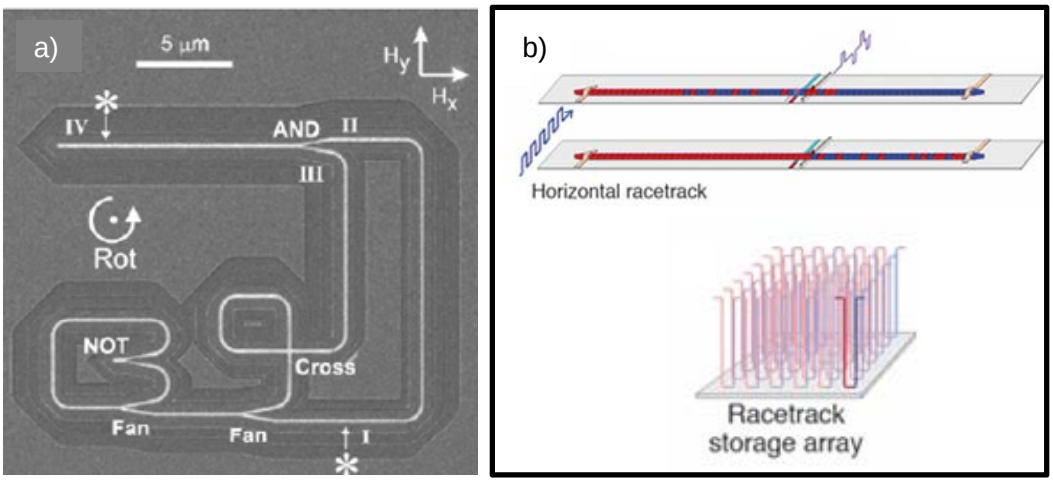

Fig. 7.14. High-impact applications of planar permalloy nanowires, with good DW conduit behavior. **(a)** Magnetic Domain Wall Logic [43]. **(b)** Racetrack (horizontal and vertical) memories [44]. Images taken from references cited.

7.6.2. Creation of L-shaped nanowires

For this study, L-shaped NWs were deposited with an electron beam energy of 10 kV, and a beam current of 2.1 nA. For the creation of these structures, we used bitmaps which determine where the beam is scanned. The thickness of the wires was fixed to be around 50 nm, with varying widths (w), from 600 and 150 nm. In figure 7.15(a), a typical bitmap used is shown. The curvature radio (R) of the L was chosen to be R=5w, to facilitate the good movement of the walls. Both ends of the NW are pointed to avoid domain nucleation [43, 45]. A 200 nm wide structure is shown in Figure 7.15(b). The time taken to fabricate this structure under the chosen conditions is approximately 2 min.

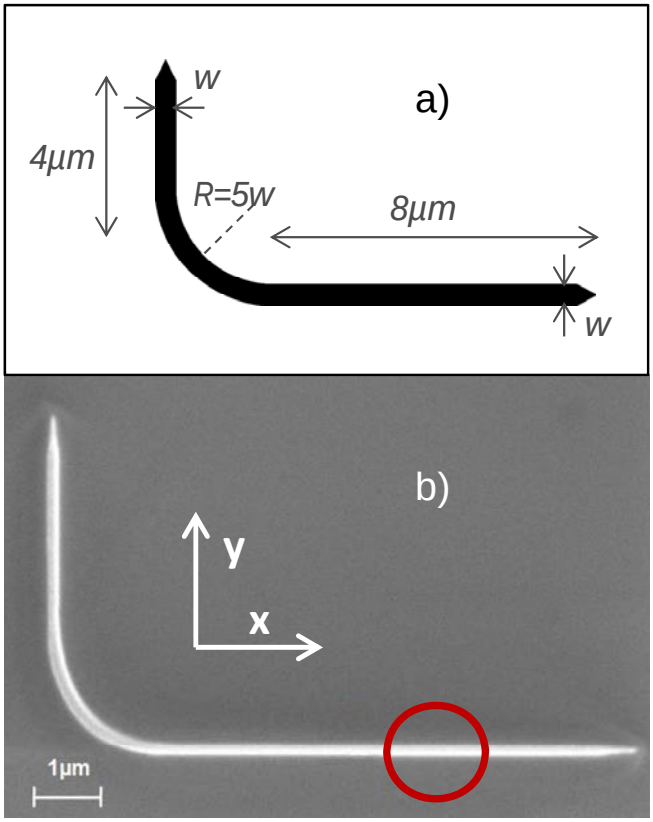

Fig. 7.15. L-shaped nanowires. (a) Bitmap used for the creation of the structures. The black color is the zone inside the field of view where the beam is scanned, getting blanked for the white part. **(b)** SEM image of a 200nm wide L-shaped cobalt nanowire. The axis nomenclature is maintained in all the section. The red circle represents the MOKE laser spot (not to scale).

AFM measurements were performed to study the uniformity of the L-shaped wires grown. Scans along different parts of the L-NWs (see dashed lines in figure 7.16(a)) permit to see that a good uniformity in the shape of the structures is attained, with deviations in the section of the wires smaller than 10 %. As an example, different scans along a 590 nm wide wire are shown in figure 7.16(b).

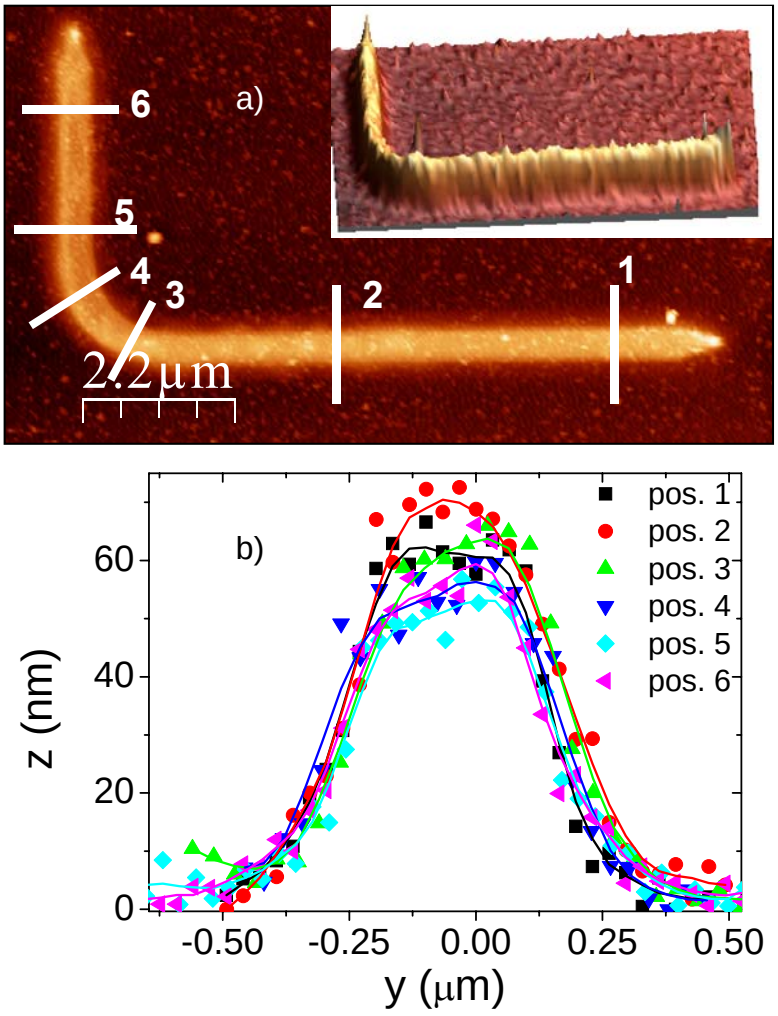

Fig. 7.16. AFM measurements of a 590 nm wide NW. **(a)** AFM image of the wire, where the white lines represent the lines scans performed to determine the profile of the structures in different zones. The inset shows the 3D-image **(b)** Profiles of the wire, showing good uniformity along the structure. Lines are guides to the eye.

7.6.3. MOKE measurements and field routines

Each structure was analyzed using the high sensitivity MOKE magnetometer. The ~5 μm diameter focused laser spot was placed on the horizontal arm of the wire (see circle in figure 7.15(b)). The component of the magnetization along the x axis was determined by measuring the longitudinal Kerr effect. A typical hysteresis loop is shown in figure 7.17., corresponding to a single-sweep experiment. The high signal obtained in only one loop indicates two things: first, this MOKE setup had demonstrated a high sensitivity for permalloy, around 10^{-12} emu (reference 29). The signal to noise ratio is also very good in these experiments on Co nanowires, allowing the clear observation of magnetic switching even in single-shot measurements. A rough estimation of the magnetic moment probed in this experiment can be done, taking into account the value for M_s determined from magnetotransport measurements (see section 7.4.1.) corresponding to around 10^{-10} emu. Second, it is another evident proof of the high Co purity of the wires grown under these conditions.

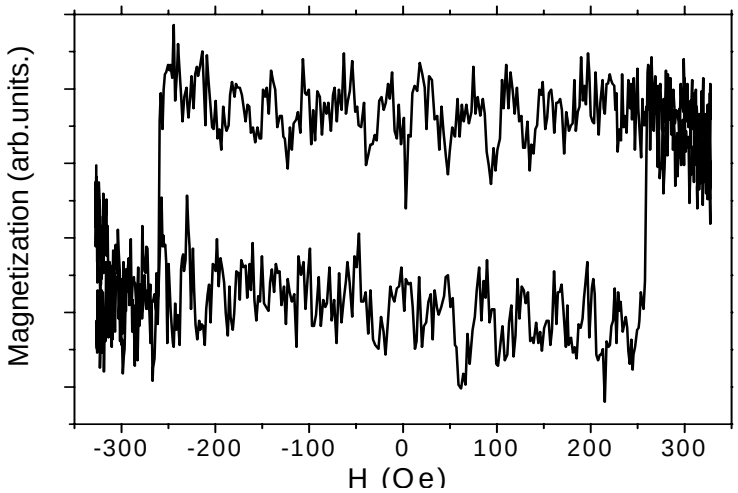

Fig. 7.17. Hysteresis loop of a 200 nm wide nanowire obtained from a single shot measurement. The relevant signal-to-noise ratio provides evidence the high purity of FEBID-Co.

To study the possible good control of DWs of the FEBID-Co, a quadrupole electromagnet was used to apply two types of (H_x, H_y) magnetic field sequences at a frequency of 1 Hz [46]. In the first procedure, a DW is initially formed at the corner of the NW. In this case, magnetization reversal occurs by the propagation of this DW in the NW. In the second field sequence, no DW is formed at the corner, so the nucleation of a DW is required to reverse the magnetization. A schematic of the processes occurring in the L-shaped structure in half a cycle (from positive to negative magnetic fields) is shown in figure 7.18(a) and 7.18(b) for the two types of measurements. The other half of the cycle is symmetric.

Hysteresis loops for two particular cases: w_1 = 500 nm, and w_2=200 nm, are shown in figure 7.19. (we will cite them as 1 and 2, respectively). To reduce the noise, 30 loops were averaged. In figure 7.19 (a_1) and (a_2), the DW initially formed at the corner is propagated through the horizontal NW, switching its magnetization, when the so-called propagation field value (H_{P1} = 30 Oe, H_{P2}=80 Oe), is reached. On the contrary, in figure 7.19(b_1) and (b_2) no DW is previously created at the corner. The reversal in this case happens at significant higher magnetic fields (at the nucleation field H_{N1} = 91 Oe, H_{N2}=259 Oe). In both NWs, H_P and H_N are very different, with H_P<H_N. This behavior is fundamental for possible applications of this material to devices which rely on the formation and control of DWs. It must be noticed that a small field offset in the y-direction was maintained in both sequences after the initialization of the magnetization, ensuring that the DW remains in the bottom of the structure and does not propagate in the y direction [47]. This offset (H_y^{off}) was chosen so that H_y^{off}>H_p for the wider NWs, and was maintained when measuring all the NWs for consistency. Systematic measurements of H_p and H_n as a function of H_y show that this transverse offset has very little effect on the switching fields (see figure 7.20.): a maximum variation of 15% was observed in H_p for a 150 nm wire when H_y varied between 20 and 80 Oe. The error bars on figure 7.21. take into account this small effect.

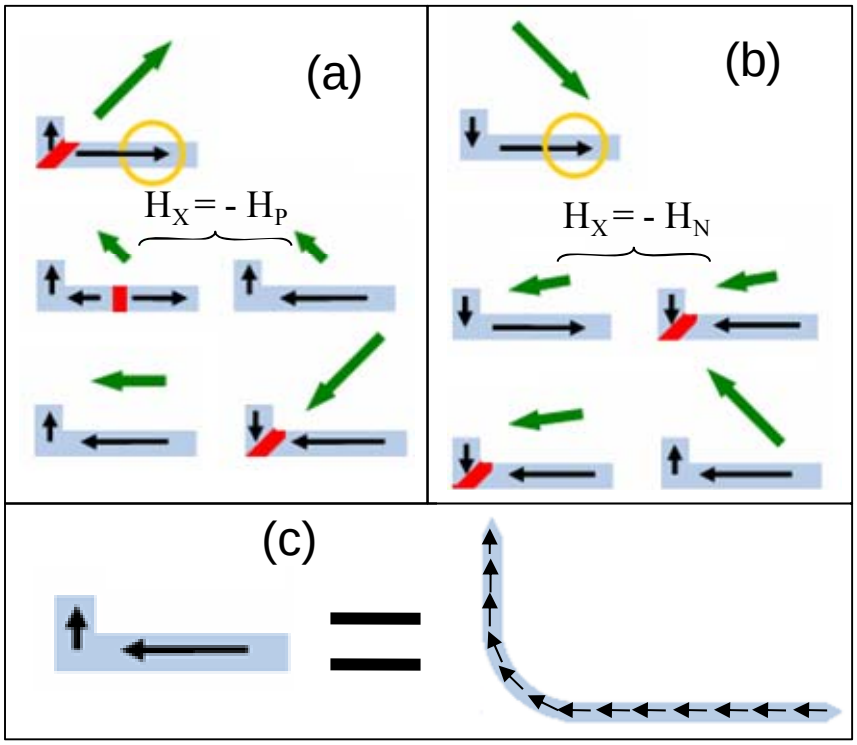

Fig. 7.18. Schematic diagrams of magnetization configurations obtained during half a field cycle (the other half cycle is identical, but with all fields reversed). External arrows show the applied magnetic field; internal arrows show the direction of magnetization in the nanostructure. The circle (not to scale) represents the MOKE laser spot. In **(a)** (propagation) the magnetic field generates a DW at the corner of the L-shaped NW. As H_x changes to negative values, this DW is propagated through the horizontal arm, switching its magnetization at $-H_P$. The subsequent change of H_y from positive to negative values again induces the generation of a DW in the corner. In **(b)** (nucleation), the external field saturates the magnetization along the NW. As H_x is reversed to negative values, a reversed domain is nucleated when $Hx = - H_N$; the magnetization in the horizontal arm switches and a DW is now present at the corner of the NW. The change of H_y to positive values again saturates the magnetization along the NW, in the opposite direction to the initial configuration. **(c)** The L-shape sketched in (a) and (b) is a simplification of the real structure, designed for a good motion of DWs. In the configuration drawn, the magnetization is saturated along the shape of the L (no 90º DW is present).

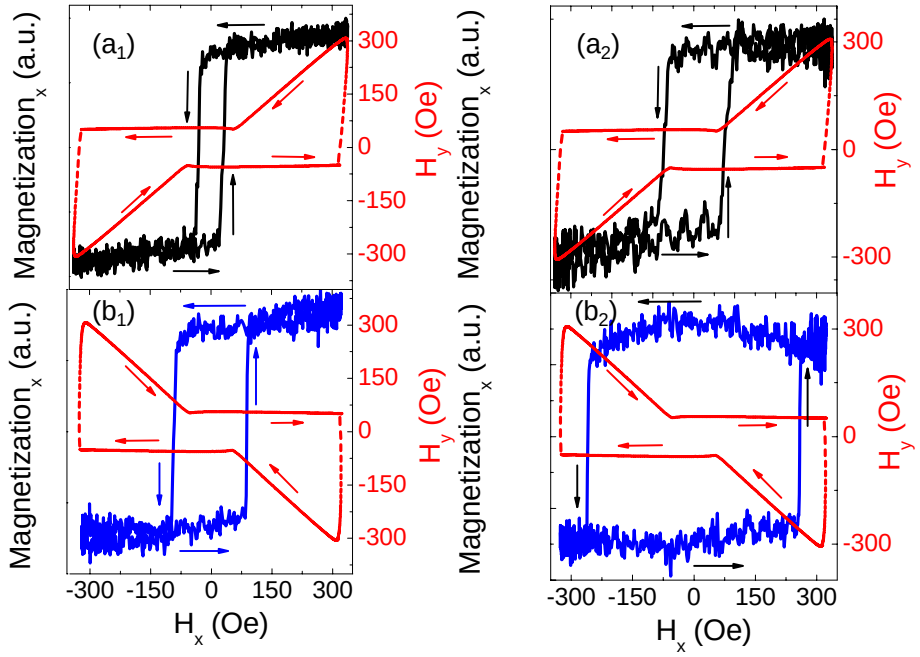

Fig. 7.19. MOKE determined magnetization hysteresis loops (solid lines) and corresponding field sequences (dashed lines) used to measure the propagation **(a)** and the nucleation field **(b)** for two NWs, with widths of 500 nm **(1)** and 200 nm **(2)**. The arrows on the graphs indicate the sense of variation of the magnetization and the field as the routine is applied.

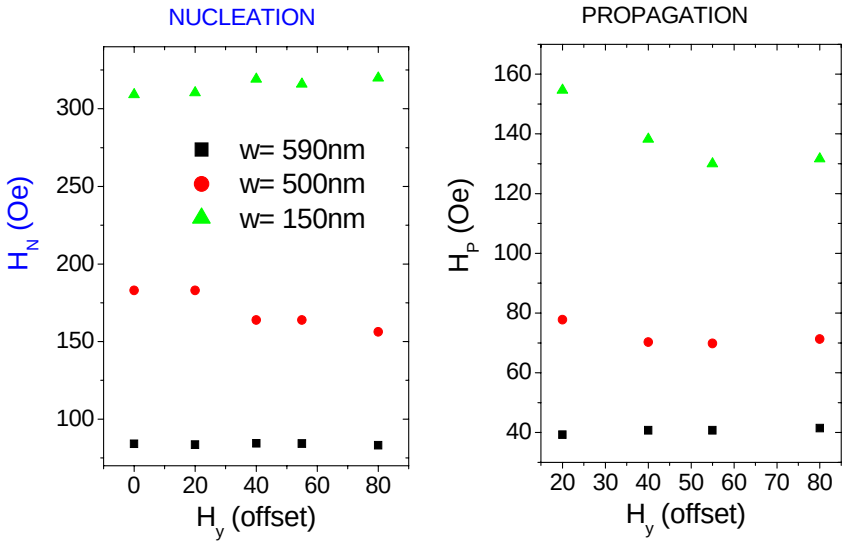

Fig. 7.20. Effect of a H_y-offset in the nucleation **(a)** and propagation **(b)** fields

In figure 7.21. the propagation and nucleation fields are shown as a function of the NW width for all the wires studied. The dependence of H_N, inverse with the width , is the same as discussed in section 7.5.3. , understood in magnetostatic terms. These nucleation fields are slightly higher than those measured for rectangular wires, due to the pointing ends. We can see that H_P has a similar dependence on width. A good fit is also obtained with the inverse of w.

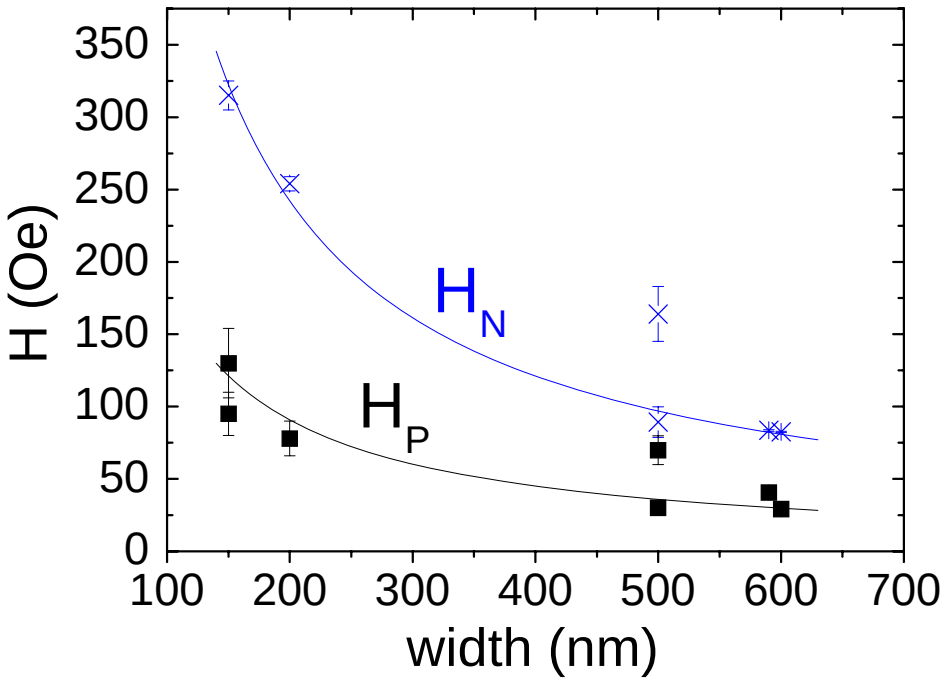

Fig. 7.21. Propagation (H_P) and nucleation fields (H_N) as a function of the nanowire width. The error bars for the fields take into account the effect of the small H_y-offset used in the field sequences (see text for details).

In the case of the nucleation loops, abrupt transitions are always observed, suggesting that the reversal mechanism is by the nucleation of domains plus propagation, starting from a monodomain state [32]. In the case of DW propagation, the transition is not as abrupt as in nucleation field measurements, especially for the narrow NWs. This widening could be thought to be caused by a series of pinning sites under the MOKE spot. However, single-shot loops (not shown here) are all sharp,

indicating this is not the case. Therefore, the relatively wider transitions for H_p are caused by the statistical averaging of abrupt switches occurring at close but slightly different fields. These results show that, for the dimensions chosen, the conduction of domain walls in FEBID Co NWs is excellent. The propagation fields are of a few tens of oersted for the wider NWs. These values are comparable with those ones obtained for thin and narrow permalloy NWs used nowadays by the scientific community in the area [43-47]. This is not the case for these narrower NWs, were H_p are too high for most practical magnetoelectronic applications. Thinner NWs should be studied to determine if good DW control is achieved for narrow FEBID Co NWs in a practical range of fields.

7.7. Conclusions

We have done a complete characterization of the compositional, microstructural and magnetotransport properties of FEBID-Co nanowires. EDX measurements show Co percentages higher than 90% in deposits grown under high beam currents, with percentages around 80% for low currents. We explain the evolution of composition, as well as the high purity attained, in terms of the high local heating induced by the Field-Emission Gun Beam. HRTEM images show that FEBID-Co is polycrystalline, with grain sizes ~2-5 nm. For high currents, Hall, Planar Hall effect and MR are the typical ones for polycrystalline cobalt, with metallic conduction. From these measurements we infer a saturation magnetization very close to the bulk value. NWs grown under low currents show degraded magnetotransport properties.

We report direct hysteresis loop measurements performed by MOKE on single Co nanowires fabricated by FEBID. We have done a systematic study of the reversal of the magnetization in cobalt wires grown by FEBID in a wide range of dimensions. The magneto-optical signal of the grown structures is high for all beam currents, giving account of the magnetic character of the FEBID-Co under the chosen conditions. The coercive field is proportional to the thickness/width ratio, indicating that the differences in the coercivity with dimensions are ruled by the magnetostatic energy. For high aspect ratios, the shape anisotropy forces the magnetization to lie in the longitudinal direction of the NW in remanence.

By the creation of L-shaped NWs, and the application of 2-directions in-plane magnetic field routines, we have demonstrated well-controlled formation and motion of DWs in cobalt FEBID NWs. In the range of dimensions studied, the process for reversal of the NW is well controlled by the magnetic fields applied, being possible to select either DW propagation, or nucleation of a new domain. Both kinds of processes occur at well-defined fields. Significant differences are found for the fields necessary to reverse the magnetization, if a DW is initially present, or not, in the nanostructure. This demonstrates the conduit properties of the Co FEBID nanowires.

The excellent results obtained for FEBID-Co, makes this technique very attractive for future applications. Implementation of complex magnetic NW networks, necessary for real applications based on DW control, is a routine task with this technique, with the enormous advantage of the simplicity with respect to others with nanometer resolution, and the possibility to create these devices, in principle, on any surface. Moreover, the good performances of FEBID for creating 3d-structures, makes this technique a unique tool for the fabrication of magnetic nanostructures.

Chapter 8

Conclusions and outlook

The work carried out throughout this Doctoral thesis concerns the study of electrical and magnetic properties in several nanometric materials, with different range of scales: thin films, atomic-sized nanoconstrictions, and micro and nanowires. In this chapter the main conclusions of the work are summarized, as well as future perspectives resulting from this work. General conclusions, especially regarding the use of experimental techniques and methods will be first shown. Secondly, the concrete conclusions of the three general subjects of the thesis will be exposed: Fe_3O_4 thin films, nanoconstrictions created by FIB and nanowires created by FEBID/FIBID.

8.1. General conclusions

The Doctoral thesis has been done thanks to the synergy of two research institutes in Zaragoza: The (mixed CSIC-University of Zaragoza) Institute of Materials Science of Aragón (ICMA), with a long and reputed experience in the materials science research, and the (University of Zaragoza) Institute of Nanoscience of Aragón (INA), interdisciplinary institute which holds state of the art equipments in the Nanoscience field. This is the first thesis defended in this region where top-down micro and nanolithography techniques using equipments of Zaragoza Institutions have been used. Novel methods and procedures have been developed, which will serve as a useful input for further research in our institutes regarding nanoscale materials and devices. I should specially mention the development of some photolithography and nanolithography processes, which require the learning of a large amount of experimental techniques and protocols. Besides, the assembly and control of equipment for the study of magnetotransport properties has been carried out. Finally, some successful procedures for the control of the resistance of devices while they are being manipulated in a Dual Beam equipment are also innovative in this work, even pioneer at the international level.

8.2. Fe_3O_4 epitaxial thin films

Due to the high spin polarization of Fe_3O_4, with potential applications in Spintronics devices, magnetotransport properties in epitaxial Fe_3O_4 thin films grown on MgO (001) have been thoroughly studied. The photolithography process performed has permitted us to study the longitudinal and transversal components of the resistivity tensor in a wide range of temperatures, above and quite deep below the Verwey transition.

Resistivity and magnetoresistance measurements reproduce previous results in the literature, supporting the epitaxial character of the films. The transport properties of the ultra-thin films are highly dominated by the scattering produced in the antiphase boundaries. This is also evidenced in the systematic study of the Planar Hall effect, giving a record value for the PHE at room temperature. Below the Verwey transition, colossal values never attained before in any material, in the mΩcm range, are measured. The changes in the AMR sign below the transition, as well as the dependence of its magnitude with temperature are not well understood yet.

An important experimental result has been obtained regarding the study of the Anomalous Hall effect, in four orders of magnitude of the longitudinal conductivity. The dependence $\sigma_H \propto \sigma_{xx}^{1.6}$ is fulfilled in all cases, with no influence of the mechanism responsible for conduction, different degree of scattering at the APBs, etc. This is a universal behavior of all magnetite results reported in literature, as well as of all compounds in the dirty regime of conductivities. In our opinion, deeper theoretical work should be done to clear out how the model predicting this behavior fits with non-metallic conduction.

The first magnetic tunnel junction based on Fe_3O_4 electrodes with MgO barrier are currently (2009) being grown in our laboratory by J. Orna. We hope that the experience gained in this thesis on the magnetotransport properties and photolithography process of Fe_3O_4 films will contribute to the successful development of these challenging devices in Zaragoza.

8.3. Creation of atomic-sized constrictions in metals using a Focused-Ion-Beam

We have developed a novel method to fabricate controlled atomic-sized constrictions in metals, by measuring the conduction of the device while a Focused-Ion-Beam etching process is being done. We have demonstrated that the technique works when using Cr and Fe, creating stable atomic-sized constrictions under vacuum inside the same chamber. This method has two main advantages with respect to more conventional (STM, MBJ, EBJ, etc) procedures. First, the FIB processes can be introduced in the standard protocols for the integrated circuits industry, so possible applications of these devices would be feasible using this methodology, which is not the case for the others. Second, regarding atomic-sized in contacts in magnetic materials, where huge magnetoresistance effects observed in the literature are under debate, we consider that the good adherence of the atoms forming the contact to a substrate can minimize artefacts, making this technique more suitable for this kind of studies.

The stability of the contacts when exposed to ambient conditions has been evidenced in iron nanoconstrictions. The results obtained are not systematic, although there is no doubt about the preservation of the magnetic character of the material after ion irradiation in some of the devices. The promising results for samples in the tunnelling regime of conduction constitutes a promising filed for the study of BMR and BAMR. New strategies for protection of the constrictions, together with the possibility to implement a device for magnetic measurements attached to the FIB chamber, to avoid the exposure of the sample to air, would be substantial advances for this research.

The method developed is now being successfully applied in our laboratory for other types of materials, with high interest from a fundamental and applied point of view.

8.4. Nanowires created by Focused Electron/Ion Beam Induced Deposition

An important part of the thesis has been devoted to the study of nanowires created by these promising nanolithography techniques. The work has been done with three types of gas precursors: $(CH_3)_3Pt(CpCH_3)$, $W(CO)_6$ and $Co_2(CO)_8$, and using in the first case both focused electrons and ions to dissociate the precursor molecules, using ions in the second case, and using electrons in the third one. In such local deposition, the material is in general composed of a mixture of carbon and metal. This wide work allows having a general view of the complex physical phenomena under these processes, which produce completely different microstructures in the material. With the $(CH_3)_3Pt(CpCH_3)$ precursor, an amorphous carbon matrix with nanometric platinum clusters embedded inside is produced. With $W(CO)_6$, an amorphous disordered carbon-tungsten microstructure is formed, whereas using $Co_2(CO)_8$, under high currents, almost pure polycrystalline cobalt is grown. Several physical phenomena have been studied in each case, all of them influenced by the particular microstructure of the material.

In the case of Pt-C nanowires, we have observed a Mott-Anderson metal-insulator transition as a function of the carbon/metal concentration. This explains, in principle, contradictory results in the literature up to now. This work shows the importance of tuning the parameters in a FEBID/FIBID process, since in this case insulator or metallic nanowires can be created. The discovery of an exponential decrease in the conductance for the most resistive samples demonstrates the validity of the theories for hopping under strong electric fields in a nanometric structure. The method for controlling the resistance as the deposit is being performed, analogous to that for constrictions, has been evidenced to be very useful, and is now of general use in our laboratory.

By the study of the low temperature electrical properties of FIBID-W micro and nanowires, we have determined that wires with sub-100nm lateral width retain the superconducting properties. This, together with the outstanding properties of this material, as determined by Scanning-Tunneling-Spectroscopy measurements in the

group of Prof. Sebastián Viera, make FIBID-W a promising nanoscale superconductor. Nano-SQUIDS and Andreev reflection nanocontacts based on this nanodeposit are some promising applications currently developed in our group.

By the use of moderately high beam currents, FEBID-Co deposits (nanowires and nanostructures) were obtained, reaching the highest, up to now, metallic purity of the 90%. As a result, magnetotransport measurements in Co nanowires deposited in these conditions are similar to those of pure Co wires fabricated by conventional nanolithography techniques. When using low currents, the degradation of these properties was observed. By the use of spatially-resolved longitudinal Magneto-Optical-Kerr-effect, we have studied hysteresis loops in single wires with different aspect ratios. The coercive field is linear with the thickness/width ratio, indicating that the magnetostatic energy dominates the configuration of the magnetization in the wires. For high aspect ratios, the shape anisotropy forces the remanent magnetization to lie in the longitudinal direction of the NW. By creating L-shaped nanowires, and using two-dimensional field routines, we have demonstrated the good domain wall conduit behavior of this material. The unique advantages of this technique for creating 3-dimensional nanostructures make this result especially interesting. Steps in this direction are in progress. Besides, next steps should be given by performing experiments where the magnetization is switched by a spin-torque effect, and not by an external magnetic field.

Following works should, in general, be devoted to the study of the resolution limits of these techniques, and determine how their functional properties are affected when the sizes are reduced substantially. Another important aspect is to try to obtain purely metallic nanostructures, of interest in nanoelectronics. Further functionality of these deposits in a wide variety of applications is strongly desired. Finally, the combination of these materials to create hybrid devices such as magnetic/superconducting ones, together with the good control of the resistance, can imply the study of fascinating phenomena.

Bibliography

Chapter 1: Introduction

[1] R.P. Feynman, *Engineering and Science, Caltech,* February (1960)

[2] C.M. Vest, dissertation in Massachusetts Institute of Technology (2005)

[3] S. Bensasson, *Technology roadmap for nanoelectronics* (2000)

[4] G. Moore, *Electronics* **5**, 114 (1965)

[5] http://web.sfc.keio.ac.jp

[6] J. Ferrer, and V.M. García-Suárez, *J. Mater. Chem.***19**, 1696 (2009)

[7] L.R. Harriott, *IEEE Proceedings* (2001)

[8] T. Ito, and S. Okazak, *Nature* 406, 1027 (2000)

[9] The name of the technology means that the channel joining the source and drain in transistor has this size. In this case 45 nm.

[10] R. Chau, B. Doyle, S. Datta, J. Kavalieros, and K. Zhang, *Nat. Mat.* **6**, 810 (2007)

[11] A. Correira, and P.A Serena, "Nanociencia y Nanotecnología en España", *Fundación Phantoms,* 7 (2008)

[12] É. du Trémolet de Laceisserie, D. Gignoux, and M. Schlenker, "Magnetism", Vol. 2 ("Materials and applications"), chapter **21**, 305 *Springer* (2005)

[13] *MRS bulletin* **31**, May 2006

[14] E.E. Fullerton, SNOW School, Nancy (France), 2008

[15] P. Grünberg, R. Schreiber, Y. Pang, M.B. Brodsky and H. Sowers, *Phys. Rev. Lett.* **57**, 2442 (1986)

[16] M.T. Béal-Monod, *Phys. Rev. B* **36**, 8835 (1987)

[17] N. Mott, *Adv. Phys.* **13**, 325 (1964)

[18] A. Fert, and I.A. Campbell, *Phys. Rev. Lett.* **21**, 1190 (1968)

[19] C. Chappert, A. Fert, and F. Nguyen Van Dau, *Nat. Mat.* **6**, 813 (2007)

[20] R. Jansen, *J. Phys. D: Appl. Phys.* **36**, R289 (2003)

[21] I. Zutic, J. Fabian, and S. Dasma, *Rev. Mod. Phys.* **76**, 323 (2004)

[22] E.E. Fullerton, and I.K. Schüller, *ACS Nano* **5**, 384 (2007)

[23] A. Fert, *Rev. Mod. Phys.* **80**, 1517 (2008)

[24] P. Grünberg, *Rev. Mod. Phys.* **80**, 1531 (2008)

[25] M.N. Baibich, J.M. Broto, A. Fert, F. Nguyen Van Dau, F. Petroff, P. Etienne, G. Creuzet, A. Friederich, and J. Chazelas, *Phys. Rev. Lett.* **61**, 2472 (1988)

[26] G.P. Binasch, F. Grünberg, F. Saurenbach, and W. Zinn, *Phys. Rev. B* **39**, 4828 (1989)

[27] Classification adapted from J.L. Kosta-Krämers, "Nanociencia y Nanotecnología en España", *Fundación Phantoms,* 80 (2008)

[28] K. Roy, K.S. Yeo, "Low Voltage, Low Power VLSI Subsystems", *McGraw-Hill Professional* (2004)

[29] D.K. Ferry, *Science* **319**, 579 (2008)

[30] K. Uchida, J. Koga, R. Ohba, and A. Toriumi, Electron Devices Meeting, 2000

[31] G.I. Haddad, P. Mazmuder, and J.N. Schulmanm, *IEEE Proceedings* **86**, 641 (1998)

[32] L. Geppert, *IEEE Spectrum* 46, September 2000

[33] K.C. Schwab, and M.L. Roukes, *Phyics. Today* 37, July 2005

[34] F. Su, K. Chakrabarty, and R.B. Fair, IEEE Trans. Design Int. Circ. Sys. **25**, 211 (2006)

[35] J. Moodera, L.R. Kinder, R.M. Wong, R. Meservey, *Phys. Rev. Lett.* **74**, 3273 (1995)

(1985)

[36] M. Bowen, M. Bibes, A. Barthélémy, J.P. Contour, A. Anane, Y. Lemaître, A. Fert, *Appl. Phys. Lett.* **82**, 233 (2003)

[37] S. Mao, Y. Chen, F. Liu, X. Chen, B. Xu, P. Lu, M. Patwari, H. Xi, C. Chang, B.

Miller, D. Menard, B. Pant, J. Loven, K. Duxstad, S. Li, Z. Zhang, A. Johnston, R. Lamberton, M. Gubbins, T. McLaughlin, J. Gadbois, J. Ding, B. Cross, S. Xue, and P. Ryan, *IEEE Trans. Magn.* **42**, 97 (2006)

[38] J.M. Kikkawa, D.D. Aschwalom, I.P. Smorchkova, N. Samarth, *Science* **277**, 1284 (1997)

[39] P.R. Hammar, B.R. Bennett, M.J. Yang, and M. Johnson, *Phys. Rev. Lett.* **83**, 203 (1999)

[40] H.J. Zhu, M. Ramsteiner, H. Kostial, M. Wassermeier, H.-P. Schönherr, and K.H. Ploog *Phys. Rev. Lett.* 87, 016601 (2001)

[41] R. Fiederling, M. Keim, G. Reuscher, W. Ossau, G. Schmidt, A. Waag and L.W. Molenkamp, *Nature* **402**, 787 (1999)

[42] S. Datta, and B. Das, *Appl. Phys. Lett.* **56**, 665 (1990)

[43] J. Barnaś, and A. Fert, *Phys. Rev. Lett.* **80**, 1058 (1998)

[44] S. Takahashi, and S. Maekawa, *Phys. Rev. Lett.* **80**, 1758 (1998)

[45] A.R. Rocha, V. M. García-Suárez, S.W. Bailey, J.C. Lambert, J. Ferrer, and S. Sanvito, *Nat. Mat.* **4**, 335 (2005)

[46] Z.H. Xiong, D. Wu, Z.V. Vardeny, and J. Shi, *Nature* **427**, 821 (2004)

[47] A. Riminucci, I. Bergenti, L.E. Hueso, M. Murgia, C. Taliani, Y. Zhan, F. Casoli, M.P. de Jong, V. Dediu, arXiv:cond-mat/0701603v1

[48] T.S. Santos,J.S. Lee, P. Migdal, I.C. Lekshmi, B. Satpati, and J.S. Moodera, *Phys. Rev. Lett.* **98**, 016601 (2007)

[49] L.E. Hueso, J.M. Pruneda, V. Ferrari, G. Burnell, J.P. Valdés-Herrera, B.D. Simons, P.B. Littlewood, E. Artacho, A. Fert, N.D. Mathur, *Nature* **445**, 410 (2007)

[50] E.W. Hill, A.K. Geim, K. Novoselov, F. Schedin, P. Blake, *IEEE Trans. Magn.* **42**, 2694 (2006)

[51] R. Allenspach, and P.-O. Jubert, *MRS bulletin* **31**, 395 (2006)

[52] R.P. Cowburn, *J. Phys. D.: Appl. Phys.* **33**, R1 (2000)

[53] T. Ono, H. Muyajima, K. Sigheto, K. Mibu, N. Hosoito, and T. Shinjo, *Science* **284**, 468 (1999)

[54] S.S.P. Parkin, M. Hayashi, and L. Thomas, *Science* **320**, 190 (2008)

[55] D.A. Allwood, G. Xiong, C.C. Faulkner, D. Atkinson, D. Petit, R.P. Cowburn, *Science* **309**, 1688 (2005)

[56] V. S. Pribiag, I. N. Krivorotov, G. D. Fuchs, P. M. Braganca, O. Ozatay, J. C. Sankey, D. C. Ralph, R. A. Buhrman, *Nature Phys.* 3, 498 (2007)

[57] M. Weigand, B. Van Waeyenberge, A. Vansteenkiste, M. Curcic,V. Sackmann, H. Stoll, T. Tyliszczak, K. Kaznatcheev, D. Bertwistle, G. Woltersdorf, C.H. Back, and G. Schütz, *Phys. Rev. Lett.* **102**, 077201 (2009)

[58] M. R. Freeman and B. C. Choi, *Science* 294, 1484 (2001)

[59] L. Berger, *J. Appl. Phys.* **3**, 2156 (1978)

[60] P.P. Freitas, L. Berger, *J. Appl. Phys.* **57**, 1266 (1985)

[61] D.C. Ralph, and M.D. Stiles, *J. Magn. Magn. Mat.* **320,** 1190 (2008)

[62] J.A. Katine, F.J. Albert, R.A. Buhrman, E. B. Myers, and D. C. Ralph, *Phys. Rev. Lett.* 84, 3149 (2000)

[63] J. Grollier, V. Cros, A. Hamzic, J.M. George, H. Jaffrès, A. Fert, G. Faini, J. Ben Youssef, and H. Legall, *Appl. Phys. Lett.* **8**, 3663 (2001)

[64] C. Chappert, A. Fert, F. Van dau, *Nature Mat.* **6**, 813 (2006)

[65] S.I. Kiselev, J.C. Sankey, I.N. Krivorotov, N.C. Emley, R.J. Schoelkopf, R.A. Buhrman, and D.C. Ralph, *Nature (London)* **425**, 308 (2003)

[66] W. H. Rippard, M.R. Pufall, S. Kaka, S.E. Russek, and T. J. Silva, *Phys. Rev. Lett.* **92**, 027201 (2004)

[67] N. Vernier, D.A. Allwood, D. Atkinson, M.D. Cooke and R.P. Cowburn, *Europhys. Lett.*, **65(4)**,526 (2004)

[68] N. Grobert, *Materials Today* **10**, 28 (2007)

[69] M.P. Anantram, and F.L. Leonard, *Rep. Prog. Phys.* **69**, 507 (2006)

[70] N. Agraït, A.L. Yeyati, and J.M. Van Ruitenbeek, *Phys. Rep.* **377**, 81 (2003)

[71] A. Yu. Kasumov, K. Tsukagoshi, M. Kawamura, T. Kobayashi, Y. Aoyagi, K. Senba, T. Kodama, H. Nishikawa, I. Ikemoto, K. Kikuchi, V. T. Volkov, Yu. A. Kasumov, R. Deblock, S. Guéron, and H. Bouchiat, *Phys. Rev. B* **72**, 033414 (2005)

[72] A.K. Goel, *IEEE* 2008

[73] M. Forshaw, R. Stadler, D. Crawley, and K Nikolíc, Nanotechnology **15**, S220 (2004)

[74] A. Steane *Rep. Prog. Phys.* **61**, 117 (1998)

[75] A. Galindo and M.A. Martín-Delgado, *Rev. Mod. Phys.* **74**, 347 (2002)

[76] K.K. Berggren, *IEEE proceedings* **98**, 1630 (2004)

[77] A.T. Dorsey, *Nature* **408**, 783 (2000)

[78] A. J. Leggett, *Science* **296**, 861 (2002)

[79] M.A. Sillanpää, I. Park, and Raymond W. Simmonds *Nature* **449**, 438 (2007)

Chapter 2: Experimental techniques

[1] For details of the growth process: juliao@unizar.es

[2] LR Harriott, IEEE Proceedings (2001)

[3] T. Ito, and S. Okazak, Nature 406, 1027 (2000)

[4] H.J. Levinson, "Principles of Lithography", SPIE Press, 2nd edition (2005)

[5] Handbook of Microlithography, Micromachining, and Microfabrication, Volume 2, SPIE Press (1997)

[6] L. Gianuzzi, and F. Stevie, Introduction to Focused Ion Beams: Instrumentation, techniques, theory and practices, Springer Science+ Business Media, Boston (2005)

[7] J. Orloff, M. Utlaut, and L. Swanson, High Resolution Focused Ion Beams: FIB and Its

Applications, Kluwer Academic/Plenum Publishers, NY (2003)

[8] S. Matsui and Y. Ochiai, Nanotechnology 7, 247 (1996)

[9] W. Li, and P.A. Warburton, Nanotechnology 18, 485305 (2007)

[10] A. De Marco, and J. Melngailis, Solid State Electronics 48, 481833 (2004)

[11] G.C. Gazzadi and S. Frabboni, J. Vac. Sci. Technol. B 23, L1 (2005)

[12] A. Romano-Rodriguez, and F. Hernández-Ramirez, Microelectron. Eng., 84, 789 (2007)

[13] I. Utke, P. Hoffmann, R. Berger, L. Scandella, Appl. Phys. Lett., 80, 4792 (2002)

[14] E.S. Sadki, S. Ooi, K. Hirata, Appl. Phys. Lett., 85, 6206 (2004)

[15] N. Silvis-Clividjan, C.W. Hagen, and P. Kruit, J. Appl. Phys., 98, 084905, (2005)

[16] I. Utke, P. Hoffmann, and J. Melngailis, J. Vac. Sci. Technol. B 26, 1197 (2008)

[17] W.F. van Dorp, and C.W. Hagen, J. Appl. Phys. 104, 081301 (2008)

[18] A. Botman, J.J. Mulders, R. Weemaes, and S. Mentik, Nanotechnology 17, 3779 (2006)

[19] R.M. Langford, T.–X. Wang, and D. Ozkaya, Micr. Eng. 84, 748 (2007)

[20] R.P. Cowburn, D.K. Koltsov, A.O. Adeyeye, and M.E. Welland, Appl. Phys. Lett. 73, 3947 (1998)

[21] D.A. Alwood, G. Xiong, M.D. Cooke, and R.P. Cowburn, J. Phys. D.: Appl. Phys. 36, 2175 (2003)

Chapter 3: Magnetotransport properties in epitaxial Fe_3O_4 thin films

[1] M.L. Glasser, and F.J. Milford, *Phys. Rev.* **130**, 1783 (1963)

[2] E.J.W. Verwey, *Nature (London)* 144, 327 (1939)

[3] F. Walz, *J. Phys.: Condens. Matter* **14**, R285 (2002)

[4] J. García and G. Subías. *J. Phys.: Condens. Matter* **16**, R145 (2004)

[5] D. Ihle, and B. Lorenz, *J. Phys. C: Solid State Phys.* **18** L647 (1985)

[6] N.F. Mott, *Metal–Insulator Transitions 2nd edn (London: Taylor and Francis)* (1990)

[7] A. Yanase and K. Siratori, J. Phys. Soc. Jpn. **53**, 312 (1984

[8] Z. Zhang, and S. Satpathy, *Phys. Rev. B* **44**, 13319 (1991)

[9] S.F. Alvarado, W. Eib, F. Meier, D.T. Pierce, K. Sattler, and H.C. Siegmann, *Phys. Rev. Lett.* **34**, 319 (1975)

[10] M. Fonin, Yu S. Dedkov, R. Pentcheva, U Rüdiger, and G. Güntherodt, *J. Phys.: Condens. Matter* **19,** 315217 (2007)

[11] G. Hu, and Y. Suzuki, *Phys. Rev. Lett.* 89, 276601 (2002)

[12] J.Y.T. Wei, N.-C. Yeh, R.P. Vasquez, A. Gupta, *J. Appl. Phys.* **83**, 7366 (1998)

[13] M. Jullière, *Phys. Lett.* **74**, 3273 (1975)

[14] J.M. De Teresa, A. Barthélèmy, A. Fert, J.P. Contour, , R. Lyonnet, F. Montaigne, and P. Seneor, *Science* **286**, 507 (1999)

[15] W.H. Butler, X.G. Zhang, T.C. Schulthess, and J.M. MacLaren. *Phys. Rev. B* **63**, 054416 (2001)

[16] S Yuasa, and D.D. Djayaprawira, *J. Phys.D: Appl. Phys.* **40**, R337 (2007)

[17] W.E. Picket, and J.S. Moodera, *Phys. Today* **54(5)**, 39 (2001)

[18] C.M. Fang, G. A. de Wijs, and R. A. de Groot, *J. Appl. Phys.* **91**, 8340 (2002)

[19] D. Reisinger, P. Majewski, M.Opel, L. Alff, and R. Gross, *Appl. Phys. Lett.* **85**, 4980 (2004)

[20] A.V. Ramos, J.-B. Mouse, M.-J. Guittet, A.M. Bataille, M. Gautier-Soyer, M. Viret, C. Gatel and P. Bayle- Guillemaud, and E. Snoeck, *J. Appl. Phys.* **100**, 103902 (2006)

[21] W. Eerestein, T.T. M. Palstra, T. Hibma, and S. Celotto, *Phys. Rev. B* **66**, 201101(R) (2002)

[22] S. K. Arora, R. G. S. Sofin, I. V. Shvets, and M. Luysberg, *J. Appl. Phys.* **100**, 073908 (2006)

[23] Y. Zhu, and J.W. Cai, *Appl. Phys. Lett.* **90**, 012104 (2007)

[24] J.F. Bobo, D. Basso, E. Snoeck, C. Gatel, D. Hrabovsky, J.L. Gauffier, L. Ressier, R. Mamy, S. Vinsnovsky, J. Hamrle, J. Teillet, and A.R. Fert, *Eur. Phys. J. B* 24, 43 (2001)

[25] G.Q. Gong, A. Gupta, G. Xiao, W. Qian, and V.P. Dravid, *Phys. Rev. B* **56**, 5096 (1997)

[26] M. Ziese, and H.J. Blythe, *J. Phys. Condens. Matter* **12**, 13 (2000)

[27] D.T. Margulies, F.T. Parker, M. L. Rudee F.E. Spada, J. N. Chapman, P. R. Aitchison, and A.E. Berkowitz, *Phys. Rev. Lett* **79**, 5162 (1997)

[28] W. Eerenstein, T.T.M. Palstra, S.S. Saxena, and T. Hibma, *Phys. Rev. Lett.* **88**, 247204 (2002)

[29] D.J. Huang, C.F. Changa, J. Chena, L.H. Tjengc, A.D. Ratad, W.P. Wua, S.C. Chunga, H.J. Lina, T. Hibmad, and C. T. Chen, J. Magn. Magn. Mat. **239**, 261 (2002)

[30] D. Serrate, J.M. De Teresa, P.A. Algarabel, R. Fernández-Pacheco, M.R. Ibarra, J. Galibert, *J. Appl. Phys.* **97**, 084322 (2005)

[31] This piece of work forms part of the thesis of Julia Orna (University of Zaragoza): juliao@unizar.es

[32] L.J. van der Pauw, *Philips Technical Review* **36**, 220 (1958)

[33] The TEM work was done by César Magén (cmagen@unizar.es) and Ettiene Snoeck in the CEMES-CNRS laboratory in Toulouse (France)

[34] X.W. Li, A. Gupta, Gang Xiao, G.Q. Gong, *J. Appl. Phys.* **83**, 7049 (1998)

[35] J.P. Wright, J.P. Attfield, and P.G. Radaelli, *Phys. Rev. Lett.* **87**, 266401 (2001)

[36] W. Eerenstein, T. Hibma, and S. Celotto, *Phys. Rev. B* **70**, 184404 (2004)

[37] J. Kondo, *Prog. Theor. Phys.* **27**, 772 (1962)

[38] V.V. Gridin, G.R. Hearne, and J.M. Honing, *Phys. Rev. B* **53**, 15518 (1996)

[39] J.S-Y. Feng, R.D. Pashley, and M-A Nicolet, *J. Phys. C: Sol. State Phys.* **8**, 1010 (1975)

[40] I.A. Campbell, and A. Fert, *Magnetic Materials* **3** 747 (1982)

[41] G. Li , T. Yang, Q. Hu, H. Jiang, and W. Lai, *Phys. Rev. B* **65**, 134421 (2002)

[42] S.T.B. Goennenwein, R.S. Keizer, S.W. Schink, I. van Dijk, T.M. Klapwijk, G. X. Miao, G. Xiao, and A. Gupta, *Appl. Phys. Lett.* **90**, 142509 (2007)

[43] A. Schuhl, F. Nguyen Van Dau, and J.R. Childress, *Appl. Phys. Lett.* **66**, 2751 (1995)

[44] A.O. Adeyeye, M.T. Win, T.A. Tan, G.S. Chong, V.Ng, T.S. Low, *Sensors and Actuators A* **116**, 95 (2004)

[45] H.X. Tang, R.K. Kawakami, D.D. Awschalom, and M.L. Roukes, *Phys. Rev. Lett* **90**, 107201 (2003)

[46] K.Y. Wang, K.W. Edmonds, R.P. Camion, L.X. Zhao, C.T. Foxon, and B.L. Gallagher, *Phys. Rev. B* **72**, 085201 (2005)

[47] W.L. Lim, X. Liu, K. Dziatkowski, Z. Ge, S. Shen, J.K. Furdyna, and M. Dobrowolska, *J. Appl. Phys.* **99**, 08D505 (2006)

[48] D.Y. Shin, S.J. Chung, S. Lee, X. Liu, and J.K. Furdyna, *Phys. Rev. Lett.* **98**, 047201 (2007)

[49] H.X. Tang, S. Masmanidis, R.K. Kawakami, D.D. Awschalom, and M.L. Roukes, *Nature* 43, 52 (2004)

[50] H.X. Tang, and M.L. Roukes, *United States Patent* 6910382 (2004)

[51] X. Jin, R. Ramos, Y. Zhou, C. McEvoy, I. V. Shvets, *J. Appl. Phys*. **99**, 08C509 (2006)

[52] Y. Bason, L. Klein, H. Q. Wang, J. Hoffman, X. Hong, V. E. Henrich, and C. H. Ahn, J. *Appl. Phys. Lett.* **101**, 09J507 (2007)

[53] Y. Bason, L. Klein, J.-B. Yau, X. Hong, and C. H. Ahn, *Appl. Phys. Lett.* **84**, 2593 (2006)

[54] Y. Bason, L. Klein, J.-B. Yau, X. Hong, J. Hoffman, and C. H. Ahn, *J. Appl. Phys.* **99**, 08R701 (2006)

[55] V. Skumpryev, H.J. Blythe, J. Cullen, J.M.D. Coey, *J. Magn. Magn. Mater.* **196-197,** 515 (1999)

[56] I. Leonov and A.N. Yaresko, *J.Phys.: Condens. Matter* **19,** 021001 (2007)

[57] J. Smit, *Physica (Utretch)* **21**, 877 (1955), **24**, 39 (1958)

[58] L. Berger, *Phys. Rev. B* **2**, 4559 (1970)

[59] A. Crepiéux, and P. Bruno, *Phys. Rev. B* **6**4, 014416 (2001)

[60] R. Karplus, and J.M. Luttinger, *Phys. Rev.* **95**, 1154 (1954)

[61] G. Sundaram, and Q. Niu, *Phys. Rev. B* **59**, 14915 (1999)

[62] S. Onoda, N. Sugimoto, and N. Nagaosa, *Phys. Rev. Lett.* **97**, 126602 (2006)

[63] T. Miyasato, N.Abe, T.Fujii, A. Asamitsu, S. Onoda, Y. Onose, N. Nagaosa, and

Y. Tokura, *Phys. Rev. Lett.* **99**, 086602 (2007)

[64] T. Fukumura, H. Toyosaki, K. Ueno, M. Nakano, T. Yamasaki, and M. Kawasaki, J*pn J. Appl. Phys.* **46**, 26 (2007) and references therein

[65] Y. Zhu, and J.W. Cai, *Appl. Phys. Lett.* **90**, 012104 (2007)

[66] H. Liu , E. Y. Jiang, R.K. Zheng, and H.L. Bai, *J. Phys. : Condens. Matter* **15** 8003 (2003)

[67] J. Lavine, *Phys. Rev.* **123**, 1273 (1961)

[68] V. Brabers, F. Waltz, and H. Kronmuller, *Phys. Rev. B* **58**, 14163 (1998)

[69] D. Kostopoulos, and A. Theodossiou, *Phys. Stat. Sol. (a)* **2**, 73 (1970)

[70] S. Todo, K. Siratori and S. Kimura, *J. Phys. Soc. Jpn.* **64**, 6 (1995)

[71] Z. Chang, D. Satpathy, *Phys Rev. B* **44**, 13319 (1991)

[72] H. Toyosaki, T. Fukumura, Y. Yamada, K. Nakajima, T. Chikyow, T. Hasegawa, H. Koinuma, and M. Kawasaki, *Nat. Mater.* **3**, 221 (2004)

[73] K. Ueno, T. Fukumura, H. Toyosaki, M. Nakano, and M. Kawasaki, *Appl. Phys. Lett.* **90**, 072103 (2007)

[74] Y. Lyanda-Geller, S.H. Chun, M.B. Salamon, P.M. Goldbart, P.D. Han, Y. Tomioka, A. Asamitsu, and Y. Tokura, *Phys. Rev. B* **63**, 184426 (2001)

[75] P. Matl, N.P. Ong, Y.F. Yan, Y.W. Li, D. Studebaker, T. Baum, and G. Doubinina, *Phys. Rev. B* **57**, 10248 (1998)

[76] Y. Onose and Y. Tokura, *Phys. Rev. B* **73**, 174421 (2006)

[77] N. Manyala, Y. Sidis, J.F. Ditusa, G. Aeppli, D.P. Young, and Z. Fisk, *Nat. Mater.* **3**, 255 (2004)

[78] Y. Tomioka, T. Okuda, Y. Okimoto, R. Kumai, K.-I. Kobayashi, and Y. Tokura, *Phys. Rev. B* **61**, 422 (2000)

[79] R. Mathieu, A. Asamitsu, H. Yamada, K.S. Takahashi, M. Kawasaki, Z. Fang, N. Nagaosa, and Y. Tokura, *Phys. Rev. Lett.* **93**, 016602 (2004)

[80] F. Matsukura, E. Abe, and H. Ohno, *J. Appl. Phys.* **87**, 6442 (2000)

[81] K.W. Edmonds, R.P. Campion, K.-Y. Wang, A.C. Neumann, B.L. Gallagher, C.T. Foxon, and P.C. Main, *J. Appl. Phys.* **93**, 6787 (2003)

[82] A. Oiwa, A. Endo, S. Katsumoto, Y. Iye, and H. Ohno, *Phys. Rev. B* **59**, 5826 (1999)

[83] H. Ohno, H. Munekata, T. Penny, S. von Molnar, and L.L. Chang, *Phys. Rev. Lett.* **68**, 2664 (1992)

[84] F. Matsukura, H. Ohno, A. Shen, and Y. Sugawara, *Phys. Rev. B* **57**, R2037 (1998)

[85] D. Chiba, Y. Nishitani, F. Matsukura, and H. Ohno, *Appl. Phys. Lett.* **90**, 122503 (2007)

[86] S.U. Yuldashev, H.C. Jeon, H.S. Im, T.W. Kang, S.H. Lee, and J.K. Furdyna, *Phys. Rev. B* **70**, 193203 (2004)

Chapter 4: Conduction in atomic-sized magnetic metallic constrictions created by FIB

[2] N. Agraït, A. L. Yeyati, and J. M. Van Ruitenbeek, *Phys. Rep.* **377**, 81 (2003)

[3] Yu.V. Sharvin, *Sov. Phys.-JETP* **21**, 655 (1965)

[3] R. Landauer, *IBM J. Res. Dev.* **1**, 223 (1957)

[4] E. Scheer, N. Agraït, J. C. Cuevas, A.L. Yeyati, B. Ludoph, A. Martín-Rodero, G.R. Bollinger, J.M. van Ruitenbeek, and C. Urbina, *Nature* **394**, 154 (1998)

[5] J.M. van Ruitenbeek , A. Alvarez, I. Pineyro, C. Grahmann, P. Joyez, M.H. Devoret, D. Esteve, and C. Urbina, *Rev. Sci. Instrum.* **67,** 108 (1996)

[6] R. Wiesendanger, *Scanning Probe Microscopy and Spectroscopy, Cambridge University Press*, Cambridge, 1994.

[7] H. Park, A.K.L. Lim, A.P. Alivisatos, J. Park, and P.L. Mceuen, *Appl. Phys. Lett.* **75** 301 (1999)

[8] A.F. Morpurgo, C.M. Marcus, and D.B. Robinson, *Appl. Phys. Lett.* **74** 2084 (1999)

[9] Schep K M, Kelly P J and Bauer G E W, *Phys. Rev. Lett.* **74** 586 (1995)

[10] N. García, M. Muñoz, and Y. W. Zhao, *Phys. Rev. Lett.* **82**, 2923 (1999)

[12] N. García, M. Muñoz, G.G. Qian, H. Rohrer, I.G. Saveliev, and Y.W. Zhao, *Appl. Phys. Lett.* **79,** 4550 (2001)

[13] N. García, G.G. Qiang, and I.G. Saveliev, *Appl. Phys. Lett.* **80,** 1785–7 (2002)

[14] J.J. Versluijs, M.A. Bari, and J.M.D. Coey, *Phys. Rev. Lett.* **87,** 026601 (2001)

[15] S.H. Chung, M. Muñoz, N. García, W.F. Egelhoff, and R.D. Gomez *Phys. Rev.Lett.* **89,** 287203 (2002)

[16] P. Bruno, *Phys.Rev. Lett.* **83** 2425 (1999)

[17] W. F. Egelhoff, Jr., L. Gan, H. Ettedgui, Y. Kadmon, C. J. Powell, P. J. Chen, A. J. Shapiro, R. D. McMichael, J. J. Mallett, T. P. Moffat, and M. D. Stiles, E. B. Svedberg, *J. Appl. Phys.* **95**, 7554 (2004)

[18] M. I. Montero, R. K. Dumas, G. Liu, M. Viret, O. M. Stoll, W. A. A. Macedo, and I.K. Schuller, *Phys. Rev. B* **70**, 184418 (2004)

[19] O. Ozatay, P. Chalsani, N. C. Emley, I. N. Krivorotov, and R. A. Buhrman, *J. Appl. Phys.* **95**, 7315 (2004)

[20] B. Doudin, and M. Viret, *J. Phys.: Cond. Matter.* **20**, 083201 (2008)

[21] N.F. Mott , *Proc. R. Soc. A* **153,** 699 (1936)

[22] J. Smit, *Physica* **17,** 612 (1951)

[23] R. Potter, *Phys. Rev. B* **10,** 4626 (1974)

[24] P. Gambardella, A. Dallmeyer, K. Maiti, M.C. Malagoli, W. Eberhardt, K. Kern, and C. Carbone, *Nature* **416,** 301 (2002)

[25] J. Velev, R. F. Sabirianov, S. S. Jaswal, and E. Y. Tsymbal, *Phys. Rev. Lett.* **94**, 127203 (2005)

[26] D. Jacob, J. Fernández-Rossier, and J. J. Palacios, *Phys. Rev. B* **77**, 165412 (2008)

[27] A. Sokolov, C. Zhang, E. Y. Tsymbal, J. Redepenning, and B. Doudin, *Nat. Nanotechnology* **2**, 171 (2007)

[28] 18. M. Viret, M. Gauberac, F. Ott, C. Fermon, C. Barreteau, G. Autes, and R. Guirado López, *Eur. Phys. J. B* **51**, 1 (2006)

[29] S. –F. Shi, and D. C. Ralph, *Nat. Nanotech.* **2**, 522 (2007)

[30] N. García, C. Hao, L. Yonghua, M. Muñoz, Y. Chen, Z. Cui, Z. Lu, Y. Zhou, G. Pan, A.A. Pasa, *Appl. Phys. Lett.* **89**, 083112 (2006)

[31] P. Krzysteczko, and G. Dumpich, *Phys. Rev. B* **77**, 144422 (2008).

[32] T. Huang, K. Perzlaimer, and C.H. Back, Phys. Rev. B **79**, 024414 (2009)

[33] O. Céspedes, S.M. Watts, J.M. Coey,K. Dörr, and M. Ziese, *Appl. Phys. Lett.* **87**, 083102 (2005)

[34] S. Khizroev, Y. Hijazi, R. Chomko, S. Mukherjee, R. Chantell. X. Wu, R. Carley, abd D. Litvinov, *Appl. Phys. Lett.* **86**, 042502 (2005)

[35] I. V. Roshchin, J. Yu, A.D. Kent, G.W. Stupian, and M.S. Leung, *IEEE. Trans. Magn. Mat*. **37**, 2101 (2001)

[36] C. Sirvent, J.G. Rodrigo, S. Vieira, N. JurczyszynMingo, and F. Flores, *Phys. Rev. B* **53** 16086 (1996)

[37] J.J. Palacios, A.J. Pérez-Jiménez, E. Louis, E. SanFabián, and J.A. Vergués, *Phys. Rev. B* **66,** 035322 (2002)

[38] A. Hasmy A, A.J. Pérez-Jiménez, J.J. Palacios, P. García-Mochales, J.L. Costa-Kramers, M. Díaz, E. Medina, and P.A. Serena, *Phys. Rev. B* **72** 245405 (2005)

[39] F. Pauly, M. Dreher, J.K. Viljas, M. Häfner, J.C. Cuevas, and P. Nielaba, *Phys. Rev. B* **74** 235106 (2006)

[40] D.R. Strachan, D.E. Johnston, B.S. Guitom, S.S. Datta, P.K. Davies, D.A. Bonell, and A.T.C. Johnson, *Phys. Rev. Lett.* **100** 056805 (2008)

[41] L. Giannuzzi L, and F.A. Stevie, Introduction to Focused Ion Beams: Instrumentation, techniques, theory and practices, *Springer Science+Business Media,* Boston (2005)

[42] J.G. Simmons, *J. Appl. Phys.* **34,** 1793 (1963)

[43] H.B. Michaelson, *J. Appl. Phys.* **48,** 4729 (1977)

[44] See chapter 5, section 5.2. for details

[45] J.S. Moodera, and G. Mathon, *J. Magn. Mag. Mat* **200**, 248 (1999)

[46] J.V. Oboňa , J.M. de Teresa, R. Córdoba, A. Fernández-Pacheco, M.R. Ibarra, *Micr. Eng.* **86**, 639 (2009)

Chapter 5: Pt-C nanowires created by FIBID and FEBID

[1] L. Peñate-Quesada, J. Mitra, and P. Dawson, Nanotech. **18**, 215203 (2007)

[2] R. M. Langford, T. –X. Wang, and D. Ozkaya, Micr. Eng. **84**, 748 (2007)

[3] J-F. Lin, J.P. Bird, L. Rotkina, and P.A. Bennett, Appl. Phys. Lett., **82**, 802 (2003)

[4] J-F. Lin, J.P. Bird, L. Rotkina, A. Sergeev, and V. Mitin, Appl. Phys. Lett. **84**, 3828 (2004)

[5] J-F. Lin, L. Rotkina J.P. Bird, A. Sergeev, and V. Mitin , IPAP Conf. Series **5**, 17 (2004)

[6] T. Tao, J. Ro, and J. Melngailis, J. Vac. Sci Technol. B **8**, 1826 (1990)

[7] J. Puretz, and L. W. Sawson, J. Vac. Sci Technol. B **10**, 2695 (1992)

[8] K. A. Telari, B. R. Rogers, H. Fang, L. Shen, R. A. Weller, and D. N. Braski, J. Vac. Sci Technol. B **20(2)**, 590 (2002)

[9] J. M. De Teresa, R. Córdoba, A. Fernández-Pacheco, O. Montero, P. Strichovanec, M.R. Ibarra, J. Nanomat. **2009**, 936863 (2009)

[10] Y. Tsukatani, N. Yamasaki, K. Murakami, F. Wakaya, abd M. Takai, Jpn. J. Appl. Phys. **44**, 5683 (2005)

[11] K. Dovidenko, J. Rullan, R. Moore, K. A. Dunn, R. E. Geer, and F. Heuchling, Mat. Rec. Soc. Symp. Proc. **739**, H7.7.1 (2003)

[12] G. De Marzi, D, Lacopino, A. J. Quinn, and G. Redmond, J. Appl. Phys. **96**, 3458 (2004)

[43] D. Spoddig, K. Schindler, P. Rodiger, J. Barzola-Quiquia, K. Fritsch, H. Mulders, and P. Esquinazi, Nanotech. **18**, 495202 (2007)

[14] M. Prestigiacomo, L. Roussel, A. Houël, P. Sudraud, F. Bedu, D. Tonneau, V. Safarov**,** and H. Dallaporta, Microel. Eng. **76**, 175 (2004)

[15] T. Scwamb, B. R. Burg, N. C. Schirmer, and D. Poulikakos, Appl. Phys. Lett. **92**, 243106 (2008)

[16] F. Hernández–Ramírez, A. Tarancón, O. Casals, E. Pellicer, J. Rodríguez, A. Romano – Rodriguez, J. R. Morante, S. Barth, S. Mathur. Phys. Rev. B, **76** 085429 (2007)

[17] G. Boero, I. Utke, T. Bret, N. Quack, M. Todorova, S. Mouaziz, P. Kejik, J.

Brugger, R.S. Popovic, and P. Hoffmann, Appl. Phys. Lett. **86**, 042503 (2005)

[18] S. Doniach., and M. Sunjic, J. Phys C **3**, 285 (1970)

[19] S. Hüfner, and G. K. Wertheim, Phys. Rev. B **11**, 678 (1975)

[20] K. Ohya, T. Ishitani, Appl. Surf. Sci. **237**, 606 (2004)

[21] I. Utke, P. Hoffmann, and J. Melngailis, J. Vac. Sci. Technol. B **26**, 4 (2008)

[22] A. D. Dubner, A. Wagner, J. Melngailis, and C. V. Thompson, J. Appl. Phys 70, 665 (1991)

[23] SRIM is a group of programs which calculate the stopping and range of ions into matter using an ion-atom collisions treatment. The simulator is available in http://www.srim.org/#SRIM

[24] W. F. van Dorp, and C. W. Hagen, J. Appl. Phys. **104**, 081301 (2008)

[25] I. Utke, J. Michler, P. Gasser, C. Santschi, D. Laub, M. Cantoni, P.A. Buffat, C. Jiao, and P. Hoffmann, Adv. Eng. Mater. **7**, 323 (2005)

[26] S. Takabayashi, K. Okamoto, K. Shimada, K. Motomitsu, H. Motoyama, T. Nakatani, H. Sakaue, H. Suzuki, and T. Takahagi, Jpn. J. Appl. Phys. **47**, 3376 (2008)

[27] J. Díaz, G. Paolicelli, S. Ferrer, and F. Comin, Phys. Rev. B **54**, 8064 (1996)

[28] V. Alderucci, L. Pino, P. L. Antonucci, W. Roh, J. Cho, H. Kim, D. L. Cocke, V. Antonucci, Mat. Chem. Phys **41**, 9 (1995)

[29] S. Frabboni, G. C. Gazzadi, A. Spessot, Physica E **37**, 265 (2007)

[30] C. D. Wagner,W. M. Riggs, L. E. Davis, J. F. Moulder, and G. E. Muilenberg, *Handbook of X-Ray Photoelectron Spectroscopy*, Perkin-Elmer Corporation, Physical Electronics Division, Eden Prairie, Minn. 55344 (1979)

[31] R. C. Baetzold, G. Apai, and E. Shustorovich, and R. Jaeger, Phys. Rev. B 26, 4022 (1982)

[32] T. T. P. Cheung, Surf. Sci. **140**, 151 (1984)

[33] A. Y. Stakheev, Y. M. Shulga, N. A. Gaidai, N. S. Telegina, O. P. Tkachenko, L. M. Kustov, and K. M. Minachev, Mendeleev. Commun **11(5)**, 186 (2001)

[34] K. Fauth, N. Schneider, M. HeβIer, and G. Schütz, Eur. Phys. J. D **29** 57 (2004)

[35] N. F. Mott, and E. A. Davis, *Electronic Processes in Non-Crystalline Materials,* Oxford University Press (1971)

[36] A. Möbius, C. Frenzel, R. Thielsch, R. Rosenbaum, C. J. Adkins, M. Cheiber, H. –D. Bauer, R. Grötzschel, V. Hoffmann, T. Krieg, N. Matz, and H. Vinzelberg, M. Witcomb, Phys. Rev. B **60**, 14209 (1999)

[37] V. Prasad, Sol. State.Com **145** 186 (2008)

[38] S. Bhattacharyya, S. R. P. Silva, Thin Solid Films **482**, 94 (2005)

[39] A. L. Efros, and B. I. Shklovskii, J. Phys. C **78**, L49 (1975)

[40] Z-M. Liao, J. Xun, D-P. Yu, Phys. Lett. A. **345**, 386 (2005)

[41] L. I. Glazman, and K. A. Matveev, Sov. Phys. JETP **67**, 1276 (1988)

[42] R. U. A. Khan, J. D. Carey, R. P. Silva, B. J. Jones, And R. C. Barklie, Phys. Rev. B **63**, 121201(R) (2001)

[43] J. Robertson, Mat. Sci. Eng. R **129** (2002)

[44] D. Yu, C. Wan, B. Wherenberg, and P. Guyot Sionnest, Phys. Rev. Lett. **92**, 216802 (2004)

[45] H. Böttger, and V. V. Bryksin, Phys. Status Solidi B **96**, 219 (1979)

[46] N. Van Lien, and B. I. Shklovskii, Solid State Commun. **38**, 99 (1981)

[47] D. I. Aladashvili, Z. A. Adamia, K. G. Lavdovskii, E. I. Levin, and B. I. Shklovskii, Phys. JETP **47**, 466 (1988)

[48] A. Grill, Diamond. Relat. Mater. **10**, 234 (2001)

[49] A.P. Mel'nikov, Yu A. Gurvich, L.N. Shestakov, and E.M. Gershenzon, JETP Lett., **73**, 50 (2001)

[50] A. V. Nenashev, F. Jansson, S. D. Baranovskii, R. Österbacka, A. V. Dvurechenskii, and F. Gebhard, Phys. Rev. B **78**, 165207 (2008)

[51] Y. Tsukatani, N. Yamasaki, K. Murakami, F. Wakaya, and M. Takai, Jpn. Jour. Appl. Phys. **44**, 5683–5686 (2005)

[52] This piece of work forms part of the thesis of Rosa Córdoba (University of Zaragoza: rocorcas@unizar.es)

Chapter 6: Superconductor W-based nanowires created by FIBID

[5] H. Kamerlingh Onnes, *Leiden Commun.* **120** b (1911)

[2] Y. Kamihara, T. Watanabe, M. Hirano, and H. Hosono, *J. Am. Chem. Soc.* **130**, 3296 (2008)

[3] K.Yu. Arutyunov, D.S. Golubev, A.D. Zaikin, *Physics Reports* **464**, 1 (2008)

[4] L.F. Chibotauro, A. Ceulemans, V. Bruyndoncx, and V.V. Moschalkov, *Nature* **408**, 833 (2000)

[5] I.V. Grigorieva, A. K. Geim, S.V. Dubonos, and K. S. Novoselov, *Phys. Rev. Lett.* **92**, 237001 (2004)

[6] M. Velez, J.I. Martín, J.E. Villegas, A. Hoffmann, E.M. González, J.L. Vicent, and I.K. Schuller, J. Magn. Magn. Mater. **320**, 2547 (2008)

[7] C. Granata, E. Exposito, A. Vettoliere, L. Petti, M. Russo, *Nanotechnology* **19**, 275501 (2008)

[8] C.H. Wu, Y.T. Chou, W. CKuo, J.H. Chen, L.M. Wang, J.C Chen, K.L. Chen, U.C. Sou, H.C. Yang, and J.T. Jeng, *Nanotechnology* **19**, 315304 (2008)

[9] J. Clarke, and F.K. Wilhelm, *Nature* **453**, 1031 (2008)

[10] A.J. Legget, Science 296, 861 (2002)

[11] E.S. Sadki, S. Ooi, and K. Hirata, *Appl. Phys. Lett.* **85**, 6206 (2004)

[12] J.G. Gibson, and R.A. Hein, *Phys. Rev. Lett.* **12**, 688 (1964)

[13] I.J. Luxmoore, I.M. Ross, A.G. Cullis, P.W. Fry, J. Orr, P.D. Buckle, and J.H. Jefferson, *Thin Solid Films* **515**, 6791 (2007)

[14] D. Spoddig, K. Schindler, P. Rödiger, J. Barzola-Quiquia, K. Fristch, H. Mulders, and P. Esquinazi, *Nanotechnology* **18**, 495202 (2007)

[15] W. Li, J. C. Fenton, Y. Wang, D.W. McComb, and P.A. Warburton, J. Appl. Phys. **104**, 093913 (2008)

[16] M. S. Osofsky, R. J. Soulen, Jr., J. H. Claassen, G. Trotter, H. Kim, and J.S. Horwitz, *Phys. Rev. Lett.* **87**, 197004 (2001)

[77] A.Y. Kasumov , K. Tsukagoshi, M. Kawamura, T. Kobayashi, Y. Aoyagi, K. Senba, T. Kodama, H. Nishikawa, I. Ikemoto, K. Kikuchi, V. T. Volkov, Yu. A. Kasumov, R. Deblock, S. Guéron, and H. Bouchiat, *Phys. Rev. B* **72**, 033414

(2005)

[18] A. Shailos, W. Nativel, A. Kasumov, C. Collet, M. Ferrier, S. Guéron, R. Deblock, and H. Bouchiat, *Europhysics Letters* **79,** 57008 (2007)

[19] This piece of work forms part of the thesis of Rosa Córdoba (University of Zaragoza: rocorcas@unizar.es)

[20] See section 5.2.2.3. of this thesis

[21] J. Luthin, and Ch. Linsmeier, *Surf. Sci.* **454-456**, 78 (2000)

[22] M. Xu, W. Zhang, Z. Wu, and S. Pu, *J. Appl. Phys* **102**, 113517 (2007)

[23] J. Díaz, G. Paolicelli, S. Ferrer, and F. Comin, *Phys. Rev. B* **54**, 8064-8069 (1996)

[24] R. Haerle, E. Riedo, A. Pasquarello, and A. Baldereschi, *Phys. Rev. B* **65**, 045101 (2002)

[25] W.L. Bond, A.S. Cooper, K. Andres, G.W. Hull, T.H. Geballe, and B.T. Matthias, *Phys. Rev. Lett.* **15**, 260 (1965)

[26] R.H. Willens, and E. Buehler, *Appl. Phys. Lett.* **7**, 25 (1965)

[27] M.M. Collver, and R.H. Hammond, *Phys. Rev. Lett.* **30**, 92 (1973)

[28] S. Kondo, J. Mater. Res. 7, 853 (1992)

[29] H. Miki, T. Takeno, T. Takagi, A. Bozhko, M. Shupegin, H. Onodera, T. Komiyama, T. Aoyama, *Diamond and Relat. Mat.* **15**, 1898 (2006)

[30] I. Guillamón, H. Suderow, S. Vieira, A. Fernández-Pacheco, J. Sesé, R. Córdoba, J.M. De Teresa, and M.R. Ibarra, *New Journal of Physics* **10**, 093005 (2008)

[31] J. M. De Teresa, A. Fernández-Pacheco, R. Córdoba, J. Sesé, M. R. Ibarra, I. Guillamón, H. Suderow, and S. Vieira, submitted to *MRS proceedings* (2009)

[32] M.C. Hellerqvist, D. Ephron, W.R. White, M.R. Beasley, and A. Kapitulnik, *Phys. Rev. Lett.* **76**, 4022 (1996)

[33] N. Kokubo T. Asada, K. Kadowaki,K. Takita, T.G. Sorop, and P.H. Kes, *Phys. Rev. Lett.* **75**, 184512 (2007)

[34] This work is part of the thesis of Isabel Guillamón (isabel.guillamon@uam.es)

[35] I. Guillamón, H. Suderow, S. Vieira, A. Fernández-Pacheco, J. Sesé, R. Córdoba, J.M. De Teresa, and M.R. Ibarra, *J. Phys. Conf. Series* **152**, 052064 (2009)

[36] I. Guillamón, H. Suderow, A. Fernández-Pacheco, J. Sesé, R. Córdoba, J.M. De Teresa, M.R. Ibarra, and S. Vieira (2009)

[37] Ø. Fischer, M. Kugler, I. maggio-Apprile, and C. Berthod, *Rev. Mod. Phys.* **79**, 353 (2007)

[38] H.F. Hess, R.B. Robinson, R.C. Dynes, J.M. Valles, and J.V. Waszczak, *Phys. Rev. Lett.* **62** 214 (1989)

[39] R.J. Soulen Jr., J.M. Byers, M.S. Osofsky, B. Nadgorny, T. Ambrose, S.F. Cheng, P.R. Broussard, C.T. Tanaka, J. Nowak, J.S. Moodera, A. Barry, J. M.D. Coey, *Science* **282,** 85 (1998)

Chapter 7: Magnetic cobalt nanostructures created by FEBID

[1] W.F. Van Dorp, and Hagen C.W. *J. Appl. Phys.* **104,** 081301 (2008)

[2] I. Utke, P. Hoffmann, and J. Melngailis *J. Vac. Sci. Technol B* **26(4)** 1197 (2008)

[3] Examples of how materials deposited by these techniques deviate from the metallic behavior can be found in chapters 5 and 6 of this thesis, for Pt- and W-based deposits, respectively

[4] R.M. Langford, T.X. Wang, and D. Ozkaya, *Microelectron. Eng.* **84** 784 (2007)

[5] A. Botman, J.J.L. Mulders, R. Weemaes, and S. Mentink, *Nanotechnology* **17** 3779 (2006)

[6] M. Takeguchi, M. Shimojo , and K. Furuya, *Nanotechnology* **16**, 1321 (2005)

[7] M. Takeguchi, M. Shimojo , R. Che, and K. Furuya, *J. Mater Sci.* **41**, 2627 (2006)

[8] M. Shimojo, M. Takeguchi, K. Mitsuishi, M. Tanaka, and K. Furuya, *Jpn.J. Appl. Phys.* **9B**, 6247 (2007)

[9] M. Beljaars' thesis, Eindhoven University of Technology (The Netherlands)

[10] A. Lapicki, E. Ahmad, and T.Suzuki, *J. Magn. Magn. Mater.* **240**, 1-3 (2002)

[11] I. Utke, P. Hoffmann, R. Berger, and L. Scandella, *Appl. Phys. Lett.* **80**, 4792 (2002)

[12] G. Boero, I. Utke, T. Bret, N. Quack, M. Todorova, S. Mouaziz, P. Kejik, J. Brugger, R.S. Popovic, and P. Hoffmann, *Appl. Phys. Lett.* **86**, 042503 (2005)

[13] I. Utke, T. Bret, D. Laub, Ph. Buffat, L.Scandella, and P. Hoffmann, *Micr. Eng.* **73**, 553 (2004)

[14] I. Utke I, J. Michler, P. Gasser, C. Santschi, D. Laub, M. Cantoni, P. A. Buffat, C. Jiao, and P. Hoffmann, *Adv. Eng. Mater.* **7,** 323 (2005)

[15] Y. M. Lau, P. C. Chee, J. T. L. Thong, and V. Ng,, *J. Vac. Sci. Technol. A* **20(4)**, 1295 (2002)

[16] D. A. Alwood, Gang Xiong, M. D. Cooke, and R. P. Cowburn., *J. Phys D: Appl. Phys.* **36**, 2175-2182 (2003)

[17] This piece of work forms part of the thesis of Rosa Córdoba (University of Zaragoza: rocorcas@unizar.es)

[18] See chapter 5 of this thesis

[19] J. Kötzler and W. Gil, *Phys. Rev. B* **72**, 060412(R) (2005)

[20] S. Onoda, N. Sugimoto, and N. Nagaosa, *Phys. Rev. Lett.* **97**, 126602 (2006)

[21] S. Sangiao, L. Morellón, G. Simón, J.M. De Teresa, J.A. Pardo, M.R. Ibarra, *Phys. Rev. B*, **79**, 014431 (2009)

[22] M. Rubinstein, F. J. Rachford, W. W. Fuller, and G. A. Prinz, *Phys. Rev. B* **37,** 8689 (1988)

[23] B. Leven, and G. Dumpich, *Phys. Rev. B* **71**, 064411 (2005)

[24] M. Brands, and G. Dumpich, *J. Appl. Phys*. **98**, 014309 (2005)

[25] W. Gil, D. Görlitz, M. Horisberger, and J. Kötzler, *Phys. Rev. B* **72**, 134401 (2005)

[26] I.A. Campbell and A. Fert, *E.P. Wohlfarth, (Ed.), Ferromagnetic Materials, North-Holland, Amsterdam*, vol. 3, p. 747 (1982)

[27] A. Himeno, T. Okuno, K. Mibu, S. Nasu, and T. Shinjo, *J. Magn. Magn, Mater.* **286**, 167 (2005)

[28] W. Wernsdorfer W, E. Bonet Orozco, K. Hasselbach, A. Benoit, B. Barbara, N. Demoncy, A. Loiseau, H. Pascard, and D. Mailly, *Phys. Rev. Lett.* **78**, 1791 (1997)

[29] R.P. Cowburn *J. Phys. D: Appl. Phys.* **33**, R1 (2000)

[30] W.C. Uhlig, and J. Shi, *Appl. Phys. Lett.* **84**, 759 (2004)

[31] J. Vogel, J. Moritz, and O. Fruchart, *C.R. Physique* **7**, 977 (2006)

[32] M. Brands, R. Wieser, C. Hassel, D. Hinzke, and G. Dumpich, *Phys. Rev. B.* **74**, 174411 (2006)

[33] T. Wang, Y. Wang, Y. Fu, T. Hasegawa, F.S. Li, H. Saito, and S. Ishio *Nanotechnology.* **20**, 105707 (2009)

[34] I. Zutic, J. Fabian, and S. Das Sarma, *Rev. Mod. Phys* **76**, 323 (2004)

[35] L. Reimer, and M. Wächter, *Ultramicroscopy* **3**, 169 (1978)

[36] H-J. Fitting, and Reinhardt *Phys. Stat. Sol. A* **88**, 245 (1985)

[37] We have performed EELS measurements (not shown here), which confirm this statement.

[38] S.Y. Yuan, H.N. Bertram, J.F. Smyth, and S. Schultz, *IEEE Trans. Magn.* **28**, 3171 (1992)

[39] H. Suhl, and H.N. Bertram, *J. Appl. Phys.* **82(12)**, 6128 (1997)

[40] R.P. Cowburn, D. Petit, Nat. Mat. **4**, 721-722 (2005)

[41] T. Ono, H. Miyajima, K. Shigeto, M. Kibu, N. Hosoito, and T. Shinjo, *Science* **284**, 468 (1999)

[42] D.C. Ralph, and M.D. Stiles, Journ. Magn. Magn. Mat. **320**, 1190 (2008)

[43] D.A. Alwood, G. Xiong, C.C. Faulkner, D. Atkinson, D. Petit, R.P. Cowburn, *Science* **309**, 1688 (2005)

[44] S.S. Parkin, M. Hayashi, L. Thomas, *Science* **320** 191 (2008)

[45] D. Atkinson, D.S. Eastwood, and L.K. Bogart, *Appl. Phys. Lett.* **92**, 022510-1 (2008)

[46] D. Petit, A.-V. Jausovec, D.E.Read, and R.P. Cowburn, J. Appl. Phys. **103**, 11437 (2008)

[47] D. Petit, A.-V. Jausovec, H. T. Zeng, E. Lewis, L. O'Brien, D. E. Read, and R. P. Cowburn, Appl. Phys. Lett. **93**, 163108 (2008)

Publications

17 articles are the result of the work of this thesis. 11 of them are already published in journals that belong to the Science Citation Index, 3 are in under review process, and 3 are in preparation. I list here all of them, classified by subject.

Magnetotransport properties in Fe_3O_4 thin films:

[I] J.M. De Teresa, A. Fernández-Pacheco, L. Morellón, J. Orna, J.A. Pardo, D. Serrate, P.A. Algarabel, and M.R. Ibarra, "Magnetotransport properties of Fe_3O_4 thin films for applications in Spin Electronics", *Microelectronic Engineering* **84**, 1660 (2007)

[II] A. Fernández-Pacheco, J.M. De Teresa, J. Orna, L. Morellón, P.A. Algarabel, J.A. Pardo, and M.R. Ibarra, "Universal Scaling of the Anomalous Hall Effect in Fe_3O_4 thin films, *Physical Review B (Rapid com.)* **77,** 100403(R) (2008)

[III] A. Fernández-Pacheco, J.M. De Teresa, J. Orna, L. Morellon, P.A. Algarabel, J.A. Pardo, M.R. Ibarra, C. Magen, and E. Snoeck, "Giant planar Hall effect in epitaxial Fe_3O_4 thin films and its temperature dependence", *Physical Review B* **78**, 212402 (2008)

[IV] A. Fernández-Pacheco, J. M. De Teresa, P.A. Algarabel, J. Orna, L. Morellón, J. A. Pardo, and M.R. Ibarra, "Hall effect and magnetoresistance measurements in Fe_3O_4 thin films up to 30 Tesla", *manuscript in preparation*

Creation of atomic-sized nanoconstrictions

[V] A. Fernández-Pacheco, J. M. De Teresa, R. Córdoba, and M.R. Ibarra, "Exploring the conduction in atomic-sized metallic constrictions created by controlled ion etching",

Nanotechnology **19**, 415302 (2008)

[VI] J. V. Oboňa, J.M. De Teresa, R. Córdoba, A. Fernández-Pacheco, and M. R. Ibarra, "Creation of stable nanoconstrictions in metallic thin films via progressive narrowing by focused-ion-beam technique and in-situ control of resistance", *Microelectronic Engineering* **86**, 639 (2009)

[VII] A. Fernández-Pacheco, J.M. De Teresa, R. Córdoba, and M.R. Ibarra, "Tunneling and anisotropic-tunneling magnetoresistance in iron nanoconstrictions fabricated by focused-ion-beam", submitted to *MRS DD proceedings* (2009)

Pt-C nanowires created by Focused Electron/Ion Beam Induced Deposition

[VIII] J.M. De Teresa, R. Córdoba, A. Fernández-Pacheco, O. Montero, P. Strichovanec, and M.R. Ibarra, "Origin of the Difference in the Resistivity of As-Grown Focused-Ion and Focused-Electron-Beam-Induced Pt Nanodeposits", *Journal of Nanomaterials* **2009**, 936863 (2009)

[IX] A. Fernández-Pacheco, J.M. De Teresa, R. Córdoba, M.R. Ibarra, "Conduction regimes of Pt-C nanowires grown by Focused-Ion–Beam induced deposition: Metal-insulator transition", *Physical Review B* **79**, 79, 174204 (2009)

W-based nanodeposits created by Focused Ion Beam Induced Deposition

[X] I. Guillamón, H. Suderow, S. Vieira, A. Fernández-Pacheco, J. Sesé, R. Córdoba, J.M. De Teresa, M.R. Ibarra, "Nanoscale superconducting properties of amorphous W-based deposits grown with a focused-ion-beam", *New Journal of Physics* **10**, 093005 (2008)

[XI] I. Guillamón, H. Suderow, S. Vieira, A. Fernández-Pacheco, J. Sesé, R. Córdoba, J.M. De Teresa, M. R. Ibarra, "Superconducting density of states at the border of an amorphous thin film grown by focused-ion-beam", *Journal of Physics: Conference Series* **152**, 052064 (2009)

[XII] J. M. De Teresa, A. Fernández-Pacheco, R. Córdoba, J. Sesé, M. R. Ibarra, I. Guillamón, H. Suderow, S. Vieira**, "***Transport properties of superconducting amorphous W-based nanowires fabricated by focused-ion-beam-induced-deposition for applications in Nanotechnology",* submitted to *MRS CC proceedings* (2009)

[XIII] I. Guillamón, H. Suderow, A. Fernández-Pacheco, J. Sesé, R. Córdoba, J. M. De Teresa, M.R. Ibarra, and S. Vieira, "Direct observation of melting in a 2-D superconducting vortex lattice" (2009)

Co nanowires created by Focused Electron Beam Induced Deposition

[XIV] A. Fernández-Pacheco, J. M. De Teresa, R. Córdoba, M. R. Ibarra, "Magnetotransport properties of high-quality cobalt nanowires grown by focused-electron-beam-induced deposition", *Journal of Physics D: Applied Physics* **42,** 055005 (2009)

[XV] A. Fernández-Pacheco, J. M. De Teresa, R. Córdoba, M. R. Ibarra D. Petit , D. E. Read, L. O'Brien, E. R. Lewis, H. T. Zeng, and R.P. Cowburn, "Domain wall conduit behavior in cobalt nanowires grown by Focused-Electron-Beam Induced Deposition", *Applied Physics Letters* **94**, 192509 (2009)

[XVI] A. Fernández-Pacheco, J. M. De Teresa, R. Córdoba, M. R. Ibarra D. Petit , D. E. Read, L. O'Brien, E. R. Lewis, H. T. Zeng, and R.P. Cowburn, "Systematic study of the magnetization reversal in Co wires grown by focused-electron-beam-induced deposition", manuscript in preparation

[XVII] A. Fernández-Pacheco, J. M. De Teresa, R. Córdoba, M. R. Ibarra D. Petit , D. E. Read, L. O'Brien, E. R. Lewis, H. T. Zeng, R.P. Cowburn, and U. Zeitler "Magnetic coupling of Co electrodes joined by a constriction: geometrical effects", manuscript in preparation